FACULTAD DE
CIENCIAS

Theoretical treatment of inelastic processes in atomic collisions involving one and many electron systems

A thesis submitted in partial fulfillment of the requirements for the Degree of Doctor of Theoretical Chemistry by

Alba María Jorge Palacios

Under supervision of

Dr. Clara Illescas Rojas

Resumen

En la primera parte de esta tesis se estudian colisiones de distintos iones con hidrógeno atómico, en el área de interés en fusión nuclear. Haces de deuterio o hidrógeno neutro son inyectados en el plasma en los reactores de fusión con el fin de calentarlo, y diferentes características propias del plasma pueden ser determinadas a través del estudio de los procesos atómicos existentes entre las partículas neutras inyectadas y las impurezas iónicas presentes en dicho plasma. Por esta razón, se tratan de manera teórica las colisiones de iones desnudos con hidrógeno, tanto en su estado fundamental como primer excitado ($n = 2$). Concretamente, hemos utilizado el método CTMC (Método de Trayectorias Clásicas de Monte Carlo) para el estudio de las colisiones C^{q+} + H($1s$) ($q = 1, 5$), C^{6+} + H($n = 2$) y N^{7+} + H($n = 2$). La colisión Be^{4+} + H($1s$) ha sido también estudiada con un método semiclásico, el GTDSE (método de resolución de la Ecuación de Scrödinger Dependiente del Tiempo en una Grilla). Se propone el uso de una ley de escala para el cálculo de secciones parciales n y nl de captura entre iones desnudos e hidrógeno en estado fundamental. Se presenta así mismo un estudio del rango de validez de los distintos métodos teóricos usados, en función de la energía y niveles de captura en los que son válidos cada uno.

Debido a la importancia que está adquiriendo el estudio de colisiones que involucran moléculas y clusters, en la segunda parte de esta tesis se trata el estudio clásico de colisiones que implican más de un electrón. En este respecto, como iniciación al tratamiento a los sistemas multielectrónicos, estudiamos las colisiones de H($1s$) + H($1s$) y H^+ + H^-($1s^2$), considerando los dos electrones activos, estudiando especialmente el problema clásico que supone la descripción de un átomo o ión con más de un electrón activoPasamos al estudio de sistemas más complejos considerando el blanco de argon y los proyectiles He^{2+}, Li^{2+}, C y C^+, utilizando el mismo tratamiento clásico además del uso del método estándar de tratamiento de procesos múltiples IPM (Modelo de Partículas Independientes). Estudiamos la validez de considerar a todos los electrones de una misma subcapa como equivalentes.

Abstract

In the first part of this thesis we treat collisions of different ions with atomic hydrogen, in the scope of fusion research. Beams of neutral hydrogen and its isotope deuterium are injected in the plasma core for a heating purpose, and different characteristics of the plasma can be obtained through the study of the atomic processes occured between the neutral particles and the ionic impurities existing in the plasma. For this reason, we have studied collisions of bare and dresses ions with hydrogen in both the ground and first excited state. Particularly, we apply the CTMC (Classical Trajectory Monte Carlo) method to the study of the collisions $C^{q+} + H(1s)$ $(q = 1, 5)$, $C^{6+} + H(n = 2)$ and $N^{7+} + H(n = 2)$. The collision $Be^{4+} + H(1s)$ is also studied with a semi-classical method, the GTDSE (Grid Time Dependent Scrödinger Equation). An scaling law to determine state-resolved electron capture in collisions of bare ions with ground state hydrogen is also presented. We study the range of applicability of the different theoretical methods which have been used, with respect to the energy and shells domains where they are valid.

Due to the importance that collisions with molecules and clusters is adquiring recently, in the second part of this thesis we propose a classical approach to treat many-electron collisions. In this respect, we first study the $H(1s) + H(1s)$ and $H^+ + H^-(1s^2)$ collisions by considering two active electrons, dealing with the classical problem of a two-electron atom with a new approach. We extend this to to the treatment of collisions involving the projectiles He^{2+}, Li^{2+}, C and C^+ impinging on argon, using also standard methodologies, such as the IPM (Independent Particle Model), to study more than two electron processes. We study the validity of considering all the electrons in the same sub-shell as equivalent.

Agradecimientos

En primer lugar quiero agradecer al Ministerio de Economía y Competitividad por haber financiado la Beca FPI con la que he podido realizar mi doctorado, en el proyecto con referencia ENE2011-28200, y la estancia de tres meses que realicé en el Instituto de Astronomía y Física del Espacio de Buenos Aires, Argentina, gracias a la ayuda con número de referencia EEBB-I-14-09081.

En segundo lugar quiero agradecer al grupo que me acogió para realizar esta tesis, a los Luises, Ismanuel, Jaime, y a mi directora de tesis, Clara, sin la que este trabajo no hubiera sido posible. Gracias Luis por haberme explicado las dudas que me han ido surgiendo estos años, fuesen de la índole que fuesen, y por haber tenido siempre un rato para mí. Gracias Jaime por haberme explicado pacientemente (una o varias veces) como manejarme con el grid. Y a Bernard, que desde la distancia siempre ha estado ahí para dar ideas, explicarme y tranquilizarme. Gracias a todos por acogerme estos años.

Quiero agradecer también a todo el grupo de atómica del IAFE, en Buenos Aires, que me recibió y cuidó maravillosamente durante los tres meses que estuve allí. A Claudia, Jorge, Diego, Carlos, gracias por el gran trato que me distéis. Gracias especialmente a Sebas, que además de discutir conmigo de doble ionización me descubrió el mate, a Galeano, y me hizo escuchar a Mercedes Sosa y Leon Gieco (cierto día de Octubre), enseñanzas fundamentales para gallegos en general. Gracias. Y un agradecimiento especial a María Silvia, no has dejado de estar ahí para ayudarme en ningún momento. Gracias por todo lo que has ido haciendo por mí, por todas las explicaciones, cuidados y fuerza que me has dado.

También quiero agradecer a todas las personas que quiero y que me han acompañado en este camino. A mi querido sector derecho, que comenzó conmigo en la Autónoma allá por finales de septiembre de 2005. A los que decidieron tomar un camino más pedagógico, opresivo o, simplemente de libertad, como Germi, Nacho e Isa. Al primero, por ser siempre tan generoso tanto a la hora de enseñar como de aprender, aunque a veces también se ponga en plan *generoso*. A Nacho, por estar ahí siempre para sacar el lado bueno de la vida. Cada *Nachada* es un puñadito de amor y fuerza que nos transmites. Y además, ir al río a buscar dratinis y no hablar de ciencia es de las mejores formas de despejarse. A Isa, porque aunque no te lo haya dicho nunca (debía estar ocupada recordándote tu vejez), eres un ejemplo de valentía y lucha para mí. Y porque te aseguro que sigo rememorando aquel trabajo de técnicas II para armarme de fuerza. A Juanki, porque desde tiempos del messenger hasta hoy hemos compartido problemas y (casi) siempre hemos conseguido resolver-

los con carcajadas y cariño. Y, con todas las cosas que nos quedan por hacer, espero que sigamos utilizando la misma estrategia. Además, sé que siempre tendrás varias chaquetas y gafas que prestarme si se me rompen las mías. El mundo es menos pesado sabiendo esto. A Paco, al que me gustaría concederle el premio TSQB de esta tesis y mandarle mucho ánimo, ya tienes que estar cerca de acabar con todos los cafés pendientes. Hemos compartido muchas cosas en esta tesis, desde las angustias iniciales a las angustias finales, pasando por las muchas ansgustias intermedias. Estoy segura de que nos quedan muchas angustias por compartir. Y muchos Ap (de ésto sí que estoy segura, pero al 100%). A mi querida Natalita, porque tú has estado ahí desde el 30 de junio del 2005. Porque has sido y eres mi compañera de camino, aquella con la que compartía los mismos tropiezos en las mismas piedras (y es que todavía nos pasa...). Porque hemos viajado juntas por la desesperación y hemos comprobado que el camino más corto entre dos puntos, concretamente Plaza Castilla y Cantoblanco, puede pasar por Vallekas (aunque Lega mole más). Ya que uno tiene que equivocarse, mejor hacerlo en la mejor compañía. Gracias por cuidarme siempre. A Ana, porque has sido y eres esa persona siempre presente, ya sea en mar o montaña, pasando frío en estaciones en obras de ciudades malditas o pasando mucho calor en Berlioz (bendita felpa), debatiendo acaloradamente sobre libertad o sobre cartas de expansión del bang. Gracias por estar, por redefinir la palabra confianza, por quererme como lo haces.

No puedo olvidarme tampoco del genial *sector centro*, consolidado en las mesitas de 13:30 a 14:30 durante estos últimos años. Porque resulta que había gente maravillosa en el sector izquierdo y cierto radicalismo no me permitió verlo antes. Por todas esas conversaciones con Willy, aunque no pudiésemos ponernos de acuerdo casi nunca. Por todas las sonrisas y ayuda que me ha regalado Ana, ojalá te hubiese descubierto antes. Por todos y cada uno de los chistes malos de Hugo, absolutamente todos han ayudado a hacer este camino más fácil. Por Jon, que nunca ha dicho una palabra más alta que la otra, ni jamás se ha quejado de nada, exactamente como yo. O sí. Lo bueno es que a veces esas discusiones venían bien para soltar pain. Y una mención especial a Marina, una de esas personas maravillosas que aparecen por azares de la vida y que se vuelven fundamentales. Eres un ejemplo para mí, en muchos sentidos.

Y en un batiburrillo entre ambos sectores, quiero mencionar a mis queridos Javi y Héctor. Os ha tocado ir juntos en mis agradecimientos, no sé si os pasa a menudo. Cuesta conoceros, no os voy a engañar, pero sin duda la espera merece la pena. Haberte conocido bien y llegar a quererte sigue siendo el único

buen motivo que me han dado para estar contenta con esto de hacerse mayor, Javi. Porfi, ten cuidado con los pogos. Y de *kumpi* qué voy a decir, que me tienes caladísima y yo sigo sin poder descubrir qué tuitstar eres. Pero algo te he calado ya, y sé que detrás de tus chistes y caretas hay una persona genial a todos los niveles. Y muy popular.

Quiero agradecer también a mis compañeros de despacho, Darek y Alberto, por haber compartido conmigo estos años, tanto con problemas con el ccc como con las cervezas y discusiones de política. Gracias chicos.

También quiero dar las gracias a mis pepineras y pepineros por haber estado a mi lado estos años. A Ito, que ha estado ahí para socorrerme y charlar durante horas, especialmente estos últimos años. A Nita, porque empezamos con aquellos gritos de espartanas y hemos acabado aquí, y porque ha sido un placer redescubrirte. A Isa y Moni, con las que llevo ya muchos años compartiendo ciclos de vida y en este, como en los anteriores, han jugado un papel protagonista. Gracias Isa, por tu punto de vista, porque a veces tus *isadas* son muy necesarias. Gracias Moni, por enseñarme siempre, por caminar a mi lado, por darme fuerza. Y gracias Luna, por haber llegado a este mundito, tu sonrisa ha dado luz a los días más nublados.

También gracias a todos los desconocidos que, desde stackoverflow y demás foros, me habéis ayudado con mis infinitas dudas sobre programación. Y a todos los que habíais tenido ya el mismo problema que yo, por agilizarme la resolución. A WebPlotDigitizer y a Detexify, herramientas muy usadas durante mi tesis. Y por supuesto, a *escijab*, porque sois muy necesarios y queda mucho camino que recorrer. 3HaHNe-BCeM!

Me gustaría añadir un agradecimiento especial a Betty Snyder Holberton (1917-2001). Betty fue seleccionada para la programación de ENIAC (Electronic Numerical Integrator And Computer), una de las primeras computadoras electrónicas, junto a otras cinco mujeres, Kathleen McNulty Mauchly Antonelli, Frances Bilas Spence, Betty Jean Jennings Bartik, Ruth Lichterman Teitelbaum y Marlyn Wescoff Meltzer, en el periodo de 1942 a 1955. Tras su paso por ENIAC, Betty trabajó en UNIVAC I (UNIVersal Automatic Computer I), la primera computadora comercial de uso no militar. Su trabajo consistió en mejorar los componentes hardware de UNIVAC I, pero fundamentalmente trabajó en lenguajes de programación y algoritmos. Betty Holberton es considerada una de las pioneras en los estándares de los lenguajes de programación FORTRAN y COBOL, además de estar involucrada en el desarrollo de algoritmos de implementación del método de montecarlo. En 1997 se convirtió en la única de las seis programadoras originales de la ENIAC en obtener el Premio Ada Lovelace, uno de los más altos honores concedidos en el campo

de la programación. Ese mismo año, junto con sus cinco compañeras en la ENIAC, ingresó al Women in Technology International Hall of Fame. Sin embargo, no sorprende saber que en su primer día de clases en la Universidad de Pennsylvania, el profesor de matemáticas de Betty le dijo que debería quedarse en su casa criando niños en lugar de perder tiempo tratando de obtener un título en matemáticas. Tampoco sorprende saber que la historia olvidó el trabajo de estas seis mujeres, siendo los ingenieros John Presper Eckert y John William Mauchly los que se llevaron el mérito por la construcción de ENIAC. Como mujer y como usuaria de FORTRAN, en ese orden, quiero agradecer con especial énfasis a Betty y a todas las mujeres que han trabajado en avanzar en programación a lo largo de los años. Esta tesis nunca habría sido posible sin ellas. Y no puedo dejar de hablar de mujer y ciencia sin recordar a todas mis compañeras, a mis chicas del espacio no mixto (aunque sean experimentales), a Marina, María Silvia, Claudia, Maitreyi, Chiara, Oriana, Rita, Karine, Ana, Alicia, Cristina, Katharina, y muchas otras. Gracias por la fuerza que me habéis transmitido todas. Y finalmente, y con una mención especial, a Clara Illescas, por haber formado conmigo el equipo que me ha llevado hasta aquí, por haberme ayudado a entender la importancia tanto de las *bepedebé* como de mantenerse fuerte. Gracias.

Por último, agradecer a mis padres y a mi hermano. Porque no sería nada sin vosotros. Gracias mami y gracias papi, por haberme querido, apoyado, aguantado y cuidado siempre. Gracias Agus, por tener siempre abrazos para mí. Os quiero.

A mis abuelitas

Contents

Chapter 1

Introduction

Ion-atom collisions have been a field of study from the early years of quantum mechanics [1, 2]. Beyond the challenge of describing basic processes as charge exchange at different collision energies, there is a current necessity of cross sections in different areas of research. One of these fields is fusion research, where a considerable advance toward exploitation of fusion as an energy source has been made with the ITER project. ITER will be an experimental tokamak reactor, designed to be the previous step to fusion power plants. Among the multiple ITER significant issues, we focus on the need of cross sections for plasma diagnostics. The charge exchange recombination spectroscopy (CXRS) method is used in tokamak fusion reactors to measure and analyze the plasma core characteristics, such as impurity ion densities or temperature [3]. Neutral beam (NB) injection, a common method to heat the plasma, is followed by electron capture to the existing impurities in the plasma, acting the neutral particles in the beam as electron donors. The constituents of the neutral beam are usually hydrogen or deuterium, and the plasma impurities are elements coming from sputtering of the plasma facing components (PFC) or which are introduced to dissipate the heat flowing to the divertor [4]. If electron capture occurs, it may give rise to an excited ion $A^*(nl)^{(q-1)+}$,

$$A^{q+} + \mathrm{H} \rightarrow A^*(nl)^{(q-1)+} + \mathrm{H}^+ \tag{1.1}$$

de-excitation of this ion will imply photoemission,

$$A(nl)^{(q-1)+} \rightarrow A(n'l')^{(q-1)+} + \gamma \tag{1.2}$$

CXRS is a powerful diagnostic tool which makes use of the light emitted by the plasma impurities due to de-excitation after the electron capture process.

CXRS usually makes use of visible lines and, consequently, the main interest is for $n \rightarrow n'$ transitions in the visible wavelength range. Therefore, there is an special interest in n-resolved electron capture cross sections to n-shells related to visible emission. The analysis of the emitted light also relies on variables such as the beam density, whose determination depends on describing properly the beam attenuation along the path in the plasma, or the population of excited states in the beam [5]. The description of both the beam penetration in the plasma and the charge-exchange process demands detailed accurate data of atomic processes [6, 7]. Not only electron capture cross sections are needed in the CXRS diagnostic, ionization or excitation of the neutral beam are processes which also have to be accurately described.

The atomic data and analysis structure (ADAS, [8]) is a database used in the fusion community which provides atomic data for fusion relevant processes. However, cross sections are scarce for collisions involving an initial excited state of the neutral atom of the beam. In contrast, more data is found for processes starting from the ground state of the neutral atom, but still there is a need to assess their uncertainties and to elaborate recommended sets of data for relevant fusion ions. A need of l distributions in state resolved capture cross sections is also found [9]. The first aim of this thesis is to provide cross sections for plasma fusion diagnostics.

Beside this necessity of recommended sets of atomic data for collisions of fusion-relevant ions with atomic hydrogen, in the previous years there has also been a growing interest on multielectronic systems. Multiple processes involving many-electron systems, from ions and atoms to molecules and clusters, are currently important areas of study. This is due not only to the theoretical challenge they imply, like description of electron-electron correlation, but also due to their applicability in different fields, like the study of collisions of charged particles with large molecules of biological interest [10]. For example, in hadron therapy [11, 12] tumor cells are damaged due to free electrons which attack their DNA [13], released from ionization of water molecules by charged particles beam. As a consequence, multiple capture and ionization of water by charged particles need to be accurately described. With respect to many-electron atoms, multiple electron loss and capture has been investigated in the last years both theoretically [14, 15, 16, 17] and experimentally [18, 19, 20, 21] for neon and argon targets, and special interest has been focused on collisions involving active electrons in both the target and projectile.

During this thesis we have worked with classical and quantal descriptions for the considered systems. The Classical Trajectory Monte Carlo (CTMC) method [22] has been extensively applied in the description of atomic colli-

sions in the last fifty years. In the energy region of the future ITER beam [23], $E \approx 100$ keV/amu, ionization, electron capture and excitation are competitive processes, and CTMC is capable of describing these three inelastic processes [24, 25, 26], providing reliable total cross sections for $E \gtrsim 15$ keV/amu. The applicability of CTMC is usually restricted to one-active-electron dynamics, since many-electron systems are classically unstable and subject to artificial autoionization. Different approaches to solve this problem have been proposed through the years, such as softening the electron-electron interaction by describing the active electrons in terms of Gaussian density distributions [27], or preventing artificial autoionization by adding to the electronic Hamiltonian a repulsive potential which prevents the electrons approaching too close to each other [28, 29]. We propose a new point of view to deal classically with two-active electrons systems.

We have also studied collisions with a quantal method which solves numerically the Time Dependent Schrödinger Equation in a grid of points (GTDSE), with a modified version of the GTDSE package, originally designed for nuclear processes in molecular dynamics [30], to treat electron dynamics. This method is valid in the whole considered energy range of this thesis (10-500 keV/amu).

In Chapter 2 we explain the different theoretical methods which have been applied during this thesis.

Chapter 3 is dedicated to collisions involving one active electron and of interest in fusion research. In this respect, we study classically electron capture for all the charges of a C^{q+} ion impinging on $H(1s)$, we analyze the existing uncertainties for Be^{4+} impinging on $H(1s)$ with recent quantal calculations, we provide an scaling law for nl- and n-resolved electron capture cross sections of bare ions with ground-state hydrogen and we treat collisions of C^{6+} and N^{7+} with excited hydrogen in section (3.1.3). These systems are studied within the scope of fusion research and consequently the involved ions and the collision energies have been chosen accordingly.

The second part of this thesis is focused on many electron systems, treating first two-active electron collisions for both two and one collision centers in Chapter 4. This study starts with the most simple collisional systems, $H(1s) + H(1s)$ and $H^+ + H^-(1s, 1s)$ and has been extended to more complex systems in Chapter 5. This chapter is devoted to the argon target, where we treat collisions of bare and dressed projectiles, both ions and clusters, making use of standar multiple electron models like the Independent Particle Model (IPM) and Independent Atom Electron model (IAE) [31, 32].

A summary of the studied systems, as well as general conclusions, will be given in Chapter 6.

Chapter 2

Theory

General considerations

Units

In this thesis, all the quantities are expressed in atomic units, in which,

$$\hbar = q_e = m_e = 1 \tag{2.1}$$

The cross sections are expressed in $[cm^2]$, and are functions of the impact projectile energy, which is given in $[\frac{\text{keV}}{\text{amu}}]$. An amu (atomic mass unity) is equal to the proton mass ($\sim 1837\ m_e$).
The relation between the energy and the collision velocity, for a non-relativistic system in atomic units, is:

$$E\left(\frac{keV}{amu}\right) = 25v^2(a.u.)^2 \tag{2.2}$$

Quantum approach

An ion-atom collision between two particles B (target) and A (projectile), with charges q_B and q_A respectively, and one active electron e, may give rise to the following processes:

$$A^{q_A}+B^{q_B}(nlm) \rightarrow \begin{cases} A^{q_A} + B^{q_B}(n'l'm') & \text{Elastic + Excitation} \\ A^{(q_A-1)}(n''l''m'') + B^{(q_B+1)} & \text{Electron capture} \\ A^{q_A} + B^{(q_B+1)} + \text{e} & \text{Ionization} \end{cases} \tag{2.3}$$

To describe them, we have to solve the three-body movement. A suitable Jacobi coordinate system must be chosen depending on which situation we want to describe:

1. System A + (B, e). The first Jacobi vector ($\boldsymbol{r}_1$) joins the target with the electron and the second ($\boldsymbol{R}_1$), the center of mass of this pair with the projectile. The reduced masses are:

$$\mu_{Be} = \frac{m_e M_B}{m_e + M_B} \qquad \mu_{A(B,e)} = \frac{M_A(M_B + m_e)}{M_A + M_B + m_e} \tag{2.4}$$

2. System (A, e) + B. The first Jacobi vector ($\boldsymbol{r}_2$) joins the projectile with the electron and the second ($\boldsymbol{R}_2$), the center of mass of this pair with the target. The reduced masses are:

$$\mu_{Ae} = \frac{m_e M_A}{m_e + M_A} \qquad \mu_{B(A,e)} = \frac{M_B(M_A + m_e)}{M_A + M_B + m_e} \tag{2.5}$$

3. System (A, B) + e. The internuclear vector ($\boldsymbol{R}$) is the first Jacobi vector, being the second the one ($\boldsymbol{r}$) which joins their center of mass with the electron. The reduced masses are:

$$\mu_{AB} = \frac{M_A M_B}{M_A + M_B} \qquad \mu_{e(A,B)} = \frac{m_e(M_A + M_B)}{M_A + M_B + m_e} \tag{2.6}$$

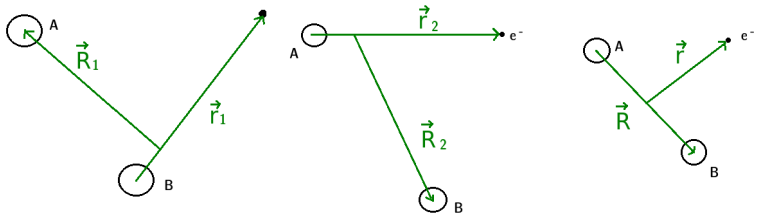

Figure 2.1: Illustration of the diffeent coordinate system.

The two first coordinate systems are useful to describe the initial state in which the electron belongs to the target, and the final state in which the electron has been captured by the projectile. The third one is practical for the intermediate situation when the three particles are close.
The corresponding hamiltonian is:

$$H = T + V \tag{2.7}$$

where T depends on which system we have chosen. As an example, for the third system we have:

$$T = -\frac{1}{2\mu_{AB}}\nabla^2_{\boldsymbol{R}} - \frac{1}{2\mu_{e(A,B)}}\nabla^2_{\boldsymbol{r}} \tag{2.8}$$

and

$$V = -\frac{Z_B}{r_{Be}} - \frac{Z_A}{r_{Ae}} + \frac{Z_A Z_B}{R} \tag{2.9}$$

being r_{Be} and r_{Ae} the distances between the electron and the target and projectile respectively, and R the internuclear distance. The time-independent Schrödinger equation for a given energy E is:

$$H(\boldsymbol{r}, \boldsymbol{R})\Psi(\boldsymbol{r}, \boldsymbol{R}) = E\Psi(\boldsymbol{r}, \boldsymbol{R}) \tag{2.10}$$

where Ψ is the wavefunction for the system. The boundary conditions are expressed in the initial and final coordinate systems.

$$\Psi(\boldsymbol{r}_1, \boldsymbol{R}_1 \to \infty) \sim e^{i\boldsymbol{k}_i \boldsymbol{R}_1}\phi_i^B + \sum_f \frac{e^{ik_f R_1}}{R_1} f_{if}(\theta)\phi_f^B \tag{2.11}$$

The wavefunction is written in terms of a superposition of an incident plane wave and a sum of spherical waves, with a difussion amplitude $f_{if}(\theta)$ which describe the elastic and inelastic processes. The ϕ_i^B and ϕ_f^B are the atomic orbitals associated to the initial and final state of the target, with energies E_i and E_f, respectively. $\boldsymbol{k}_i$ and $\boldsymbol{k}_f$ are the initial and final momenta of the projectile:

$$\cos(\theta) = \hat{\boldsymbol{k}}_i \cdot \hat{\boldsymbol{k}}_f \tag{2.12}$$

$$E = \frac{k_i^2}{2\mu_{A(B,e)}} + E_i = \frac{k_f^2}{2\mu_{A(B,e)}} + E_f \tag{2.13}$$

In the charge-exchange channel, we have:

$$\Psi(\boldsymbol{r}_2, \boldsymbol{R}_2 \to \infty) \sim \sum_f \frac{\mathrm{e}^{\mathrm{i}k'_f R_2}}{R_2} f'_{if}(\theta)\phi_f^A \tag{2.14}$$

with

$$E = \frac{k_f'^2}{2\mu_{B(A,e)}} + E'_f \tag{2.15}$$

where ϕ_f^A are the atomic orbitals corresponding to the projectile, with energies E'_f. Both ϕ^B and ϕ^A are eigenvectors of the atomic Hamiltonians of the target

and the projectile respectively, and the associated energies are the discrete corresponding eigenvalues. Expressions (2.11) and (2.14) will correspond to excitation ($E_f < 0$) and capture ($E'_f < 0$) collision channels respectively. The wave functions which fulfill these conditions will have another component corresponding to positive energies ($E_f > 0$) and ($E'_f > 0$), which is the case of the ionization process.
The amplitudes of expressions (2.11) and (2.14) are directly related to the cross sections, since the quantities $|f_{if}(\theta)|$ and $|f'_{if}(\theta)|$ are proportional to the experimentally measurable differential cross section $\mathrm{d}\sigma/\mathrm{d}\Omega$ [33]

$$\frac{\mathrm{d}\sigma}{\mathrm{d}\Omega} = \frac{\text{outgoing flux/solid angle}}{\text{incoming flux/area}} = |f|^2 \tag{2.16}$$

being Ω the solid angle around the $\boldsymbol{k}_i$. Due to the cilindrical symmetry of the system, the integration around ϕ is simply 2π and we have the total cross section for excitation,

$$\sigma = 2\pi \int |f_{if}(\theta)|^2 \mathrm{d}\cos(\theta) \tag{2.17}$$

and for electron capture,

$$\sigma = 2\pi \int |f'_{if}(\theta)|^2 \mathrm{d}\cos(\theta) \tag{2.18}$$

Eikonal approximation

In the range of impact velocities that are of interest in this work (0.2-5 a.u.), the de Broglie wave length of the relative movement of the nucleus λ_{rel} is very small. For example, in the collision of Be^{4+} with H, for a given velocity of 0.2 a.u. (the smallest velocity we have worked with) we have

$$\lambda_{rel} = \frac{2\pi}{k} = \frac{2\pi}{\mu v} = 1.9 \cdot 10^{-2} \text{a.u.} \tag{2.19}$$

The corresponding wave length for the electron, being captured, ionized or remaining in the target is, at least, of order 1. Therefore, the wave vector $k = \frac{2\pi}{\lambda_{rel}}$ is very large, and both expressions (2.11) and (2.14) have strong oscillations. We can extract these oscillations with a phase of the type $e^{i\boldsymbol{kR}}$, being $\boldsymbol{k} = \mu\boldsymbol{v} = \sqrt{2E\mu}\hat{u}_{\boldsymbol{k}_i}$. This allow us to expand $\Psi(\boldsymbol{r}, \boldsymbol{R})$ on μ^{-1} powers:

$$\Psi(\boldsymbol{r}, \boldsymbol{R}) = e^{i\boldsymbol{kR}}(\psi_0(\boldsymbol{r}, \boldsymbol{R}) + \mu^{-1}\psi_1(\boldsymbol{r}, \boldsymbol{R}) + ...) \tag{2.20}$$

If we substitute (2.20) in the Schrödinger equation we have

$$e^{i\boldsymbol{k}\boldsymbol{R}}\left[-\frac{1}{2\mu}\nabla^2_{\boldsymbol{R}}-\frac{i}{\mu}\boldsymbol{k}\nabla_{\boldsymbol{R}}+H_{el}\right](\psi_0(\boldsymbol{r},\boldsymbol{R})+\mu^{-1}\psi_1(\boldsymbol{r},\boldsymbol{R})+...)=0 \quad (2.21)$$

with

$$H_{el}=-\frac{1}{2}\nabla^2_{\boldsymbol{r}}-\frac{Z_A}{r_{Ae}}-\frac{Z_B}{r_{Be}}+\frac{Z_AZ_B}{R} \quad (2.22)$$

where H_{el} is the Born-Oppenheimer electronic hamiltonian.
Since μ is a very large magnitude, we can neglect the terms of order larger than zero in μ^{-1}. This is called the Eikonal approximation. Therefore, we have:

$$[H_{el}-i\boldsymbol{v}\nabla_{\boldsymbol{R}}]\psi_0(\boldsymbol{r},\boldsymbol{R})=0 \quad (2.23)$$

The Eikonal approximation is equivalent to assume that most part of the outgoing flux is concentrated in a very small solid angle, $\cos\theta\simeq 1$. From now on, we can substitute ψ_0 by Ψ when adopting this approximation. Therefore the nuclear movement can be described with the linear trajectory

$$\boldsymbol{R}=\boldsymbol{b}+\boldsymbol{v}t \quad (2.24)$$

where $\boldsymbol{b}=b\hat{u}_x$ is the impact parameter and $\boldsymbol{v}=\boldsymbol{k}/\mu=v\hat{u}_z$ is the nuclear relative velocity. The internuclear vector is simply expressed as in (2.24), what means that the collision plane is the OXZ plane. Using (2.24), the equation (2.23) can be written as follows

$$i\left(\frac{\partial\Psi(\boldsymbol{r},t)}{\partial t}\right)=H_{el}\Psi(\boldsymbol{r},\boldsymbol{R}) \quad (2.25)$$

which is the time-dependent Schrödinger equation and has to be solved for each rectilinear nuclear trajectory $\boldsymbol{R}$. This approximation is also called the Impact Parameter Approximation (IPA) [2], which is commonly used in the intermediate and high collision energy range. It has been checked [34, 24] that this approximation saves computing time without losing accuracy in total, partial and differential cross sections, and it is completely valid in the considered collision velocity range in this thesis.

Classical method: The Classical Trajectory Monte-Carlo Method (CTMC)

The Classical Trajectory Monte Carlo method (CTMC) for the treatment of atomic collisions was first developed by Abrines and Percival in 1966 [22]. It has been shown that it provides reliable total cross sections for both capture and ionization [35, 24, 36] processes for collision energies $E \gtrsim 15$ keV/amu and also, in general, for excitation cross sections [26]. We outline this method in the following.

Classical distribution functions

The classical correspondence of a quantum wave function is the electronic distribution function

$$\Psi(\boldsymbol{r}) \to \rho(\boldsymbol{r}, \boldsymbol{p}, t) \tag{2.26}$$

where $\rho(\boldsymbol{r}, \boldsymbol{p}, t)$ must satisfy Liouville equation

$$\frac{\partial \rho}{\partial t} = -[\rho, H_e] = -\frac{\partial \rho}{\partial \boldsymbol{r}}\frac{\partial H_e}{\partial \boldsymbol{p}} + \frac{\partial \rho}{\partial \boldsymbol{p}}\frac{\partial H_e}{\partial \boldsymbol{r}} \tag{2.27}$$

being $[\rho, H_e]$ the Poisson's bracket, and H_e is the classical electronic hamiltonian function, no longer an operator. To describe and solve the problem for an atom with an electron, a statistical colective of N ($\sim 10^6$) non-interacting particles is defined for each nuclear trajectory.

$$\rho(\boldsymbol{r}, \boldsymbol{p}, t) = \frac{1}{N}\sum_{j=1}^{N} \delta(\boldsymbol{r} - \boldsymbol{r}_j(t))\delta(\boldsymbol{p} - \boldsymbol{p}_j(t)) \tag{2.28}$$

The equations of motion can be obtained as follows

$$\frac{\partial \rho}{\partial t} = \frac{1}{N}\sum_{j=1}^{N}\left[\frac{\partial \delta(\boldsymbol{r} - \boldsymbol{r}_j)}{\partial t}\delta(\boldsymbol{p} - \boldsymbol{p}_j(t)) + \frac{\partial \delta(\boldsymbol{p} - \boldsymbol{p}_j)}{\partial t}\delta(\boldsymbol{r} - \boldsymbol{r}_j(t))\right] \tag{2.29}$$

Applying the chain rule

$$\frac{\partial \delta(\boldsymbol{x} - \boldsymbol{x}_j)}{\partial t} = \frac{\partial \delta(\boldsymbol{x} - \boldsymbol{x}_j)}{\partial \boldsymbol{x}}\frac{\partial \boldsymbol{x}}{\partial t} \tag{2.30}$$

we have

$$\frac{\partial \rho}{\partial t} = \frac{1}{N}\sum_{j=1}^{N}\left[-\dot{\boldsymbol{r}_j}\frac{\partial \delta(\boldsymbol{r} - \boldsymbol{r}_j)}{\partial \boldsymbol{r}}\delta(\boldsymbol{p} - \boldsymbol{p}_j(t)) - \dot{\boldsymbol{p}_j}\frac{\partial \delta(\boldsymbol{p} - \boldsymbol{p}_j)}{\partial \boldsymbol{p}}\delta(\boldsymbol{r} - \boldsymbol{r}_j(t))\right] \tag{2.31}$$

On the other hand, by substituting (2.28) in equation (2.27), we obtain

$$\frac{\partial \rho}{\partial t} = \frac{1}{N}\sum_{j=1}^{N}\left[-\frac{\partial \delta(\boldsymbol{r}-\boldsymbol{r}_j)}{\partial \boldsymbol{r}}\delta(\boldsymbol{p}-\boldsymbol{p}_j(t))\frac{\partial H}{\partial \boldsymbol{p}} + \frac{\partial \delta(\boldsymbol{p}-\boldsymbol{p}_j)}{\partial \boldsymbol{p}}\delta(\boldsymbol{r}-\boldsymbol{r}_j(t))\frac{\partial H}{\partial \boldsymbol{r}}\right] \tag{2.32}$$

The equations of motion in the classical collision treatment are therefore the Hamilton's equations:

$$\dot{\boldsymbol{r}}_j(t) = \frac{\partial H}{\partial \boldsymbol{p}_j(t)} \tag{2.33}$$

$$\dot{\boldsymbol{p}}_j(t) = -\frac{\partial H}{\partial \boldsymbol{r}_j(t)} \tag{2.34}$$

Initial conditions

Different classical initial distributions ρ have been proposed through the years [22, 37, 38, 39, 40, 41, 36] to proper describe the electron bound to the atomic target. A good initial distribution must fulfill the Liouville equation (2.27) and reproduce as good as possible the quantum radial and momentum densities, which are defined as:

$$\int_\Omega \mathrm{d}\Omega |\Psi(r,\theta,\phi)|^2 \tag{2.35}$$

$$\int_\Omega \mathrm{d}\Omega |\Psi(p,\theta,\phi)|^2 \tag{2.36}$$

In the following, we present the two initial distributions we have used along this thesis, the Microcanonical and the Hardie and Olson ones, with a brief introduction to the last based on the Eichenauer distribution.

The Microcanonical distribution

Proposed by Abrines and Percival [22] in 1966, the microcanonical initial distribution is a collective of classical trajectories with the exact binding energy E of the electron bound to the atom we want to describe. It is expressed as follows:

$$\rho_M(\boldsymbol{r},\boldsymbol{p};Z,E) \equiv \frac{1}{K}\delta(H_0(\boldsymbol{r},\boldsymbol{p})-E) \tag{2.37}$$

where δ is the delta function, K is the normalization constant and H_0 is the hamiltonian for the isolated atom:

$$H_0(\boldsymbol{r},\boldsymbol{p}) = \frac{p^2}{2\mu} + V(r) \tag{2.38}$$

To obtain the value of K we use the normalization conditions:

$$\int \mathrm{d}\boldsymbol{r}\rho_M(\boldsymbol{r}) = 1 \quad \text{with} \quad \rho_M(\boldsymbol{r}) = \int \mathrm{d}\boldsymbol{p}\rho_M(\boldsymbol{r},\boldsymbol{p};Z,E) \tag{2.39}$$

$$\int \mathrm{d}\boldsymbol{p}\rho_M(\boldsymbol{p}) = 1 \quad \text{with} \quad \rho_M(\boldsymbol{p}) = \int \mathrm{d}\boldsymbol{r}\rho_M(\boldsymbol{r},\boldsymbol{p};Z,E) \tag{2.40}$$

Since the microcanonical distribution is a function of the hamiltonian, it automatically satisfies the Liouville equation:

$$\frac{\partial\rho_M}{\partial t} = -\frac{\partial\rho_M}{\partial H}\frac{\partial H}{\partial \boldsymbol{r}}\frac{\partial H}{\partial \boldsymbol{p}} + \frac{\partial\rho_M}{\partial H}\frac{\partial H}{\partial \boldsymbol{p}}\frac{\partial H}{\partial \boldsymbol{r}} = 0 \tag{2.41}$$

In order to obtain (2.37), six random independent variables (A_0) must be chosen to describe the phase space of the active electron in the atom. For each of them, the microcanonical distribution must fulfill

$$\rho(A_0) = \int \mathrm{d}\boldsymbol{r}\mathrm{d}\boldsymbol{p}\rho(\boldsymbol{r},\boldsymbol{p})\delta(A(\boldsymbol{r},\boldsymbol{p}) - A_0) = \text{constant} \tag{2.42}$$

The energy E is one of the variables and the other five must be chosen accordingly to (2.42). The selection of these five variables depends on the potential involved in (2.38). We have employed two different sets for Coulomb (bare ions) and non-Coulomb (dressed ions) potentials, depending on the studied collision. In the following we explain how to construct a microcanonical distribution depending on the considered potentials.

1. **Pure Coulomb potential** For initial distributions describing hydrogen or hydrogen-like ions the other five random variables are [42]

$$\begin{array}{lll} \beta = \frac{L^2}{L^2_{max}} \in (0,1) & \cos(\theta) \in (-1,1) & \\ \phi \in (0,2\pi) & \phi_p \in (0,2\pi) & \tau \in (0,2\pi) \end{array} \tag{2.43}$$

   where L is the angular momentum, θ and ϕ are the polar angles of $\boldsymbol{r}$, ϕ_p the azimutal angle of $\boldsymbol{p}$ and τ is a random time of integration of the Hamilton equations of the electron orbiting around the target.
   In the case of central forces in classical mechanics, for a particle with a fixed value of energy E, Kepler's laws are satisified and the angular momentum $\vec{L} = \boldsymbol{r} \times \boldsymbol{p}$ is conserved. The value of β varies between 0 for a rectilinear trajectory to 1 for a circular one, in which $L = L_{max} = Z/\sqrt{2E}$.
   In order to obtain initial conditions in the phase space (x, y, z, p_x, p_y, p_z),

with the chosen variables, a relation is needed: In the perihelion, the vectors $\boldsymbol{r}$ and $\boldsymbol{p}$ are perpendicular, therefore:

$$L^2 = r^2p^2 \rightarrow \beta = \frac{2E}{Z^2}r^2p^2 \tag{2.44}$$

And with the condition $E = \frac{p^2}{2} - \frac{Z}{r}$ we can find the values of r, p and θ_p

$$r = \frac{Z}{2E}(1 + \sqrt{1-\beta}) \tag{2.45}$$

$$p = \sqrt{2\left(E + \frac{Z}{r}\right)} \tag{2.46}$$

$$\theta_p = -\arctan\left(\frac{1}{\tan\theta \;\; \cos(\phi - \phi_p)}\right) \tag{2.47}$$

Computationally, the variables are defined as follows:

$$\begin{array}{ll} \beta = \text{random} & \theta = \arccos(-1 + 2 \cdot \text{random}) \\ \phi = 2\pi \cdot \text{random} & \phi_p = 2\pi \cdot \text{random} \end{array} \tag{2.48}$$

which are integrated for a time $\tau = 2\pi \cdot$random a.u., for each electron trajectory. Finally, the electron vector (x, y, z, p_x, p_y, p_z) can be expressed with the chosen variables:

$$\begin{array}{lll} x = r\sin\theta\cos\phi & y = r\sin\theta\sin\phi & z = r\cos\theta \\ p_x = p\sin\theta_p\cos\phi_p & p_y = p\sin\theta_p\sin\phi_p & p_z = p\cos\theta_p \end{array} \tag{2.49}$$

defining the initial phase space coordinates to be included in the collision dynamical calculation.

2. **Non-Coulomb potential** For non-Coulomb potentials, Reinhold and Falcon [43] proposed a different set of random variables which did not need to solve the Kepler orbit. As in the approach of Abrines and Percival, the initial state is described with a delta function, δ, in energy

$$f(\boldsymbol{r}, \boldsymbol{p}) = K\delta(E_i - p^2/2\mu - V(r)) \tag{2.50}$$

being K the normalization constant. The values of r are confined from 0 to r_0, the root of $E_i - V(r) = 0$. A transformation from $(\boldsymbol{r}, \boldsymbol{p})$ to a set of uniformly distributed variables is performed with two changes of coordinates, being the first:

$$(\boldsymbol{r}, \boldsymbol{p}) \rightarrow (E, r, \nu_r, \nu_p, \varphi_r, \varphi_p) \tag{2.51}$$

with these variables in the ranges:

$$E \in (-\infty, 0) \qquad r \in [0, r_0] \qquad \nu_r, \nu_p \in [-1, 1] \qquad \varphi_r, \varphi_p \in [0, 2\pi] \tag{2.52}$$

The distribution becomes

$$f = k\mu r^2 \sqrt{2\mu[E_i - V(r)]}\delta(E - E_i) \tag{2.53}$$

The second transformation is done from r to ω

$$\omega(r) = \int_0^r \mathrm{d}r' \mu r'^2 \sqrt{2\mu[E_i - V(r')]} \tag{2.54}$$

with $r < r_0$ and $0 < \omega(r) < \omega(r_0)$. This leads to

$$f(E, \omega, \nu_r, \nu_p, \varphi_r, \varphi_p) = k\delta(E - E_i) \tag{2.55}$$

with

$$\omega \in [0, \omega(r_0)] \qquad \nu_r, \nu_p \in [-1, 1] \qquad \varphi_r, \varphi_p \in [0, 2\pi] \tag{2.56}$$

We obtain the phase-space variables as follows:

$$\begin{aligned} &x = r\sqrt{1-\nu_r^2}\cos\varphi_r \qquad y = r\sqrt{1-\nu_r^2}\sin\varphi_r \qquad z = r\nu_r \\ &p_x = \sqrt{2\mu[E - V(r)]}\sqrt{1-\nu_p^2}\cos\varphi_p \\ &p_y = \sqrt{2\mu[E - V(r)]}\sqrt{1-\nu_p^2}\sin\varphi_p \\ &p_z = \sqrt{2\mu[E - V(r)]}\nu_p \end{aligned} \tag{2.57}$$

for random values of ω, ν_r, ν_p, φ_r, φ_p.

Once we have constructed the microcanonical distribution, for a Coulomb or non Coulomb potential, we can obtain the coordinate and momentum distributions separately:

$$\rho_M(r) = 4\pi r^2 \int \rho_M(\boldsymbol{r}, \boldsymbol{p})\mathrm{d}\boldsymbol{p} \tag{2.58}$$

$$\rho_M(p) = 4\pi p^2 \int \rho_M(\boldsymbol{r}, \boldsymbol{p})\mathrm{d}\boldsymbol{r} \tag{2.59}$$

which we compare to the quantum densities from (2.35) and (2.36). The accuracy of the CTMC method will depend strongly on how close are the quantum and classical distributions, in both coordinate and momentum spaces. We show in figure (2.2) this comparison for the description of one electron in the ground-state of the atomic hydrogen H(1s).

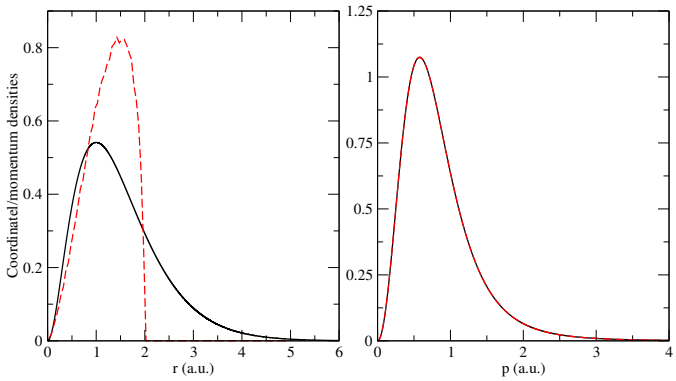

Figure 2.2: Comparison of the quantum (—) and microcanonical (– – –) distributions of H($1s$), for both the coordinate and momentum spaces, for the description of the H(1s) atom.

The main problem is the cut-off which appears irredeemably in the radial distribution, which can be observed in the left pannel of Fig. (2.2). This implies an overstimation of the probability of finding the electron around $r \sim 1.5$ a.u. and a nule probability in the radial tale, which represents around a 23% of the total quantum density. This bad description has motivated the research of alternative initial distributions [37, 38, 39, 40, 41, 36]. In order to obtain a classical radial density beyond the cutt-off value, we need less bound electron energies in the atom description. The radial distribution can be fitted with a continuum or discrete set of different bound energies, being this last approach the one used in this work. We explain in the following the proposed methods around this idea by Eichenauer [38] and Hardie and Olson [37].

Eichenauer distribution

Eichenauer [38] proposed in 1981 to use the Wigner distribution function $\rho_W(\boldsymbol{r}, \boldsymbol{p}, t)$ [44], which is defined like

$$\rho_W(\boldsymbol{r}, \boldsymbol{p}) = \frac{1}{(2\pi\hbar)^3} \int \mathrm{d}^3 r' \exp(\mathrm{i}\boldsymbol{p}\boldsymbol{r}'/\hbar)\psi^*(\boldsymbol{r} - \boldsymbol{r}'/2)\psi(\boldsymbol{r} + \boldsymbol{r}'/2) \tag{2.60}$$

This distribution function can be related to the quantum probability densities as:

$$\int \mathrm{d}\boldsymbol{p}\rho_W(\boldsymbol{r}, \boldsymbol{p}) = |\langle \boldsymbol{r}|\psi\rangle|^2 \tag{2.61}$$

$$\int \mathrm{d}\boldsymbol{r}\rho_W(\boldsymbol{r},\boldsymbol{p}) = |\langle \boldsymbol{p}|\psi\rangle|^2 \tag{2.62}$$

and therefore we have the exact quantum densities in $\boldsymbol{r}$ and $\boldsymbol{p}$.
As explained in [38], ρ_W is not positive everywhere and, therefore, $\int \rho_W \mathrm{d}\boldsymbol{p}\mathrm{d}\boldsymbol{r}$ can not be interpreted as a probabilty. From the associated energy distribution

$$\rho(E) = \int \mathrm{d}\boldsymbol{p}\mathrm{d}\boldsymbol{r}\rho_W(\boldsymbol{r},\boldsymbol{p})\delta(H(\boldsymbol{r},\boldsymbol{p}) - E) \tag{2.63}$$

we find that the mean value of energy is the exact one. For the case of H(1s) we have

$$\langle E\rangle = \int_{-\infty}^{+\infty} E\rho_W(E)\mathrm{d}E = -0.5 \text{ a.u.} \tag{2.64}$$

But it is also found that (2.63) does not vanish for positive energy values, as illustrated in figure (2.3). There is need to cut the distribution for certain values of E to avoid these problems. But, even doing this, the Eichenauer distribution does not fulfill the Liouville equation (2.27).

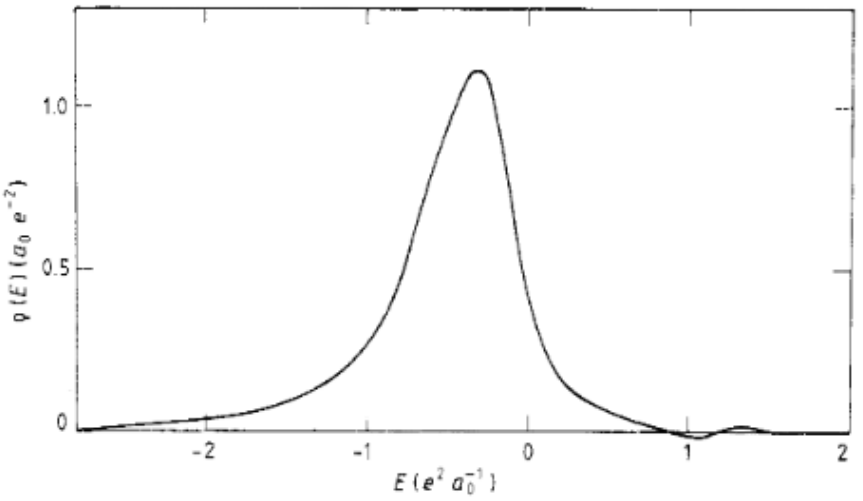

Figure 2.3: Eichenauer energy distribution (extracted from [38]) where it can be observed that it takes negative values and does not vanish for $E > 0$.

However, the main idea of having a distribution with different values of energy, with the correct mean value of the ionization potential energy and which fulfills (2.27), from where we can extract a probability value, can be done. It is explained in the next section.

Hardie and Olson distribution

The distribution proposed by Hardie and Olson in 1983 [37], also known as "hydrogenic initial distribution", consists in a weighted sum of microcanonical distributions with different energies which fits better the quantum radial distributions.

It is defined as a superposition of a set of microcanonical distributions, each of them with a different energy.

$$\rho_H(\boldsymbol{r}, \boldsymbol{p}; Z, E) \equiv \sum_{j=1}^{m} a_j \rho_M(\boldsymbol{r}, \boldsymbol{p}; Z, E_j) \tag{2.65}$$

where m is the number of microncanonical distributions considered. The weights a_j must satisfy

$$\sum_j a_j = 1 \tag{2.66}$$

and the weighted energy must be as closer as possible to the experimental ionization potential:

$$E = \sum_j a_j E_j \simeq U \tag{2.67}$$

The energies and weights are chosen, by least-squares fitting, to fit as better as possible the quantum radial distribution. In this thesis we have used a sum of ten microcanonical distributions, whose energies and weights can be observed in table (2.1)

Table 2.1: Energy and weights of the hydrogenic distribution of H($1s$) used in this work.

E_j (a.u.)	a_j
-1.25	0.031
-1.00	0.045
-0.80	0.069
-0.66	0.150
-0.50	0.188
-0.43	0.135
-0.36	0.159
-0.30	0.099
-0.26	0.032
-0.24	0.092

It can be checked in figure (2.4) the improvement in the radial distribution when only very small differences have been introduced in the momentum space.

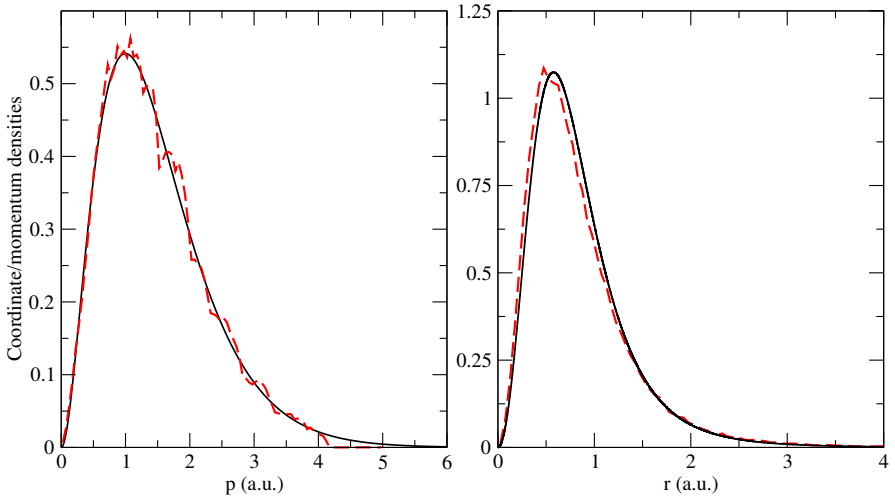

Figure 2.4: Hydrogenic (– – –) and quantum (—) radial and momentum probabilities compared in the case of H(1s).

The hydrogenic distribution satisfies automatically the Liouville equation (2.27) due to its own definition as a superposition of functions of the hamiltonian.

Selection of the processes and final probabilities

After a sufficiently long integration time of the Hamilton equations, $t_{max} \sim \frac{500}{v} - \frac{2000}{v} a.u.$, the final collision processes are selected by applying the well-known energy criteria. The final energies of the electron will associate each electron trajectory to a different process. Electrons with positive energies with respect to the target ($E_B > 0$) and projectile ($E_A > 0$) will imply ionization, and the bound states will be differentiated as electron capture ($E_A < 0$ and $E_B > 0$) and elastic/excitation ($E_A > 0$ and $E_B < 0$) processes.

Once this energy criteria has been applied, the probability corresponding to a process i (ionization, capture or excitation in the 1 electron scheme) will be obtained simply dividing the number of trajectories giving rise to this

process, N_i, by the total number of considered trajectories, N.

$$P_i(v,b) = \frac{N_i}{N} \tag{2.68}$$

For a given collision velocity, the integration of the opacity function $bP_i(v,b)$ over all impact parameters will lead to the associated total cross section:

$$\sigma_i = 2\pi \int_0^\infty \mathrm{d}b \cdot b \cdot P_i(v,b) \tag{2.69}$$

Partial electron capture cross sections

The final quantum states n and l for the trapped electron in a capture process by the impinging projectile can also be determined by using the Becker and Mckellar subdivision of the phase space [45]. The classical definition of n is

$$n_c = \frac{Z_A}{\sqrt{-2E_A}} \tag{2.70}$$

where E_A is the bound energy of the electron to the projectile. The classical 'boxes' are defined like

$$c^n \leq n_c < c^{n+1} \quad \equiv \quad E^n \leq E_A < E^{n+1} \tag{2.71}$$

with $E^n = -Z_A^2/2(c^n)^2$. Becker and McKellar proposed the following relation with $c^1 = 0$, obtained from the condition that the volume of the phase space per bin divided by h^3 equals the multiplicity of the n shell:

$$n\left(n-\frac{1}{2}\right)(n-1) \leq n_c^3 < n\left(n+\frac{1}{2}\right)(n+1) \tag{2.72}$$

For different values of n_c, one integer quantum n is directly associated.
A similar process was employed to obtain the partial nl cross sections [46]. The classical angular momentum must be normalized by n_c

$$L_c = \frac{n}{n_c}(\boldsymbol{r}_{Ae} \times \boldsymbol{p}_{Ae}) \quad \text{and} \quad l \leq L_c < l+1 \tag{2.73}$$

The cross sections σ_n and σ_{nl} are obtained integrating the opacity functions associated to the n and nl probabilities, $P_n(v,b)$ and $P_{nl}(v,b)$, obtained applying these binning partition to the ensemble of captured trajectories. Associated cross sections are obtained like in equation (2.69),

$$\sigma_n = 2\pi \int_0^\infty \mathrm{d}b \cdot b \cdot P_n(v,b) \tag{2.74}$$

$$\sigma_{nl} = 2\pi \int_0^\infty \mathrm{d}b \cdot b \cdot P_{nl}(v, b) \tag{2.75}$$

CTMC for two active electrons

In the classical approach we can deal with two active electron collisions. Apart from the two nucleus B (target) and A (projectile), with charges q_B and q_A, we can differenciate the two classical electrons e_1 and e_2. In this work, we have treated two types of collisions: those in which the two electrons are initially bound to different nucleus ($A^{q_A}(e_2) + B^{q_B}(e_1)$) and those in which they are bound initially to the target ($A^{q_A} + B^{q_B}(e_1, e_2)$). The procceses for the first reaction are named as follows

$$A^{q_A}(e_2)+B^{q_B}(e_1) \rightarrow \begin{cases} A^{q_A}(e_2) + B^{q_B}(e_1) & \text{Direct Elastic/Excitation} \\ A^{q_A}(e_1) + B^{q_B}(e_2) & \text{Exchange Elastic/Excitation} \\ A^{q_A}(e_2) + B^{(q_B+1)} + e_1 & \text{Direct target ionization} \\ A^{q_A}(e_1) + B^{(q_B+1)} + e_2 & \text{Exchange target ionization} \\ A^{(q_A+1)} + B^{q_B}(e_1) + e_2 & \text{Direct projectile ionization} \\ A^{(q_A+1)} + B^{q_B}(e_2) + e_1 & \text{Exchange projectile ionization} \\ A^{(q_A+1)} + B^{(q_B+1)} + e_1 + e_2 & \text{Double ionization} \\ A^{(q_A+1)} + B^{(q_B-1)}(e_1, e_2) & \text{Target electron capture} \\ A^{(q_A-1)}(e_1, e_2) + B^{(q_B+1)} & \text{Projectile electron capture} \end{cases} \tag{2.76}$$

and for the second reaction the processes are named as

$$A^{q_A}+B^{q_B}(e_1, e_2) \rightarrow \begin{cases} A^{q_A} + B^{q_B}(e_1, e_2) & \text{Elastic/Excitation} \\ A^{(q_A-1)}(e_2) + B^{(q_B+1)}(e_1) & \text{Mutual neutralization 1} \\ A^{(q_A-1)}(e_1) + B^{(q_B+1)}(e_2) & \text{Mutual neutralization 2} \\ A^{(q_A-1)}(e_2) + B^{(q_B+2)} + e_1 & \text{Transfer ionization 1} \\ A^{(q_A-1)}(e_1) + B^{(q_B+2)} + e_2 & \text{Transfer ionization 2} \\ A^{q_A} + B^{(q_B+1)}(e_1) + e_2 & \text{Detachment 1} \\ A^{q_A} + B^{(q_B+1)}(e_2) + e_1 & \text{Detachment 2} \\ A^{q_A} + B^{(q_B+2)} + e_1 + e_2 & \text{Double ionization} \\ A^{(q_A-2)}(e_1, e_2) + B^{(q_B+2)} & \text{Electron capture} \end{cases} \tag{2.77}$$

We can classically differenciate the processes in a general form, separating e_1 and e_2. When we compare our cross sections to available experiments we obviously treat the electrons as indistinguishables.

Four-body treatment

In order to treat the 4-body collision we need three Jacobi coordinates for the two nuclei and the two electron which can be anywhere. We have chosen the following Jacobi coordinate system:

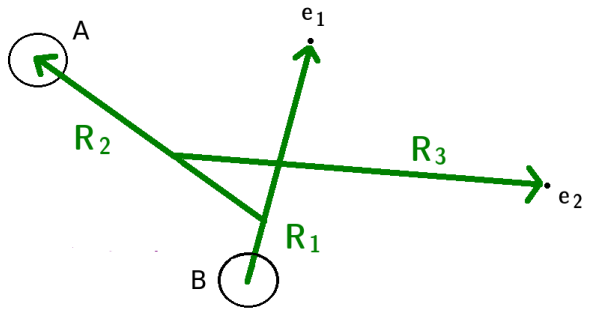

Figure 2.5: Jacobi coordinates for the 4-body system: the target B, the projectile A and the electrons e_1 and e_2.

The Jacobi coordinates and their corresponding momentum vectors are:

$$\begin{aligned} \boldsymbol{R}_1 &= \boldsymbol{r}_{e_1} & \boldsymbol{P}_1 &= m_B \boldsymbol{v}_{e_1} \\ \boldsymbol{R}_2 &= \boldsymbol{r}_A - \boldsymbol{r}_{\mathrm{CM}\{B-e_1\}} & \boldsymbol{P}_2 &= \mu_a(\boldsymbol{v}_A - \boldsymbol{v}_{\mathrm{CM}\{B-e_1\}}) \\ \boldsymbol{R}_3 &= \boldsymbol{r}_{e_2} - \boldsymbol{r}_{\mathrm{CM}\{A-B-e_1\}} & \boldsymbol{P}_3 &= \mu_b(\boldsymbol{v}_{e_2} - \boldsymbol{v}_{\mathrm{CM}\{A-B-e_1\}}) \end{aligned} \tag{2.78}$$

$\boldsymbol{r}_{e_1}$ ($\boldsymbol{r}_{e_2}$) is the vector which joins the target and e_1 (e_2), and $\boldsymbol{v}_{e_1}$ ($\boldsymbol{v}_{e_2}$) its corresponding velocity; $\boldsymbol{r}_A$ and $\boldsymbol{v}_A$, the projectile coordinate and velocity vectors from the origin, placed at the target B. $\boldsymbol{r}_{\mathrm{CM}\{B-e_1\}}$ and $\boldsymbol{v}_{\mathrm{CM}\{B-e_1\}}$ are the center of mass position and velocity vectors referred to the system $(B-e_1)$, while $\boldsymbol{r}_{\mathrm{CM}\{A-B-e_1\}}$ and $\boldsymbol{v}_{\mathrm{CM}\{A-B-e_1\}}$ those to the system $(A-B-e_1)$. They can be expressed as follows:

$$\boldsymbol{r}_{\mathrm{CM}\{B-e_1\}} = \frac{m_e}{m_e + M_B}\boldsymbol{R}_1 \tag{2.79}$$

$$\boldsymbol{v}_{\mathrm{CM}\{B-e_1\}} = \frac{m_e}{m_e + M_B}\boldsymbol{v}_{e_1} \tag{2.80}$$

$$\boldsymbol{r}_{\mathrm{CM}\{A-B-e_1\}} = \frac{m_e}{m_e + M_B + M_A}\boldsymbol{R}_1 + \frac{M_A}{m_e + M_B + M_A}\boldsymbol{r}_A \tag{2.81}$$

$$\boldsymbol{v}_{\mathrm{CM}\{A-B-e_1\}} = \frac{m_e}{m_e + M_B + M_A}\boldsymbol{v}_{e_1} + \frac{M_A}{m_e + M_B + M_A}\boldsymbol{v}_A \tag{2.82}$$

M_B, M_A and m_e are the masses of the target, projectile and electron. The reduced masses are

$$m_a = \frac{m_e M_B}{m_e + M_B} \quad \mu_a = \frac{M_A(M_B + m_e)}{M_B + M_A + m_e} \quad \mu_b = \frac{m_e(M_B + M_A + m_e)}{M_B + M_A + 2m_e} \tag{2.83}$$

Then, the hamiltonian for the 4-body (4b) problem is given by:

$$H_{4\mathrm{b}} = \frac{\boldsymbol{P}_1}{2m_a} + \frac{\boldsymbol{P}_2}{2\mu_a} + \frac{\boldsymbol{P}_3}{2\mu_b} - \frac{Z_B}{r_{e_1}} - \frac{Z_B}{r_{e_2}} - \frac{Z_A}{r_{A-e_1}} - \frac{Z_A}{r_{A-e_2}} + \frac{Z_B Z_A}{r_A} + \frac{1}{r_{12}} \tag{2.84}$$

where r_{A-e_1} and r_{A-e_2} stand for the distance between the projectile and the electrons e_1 and e_2, and r_{12} for the interelectronic distance.
The initial conditions in a collision with two electrons are given with two initial distributions, ρ_1 and ρ_2, each of them with N trajectories. Therefore, the total statistics for a two-active electron collision is $N \times N$.
It is known that the system in which two electrons are bound to the same nucleus is classically unstable and subject to artificial autoionization [47]. There are few stable configurations for two classical electrons bound to one nucleus [27], but under an external perturbation the stability is lost.
Several methods have been proposed to obtain an stable initial two-electron classical atom, such as the Heisenberg Core [28] developed by Kirschbaum and Wilets, the quasiclassical-trajectory Monte Carlo (CTMC) [48] from Cohen, or the dynamic target screening [49] by Montemayor and Schiwietz. These approaches add new potentials to the hamiltonian or modify the interelectronic potential so that the autoionization is prevented.
We focus first our attention in the two-electron system in which each electron is bound to a different nucleus. In order to study the classical instability of the two electrons bound to the same nucleus, we look at the last two processes from reaction (2.76). The energy conditions to be fulfilled in the formation of $A^-(e_1, e_2)$ or $B^-(e_1, e_2)$ are:

$$E_1 = \frac{p_{e_1 i}^2}{2\mu_{e_1 i}} + V_{e_1 i} < 0 \qquad E_2 = \frac{p_{e_2 i}^2}{2\mu_{e_2 i}} + V_{e_2 i} < 0 \qquad E_1 + E_2 + \frac{1}{r_{12}} < 0 \tag{2.85}$$

where i stands for A or B, and $p_{e_1 i}$, $\mu_{e_1 i}$, $p_{e_2 i}$ and $\mu_{e_2 i}$ are the relative momentum and reduced masses of the electrons with respect to the nucleus i. The classical instability of the $A^-(e_1, e_2)$ and the $B^-(e_1, e_2)$ will make them ionize at some point after they have been formed. For example, for the most simple reaction

$$\mathrm{H(1s)} + \mathrm{H(1s)} \tag{2.86}$$

we have that the probability of finding an H^- anion (in the target or projectile) falls as illustrated in figure (2.6)

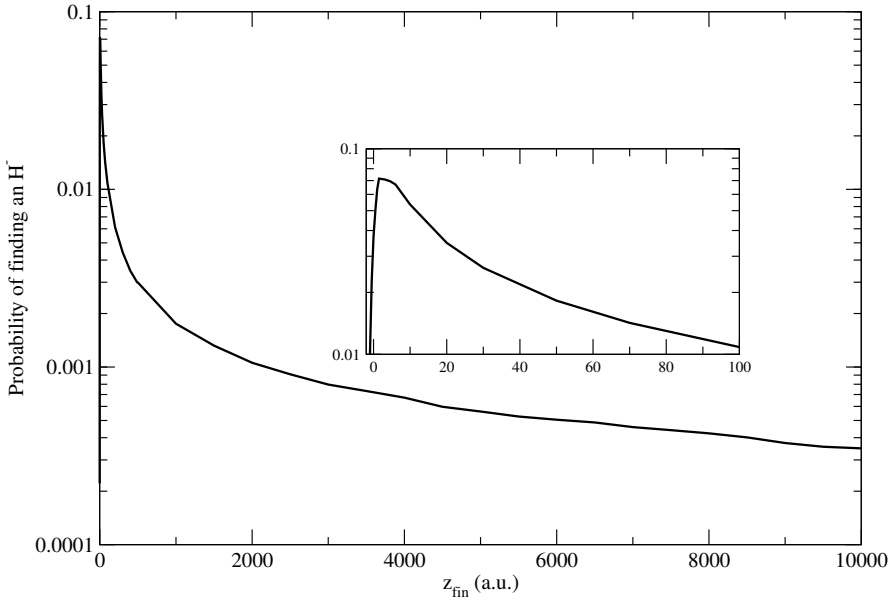

Figure 2.6: Probability of finding an H^- ion after the collision H + H, where $z_{fin} = vt = 1.095t$ a.u., and the impact parameter is of $b = 1$ a.u..

The illustrated collision is for a projectile velocity of 1.095 a.u. and impact parameter of 1 a.u. After some time t the probability converges to zero and, until then, we cannot extract a time-independent probability value. Note the 10^{-4} order for $t = 10^4/1.095$ a.u..
One of the first classical works which dealt with this collision system, from Olson in 1979 [50], obtained higher cross sections than the available measurements [51, 52]. This suggests that the calculations were stopped when the two nucleus were still close to each other. In fact, as stated in [47], Olson informed to Becker and MacKellar (in private communication) that *when he followed the trajectories for a longer time his H^- states did autodetach.* This implies that converged probability calculations lead to a nule probabiliy for the target and projectile electron capture processes and, therefore, this causes an overestimation of the ionization probabilities of reactions (2.76). It is important to state that the time-depen probability from figure (2.6) has, at some time of integration t, the real capure probability for H^- formation. Next, we present

an approach to solve these problems taking this fault into account.

The Switching approach

We introduce what we have called the Switching approach, developed in this thesis under the main assumption that the 4-body CTMC method is capable of reproducing the capture process for two active electrons to the same nucleus, but not the stability of the ion once it is formed. To solve this deficiency, we propose the following. Once the $A^{(q_A-1)}(e_1, e_2)$ or $B^{(q_B-1)}(e_1, e_2)$ from reaction (2.76) is formed, we switch the 4-body (4b) dynamical resolution of the problem to two 3-body (2x3b) problems, where the interaction potential for each electron changes from

$$V_{4\mathrm{b}} = -\frac{Z_i}{r_i} - \frac{Z_j}{r_j} + \frac{1}{r_{12}} \tag{2.87}$$

to

$$V_{3\mathrm{b}} = -\frac{Z_i}{r_i} - \frac{(Z_j - 1)}{r_j} - \frac{1}{r_j}(1 + \alpha r_j)\exp(-2\alpha r_j) \tag{2.88}$$

where j is the ion which the two electrons are bound to, while i is the fully ionized ion. The potential describing the interaction of an electron in the presence of a neutral H, forming therefore an H^-, has been determined with the Talman method [53, 54] (see Appendix D) and has been adjusted to a standar form of model potential

$$V_{mod}(r) = -\frac{(Z - 1)}{r} - \frac{1}{r}(1 + \alpha r)\exp(-2\alpha r) \tag{2.89}$$

with a value $\alpha = 0.65$ (a.u.)$^{-1}$. The bound energy of each electron is calculated at each integration time and, if one of the electrons is ejected, we switch back to the 4-body problem. This approach is easy to implement and yields converged and non-zero probabilities for the H^- formation, as it will be shown in the Chapter 4. This CTMC approach for two active electrons is free from any additional parameter that constrains the electronic repulsion until the unstable two-electron ion is formed.
We can apply this same approach to the second reaction of equation (2.77), whose equivalent to the H + H collision is

$$\mathrm{H}^+ + \mathrm{H}^-(\mathrm{e}_1, \mathrm{e}_2) \tag{2.90}$$

In this case we start with two 3-body problems to describe the initial H^- anion and we switch to a 4-body problem if any of the electrons is ejected during the

collision. Results of collisions (2.86) and (2.90) will be presented in Chapter 4, and a more complex system studied with this classical two-active electrons approach will be shown in Chapter 5.

Ground-state energy of the H^- anion

In order to study the initial two-electron atom with nuclear charge Z, we isolate it and let it evolve in time without any external perturbation. The time evolution is performed up to 1000 a.u. for each electron under the two monoelectronic hamiltonians

$$\begin{aligned} H_1 &= \frac{p_{e_1}^2}{2\mu} - \frac{Z-N_e}{r_{e_1}} - \frac{1+\alpha r_{e_1}}{r_{e_1}} \exp(-2\alpha r_{e_1}) \\ H_2 &= \frac{p_{e_2}^2}{2\mu} - \frac{Z-N_e}{r_{e_2}} - \frac{1+\alpha r_{e_2}}{r_{e_2}} \exp(-2\alpha r_{e_2}) \end{aligned} \tag{2.91}$$

$N_e = 1$, α and Z depend on the atom; $\mu = \frac{m_e M}{m_e+M}$, being M the mass of the nucleus; r_{e_1} and r_{e_2} are the distances from each electron to the nucleus; $\boldsymbol{p}_{e_1}$ and $\boldsymbol{p}_{e_2}$ are the corresponding momentum vectors associated to the Jacobi independent vectors $\boldsymbol{r}_{e_1}$ and $\boldsymbol{r}_{e_2}$.
At each integration step we can calculate the total energy associated to the bielectronic hamiltonian

$$H_{2\mathrm{e}} = \frac{p_1^2}{2\mu} + \frac{p_2^2}{2\mu} - \frac{Z}{r_{e_1}} - \frac{Z}{r_{e_2}} + \frac{1}{r_{12}} \tag{2.92}$$

$\boldsymbol{p}_1$ is equal to $\boldsymbol{p}_{e_1}$ and $\boldsymbol{p}_2$ is the momentum vector of e_2 with respect to the center of mass of the nucleus and e_1; r_{12} the interelectronic distance and $\mu = \frac{m_e(m_e+M)}{2m_e+M}$. We calculate this total energy for the most simple two-electron atomic systems in their ground state, H^- and He. First, we construct two initial microcanonical distributions, using the Reinhold and Falcon approach explained in section (2.2.2.1), for the two model potentials obtained with Talman's method [53, 54] (see Appendix D). In the case of the H^- anion we have $Z = N = 1$ and $\alpha = 0.65$ (a.u.)$^{-1}$, being the ionization potential $E = -0.027$ a.u.; for the He atom we have $Z = 2$, $N = 1$ and $\alpha = 1.75$ (a.u.)$^{-1}$, with $E = -0.9$ a.u. The time-integration is perfomed with the Hamilton equations associated to the modelled hamiltonians of the form (2.91), and the ionization potential E remains constant and equal to the initial values. The total energy $H_{2\mathrm{e}}$ from equation (2.92) oscillates between positive and negative values. We can determine the mean value of energy for each individual pair of trajectories, and extract an energy probability distribution $F(H_{2\mathrm{e}})$ of mean energies. From

this probability, we can extract the expected value of energy $\langle H_{2e} \rangle$ as follows

$$\langle H_{2e} \rangle = \int_{-\infty}^{\infty} H_{2e} F(H_{2e}) \mathrm{d}H_{2e} \tag{2.93}$$

The following results are determined for a total integration time of 1000 a.u. and a statistics of 10000 trajectories (each microcanonical distribution is composed of 100 trajectories). We find that the mean energy values for the H^- ion and He atom are, compared to their corresponding experimental total energies ϵ_{exp}, are

$$\langle H_{2e} \rangle^{H^-} = -0.450 \text{ a.u. to be compared to } \epsilon_{exp}^{H^-} = -0.5027 \text{ a.u.}$$
$$\langle H_{2e} \rangle^{He} = -2.89 \text{ a.u. to be compared to } \epsilon_{exp}^{He} = -2.90 \text{ a.u.}$$

In figure (2.7) we show the probability distribution $F(\langle h_{2e} \rangle)$ for the H^- ion and the He atom, respectively This analysis shows that the initial H^- anion is stable in time, with the two electrons bound with the experimental ionization potential, and the mean value of energy calculated with the total Hamiltonian is really close to the experimental one.

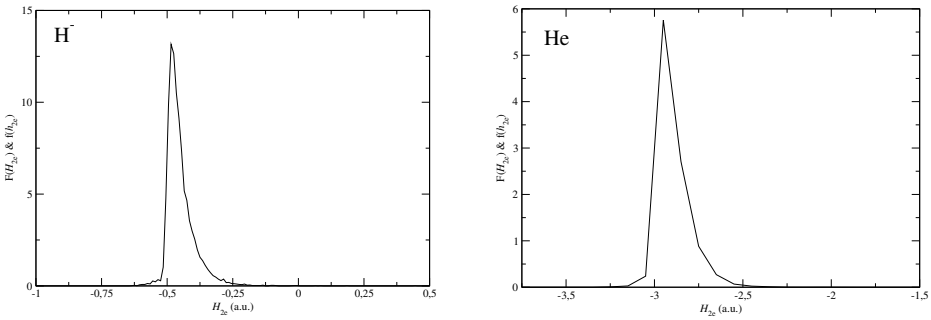

Figure 2.7: Total energy distribution probability $F(H_{2e})$ for the H^- anion (in the upper panel) and for the He atom (in the lower one), for 10000 trajectories during 1000 a.u.

A similar calculation could be done for more than 2 electron atoms. We show an example for the Li, Be, B and C atoms. For each nl state we can obtain an effective potential, assuming that each electron is perturbed by the nucleus and more inner electrons. For example, for the Be atom we obtain two effective potentials using the Talman's method [53, 54], one which models the two $1s$ electrons and one for the two $2s$ ones. Each of the $1s$ electrons are under the interaction of the nuclear charge and one frozen electron, while

each of the $2s$ electrons are perturbed by the nucleus and 3 frozen electrons. We can obtain 4 microcanonical distributions with these effective potentials, using the ionization potentials of the Be^{2+} (for the $1s$ electrons) and the Be (for the $2s$ ones). While the Hamilton equations are integrated in time for four independent monoelectronic systems with these effective potentials, we can calculate the total energy of the Be atom with

$$\sum_{i=1}^{4}\left(\frac{p_i^2}{2\mu}-\frac{4}{r_i}+\sum_{\substack{j=1\\ j\neq i}}^{4}\frac{1}{r_{ij}}\right) \tag{2.94}$$

being r_i the distance of the electron to the nucleus and r_{ij} the interelectronic distances. The mean value of this total energy is shown in table (2.2) for the beryllium and also for the Li, B and C atoms, compared to values obtained applying the Hartree Fock and Configuration Interaction methods (extracted from NIST [55]). These calculations have been integrated 100 a.u. of time, and the statistics have been around 10^4 trajectories. The good agreement shows how a many electron atom can be described with j independent classical monoelectronic systems, one for each electron and described with an effective potential. The parameters which have been used for these effective potentials can be found in section D.1 from Appendix D.

Table 2.2: Obtained total energy (in a.u.) compared to HF and CI calculations from NIST [55]

	Obtained value	HF value	CI value
H^-	-0.450	-0.487	-0.526
He	-2.890	-2.861	-2.909
Li	-7.238	-7.405	-7.490
Be	-14.373	-14.751	-14.618
B	-24.038	-24.532	-24.596
C	-36.622	-37.690	-37.777

Semiclassical method: Grid resolution of the Time Dependent Schrödinger Equation (GTDSE)

The Grid Time Dependent Schrödinger Equation (GTDSE) is a semiclassical method to treat one-electron collisions in which the TDSE is solved numerically in a 3-dimensional grid. We can represent the wavefunction Ψ with a vector whose elements are the wavefunction values at each grid point.

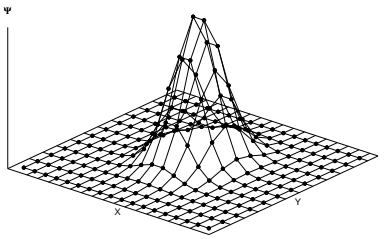

$$\Psi = \begin{pmatrix} \Psi(x_1) \\ \Psi(x_2) \\ \Psi(x_3) \\ \vdots \\ \Psi(x_7) \\ \Psi(x_8) \\ \vdots \\ \Psi(x_{n_{dim}}) \end{pmatrix}$$

where the dimension of Ψ is $n_i^x \cdot n_i^y \cdot n_i^z$.

Under the impact parameter approximation with the internuclear vector defined as in equation (2.24) $\boldsymbol{R}(t) = \boldsymbol{b} + \boldsymbol{v}t$, the electronic motion is described by the wave function $\Psi(\boldsymbol{r}, t)$, solution of the semiclassical equation:

$$\left[H_{\text{el}} - \mathrm{i} \left. \frac{\partial}{\partial t} \right|_{\boldsymbol{r}} \right] \Psi = 0 \tag{2.95}$$

with

$$H_{\text{el}}(\boldsymbol{r}, \boldsymbol{R}(t)) = -\frac{1}{2}\nabla_{\boldsymbol{r}}^2 + V_B + V_A \tag{2.96}$$

where V_B and V_A are the target and projectile potentials, and $\boldsymbol{r}$ is the electron position vector.

The diagonal elements of the Hamiltonian matrix include the values of the two involved potentials V_B and V_A, and in the non-diagonal positions elements those of the kinetic energy operator, which is a non-diagonal sparse matrix.

The present code is an adaptation of the GridTDSE package [30] which solves numerically the Eq. (2.95) for polyatomic molecules with N atoms in cartesian coordinates. The code takes advantage in molecular dynamics of the simplicity of the hamiltonian in these coordinates, even when the number of degrees of freedom is incresed [30].

Differentiation of the processes

For a given collision of an stripped ion with atomic hydrogen $A^{q+} + \mathrm{H}$ we differentiate the calculations in two systems, depending on the process of interest. For the electron capture process the projectile has to be positioned in the center of the grid, while for the excitation processes the target will be the one located in the center of the grid. During the collision, one nucleus will remain in the origin and the other will move through the grid until it gets out of it. The final wavefunction in the grid will be expressed in terms of the eigenvectors associated to the bound states of the nucleus located in the origin.

Electron capture channel

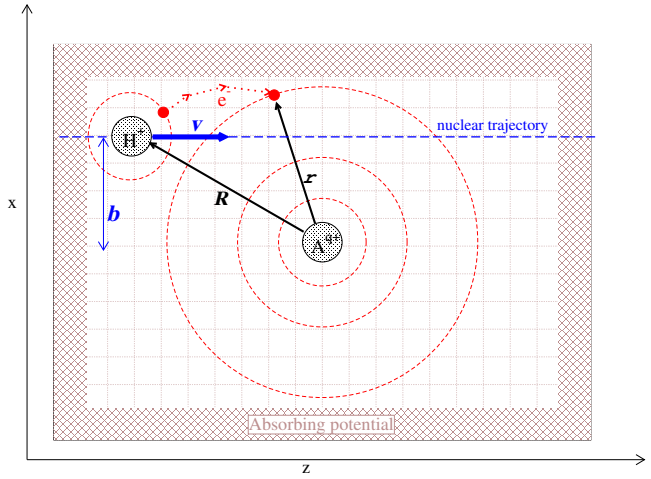

Figure 2.8: Electron capture scheme in GTDSE, where the projectile is in the origin.

The projectile A^{q+} is located in the origin of the grid and the target $\mathrm{H}(1s)$ in its initial position at t_0, which is $\boldsymbol{R}_0 = \boldsymbol{b} + z_{\mathrm{ini}}\hat{u}_z$, see figure (2.8). Its initial condition is the grid representation of the travelling $\mathrm{H}(1s)$ orbital, that represents the target atom.

$$\Psi(\boldsymbol{r}, t_0) = \varphi_{1s}^{\mathrm{H}}\left(\boldsymbol{r} - \boldsymbol{R}(t_0)\right) \exp\left(-\mathrm{i}\boldsymbol{v}\cdot\boldsymbol{r} - \mathrm{i}/2v^2 t_0\right) \tag{2.97}$$

The initial wavefuntion is propagated through the grid, as the target moves in a linear trajectory under the impact parameter approximation, and part of it will be captured by the fixed potential of the projectile. We will be able to obtain the P_{nlm} capture probabilities as the projection of the atomic orbitals of the $\mathrm{A}^{(q-1)+}$ on the wavefunction in the grid.

$$\mathrm{P}^{\mathrm{cap}}_{nlm} = |\langle \varphi^{A^{(q-1)+}}_{nlm} | \Psi \rangle|^2 \tag{2.98}$$

The calculation will finish when, after a sufficient long integration time, the potential of the target has evolved enough so that the $\mathrm{P}^{\mathrm{cap}}_{n}$ probabilities have converged.

Excitation channel

In this case, the target $\mathrm{H}(1s)$ is located in the origin of the grid and the travelling projectile A^{q+} at $\boldsymbol{R}_0$.

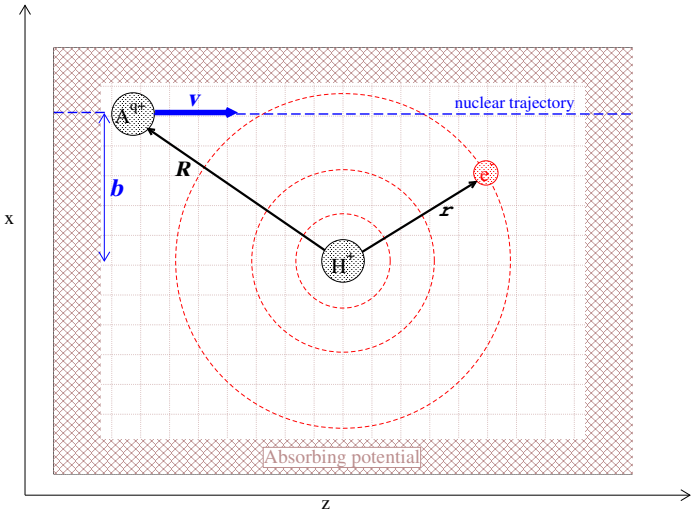

Figure 2.9: Excitation scheme in GTDSE, where the target is in the origin.

The wavefunction of the $\varphi^{\mathrm{H}}_{1s}$ is located in the origin of the grid, and the projectile is represented by a moving potential with the initial position $\boldsymbol{R}_0$. Equivalently to the previous case, we are able to obtain the excitation and elastic probabilities projecting the atomic orbitals of the H on the wavefunction which is in the grid.

$$\mathrm{P}^{\mathrm{exc}}_{nlm} = |\langle \varphi^{\mathrm{H}}_{nlm} | \Psi \rangle|^2 \tag{2.99}$$

The calculation ends when the projectile is far enough so that its potential does not affect anymore the converged P_n^{exc} probabilities.

Grid description

The grid has an extension of $-L_{\max} \leq q \leq L_{\max},\ q = x, z$ and $0 \leq y \leq L_{\max}$, where we have taken advantage of the symmetry of the Hamiltonian upon reflection in the collision plane (OXZ).
The main characteristic of a grid is its separation between points $\Delta_q = L/n$, where $L = 2L_{\max}$ for x, z and $L = L_{\max}$ for y, and n is the total number of points in each direction. The value of Δ_q will depend on which system we are studying. We name the grids depending on this parameter, and five different values of Δ_q have been employed in this work, naming therefore the grids as follows: G1 ($\Delta_q = 0.2$ a.u.), G2 (0.137 a.u.), G3 (0.1 a.u.), G4 (0.05 a.u.) and G5 (0.025 a.u.). At the end of this section we give a detailed explanation of how to properly chose the Δ_q value for a given system.

Algorithm details

Soft-core parameters

As in previous numerical treatments [56], a soft-core approximation needs to be introduced to allow the integration near the Coulomb singularity. The employed potentials are:

$$V_B = -\frac{Z_T}{(x_i^2 + \epsilon_{\mathrm{T}})^{1/2}};\ \ V_A = -\frac{Z_P}{(x_j^2 + \epsilon_{\mathrm{P}})^{1/2}} \tag{2.100}$$

where $x_i = |\boldsymbol{r} - \boldsymbol{R}(t)|$, $x_j = r$ for electron capture and the other way around for excitation.

The soft-core parameters $\epsilon_{\mathrm{T,P}} \ll h$, have to be chosen by fitting the atomic energies for each grid Δ_q. This process is implemented by using the Lanczos method [57], which is an iterative algorithm to obtain the eigenvalues of a symmetric matrix $\boldsymbol{A}$ of dimension $n \times n$. It starts with a random normalized vector $\boldsymbol{v}_1$, and the following steps

1. $\alpha_j = \boldsymbol{v}_j^T \boldsymbol{A} \boldsymbol{v}_j$
2. $\boldsymbol{r}_j = \boldsymbol{A}\boldsymbol{v}_k - \alpha_j \boldsymbol{v}_j - \beta_{j-1}\boldsymbol{v}_{j-1}$
3. $\beta_j = \|\boldsymbol{r}_j\|$

4. $\boldsymbol{v}_{j+1} = \boldsymbol{r}_j/\beta_j$

are repeated to form a subspace of normalized vectors $\boldsymbol{v}_i$, $\boldsymbol{V} = (\boldsymbol{v}_1, \boldsymbol{v}_2, \boldsymbol{v}_3, ..., \boldsymbol{v}_k)$, where the α_j and β_j are constants, with the initial value of $\beta_0 = 0$. Once we know $\boldsymbol{V}$, we can generate the tridiagonal matrix $\boldsymbol{T} = \boldsymbol{V}^T \boldsymbol{A} \boldsymbol{V}$, which is

$$\boldsymbol{T} = \begin{pmatrix} \alpha_1 & \beta_2 & & & & 0 \\ \beta_2 & \alpha_2 & \beta_3 & & & \\ & \beta_3 & \alpha_3 & \beta_4 & & \\ & ... & ... & ... & ... & \\ & & & \beta_{k-1} & \alpha_{k-1} & \beta_k \\ 0 & & & & \beta_k & \alpha_k \end{pmatrix} \tag{2.101}$$

The eigenvalues of matrix $\boldsymbol{T}$ are approximated values of the eigenvalues of the initial symmetric matrix $\boldsymbol{A}$ in the subspace generated by the vectors $\boldsymbol{V}$. Therefore, the conversion of the tridiagonal matrix $\boldsymbol{T}$ to a diagonal form is the last step to find the approximate eigenvalues of the initial matrix. For a given nucleus A^{q+} (or H^+), we apply the Lanczos method to the bound isolated hamiltonian of $A^{(q-1)+}$ (or H) for different values of ϵ_P (ϵ_T). We choose the ϵ_i which fits better the eigenvalues to the energies $E_n = -\frac{Z^2}{2n^2}$.

Treatment of the spatial derivatives

The kinetic energy operator $\hat{T}$ is obtained by applying the Finite Differences method (see [58]), that is a local approximation of a certain function $f(x)$, which is approximated at the grid points with an ensemble of n_s Lagrange interpolation polynomial functions. This yields the approximation formula:

$$\left.\frac{\mathrm{d}^m f(x)}{\mathrm{d}x^m}\right|_{x=x_k} \simeq \sum_{j=1}^{n_s} b^m_{n_s} f(x_j) \tag{2.102}$$

where the $b^m_{n_s j}$ coefficients are computed using the Fornberg's algorithm [59]. The n_s points, called stencil, in equation (2.102) contain the information from the $\pm s$ neighboring points plus the value of the function at the specific grid point ($n_s = 2s + 1$), needed for the evaluation of the spatial derivative at each dimension.

Treatment of the time derivatives

The equation

$$\hat{H}\Psi = \mathrm{i}\frac{\partial \Psi}{\partial t} = \left[-\frac{\nabla^2}{2} + V(\boldsymbol{r},t)\right]\Psi \tag{2.103}$$

is solved by applying the Second-Order Differences method (SOD).

$$\Psi(t) = \mathrm{e}^{-i\hat{H}t/\hbar}\Psi(0) \quad \Rightarrow \quad \Psi(t+\Delta t) \approx \Psi(t-\Delta t) - \left(\frac{2\mathrm{i}\Delta t}{\hbar}\right)\hat{H}\Psi(t) \tag{2.104}$$

The position of the target (or projectile) in capture (excitation) changes throughout the collision, and the potential operator must be modified accordingly. To simulate a continuous motion the integration requires very small timesteps ($\sim 10^{-2}$ a.u.), and under this assumption the SOD scheme is perfectly valid [30].

Mask function

In order to avoid unphysical reflections in the walls of the box, we have introduced the mask function [60, 61]:

$$M(\boldsymbol{r}) = \prod_{i=1,3} \begin{cases} \exp\left\{-\alpha(|q_i| - L_{\max} + \delta)^2\right\} & \text{if} \quad L_{\max} - |q_i| < \delta \\ 1 & \text{elsewhere} \end{cases} \tag{2.105}$$

with $\delta = 3$ a.u. and $\alpha = 0.002$ a.u.$^{-2}$. In the SOD scheme, the mask function is equivalent to a complex optical potential. The mask function has the purpose of absorbing completely the part of the wave function that correlates assymptotically to ionization and bound states of the leaving nucleus, while only bound states of the remaining one, with the electronic density circunscribed to $L_{\max}$, are then properly described.

Study on the minimum value of Δ_q for different ion charges

As explained in section (2.4.2), different separation between points in the grid have been used (G1-G5).Some points need to be discussed to properly choose a value of Δ_q for a given collision A^{q+} + H(1s).

1. The main limitation of the GridTDSE method is the memory needed to perform the calculations. This memory is proportional to the number of points in each direction, $n_i^x \cdot n_i^y \cdot n_i^z$ (even taking advantage of the symmetry of the Hamiltonian upon reflection in the collision plane (XZ),

and having therefore $n_i^x = n_i^z = 2n_i^y - 1 = 2L_{\max}\Delta_q + 1)$. The $L_{\max}$, half the extension of the grid, needs to fulfill

$$L_{\max} \geq R_{nl_{\max}} + \delta \tag{2.106}$$

where $\delta = 3$ a.u., from equation (2.105), is the size of the optical potential. $R_{nl_{\max}}$ is the radial part (of the maximum nl allowed) of the wavefunction cointained in the grid at the end of the collision. This wavefunction corresponds to $A^{(q-1)+}$ (H) in the capture (excitation) scheme. For example, in the collision Be^{4+} + H(1s), we look for the maximum values of nl, for both capture and excitation, in a grid of $L_{\max} = 43$ a.u. In figure (2.10) the R_{nl} for the $n = 8$ states of Be^{3+} and for $n = 4$ of H are shown. Around a 99.86% of the $R_{8l}^{Z=4}$ and a 98.90% of $R_{4l}^{Z=1}$ are contained in $r \leq 40$ a.u.. In order to calculate the percentage which is not contained in $r < 40$ a.u. we use the radial density, defined as $\int_0^{r_{\max}} r^2 R_{nl}^2 \mathrm{d}r$, where $r_{\max}$ has been set at 40 a.u. in this example. Therefore, the radial density which is not contained in the box is determined by

$$\frac{\int_0^{\infty} r^2 R_{nl}^2(r)\mathrm{d}r - \int_0^{40} r^2 R_{nl}^2(r)\mathrm{d}r}{100} = \frac{1 - \int_0^{40} r^2 R_{nl}^2(r)\mathrm{d}r}{100} \tag{2.107}$$

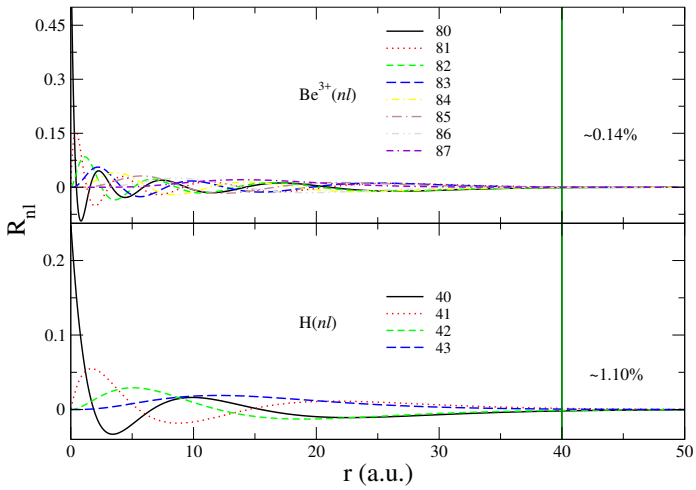

Figure 2.10: R_{nl} for $Be^{3+}(8l)$ and $H(4l)$. The percentage of radial density corresponding to $r > 40$. a.u with respect to the same for all r.

2. As explained in 2.4.3.1, the soft-core parameters $\epsilon_{\mathrm{T,P}}$ have to be chosen fitting the atomic energies for each Δ_q. The way of proceeding is applying the Lanczos algorithm [57] for different values of ϵ_i and trying to fit as accurate as possible the different energies $E_n = -Z^2/(2n^2)$. A proper ϵ_i for a given Δ_q should imply small deviations in these energies. But, of course, not all ions can be described with the same accuracy for the same Δ_q. For bigger Z, ions have more compacted R_{nl}, as shown in figure (2.10), and therefore we will need smaller values of Δ_q. We find an ϵ which fits the energy correponding to $n = 1$ so that, at least, $|E^{n=1}_{\mathrm{LANCZOS}} - E^{n=1}| < 10^{-5}$ a.u.. As an example, we can look at the relative errors of the Lanczos energy with respect to the real energy, corresponding to $n = 2$ for $Z = 3, 4, 5$ in a grid of $\Delta_q = 0.2$ a.u., when the ϵ has been obtained under the explained condition. These errors are of 0.6%, 1.3% and 2% for $Z = 3, 4, 5$ respectively.

3. According to the uncertainty principle, we need smaller integration steps for smaller Δ_q. The time step Δt has to fulfill [62]:

$$\Delta t < \frac{1}{E_{\max}} \qquad \text{with} \qquad E_{\max} = \frac{\pi^2}{2\Delta_q^2} \tag{2.108}$$

   This means that for a $\Delta_q^2 = \Delta_q^1/2$, the computing time increases for both taking a smaller Δt and having a greater dimension of the hamiltonian and Ψ.

In conclusion, the value of $\Delta_q = 2L_{\max}/(n_i^x - 1)$ must be chosen in a balance taking into account the $R_{nl_{\max}}$ that can be contained, the computation memory available, the required minimization of the energy error for the different states and the total time we are disposed to spend.

We will study the Be^{4+} + H($1s$) collision with this treatment in Chapter 3.

Approaches to treat more than two electrons collisions from one electron calculations

There are different approaches to treat two (or more) electron systems which rely on one active electron calculations. The probabilities associated to the different processes in equation (2.3) fulfill $1 = \mathrm{P_{ion}} + \mathrm{P_{capt}} + \mathrm{P_{exc}}$, where $\mathrm{P_{ion}}$, $\mathrm{P_{capt}}$ and $\mathrm{P_{exc}}$ stand for ionization, capture and elastic/excitation channels probabilities. In this section we present different multielectronic approaches that make use of the monoelectronic probabilities and which reproduce accurately certain multielectronic processes.

Independent Particle Model (IPM)

For a given collision involving a multielectronic target B with charge q_B, and/or multielectronic projectile A with charge q_A, some of the different multiple procesess which can happen are:

$$A^{q_A}+B^{q_B} \rightarrow \begin{cases} A^{(q_A-n)} + B^{(q_B+n)} & \text{Projectile electron capture of } n \text{ electrons} \\ A^{q_A} + B^{(q_B+n)} + ne & \text{Target ionization of n electrons} \\ A^{(q_A+n)} + B^{(q_B-n)} & \text{Target electron capture of } n \text{ electrons} \\ A^{(q_A-n)} + B^{(q_B+m)} & \text{Projectile capture accompanied by} \\ + (m-n)\mathrm{e}^- & \text{target ionization} \\ ... & \end{cases} \tag{2.109}$$

The Independent Particle Model [63, 64] is based on the idea of using the one-electron probabilities from one-electron calculations (see equation 2.3) to obtain those associated to the multielectronic processes of reaction (2.109). It assumes that in a given shell with j electrons, the probability of being ionized or captured by the other nucleus is the same for all the electrons. For a given inelastic process we have the monoelectronic probability P_k and the associated probability of not occuring that process k is (1-P_k). The number of possibilities (as well as the weigth of each of them) of finding n electrons ionized (or captured) from the total N electrons is given by the binomial coefficient $\binom{N}{n}$, expressed as

$$\binom{N}{n} = \frac{N!}{n!(N-n)!} \tag{2.110}$$

Therefore, the associated probability P_K for the multielectronic process (n electrons being ionized or captured from a shell with N electrons) is given by

$$\mathrm{P}_K = \binom{N}{n} \mathrm{P}_k^n (1 - \mathrm{P}_k)^{N-n} \tag{2.111}$$

Accordingly, K means a multiple process of the simple process k.
However, in a monoelectronic system, $(1 - \mathrm{P}_{\mathrm{ion}})$ will not only imply that ionization is not taking place; it also means that a capture process is taking place (since $1 = \mathrm{P}_{\mathrm{e}} + \mathrm{P}_{\mathrm{ion}} + \mathrm{P}_{\mathrm{capt}}$, where P_{e} stands for excitation and elastic probability). If instead of $(1 - \mathrm{P}_{\mathrm{ion}})$ we use $(1 - \mathrm{P}_{\mathrm{ion}} - \mathrm{P}_{\mathrm{capt}}) = \mathrm{P}_{\mathrm{e}}$ we will have

$$\mathrm{P'}_K = \binom{N}{n} \mathrm{P}_k^n {\mathrm{P}_{\mathrm{e}}}^{N-n} \tag{2.112}$$

which means that n electrons are being ionized (or captured) while the others $(N - n)$ rest in their initial ion, being explicitely excluded the possibility of being captured (or ionized, respectively). Consequently, we define

1. **Inclusive probability** P_K: Probability for a given multielectronic process K derived from its monoelectronic equivalent k and from all the monoelectronic probabilities which do not give rise to k. It is used when we want to simulate an experiment in which only the final charge of one of the ions is known.

2. **Exclusive probability** $\mathrm{P'}_K$: Multielectronic probability for a given process K derived from its monoelectronic equivalent k and from the monoelectronic probability for the electron resting in its initial ion. It is used when we want to simulate an experiment in which the final charge of both the target and projectile are known.

Independent Atom and Electron (IAE) model

The Independent Atom and Electron approach consists on the assumption that a molecule is made of independent atoms in which the electrons also move independently. It was first used for predicting multi-ionization of O_2 molecules [65] and has also been employed to describe the ionization of C_n clusters-atom collisions [31, 66, 21]. Cluster-atom collisions are described in terms of combinatorial products of one- electron probabilities for each ionic constituent of the cluster, similarly to the IPM. For example, the C_n^+ cluster is described as a C^+ ion surrounded by $n-1$ neutral carbons. Therefore, in a

collision between a C_n^+ cluster and a given target B, probabilities for both C + B and C^+ + B collisions have to be calculated.

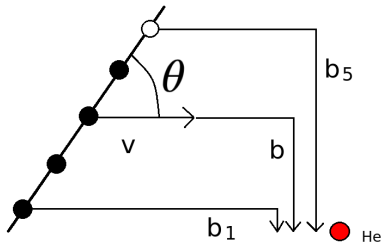

Figure 2.11: Representation of a C_n^+ + He cluster collision, where the black circles are the neutral carbons and the white one the C^+ ion. The individual b_i are functions of b and θ, the cluster orientation.

Under the IPA approximation, given a velocity v and an impact parameter b, the cluster and atom collision is modelled as it is shown in figure (2.11). The individual b_i, where i stands for the number of each atom in the cluster, depends on b and also on the cluster orientation with respect to the target, denoted by θ; then $b_i = b_i(b, \theta)$
For example, the neutralization probability in a $C_n^+ + He \rightarrow C_n + He^+$ collision is given by:

$$P_{C_n^+ \rightarrow C_n} = \sum_{i=1}^{n} P_{\text{capt}}^{(1)}(b_i) \prod_{i=1}^{n}(1 - P_{\text{ion}}(b_i)) \prod_{j>i}(1 - P_{\text{capt}}(b_j)) + \left[\sum_{i=1}^{n} P_{\text{capt}}^{(2)}(b_i) + \sum_{i=1}^{n} \sum_{j>i} 2P_{\text{capt}}^{(1)}(b_i) P_{\text{capt}}^{(1)}(b_j) \right] \times \left[\sum_{i=1}^{n} P_{\text{ion}}^{(1)}(b_i) \prod_{j>i}(1 - P_{\text{ion}}^{(1)}(b_j)) \right] \tag{2.113}$$

where b_i is the impact parameter of the $i-$th centre with respect to the target, $P_{\text{capt}}^{(1)}(b_i)$, $P_{\text{capt}}^{(2)}(b_i)$ and $P_{\text{capt}}(b_i)$ are the single, double and total capture probabilities on the centre i, and $P_{\text{ion}}^{(1)}(b_i)$ and $P_{\text{ion}}(b_i)$ are the probabilities for single and total ionization for centre i (C or C^+). These multiple probabilities can be extracted with the IPM explained in the previous section.
In order to obtain the cross section associated to a given probability the in-

tegration must be done over all the impact parameters and all the equally probable cluster orientations,

$$\sigma = \frac{1}{2\pi} \int_0^{2\pi} \mathrm{d}\phi \int_0^{\pi} \sin(\theta) \mathrm{d}\theta \int P(b, \theta, \phi) \mathrm{d}b \tag{2.114}$$

Chapter 3

Results for one active electron collisions

Classical results for A^{q+} + H reactions

The CTMC method has been extensively used for decades in the treatment of ion-atom collisions, in particular for reactions of stripped ions with atomic hydrogen. The microcanonical initial distribution is commonly chosen to reproduce the initial hydrogen atom although it has been proven that the cut-off in the radial distribution implies a bad description of the initial radial density (see Fig. 2.2) and therefore an underestimation of the ionization cross section [24]. In the case of the electron capture process, the microcanonical and the hydrogenic total cross sections do not show such a big difference in the intermediate energy range, but still the microcanonical results are lower than the hydrogenic ones in the range where the ionization starts to be a competitive process ($E \lesssim 50$ keV/amu). This behaviour of the ionization and electron capture results as a function of the initial distribution is shown in figure (3.1), where the total cross secions for ionization and electron capture is shown for the projectil C^{6+}. A further discussion of this system can be found in [67].

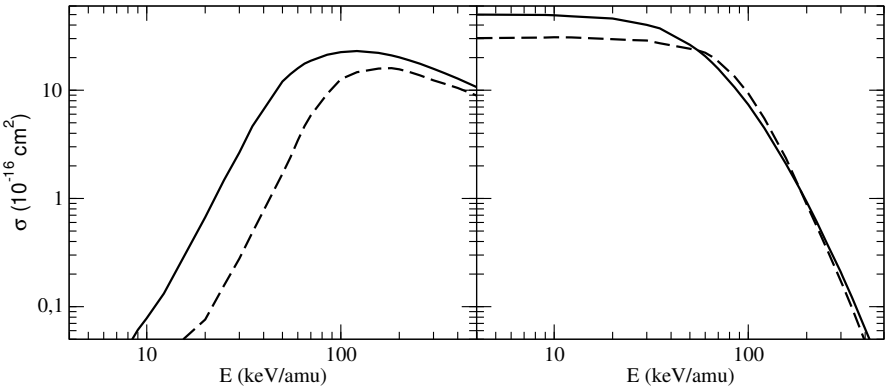

Figure 3.1: Comparison of the CTMC results for ionization (left panel) and electron capture (right panel) obtained employing an hydrogenic (full line) and microcanonical (dashed line) in the collision C^{6+} + H($1s$).

Considered energy ranges

We are interested in studying the electron capture process as a function of the initial distribution employed to model the H($1s$). To do that, we analyze the microcanonical and hydrogenic results by separating the energy range in three regions, low, intermediate and high. We have chosen the

$$C^{6+} + H(1s) \rightarrow C^{5+} + H^{+} \tag{3.1}$$

reaction to make this analysis; the references used in each energy range to compare with are the following:

1. **Low energy range E $\lesssim$ 20 keV/amu**: We find experimental results of Meyer *et al.* [68] up to 10 keV/amu.

2. **Intermediate energy range 20 $\lesssim$ E $\lesssim$ 250 keV/amu**: In the intermediate energy range we find experimental results from Goffe *et al.* [69] for energies greater than 100 keV/amu. For lower energies than 100 keV/amu we use recent atomic orbital close-coupling calculations from Igenbergs *et al.* [70]. Total capture cross sections from Igenbergs are not reliable for energies higher than $\sim$ 150 keV/amu, since they are calculated as a sum of the $n-$partial cross sections for $n < 12$. For impact energies $E \lesssim 150$ keV/amu the contributing $n-$partial cross sections for $n \geq 12$ is negligible, but for $E \gtrsim 150$ keV/amu it is not. This is checked

in figure (3.2), where we show the $n-$partial cross sections from [70] for 10 keV/amu (left panel) and 250 keV/amu (right panel) as well as the contribution for $n > 11$, obtained with an extrapolation made with the $1/n^3$ Oppenheimer rule up to $n = 50$. In the graphs it is also shown the relative error of the total cross section due to not taking into account n levels higher than $n = 11$. We find for 10 keV/amu an error around 0.28 % and in the case of 250 keV/amu an error around 18%. Since the results for the highest energies considered in [70] are therefore underestimated, we take Igenbergs cross sections as a reference up to 150 keV/amu.

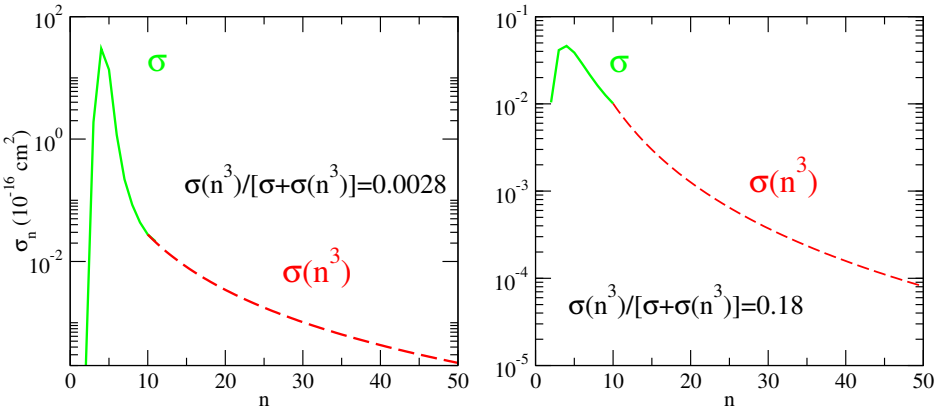

Figure 3.2: $n-$partial cross sections for $E = 10$ keV/amu (left panel) and $E = 250$ keV/amu (right panel) from Igenbergs *et al.* [70]. It is also shown the contribution for $n > 11$, obtained using the $1/n^3$ rule, and the relative error of the total cross section due to not taking into account this contribution of n levels higher than 11.

3. **High energy range E $\gtrsim$ 250 keV/amu**: Perturbative calculations are recommended at high energies; we use the Eikonal Impulse Approximation (EIA) results from Gravielle *et al.* [71] for impact velocities higher than ~ 3 a.u. (see section 3.1.2 for more details on this approach).

In figure (3.3) we show the total electron capture cross section for the reaction (3.1) obtained with both the hydrogenic and microcanonical initial distributions, compared with the experimental results from [69, 68] and the theoretical ones from [70, 71].

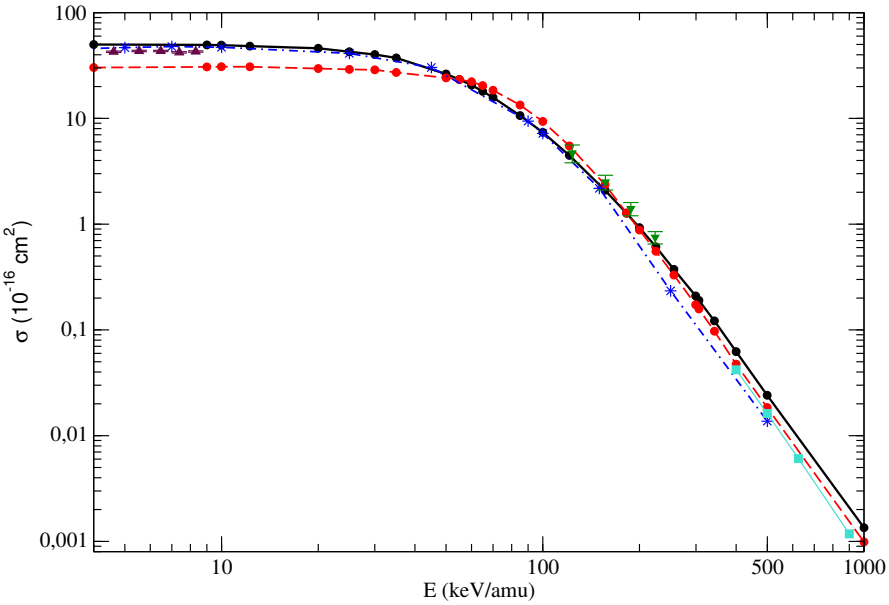

Figure 3.3: Total electron capture cross section for the reaction from Eq. (3.1). (●–●) CTMC-hydrogenic; (●– –●) CTMC-microcanonical. Theory: (∗– · –∗) AOCC [70]; (■–■) EIA [71]. Experiments: (▲) [68]; (▼) [69]

By taking into account the reference data for each energy range, we can construct a recommended cross section, and then compare it with the hydrogenic and microcanonical results, in order to analyze their validity in each energy range.
In figure (3.4) we show the recommended cross section with the CTMC results, showing also the three regions separately.

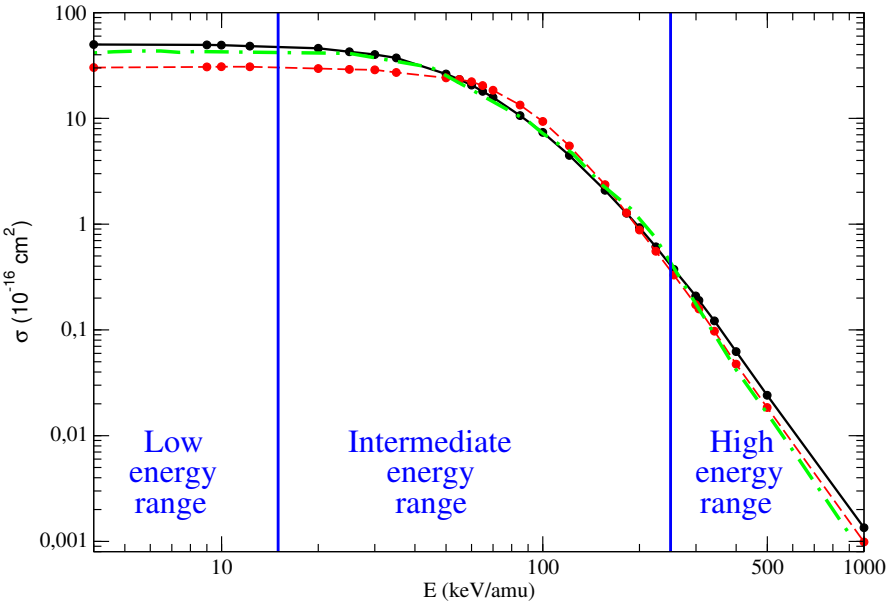

Figure 3.4: Total electron capture cross section for the reaction from Eq. (3.1). (●–●) CTMC-hydrogenic; (● – –●) CTMC-microcanonical. (– · –) Recommended cross section based of the references from section 3.1.0.1

The following analysis is based on the study of the initial energy of the captured trajectories in the hydrogenic distribution, which is composed of 10 different initial bound energies. In figure (3.5) we show the distribution of energies which compose the hydrogenic distribution used along this thesis, as well as the distribution of their associated $r_{\mathrm{cut-off}} = -1/E$. It is important to remember that the microcanonical distribution is simply composed of one initial bound energy, -0.5 a.u., whose $r_{\mathrm{cut-off}}$ is 2 a.u..

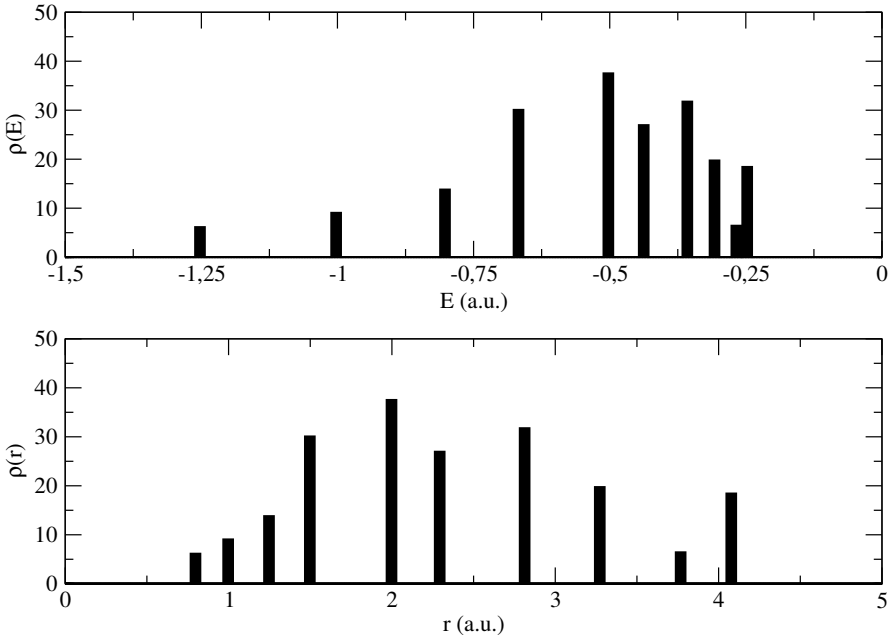

Figure 3.5: Distribution of the energies used to compose the hydrogenic distribution and of their associated $r_{\mathrm{cut-off}} = -1/E$

The main advantage of the hydrogenic distribution is its reproduction of the quantum radial distribution without almost modifying the momentum distribution. This implies the use of different initial binding energies with a weight associated to each of them and whose weighted sum is the exact ionization energy, -0.5 a.u. for the H($1s$). We can check from which of these initial bins of energies, varying between -2 and -0.25 a.u., the captured trajectories come from, and look at the distribution of initial energies for the total number of captured trajectories. This can be performed for a given impact parameter, but also for a whole impact velocity including therefore all the impact parameters, or for a given capture n level of the $\mathrm{A}^{(q-1)+}$, etc. For each energy distribution $\rho(E)$, we can determine its expected value of energy:

$$\langle E \rangle = \int_{-\infty}^{\infty} E\rho(E)\mathrm{d}E \tag{3.2}$$

We can expect a good representation of the capture probability if the expected value of energy from the distribution of initial energies of the captured trajectories is close to -0.5 a.u.. In the case of the microcanonical distribution

all the trajectories contributing to capture come from the exact value of -0.5 a.u.. A value of $\langle E \rangle$ close to -0.5 a.u. in the hydrogenic distribution would mimic the main advantage of the microcanonical distribution, keeping a good radial initial distribution.
In order to show that this expected energy value $\langle E \rangle$ is a meaningful variable, we look first at the capture to two representative n levels of the C^{5+} ion production: $n = 2$ and $n = 5$. It is known that the hydrogenic distribution is not capable of reproducing $n-$partial capture to low lying n levels [25]. We show in figure (3.6) and (3.7) the distributions of initial energies of trajectories leading to capture into $C^{5+}(n = 2)$ and $C^{5+}(n = 5)$, respectively, in reaction from Eq. (3.1) for five collision velocities: 0.4 a.u. ($E = 4$ keV/amu), 1.095 a.u. ($E \simeq 30$ keV/amu), 1.4142 a.u. ($E \simeq 50$ keV/amu), 2 a.u. ($E = 100$ keV/amu) and 4.47 a.u. ($E \simeq 500$ keV/amu). Now we assume that, in principle, all these energies are *valid* for a classical treatment with the hydrogenic distribution. We can check in figures (3.6,3.7) that, independently of the impact velocity, the expected values of the distributions of initial energies leading to capture into the $n = 2$ level are quite different from -0.5 a.u., while for capture into the $n = 5$ level this only happens for the lowest and highest impact velocities considered. It is also worth noting that those distributions whose expected value is close to -0.5 a.u. have a higher weight than the proper initial distribution (in black in figures 3.6 and 3.7) in the initial energy of -0.5 a.u.. Accordingly, capture into low n levels cannot be reproduced using an hydrogenic initial distribution, as it was stated in [25]. The behaviour of the $n = 5$ expected values would indicate that for the low ($E \lesssim 15$ keV/amu) and high ($E \gtrsim 250$ keV/amu) energy range this problem is also presented, which is true in fact, but a more complete analysis will be done in the next section.

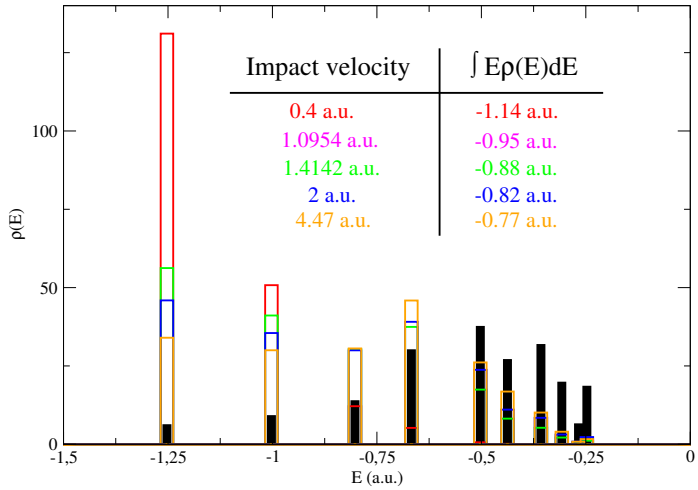

Figure 3.6: Distribution of initial energies from the hydrogenic distribution of H($1s$) leading to capture into $C^{5+}(n = 2)$, for the impact velocities of 0.4, 1.0954, 1.4142, 2 and 4.47 a.u..

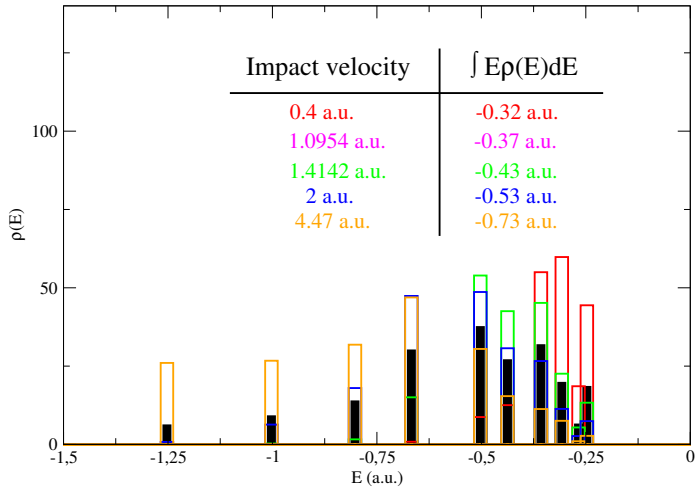

Figure 3.7: Distribution of initial energies from the hydrogenic distribution of H($1s$) leading to capture into $C^{5+}(n = 5)$, for the impact velocities of 0.4, 1.0954, 1.4142, 2 and 4.47 a.u..

In figure (3.8) we show the $n-$partial cross sections for $n = 2$ and $n = 5$ in the whole energy range, compared to the results from Igenbergs [70]. Compared to the AOCC calculation, the hydrogenic results are overestimated for capture into $n = 2$ in the whole energy range, almost five orders of magnitudes for the lowest energies. In the case of $n = 5$ we find a much better comparison, and the level of agreement can be directly related to the distributions and expected energy values from figure (3.7).

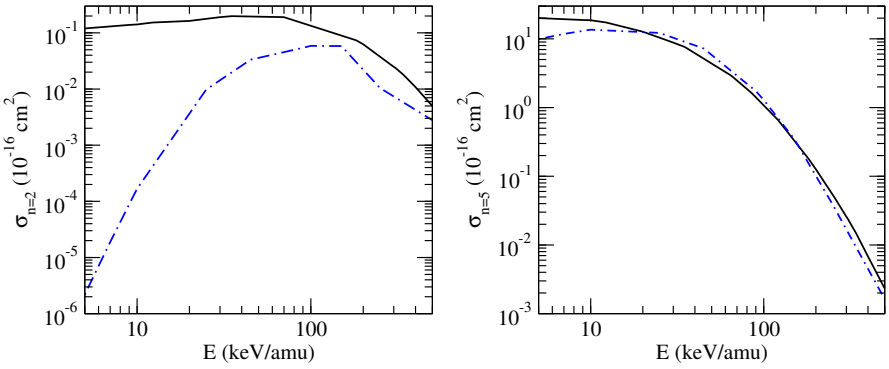

Figure 3.8: $n-$partial cross sections for reaction from Eq. (3.1) into the $n = 2$ (left panel) and $n = 5$ (right panel). $(- - -)$ CTMC-hydrogenic; AOCC calculations from [70] $(\cdot - \cdot)$.

Once we have shown the procedure to check the validity of the hydrogenic distribution for state-selective electron capture, we make a further analysis for total electron capture in the three collision energy regions. The error in the expected values will be computed as $100 \times \frac{|\langle E\rangle + 0.5|}{0.5}$.

Analysis of the CTMC-hydrogenic capture cross sections in the low energy range

It is known that the CTMC method, independently of the employed initial distribution, cannot reproduce accurate capture cross sections for energies lower than $\sim 10 - 20$ keV/amu, since it has serious limitations to describe the strong adiabatic character of the pseudocrossings in the molecular framework, relevant at these energies [25]. Nevertheless, the hydrogenic distribution reproduces better than the microcanonical one the total capture cross section in the low energy range, as it is shown in the first region of figure (3.4). For the lowest impact velocity considered there, 0.4 a.u., we show in figure (3.9)

the distributions of initial energies from the hydrogenic distribution of H($1s$) associated to the total capture process.

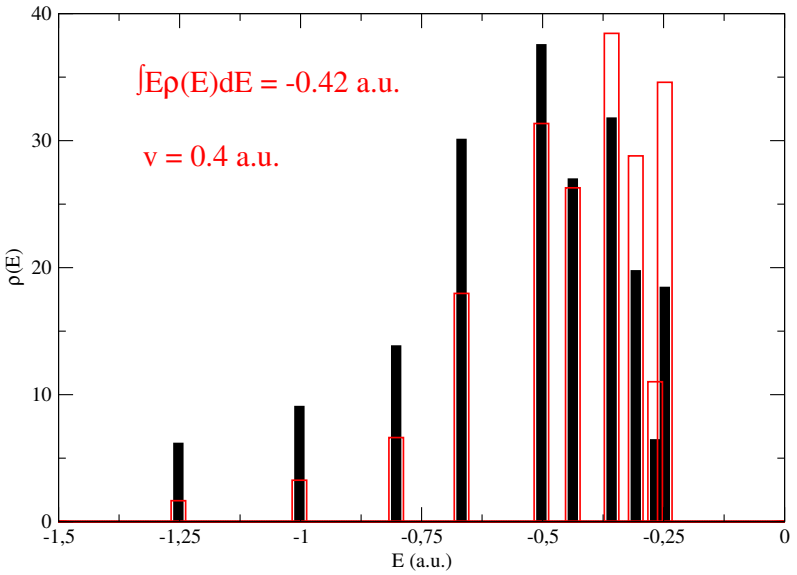

Figure 3.9: Distribution of initial energies from the hydrogenic distribution of H($1s$) leading to total capture for the impact velocity of 0.4 a.u..

We find an expected energy value of -0.42 a.u., which implies an error of 16%. For this same velocity we had an error of 128% for $n = 2$ and of 36% for $n = 5$. The total cross sections in the low energy range have a problem with the classical description, but still the hydrogenic distribution has a better description than the microcanonical one. In general, hydrogenic capture cross sections are higher than the microcanonical ones, since the better description of the spatial density implies a bigger range of interaction and therefore a larger maximum impact parameter in the collision. This improvement due to the hydrogenic distribution will imply a better capture description if the expected value of energy from the distribution of initial energies is close to -0.5 a.u.. We show in figure (3.10) the opacity function $bP(b)$ as a function of the impact parameter b, for capture at the impact velocity of 0.4 a.u., where the larger extension of the hydrogenic compared to the microcanonical distribution is illustrated.

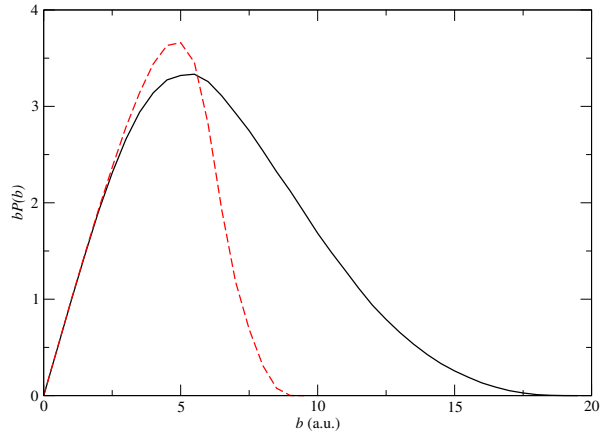

Figure 3.10: $bP(b)$ versus b for for reaction from Eq. (3.1) at the impact velocity of 0.4 a.u.. (—) Hydrogenic; (– – –) Microcanonical

Therefore, the differences of the hydrogenic capture cross sections compared to the recommended set (see figure 3.4) at low energies are due to the classical description, being the error of the expected enery value 16%.

Analysis of the CTMC-hydrogenic total capture cross sections in the intermediate energy range

In the intermediate energy range, $10 \lesssim E \lesssim 250$ keV/amu, we can differenciate two regions, due to the competition of the inelastic processes: $E < 50$ keV/amu and $E \geq 50$ keV/amu. In this first region the impact velocity is close or equal to the electron velocity in the H($1s$) target and the quantum effects do not play the main role anymore in the capture process. The hydrogenic results compare quite well with the recommended set, while the microcanonical ones are underestimated. This is due to the shorter interaction and therefore smaller maximum impact parameter, which is shown in figure (3.11) for an impact energy of 30 keV/amu. The distribution of initial energies from the hydrogenic distribution which give rise to capture at this impact energy is shown in figure (3.12), whose expected energy value is of -0.44 a.u. (difference of 12%).

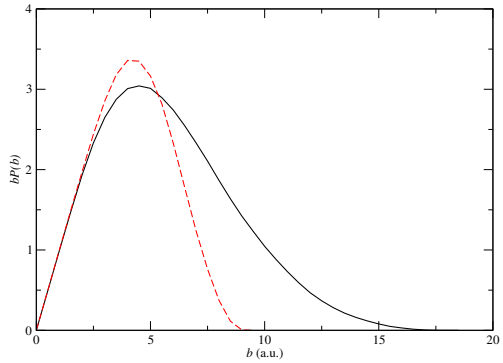

Figure 3.11: $bP(b)$ versus b for for reaction from Eq. (3.1) at the impact velocity of 1.0954 a.u.. (—) Hydrogenic; (– – –) Microcanonical

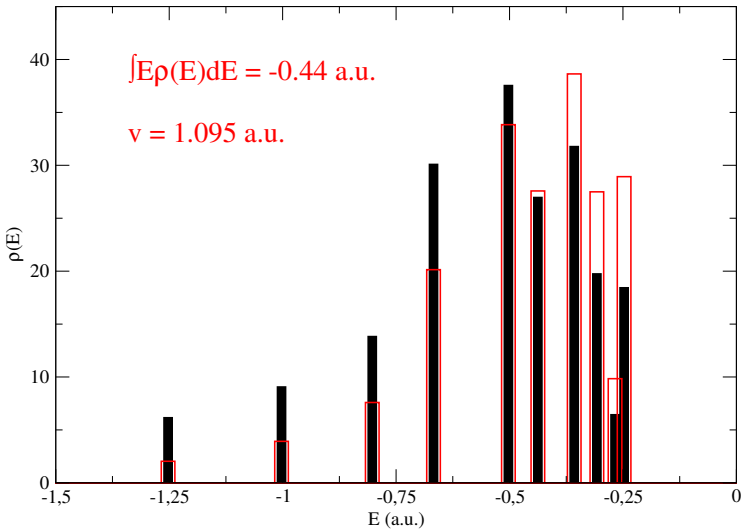

Figure 3.12: Distribution of initial energies from the hydrogenic distribution of H($1s$) leading to total capture for the impact velocity of 1.0954 a.u..

In the second region of the intermediate energy range $E \geq 50$ keV/amu, where the fall of the total electron capture begins, there are not big differences between the microcanonical and hydrogenic results. But still we find a better agreement with the recommended set of the hydrogenic cross sections. In this region we find that, for some impact energies, the microcanonical results are

slightly higher than those of the hydrogenic ones, while the impact parameter region is very similar. This can be seen in figure (3.13), where the $bP(b)$ versus b for $v = 2$ ($E = 100$ keV/amu) is shown for the two initial distributions.

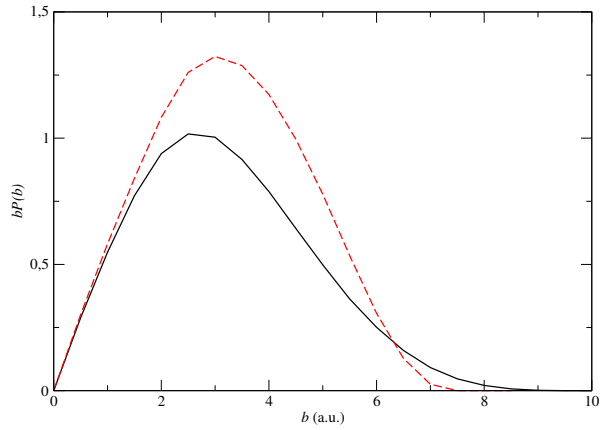

Figure 3.13: $bP(b)$ versus b for for reaction from Eq. (3.1) at the impact velocity of 2 a.u.. (—) Hydrogenic; (– – –) Microcanonical

The good description of the hydrogenic distribution can be checked not only on the comparison of the total cross sections from figure (3.4) but also on the distribution of initial energies shown in figure (3.14), whose expected value of energy is -0.56 a.u. (error of 12%).

We have not included the distributions for the intermediate point between these two regions, $v = 1.4142$ a.u., for the sake of conciseness. The associated $bP(b)$ behaviour is the middle point between 30 and 100 keV/amu, being its expected energy value -0.47 a.u..

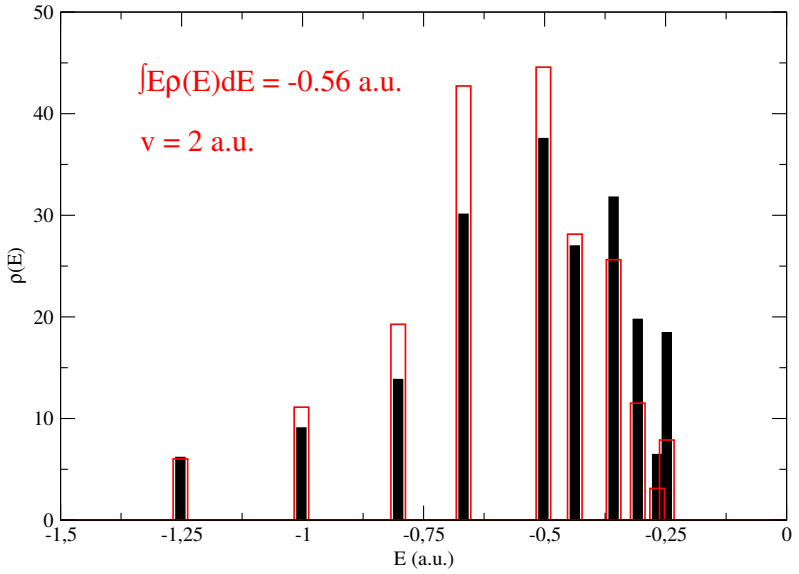

Figure 3.14: Distribution of initial energies from the hydrogenic distribution of H($1s$) leading to total capture for the impact velocity of 2 a.u..

Analysis of the CTMC-hydrogenic capture cross sections in the high energy range

Similarly to the low energy case, it has been investigated the fail of the CTMC cross sections at high energies [72] stating that the increasing overestimation of the total capture cross sections at high energies is due mainly to capture to deeper states than the $1s$ states. However, this depends on the charge of the projectile, and for C^{6+} we have checked that only for the first considered impact parameter in these calculations (0.2 a.u.) there are trajectories leading to capture into a forbidden deep state. And they imply only a 0.8% of the total trajectories leading to capture at this impact parameter. So this effect would appear at higher energies, but it is not the problem at 500 keV/amu. It is also stated in [72] that electron capture at high energy collisions is mainly due to a double scattering mechanism, which could not be described with the CTMC method. Nevertheless, and as it can be checked in figure (3.4), in the high energy regime the hydrogenic results overestimate the already overestimated microcanonical cross sections. The fail of the initial distributions which mimic the radial quantum denity to describe capture at high impact energies was already discussed by Reinhold and Falcón in [73]. In the low energy range

we had a failure of the classical description, but still the hydrogenic capture cross section had a better agreement with the recommended set than the microcanonical one due to two factors: the greater interaction extension and the good distribution of initial energies leading to capture. In figure (3.15) we show the $bP(b)$ for $v = 4.47$ a.u. (500 keV/amu) for the two initial distributions, where it can be checked that the extension of the interaction with the hydrogenic distribution does not apply anymore at high energies.

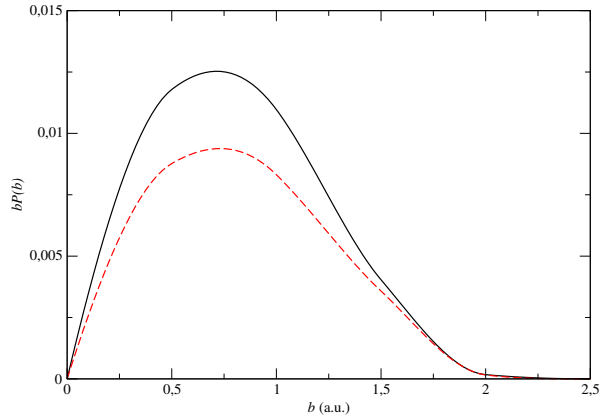

Figure 3.15: $bP(b)$ versus b for for reaction from Eq. (3.1) at the impact velocity of 4.47 a.u.. (—) Hydrogenic; (– – –) Microcanonical

The extension of the $bP(b)$ is the same for the two distributions, something that did not occur at lower velocities and which, in principle, is not responsible of the overestimation of the hydrogenic results. In figure (3.16) the distribution of initial energies leading to capture is shown, where we can check that the expected value of energy is of -0.76 a.u., which implies a difference of 52% from the real -0.5 a.u. value. Therefore, we find that in the high energy regime there is an uncorrected classical description, and also that the two characteristics that are responsible of the good results of the hydrogenic distribution, the greater interaction extension and a distribution whose expected value is close to -0.5 a.u., are not fulfilled simultaneously. For higher impact energies than 500 keV/amu this behaviour keeps on worsing the overestimation of the capture cross sections.

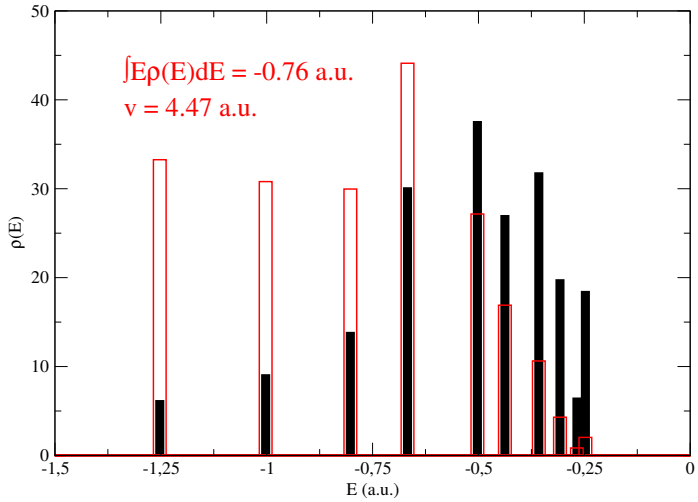

Figure 3.16: Distribution of initial energies from the hydrogenic distribution of H($1s$) leading to total capture for the impact velocity of 4.47 a.u..

In conclusion, we have investigated the behaviour of the hydrogenic initial distribution to describe the electron capture process in the energy range from 4 to 1000 keV/amu for the reaction C^{6+} + H($1s$) $\rightarrow$ C^{5+} + H^{+}. The study has been done with an energetic criteria, since the momentum and radial distributions were already really close to the quantum ones. We have analyzed the description of the capture process for the H($1s$) target through the study of the initial conditions of the captured trajectories, linking a good description with a good distribution of the initial energies leading to capture. The relative error of $\langle E \rangle$ with respect to the ionization energy in the H($1s$) target needs, in general, to be lower than $\sim 20\%$ in order to have a proper descrtipion. The limits of the energy regions may vary for different projectiles, but in general the behaviour is the same. For the lowest energies, the classical description cannot describe quantum effects which are responsible of the capture process, but the hydrogenic initial distribution offers better cross sections; for the lowest energy considered the value of the error is 16%. In the intermediate energy region the quantum effects are not longer the main responsibles of capture and, with values of relative differences lowers in all the cases than 15%, we obtain accurate capture cross sections with the hydrogenic distribution. In the high energy regime, however, the classical description is not accurate and neither the hydrogenic distribution should be used.

C^{q+} + H(1s) with $q = 1, 5$

We can treat collisions involving dressed projectiles by considering one active electron perturbed by an effective potential which models the nucleus and the core electrons of the C ion. In this section we implement model potentials to treat collisions of the type

$$C^{q+} + H(1s) \rightarrow C^{(q-1)+} + H^{+}. \tag{3.3}$$

for q values from 1 to 5 in the 10-300 keV/amu energy range. The main aim to study these collisions is that carbon ions are common impurities in tokamak fusion devices, since carbon is used in the first wall, specially in the divertor. Even when carbon will not be used in the same manner in ITER (where the first wall is expected to be completely made of Be and W), carbon impurities will be present. The electron capture reactions for the different values of q were reviewed in 2006 by Suno and Kato [74], who created a set of recommended data obtained from the bibliography. This allows us to check the validity of the use of a model potential to treat these collisions with one-active electron calculations, taking into account that an effective potential should work properly only in the cases where the active electron interacts with a closed-shell (such as the C^{4+}).
We use a model potential with the general form:

$$V_{\text{eff}} = -\frac{Z - N_e}{r} - \frac{N_e}{r}\exp(-2\alpha r)(1 + \alpha r) \tag{3.4}$$

to describe the interaction of a C^{q+} ion with an electron, where N_e is the number of frozen electrons in the core, $Z = 6$, and α is a parameter which fits the ionization potential of the ground-state of the $C^{(q-1)+}$ ion. The values of the α parameter obtained for each $C^{(q-1)+}$ ion are:

Table 3.1: Value of the parameter α of equation (3.4) for $C^{(q-1)+}$.

	C	C^{+}	C^{2+}	C^{3+}	C^{4+}
α	1.18	1.41	1.85	3.72	5.67

We must take into account that captured trajectories in reaction (3.3) can be bound with energies below to those corresponding to the core electrons. This would imply an overestimation of the electron capture cross section, as

well as a subestimation of the excitation/elastic and ionization cross sections. We can apply a simple energy condition in the CTMC calculations to estimate this deficiency for the considered ions. When the collision has finished, we check the binding energies of the captured electrons of the $C^{(q-1)+}$ ion. We define the forbidden trajectories N_f as those whose final energy is smaller than a certain value, the forbidden energy E_f that coincides with the ionization potential. We can now define two different sets of probabilities for each impact parameter, the *including forbidden energies* probability P_C^{ife} and the *excluding forbidden energies* probability P_C^{efe}, where C stands for electron capture.

$$P_C^{ife} = \frac{N_C}{N} \qquad\qquad P_C^{efe} = \frac{N_C - N_f}{N - N_f} \tag{3.5}$$

N is the total number of trajectories and N_C is the number of trajectories leading to electron capture. To compare with, we use the recommended data of Suno and Kato [74] and, for the C^+ impact ion, also recommended set from Stancil *et al.* [75]. Experimental results from Goffe *et al.* [69], Phaneuf *et al.* [76] and, for the C^{3+} reaction, measurements from Sant'Anna *et al.* [77]. In the following figures (3.17-3.21) we show the CTMC electron capture cross sections for both the hydrogenic and microcanonical distributions compared to these data from the bibliography. The best comparison with respect to the experimental values and recommended set is for the C^{4+} impact ion, where the frozen core is a closed shell and, as it was expected, the model potential offers a good description. For the rest of the ion charges there is a good agreement except for the C^{2+} ion. In the capture process for this collision the main exit channel is $C^+(1s^2 2s 2p^{2\,2}D)$ which involves a two-electron mechanism, one electron is captured while other one is excited, and this two-electron process cannot be described with a one-electron model.

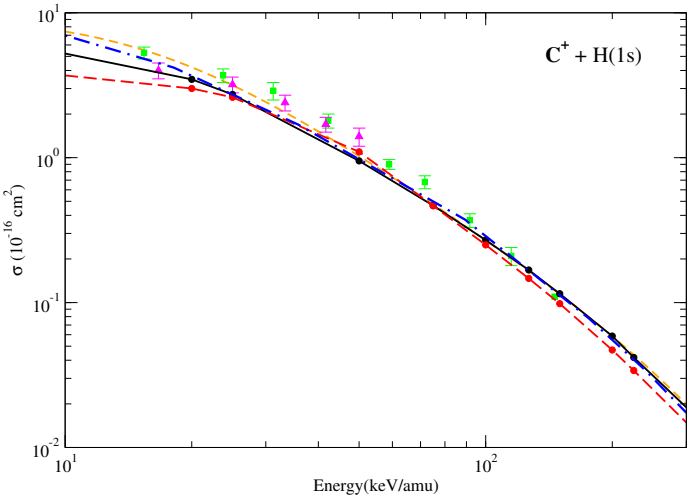

Figure 3.17: Total electron capture cross section for reaction $C^+ + H(1s)$ $\rightarrow$ C + H^+. CTMC results: hydrogenic (●—●); microcanonical (● – –●). Recommended data of Stancil *et al.* [75] (– – –) and of Suno and Kato [74] (· – ·); experimental data from Phaneuf *et al.* [76] (▲) and Goffe *et al.* [69] (■).

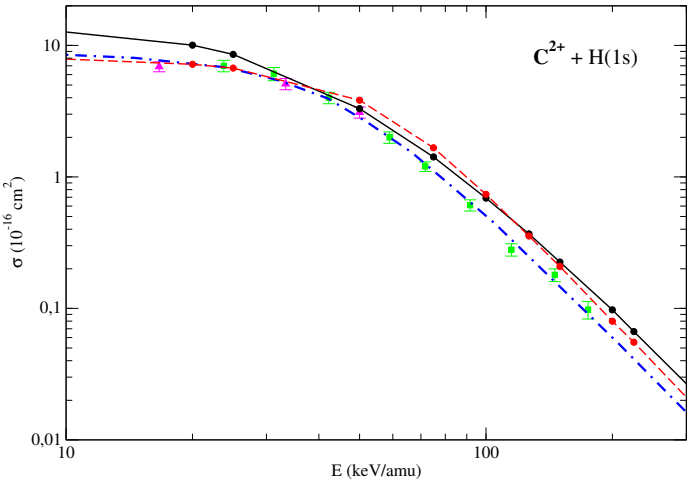

Figure 3.18: Total electron capture cross section for reaction $C^{2+} + H(1s) \rightarrow$ $C^{2+} + H^+$. Same symbols as in figure (3.17) .

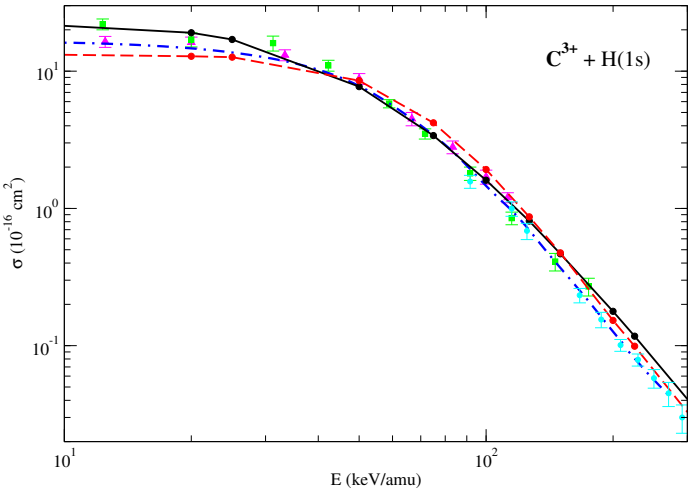

Figure 3.19: Total electron capture cross section for reaction C^{3+} + H($1s$) $\rightarrow$ C^{2+} + H^{+}. Same symbols as in figure (3.17) Experimental results from Sant'Anna *et al.* [77] (•).

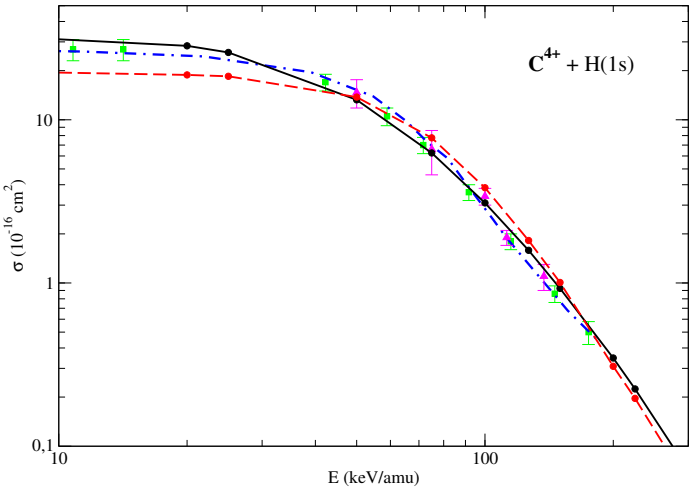

Figure 3.20: Total electron capture cross section for reaction C^{4+} + H($1s$) $\rightarrow$ C^{3+} + H^{+}. Same symbols as in figure (3.17) .

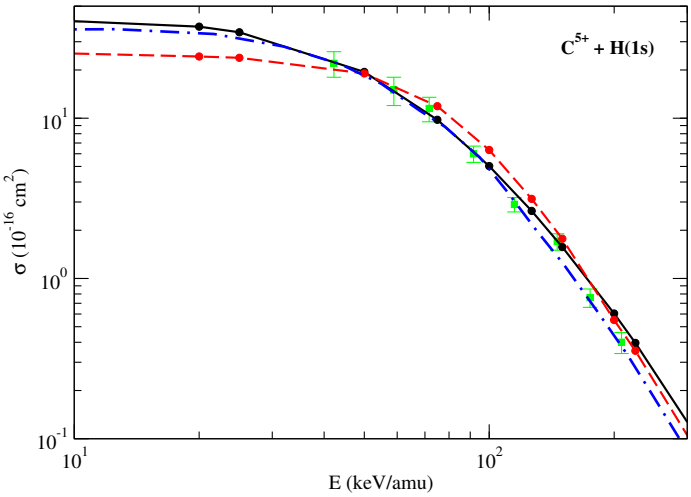

Figure 3.21: Total electron capture cross section for reaction $C^{5+} + H(1s) \rightarrow C^{4+} + H^{+}$. Same symbols as in figure (3.17) .

Stancil *et al.* [75] also performed CTMC calculations for $C^{+} + H(1s)$ collision, with a microcanonical distribution for $H(1s)$ target and are not shown in figure (3.17) for the sake of conciseness. Classical cross sections at low energy (E< 1 keV/amu) were overestimated, and it was argued that it was due to trajectores leading to capture to already occupied levels. In figure (3.22) we show the differences in the cross sections when we exclude forbidden trajectories. For $q > 3$ the including and excluding forbidden trajectories cross sections are indistinguishable for both the microcanonical and hydrogenic distribution. Even when this effect is higher for the C^{+} ion, it can be checked that it turns important for energies much higher than 1 keV/amu.

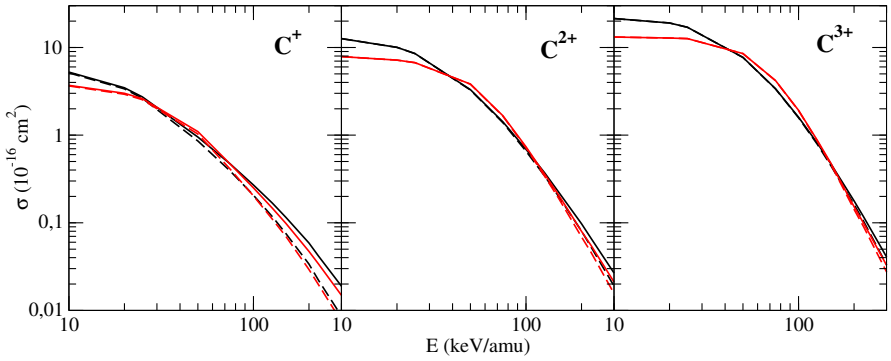

Figure 3.22: Cross section including (—) and excluding (− − −) forbidden trajectories. Hydrogenic results in black and microcanonical ones in red.

For the impact energy of 115 keV/amu, where both the CTMC and hydrogenic distribution should work better, we check the relative error with respect to the Goffe *et al.* experimental results [69], as well as with respect to the data of C^{3+} from Sant'Anna *et al.* [77]. This relative error $\frac{|\sigma_{\rm Exp}-\sigma_{\rm CTMC}|}{\sigma_{\rm Exp}}$ turns to be lower than 20% for $q = 1, 4, 5$ when computed with the Goffe *et al.* experimental results, while it increases to 26% for the C^{3+} projectile and up to 70% in the case of C^{2+}. For the C^{3+} ion, the relative error computed with the Sant'Anna *et al.* data is of 7%. In general the agreement is good and the description with the model potential is accurate. The requirement of the core being a closed shell seems not to be as important as expected, being the worst description (C^{2+}) due to a two-electron process which cannot be described.

In conclusion, we have employed model potentials to describe one-electron collisions of dressed ions with hydrogen. A good description is found if the process we want to simulate is due to a one-electron mechanism, even when dealing with open shells. The behaviour of the hydrogenic distribution is the same as for naked projectiles, being the intermediate energy region the best described, as it was pointed out in section (3.1.0.1.2).

Scaling law for partial electron capture cross sections

Scaling rules consist on simple formulas which provide cross sections for a given process (such as electron capture). These scaling laws are usually a function of variables such as the impact energy, charge of the projectile and target, and n or l level in the case of partial capture cross sections.
Scaling rules to provide cross sections are a widely used tool which has been investigated by many authors through the years. In the case of collisions of naked ions with atomic hydrogen, we can find many scaling rules for total and n-partial capture cross sections in the bibliography [69, 78, 24, 79, 80]. However, scaling rules for the nl-partial capture cross sections are scarce [81] and, in the case of the work developed by Gravielle [82, 83], it is limited to capture up to $n = 4$. This work was done with the prior version of the Eikonal Impulse (EI) approximation, a distorted wave method that can provide reliable results for the capture process in the collision high-energy range. The energy range in which the EI approximation starts to be valid is approximately the same in which the CTMC capture results start to be overstimated, around 200 keV/amu (see section 3.1). This encouraged us to combine the two different methodologies by merging the results in the point where they join, which depends on the charge of the naked ion implied in the collision. The main objectives in this section are to extend the proposed scaling rule from [82, 83] to higher n-values and to lower energies (by merging with the classical results). We also simplify the application of the scaling rule by studying the behaviour of the $n-$ and $nl-$ results, in order to provide some simple formulas and tables which can be used to predict $n-$ and $nl-$ partial capture cross sections in the energy range of 50-2000 keV/amu. We are going to show the validity of the proposed scaling rules for different projectile charges in collisions with atomic hydrogen.

Brief description of the Eikonal Impulse approximation (EIA)

In formal scattering theory, the cross section for a given process with an initial (i) and final (f) state is, in general, proportional to the square of the corresponding matrix element T_{fi} [84]. These matrix elements depend on the description of the initial and final states.
The continuum wavefunction for two particles, reduced mass μ and relative momenta $\boldsymbol{k}$, interacting with an attractive Coulomb ($-Z/r$) potential is [85]

$$\Psi^{\pm}(Z,k,r) = \mathrm{e}^{i\boldsymbol{kr}} D^{\pm}(Z,\boldsymbol{k},\boldsymbol{r}) \tag{3.6}$$

where $D^{\pm}$ is the Coulomb distortion term

$$D^{\pm}(Z,\boldsymbol{k},\boldsymbol{r}) = \mathrm{e}^{(\pi/2)a}\Gamma(1\mp ia)\,{}_1F_1(\pm ia,1,\pm ikr - i\boldsymbol{k}\cdot\boldsymbol{r}) \tag{3.7}$$

with $a = \mu Z/k$ the Coulomb parameter, ${}_1F_1(\pm ia,1,\pm ikr - i\boldsymbol{k}\cdot\boldsymbol{r})$ the confluent hypergeometric function and Γ the gamma function.
In distorted-wave methods, the involved states in the matrix elements of a three-body collision are distorted waves. For an electron capture reaction, these can be of the type [86]

$$\chi_i^+ = \psi_i(\boldsymbol{r}_T,\boldsymbol{R}_T)D^+(Z_P,-\boldsymbol{K}_i,\boldsymbol{r}_P) = \phi_i(\boldsymbol{r}_T)\mathrm{e}^{i\boldsymbol{k}_i\boldsymbol{R}_T}D^+(Z_P,-\boldsymbol{K}_i,\boldsymbol{r}_P) \tag{3.8}$$

$$\chi_f^- = \psi_f(\boldsymbol{r}_P,\boldsymbol{R}_P)D^-(Z_T,\boldsymbol{K}_f,\boldsymbol{r}_T) = \phi_f(\boldsymbol{r}_P)\mathrm{e}^{i\boldsymbol{k}_f\boldsymbol{R}_P}D^-(Z_T,\boldsymbol{K}_f,\boldsymbol{r}_T) \tag{3.9}$$

where $\phi_i(\boldsymbol{r}_T)$ and $\phi_f(\boldsymbol{r}_P)$ are the initial and final bound states of energies ϵ_i and ϵ_f, respectively; $\psi_i(\boldsymbol{r}_T,\boldsymbol{R}_T)$ and $\psi_f(\boldsymbol{r}_P,\boldsymbol{R}_P)$ are defined by

$$H_i\psi_i(\boldsymbol{r}_T,\boldsymbol{R}_T) = E\psi_i(\boldsymbol{r}_T,\boldsymbol{R}_T) \tag{3.10}$$

$$H_f\psi_f(\boldsymbol{r}_P,\boldsymbol{R}_P) = E\psi_f(\boldsymbol{r}_P,\boldsymbol{R}_P) \tag{3.11}$$

being $H_i = H_0 + V_T(r_T)$ and $H_f = H_0 + V_P(r_P)$ the unperturbed initial and final channel Hamiltonians, with H_0 the kinetic energy operator; $E = k_i^2/(2\mu_i) + \epsilon_i = k_f^2/(2\mu_f) + \epsilon_f$ is the total energy.
The eikonal wavefunction is defined like [87]

$$\xi_i^+ = \psi_i(\boldsymbol{r}_T,\boldsymbol{R}_T)E^+(Z_P,-\boldsymbol{K}_i,\boldsymbol{r}_P) \tag{3.12}$$

$$\xi_f^- = \psi_f(\boldsymbol{r}_P,\boldsymbol{R}_P)E^-(Z_T,\boldsymbol{K}_f,\boldsymbol{r}_T) \tag{3.13}$$

where

$$E^{\pm}(Z,\boldsymbol{k},\boldsymbol{r}) = \lim_{r\to\infty} D^{\pm}(Z,\boldsymbol{k},\boldsymbol{r}) = \mathrm{e}^{\mp ia\ln(kr\mp\boldsymbol{k}\cdot\boldsymbol{r})} \tag{3.14}$$

The impulse hypothesis neglects the effect of the binding potential for a bound target or projectile, but determines the momentum distributions of the bound states [1]. The electron is represented by a continuum state centred on the target (final channel) or projectile (initial channel), instead of a plane wave [85]. For the final channel, the impulse wavefunction in the coordinate system given by $\{\boldsymbol{r}_T,\boldsymbol{R}_T\}$ reads

$$\psi_f^I = \int \frac{1}{(2\pi)^3}\mathrm{d}\boldsymbol{q}\phi_{n,l,m}(\boldsymbol{q})\mathrm{e}^{i(\boldsymbol{K}_f-\boldsymbol{q})\cdot\boldsymbol{R}_T}\mathrm{e}^{i(\boldsymbol{q}+\boldsymbol{v})\cdot\boldsymbol{r}_T}D^-(Z_T,\boldsymbol{q}+\boldsymbol{v},\boldsymbol{r}_T) \tag{3.15}$$

where $\phi_{n,l,m}$ is the Fourier transform of the final electronic wave function of the n,l,m state bounded to the projectile, with final electronic energy $\varepsilon_{n,l}$,

$\boldsymbol{v}$ is the impact velocity and $\boldsymbol{K}_f$ is the final momentum of the projectile. In electron capture for asymmetric collisions, where the nuclear charge of one of the particles is larger than the other, the *prior* version of the EI approximation has been successfully applied, providing proper cross sections for multicharged ions colliding with both H and He [82]. In the *prior* version of the EI approximation, the final collision channel is described with the exact impulse wave function and the initial channel with the eikonal wave function [88].
For the reaction

$$\mathrm{A}^{Z_P+} + \mathrm{H}(1s) \rightarrow \mathrm{H}^+ + \mathrm{A}^{(Z_P-1)+}(n,l,m), \tag{3.16}$$

the EI transition matrix elements reads [89]:

$$T^{(EI)}_{n,l,m} = \int \frac{d\boldsymbol{q}}{(2\pi)^{3/2}} \phi^*_{n,l,m}(\boldsymbol{q}) L^*_T(\boldsymbol{q}, \boldsymbol{W}_P - \boldsymbol{v}) \times \left\{ \left(\frac{q^2}{2} - \varepsilon_{n,l} \right) I_P(-\boldsymbol{v}, -\boldsymbol{q} + \boldsymbol{W}_P) + J_P(-\boldsymbol{v}, -\boldsymbol{q} + \boldsymbol{W}_P) \right\}, \tag{3.17}$$

where $\boldsymbol{W}_P = \boldsymbol{K}_i - \mu_P \boldsymbol{K}_f$ is the projectile momentum transfer, with $\boldsymbol{K}_i$ the initial momentum of the projectile and μ_P its final reduced mass, and the functions L_T, I_P, and J_P represent the Nordsiek-type integrals defined in [89].

Join of the EI and CTMC results

In order to extend the scaling rule from Gravielle and Miraglia [82, 83] in both the energy range nd the n levels considered, we first study the join of the CTMC and EIA total capture cross sections for different projectile charges. In figure (3.23) we show the join of the two theoretical approaches for the total electron capture process, compared to the availabe bibliography.

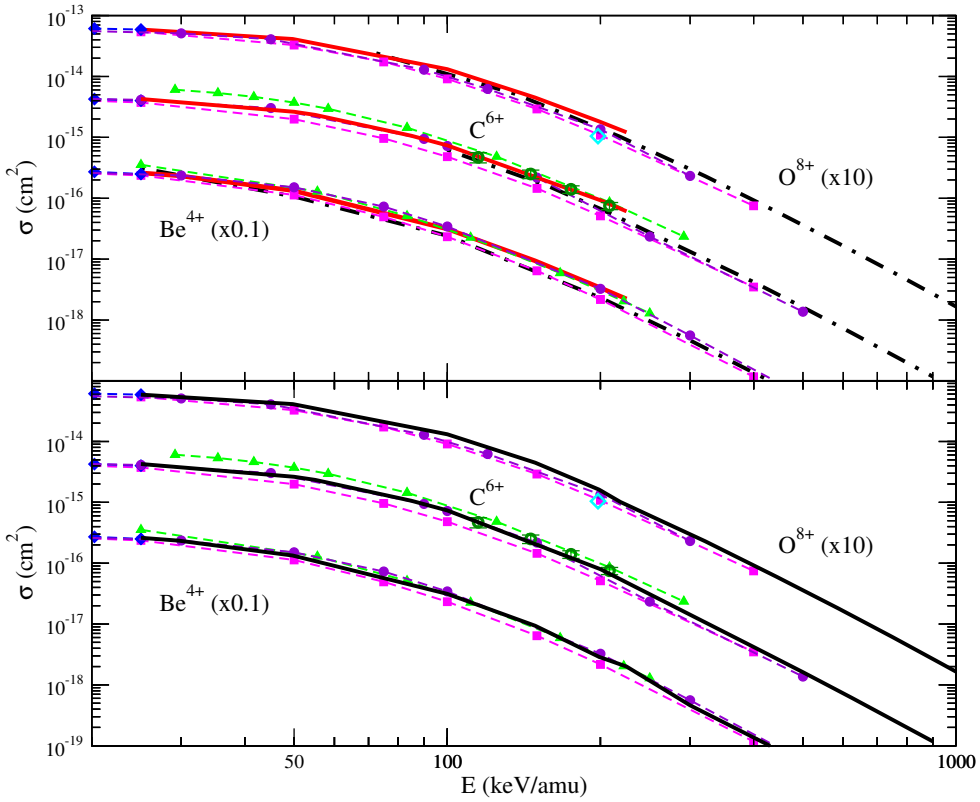

Figure 3.23: Total electron capture cross sections for Be^{4+}, C^{6+} and O^{8+} ions impinging on H(1s) as a function of the incident energy. In the upper panel the EI ▪--▪ and CTMC — results are shown separately. In the lower one they are joint. From the bibliography, calculations: ▪–-▪ AOCC [90], ♦–-♦ MOCC [91], ▲ — —▲ FBA [92], ● – —● AOCC [93]; and experiments: ○ [69] and ◊ [94].

As it can be checked in Fig. (3.23), both approaches agree each other in the intermediate energy region, around 100 keV/amu. The combined CTMC and EI results show a good agreement in the total cross sections with values derived from other theories, such as semiclassical close-coupling approaches with molecular (MOCC) [91] or atomic (AOCC) [90, 93] wave functions, or the First Born Approximation (FBA) [92].

Scaling law for n-partial cross sections

The electron capture cross sections to the $\{n, l, m\}$ states, suggested by Gravielle and Miraglia, nearly satisfies [82]

$$\sigma_{nlm}^{EI} \simeq \tilde{z}_P^{-7} \left|C(Z_P/v)\right|^2 \tilde{\sigma}_{nlm}(\tilde{v}, \tilde{W}), \tag{3.18}$$

where $\tilde{z}_P = Z_P/n$ is the scaled variable associated to the projectile charge, v is the impact velocity, and

$$C(a) = exp(\pi a/2)\Gamma(1 - ia) \tag{3.19}$$

is the projectile-electron Coulomb factor coming from the asymptotic conditions. The function $\tilde{\sigma}_{nlm}(\tilde{v}, \tilde{W})$ depends on the scaled parameters $\tilde{v} = \frac{v}{\tilde{z}_P}$ and

$$\tilde{W} = \frac{W}{\tilde{z}_P} = \frac{\tilde{v}^2 + \tilde{z}_T^2 - 1}{2\tilde{v}}, \tag{3.20}$$

where $W = (\boldsymbol{K}_i - \mu_P \boldsymbol{K}_f).\widehat{v}$ is the component of the projectile transferred momentum parallel to the incidence velocity $\boldsymbol{v}$. The scaled variable associated to the target charge is $\tilde{z}_T = \frac{Z_T}{\tilde{z}_P}$, which is in our case $Z_T = 1$. For positive $\tilde{W}$ values, $\tilde{\sigma}_{nlm}(\tilde{v}, \tilde{W})$ has a weak dependence on $\tilde{v}$ and can be approximated by an universal function of $\tilde{W}$, denoted as $u_{nlm}(\tilde{W})$.

$$\tilde{\sigma}_{nlm}(\tilde{v}, \tilde{W}) \approx u_{nlm}(\tilde{W}) \tag{3.21}$$

This approximation starts to fail if the condition $\tilde{z}_P > 1$ is not verified, which means $n > 4$ for Be^{4+}, $n > 6$ for C^{6+}, etc.
We take equations (3.18) and (3.21) to define the following relation for the n-partial electron capture cross section σ_n:

$$S_n = \frac{\tilde{z}_P^7 \sigma_n}{|C(Z_P/v)|^2} \simeq U_n(\tilde{W}) \simeq \sum_{lm} u_{nlm}(\tilde{W}), \tag{3.22}$$

where U_n is a universal function of $\tilde{W}$.

Application of the scaling law for n-partial cross sections

In order to ease the application of the suggested scaling law, we propose the next function, which reproduces the universal curve $U(\tilde{W})$. The proposed function (for σ_n expressed in cm^2) is given by:

$$U(\tilde{W}) = \frac{a_1}{(b_1 + c_1\tilde{W}^2)^4} - \frac{a_2}{(b_2 + c_2\tilde{W}^2)^4}, \tag{3.23}$$

where $a_1 = 3.46 \times 10^{-14}$ cm^2, $b_1 = 2.63$, $c_1 = 6.23$, $a_2 = 1.0 \times 10^{-16}$ cm^2, $b_2 = 2.21$, $c_2 = 1.43$. This function, represented with a solid black line in figure (3.24), is valid for evaluating the n-partial cross sections up to $n = 9$ in collisions of A^{q+} with H($1s$), for positive values of $\tilde{W}$. In figure (3.24) we show this curve alongside scaled $n-$partial cross sections as a function of $\tilde{W}$, for the range $n = 4 - 9$, using the S_n (or $U_n(\tilde{W})$) for different projectiles. In the left pannels we show the scaling applied to the present EI and CTMC results, while in the right ones when applied to other results from the bibliography: AOCC of Igenbergs *et al.* [93] and Toshima and Tawara [95]; CTMC from Schultz *et al.* [96] and Olson *et al.* [97]; CDW of Mandal *et al.* [98]; and FBA from Belkić *et al.* [92].

The utility of the n-resolved scaling law is shown in figure (3.25), where partial cross sections for Ne^{10+} projectiles derived from Eqs. (3.22) and (3.23) are compared to data from the bibliography. These results confirm that the proposed scaling provides reasonable predictions for projectiles with $Z_P > 8$.

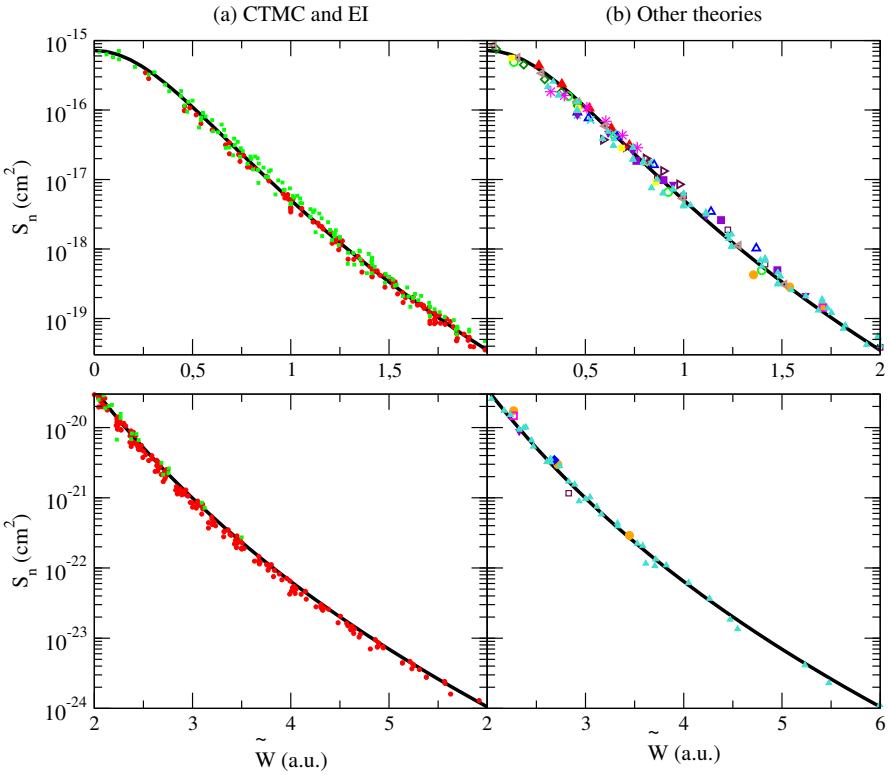

Figure 3.24: Scaled cross sections S_n, as a function of the scaled momentum $\tilde{W}$, for different n values in the range $n = 4 - 9$. Solid black line, proposed curve given by Eq. (3.23). Column (a) (left pannels), results derived with the considered approaches: ● EI, ■ CTMC; column (b) (right pannels), results from other theories: ●, ○ and ■ AOCC for $Z_P = 4$, 6, 8, $n = 6$, 4, 7, respectively [93]; □ and ♦ CTMC for $Z_P = 4$, $n = 6$, 7 [96]; ◊ and ▲ CDW for $Z_P = 6$, $n = 3$, 4 [98]; △ FBA for $Z_P = 6$, $n = 5$ [92]; ×, ∗ and ▷ CTMC for $Z_P = 6$, $n = 5$ and $Z_P = 8$, $n = 6$, 7 [97]; ▫, ▼, ◀ and ■ AOCC for B^{5+} $n = 5$, C^{6+} $n = 5$, N^{7+} $n = 4$ and O^{8+} $n = 3$ [95].

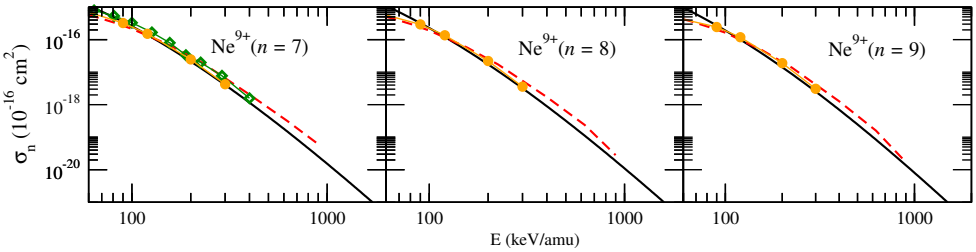

Figure 3.25: Partial CX cross sections σ_n, as a function of the impact energy, for Ne^{10+} + H(1s) collisions. Solid black line, present scaling; calculations: -- CTMC [99], ◇ one-electron-diatomic-molecule (OEDM) [99], ● AOCC [93].

Scaling for nl- distributions

In the case of the partial CX cross section into the nl sub-shell, which is obtained as $\sigma_{nl} = \sum_m \sigma_{nlm}$, the nl- distributions are defined as $P_{nl} = \sigma_{nl}/\sigma_n$. Using equation (3.18) the following scaling rule for P_{nl} is derived:

$$P_{nl} = \frac{\sigma_{nl}}{\sigma_n} \simeq U_{nl}(\tilde{W}) \simeq \sum_m \frac{u_{nlm}(\tilde{W})}{U_n(\tilde{W})}, \tag{3.24}$$

where U_{nl} is assumed as an universal function.
In figure (3.26) the join CTMC and EI results for the P_{nl} distributions of Be^{4+}, C^{6+}, N^{7+}, and O^{8+} projectiles, are plotted as a function of $\tilde{W}$, considering final n levels from $n = 4$ to $n = 9$. To build these curves we have used the join CTMC-EI method, connecting the results of both theories at an impact velocity $v \approx 2.2$ a.u. The CTMC method is used in the lowest values of $\tilde{W}$, i.e. $\tilde{W} \leq 1.5$ a.u., while the EI approach is employed in the high energy region, which corresponds to $\tilde{W} \geq 2.0$ a.u. In all the cases, the P_{nl} values derived from the CTMC method match with those obtained with the EI method in the intermediate scaled transferred momenta $\tilde{W}$ range, between 1.5 and 2.0 a.u.

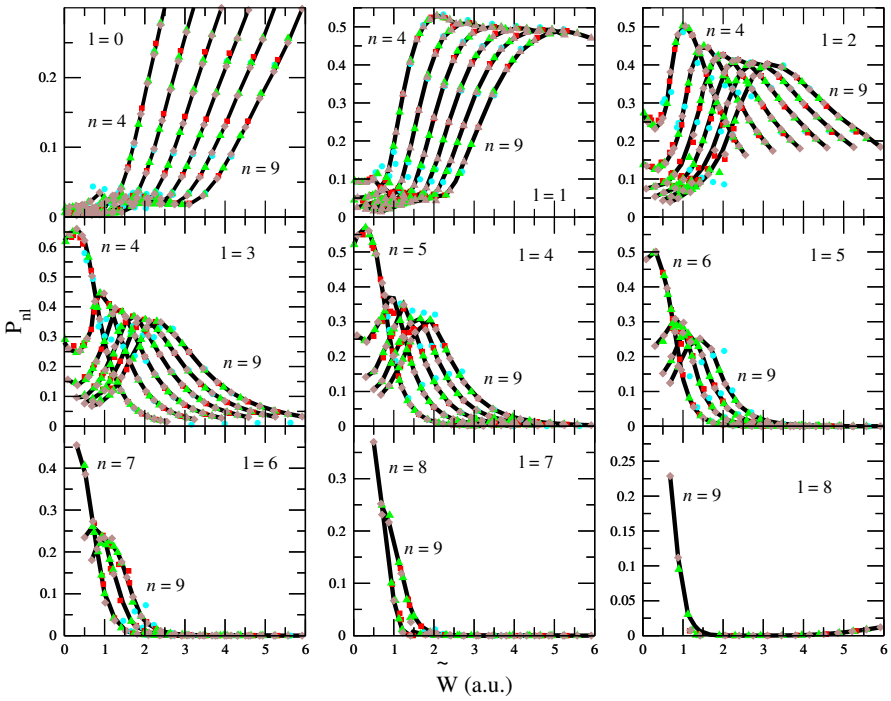

Figure 3.26: Joined CTMC and EI P_{nl} distributions as a function of $\tilde{W}$. Solid black line, present scaling, given by Eq. (3.24); results for different projectiles: • Be^{4+}, ■ C^{6+}, ▲ N^{7+}, ♦ O^{8+}. In each panel the curves shift from left to right as n increases.

Therefore, the curves of figure (3.26) are practically universal functions U_{nl} for the different nl- sub-shells. This result can be used to estimate partial angular momentum distributions for other projectiles with larger nuclear charges than those considered in this work.
In figure (3.27) the P_{nl} distributions for the orbital quantum numbers $l = n-1$ and $l = n-2$ are displayed as a function of $\tilde{W}$. As it is shown, for low $\tilde{W}$ values ($\tilde{W} \lesssim 0.5$ a.u.) the capture proceeds to the subshell with the highest orbital momentum, i.e. $l = n - 1$, but the l-value corresponding to the maximal contribution decreases as the scaled momentum $\tilde{W}$ augments. Altough all the curves for $l = n - 1$ (or $l = n - 2$) present similar behaviours, the population of the nl level depends on the main quantum number n too; as n increases the maximum slightly shifts towards lower $\tilde{W}$ values, decreasing its relative contribution. This behavior is expected to hold for higher Z_P charges.

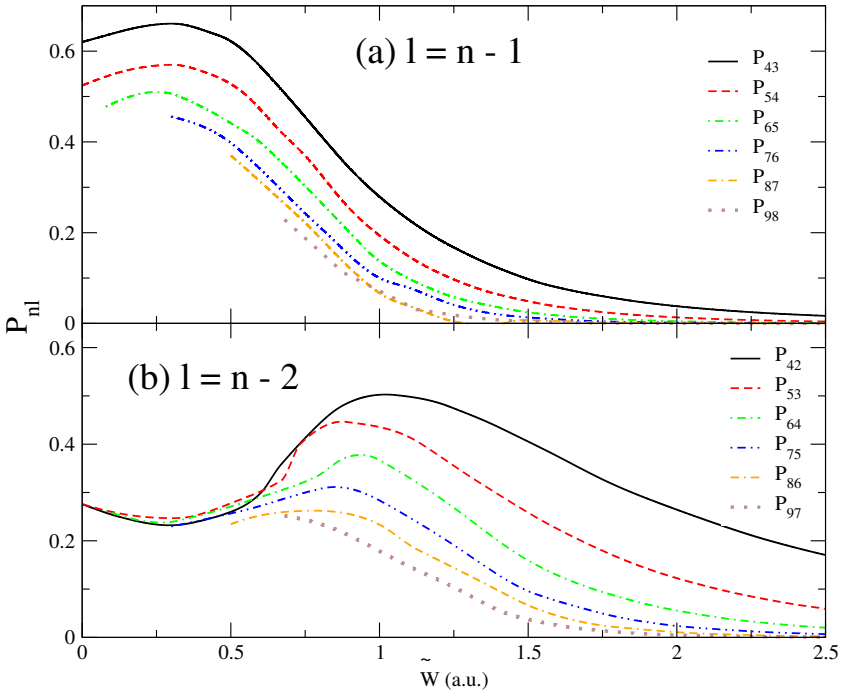

Figure 3.27: P_{nl} distributions, as a function of $\tilde{W}$, for (a) $l = n - 1$, and (b) $l = n - 2$. Solid lines, scaled nl-populations for different n shells, derived within the join CTMC-EI method considering projectile charges $Z_P = 4 - 8$.

In order to provide a more precise representation of the U_{nl} functions for the different n and l values, numerical values corresponding to these universal distributions are presented in tables in the Appendix (C).These tables can be easily used to compute a partial nl cross section for a given electron transition and impact velocity. We show an example, for σ_{43} for the $C^{6+} + H \rightarrow C^{5+}(nl = 43)$ capture process. The steps to calculate σ_{43} are

1. We calculate σ_4 by applying Eq. (3.18) with $Z_P = 6$, $\tilde{z_P} = 6/4$ and $\tilde{z}_T = 4/6$ as follows:

$$\sigma_4 = \left(\frac{6}{4}\right)^{-7} |C(6/v)|^2 U(\tilde{W}), \quad \tilde{W} = \frac{\tilde{v}^2 + (4/6)^2 - 1}{2\tilde{v}}$$

   and $U(\tilde{W})$ from Eq. (3.23).

2. Once we have computed σ_4, we only need to use Eq. (3.24) and Table C.1 to obtain σ_{43} as $\sigma_4 \times P_{43}$.

In figure (3.28) we display, as an example, some partial CX cross sections derived from the proposed scaling functions, as a function of the impact energy, considering: (a) $Z_P = 6$, $n = 4$, $l = 3$; (b) $Z_P = 7$, $n = 5$, $l = 4$; (c) $Z_P = 8$, $n = 8$, $l = 3$. In all the cases, the scaled derived curve, displayed with a black line, runs close to the CTMC and EI results, as well as to the theoretical data extracted from Refs. [93, 70]. Only for the O^{8+} example with $n = 8$, the scaling slightly overstimates the data for the lowest energies, since the condition $Z_P/n > 1$ is not verified. These cases were chosen as a proof of the efficacy of the proposed scaling rule.

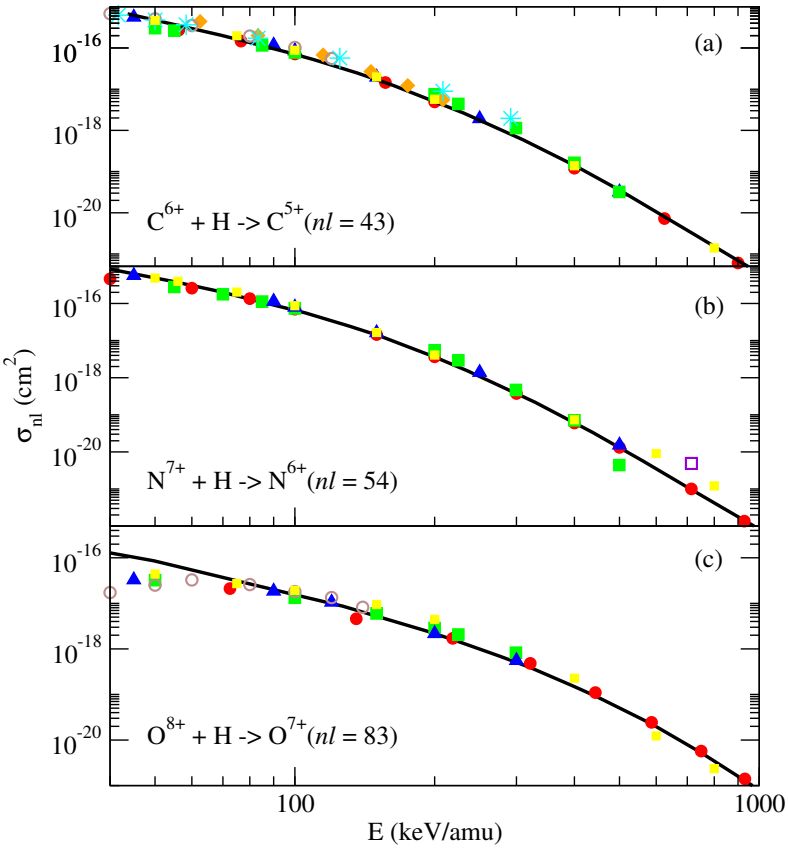

Figure 3.28: Partial CX cross sections σ_{nl} for: (a) $Z_P = 6$, $nl = 43$; (b) $Z_P = 7$, $nl = 54$; (c) $Z_P = 8$, $nl = 83$. Solid black line, present scaling; calculations: ● EIA, ■ CTMC, ▲ AOCC [93], ♦ CDW [98], ○ CTMC [97], ∗ FBA [92], □ CDW [100], ■ AOCC [95].

In conclusion, we propose an easily applicable scaling law for partial $n-$ and $nl-$, with $n < 10$, capture cross sections in collisions of stripped ions with H($1s$). This scaling law has been formulated using previous results up to $n = 4$ of Gravielle *et al* [82, 83] and joining EI and CTMC results, providing tools to predict partial electron capture cross sections in a wide energy range. The good behaviour of the scaled cross sections derived with equation (3.18) and tables (C.1...C.6) has been shown.

$\mathbf{C^{6+} + H}(n=2)$ **and** $\mathbf{N^{7+} + H}(n=2)$

As it was previously remarked, cross sections for collisions of bare ions with excited hydrogen is one of the most current needs in fusion research. The neutral beam used in plasma diagnostic is mainly formed by atoms in the ground state, although it can also contain atoms in excited states, and a small fraction of the ground state atoms can be excited in collisions with the plasma particles [101, 102]. Electron capture cross sections for collisions with H(n=2) are one order of magnitude greater that those with H(1s) at $E \approx 40$keV/amu, which can lead to sizeable values of the corresponding effective emission coefficients [103, 104]. Experimental cross sections for electron capture and ionization in collisions with excited hydrogen are not available, and there is a need of theoretical calculations to obtain these cross sections. In this section we study the collisions of C^{6+} and N^{7+} impinging on H($n=2$). Even when carbon will not be used as a plasma facing material in ITER, since it traps large quantities of tritium by codeposition, C^{6+} is an expected impurity in ITER, where it will be used in spectroscopic diagnostics [4]. With respect to nitrogen, it is one of the elements used to cool the plasma edge; N_2 seeding has become a routine tool in the ASDEX tokamak [105], which leads to the presence of fully stripped Nitrogen ions in the core plasma.

In this section we study the following reactions:

$$\begin{aligned} C^{6+} + H(n=2) &\rightarrow \begin{cases} C^{6+} + H^+ + e \\ C^{5+}(nl) + H^+ \end{cases} \\ N^{7+} + H(n=2) &\rightarrow \begin{cases} N^{7+} + H^+ + e \\ N^{6+}(nl) + H^+ \end{cases} \end{aligned} \tag{3.25}$$

with the CTMC method in the energy range of 5-300 keV/amu. We are interested the description of in both ionization and electron capture processes. State resolved capture cross sections will be studied for the n levels of interest in fusion, those leading to transitions whose emission is in the visible range.

Initial distributions

We consider both a microcanonical and an hydrogenic initial distribution to describe the excited hydrogen. Similarly to the case of the ground-state hydrogen, the microcanonical distribution leads to a radial distribution with a cut-off at $r_0 = 8$ a.u.. In order to improve this spatial distribution, an hydrogenic distribution formed of a weighted combination of six microcanonical

distributions has been used for the description of the H($n = 2$), whose energies and weights are shown in table (3.2).

Table 3.2: Energy and weights of the hydrogenic distribution of H($n = 2$).

E_j (a.u.)	a_j
-0.240	0.200E-02
-0.178	0.168
-0.153	0.206
-0.125	0.264
-0.105	0.212
-0.082	0.148

A comparison of the quantal and two classical spatial and momentum distributions is shown in figure (3.29).

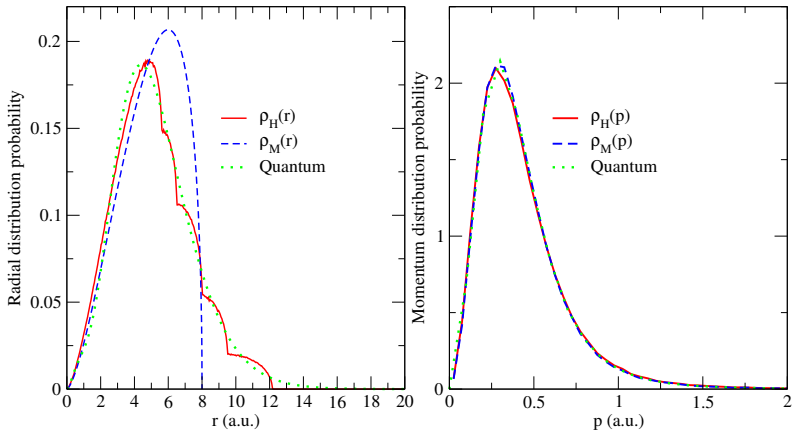

Figure 3.29: Comparison of classical, microcanonical (ρ_{M}) and hydrogenic (ρ_{H}), and quantum distribution of H(n=2)

A recent CTMC work has also dealt with the H($n = 2$) target and the C^{6+} and N^{7+} projectiles [106]. In this work, two different distributions for an initial $2s$ and $2p$ electron were proposed, trying to fit the quantum momentum densities, including the node of the $2s$ state. However, obtaining nodes is imposible with a classical distribution, and it was proven that the proposed initial distribution of [106] for the $2s$ and $2p$ electrons did not satisfy the Liouville equation. This proof can be found in Appendix A.

Total cross sections

In this section we present our total charge exchange and ionization cross sections for C^{6+} and N^{7+} projectiles in collision with H(n=2), compared to the AOCC calculations of Igenbergs *et al.* [93]. These results are shown in figures (3.30, 3.31).

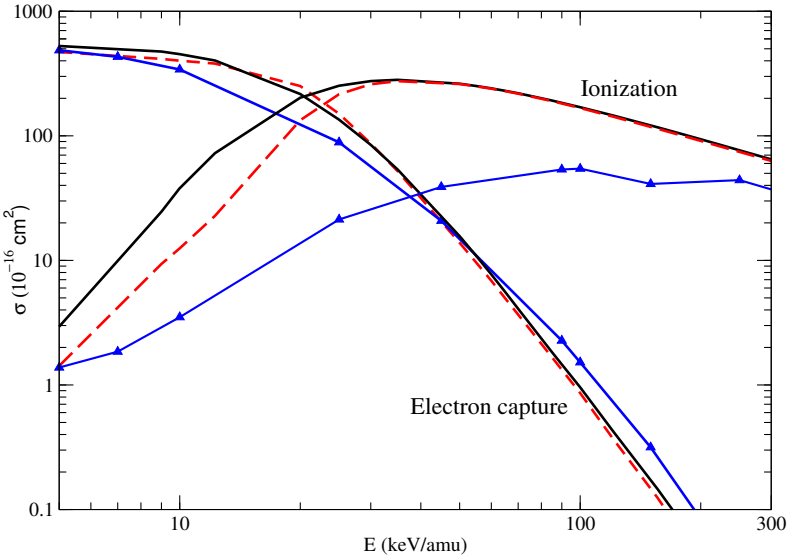

Figure 3.30: Total charge exchange and ionization cross sections for C^{6+}+H(n=2) collisions: (—) hydrogenic-CTMC; (−−) microcanonical-CTMC and (▲ − ▲); AOCC results from [93].

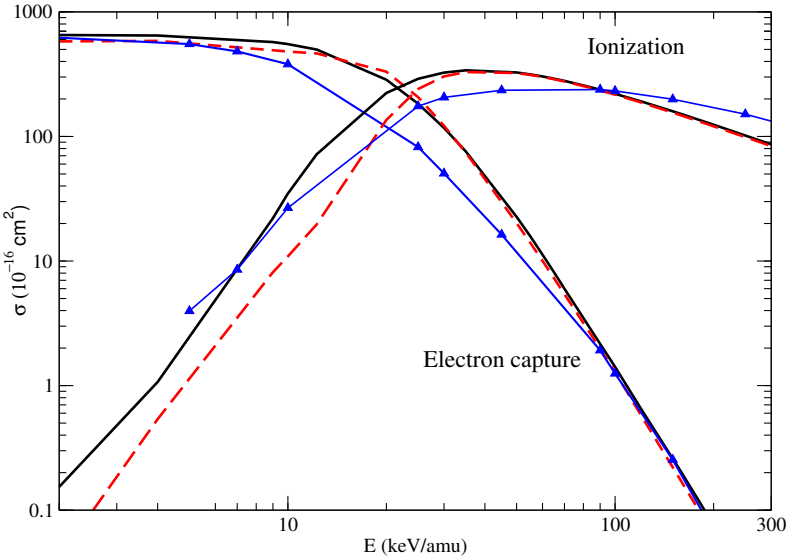

Figure 3.31: Total charge exchange and ionization cross sections for N^{7+}+H(n=2) collisions: (—) hydrogenic-CTMC; (−−) microcanonical-CTMC and (▲ − ▲) AOCC results from [93].

It is worth noting that in the case of excited H(n=2) targets, both classical calculations, microcanonical and hydrogenic, lead to similar total electron capture cross sections, in good agreement with the semiclassical results from reference [93] in the whole energy range considered in this work. The CTMC microcanonical cross sections from [93] are very similar to those obtained in this work, and also to those stored in ADAS (for C^{6+} collisions and $5 < E < 50$ keV/amu) [103], so we have plotted only our data for sake of clarity. With respect to the ionization cross section, we observe the well-known differences between the microcanonical and hydrogenic results in the threshold region that start to disappear for $E \gtrsim 30$keV/amu.

The disagreement with the AOCC ionization cross section observed for the C^{6+} projectile in figure (3.30) is more pronounced than in the case of N^{7+} + H($n = 2$) collisions (3.31). The number of unbound orbitals centered in the H nucleus in the AOCC calculation is lower in the case of the C^{6+} projectile than in the case of the N^{7+} (34 and 63 respectively). This may be the consequence of the underestimation of the ionization cross section for the C^{6+} + H($n = 2$) collision.

We compare in figure (3.32) the charge exchange and ionization transition

probabilities for C^{6+} + H($n = 2$) collisions, calculated using the microcanonical and the hydrogenic initial distributions for $E = 20$ and 50 keV/amu.

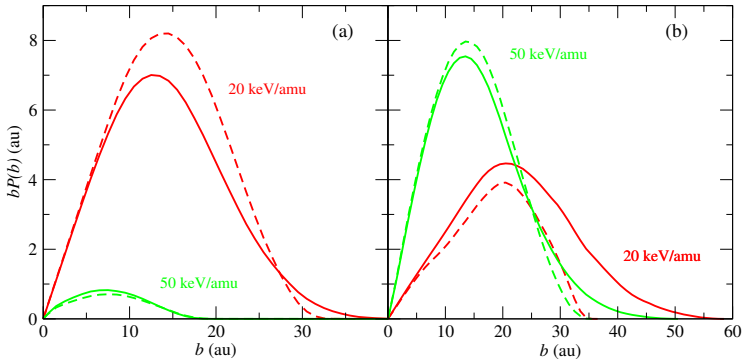

Figure 3.32: Classical charge exchange (a) and ionization (b) opacity functions $bP(b)$, as functions of the impact parameter b for C^{6+}+H(n=2) collisions at E=20 keV/amu and 50 keV/amu, obtained using hydrogenic (——) and microcanonical (**- - -**) initial distributions.

In general, both calculations lead to similar $bP(b)$ values, and therefore, similar total cross sections. However, the cut-off in the radial microcanonical distribution limits the range of impact parameters where the ionization process takes place in the threshold region ($E \approx$ 20keV/amu). This effect in much more noticeable in the case of the H($1s$) target, due to a less extended radial distribution.

n-partial cross sections

In this section we present our n-resolved electron capture cross sections. We are mainly interested in the populations of the levels near n=7-9 because the transitions $n_i = 8 \rightarrow n_f = 7$ (C^{5+}) and $n_i = 9 \rightarrow n_f = 8$ (N^{6+}) lie in the visible spectrum and therefore are of interest in CXRS diagnostics. We have plotted in figure (3.33) our hydrogenic-CTMC n-resolved partial cross sections for C^{6+}, N^{7+}+H(n=2) collisions, for those levels decaying in the visible spectrum that incidentally are the largest n-partial cross sections. It can be noted that these cross sections drop off very fast, almost three orders of magnitude from 10 to 100 keV/amu. AOCC results from [93] are also plotted and we find a very good agreement throughout the energy range of figure (3.33), only at $E >$ 100 keV/amu AOCC data show an overestimation compared to the classical cross sections, this effect is more prominent at the highest n level,

and we believe that, at these energies, the CTMC calculation provides a better description of the electron capture into high n, since the AOCC calculation begins to undergo basis limitations, which are more severe in the case of C^{6+} projectiles.

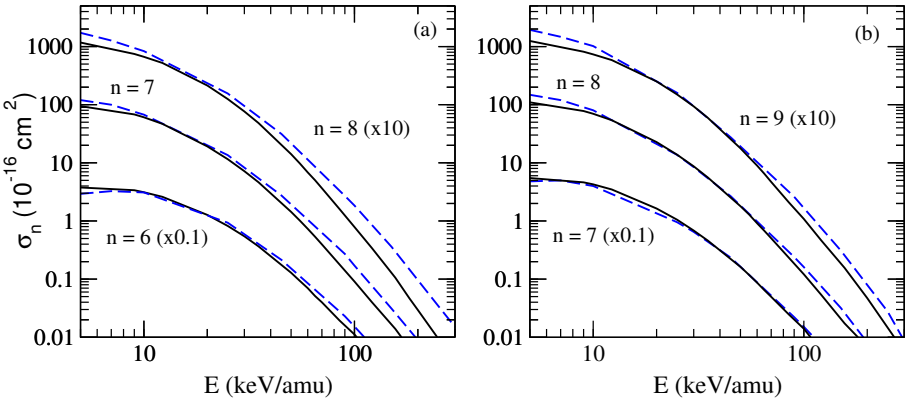

Figure 3.33: Partial n-resolved electron capture cross sections for C^{6+}+H(n=2) (a) and N^{7+}+H(n=2) collisions (b): (—) hydrogenic-CTMC and (−−) AOCC results [93].

The value of $n_{\max}$, the most populated n level after the electron capture process, shows a strong dependence on the impact energy in collisions with H($n = 2$), in contrast to the behaviour of collisions with H($1s$) [67]. This behaviour can be observed in figure (3.34) and also in table (3.3), where the value of $n_{\max}$ for a wide range of impact energies is shown.

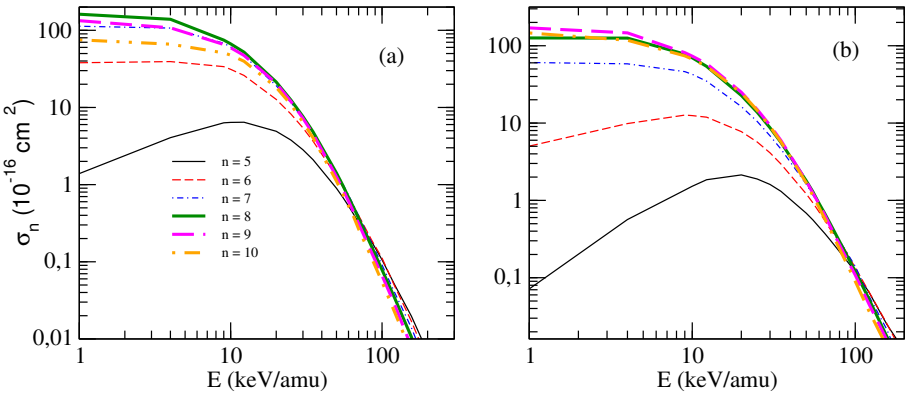

Figure 3.34: Partial n-resolved electron capture cross sections for C^{6+}+H(n=2) (a) and N^{7+}+H(n=2) collisions as a function of energy, obtained with the hydrogenic-CTMC.

Table 3.3: The most populated n level after electron capture process as a function of the impact energy.

E(keV/amu)	C^{6+}+H(n=2)	N^{7+}+H(n=2)
10	8	9
15	8	9
65	7	8
100	6	7
125	6	6
150	5	6
200	4	5

Previous works [35, 107, 108] have dealt with the probability of population for nl states in $A^{(q-1)+*}(n,l)$ in the capture process. In particular, the classical over barrier model of [108] predicts $n_{\max} = 9$ for C^{6+} + H(n=2) collisions respectively, and $n_{\max} = 10$ for N^{7+} + H(n=2), which qualitatively agree with our low-energy results. The low-energy electron capture mechanism involves the polarization and subsequent delocalization of the electronic cloud, which implies that the capture takes place at large internuclear distances compared with the sizes of the initial radial distributions. The relative populations of the atomic levels are determined by their energies, being the most populated states those with energies close to that of the entrance channel. As E increases, the polarization of the electronic cloud becomes less important and the elec-

tron capture process takes place in a narrow range of impact parameters. In collisions with H($n = 2$) the dominant channels at low E are diffuse orbitals, populated at large b, and these populations decrease when the efficiency of the low-energy mechanism diminishes. This effect leads to the variation of $n_{\max}$ with E shown in table (3.3).

nl-partial cross sections

We plot in figure (3.35), as an illustration, our l-resolved partial cross sections for C^{6+} + H($n = 2$) at two collision energies, which have been selected for the importance of the capture process.

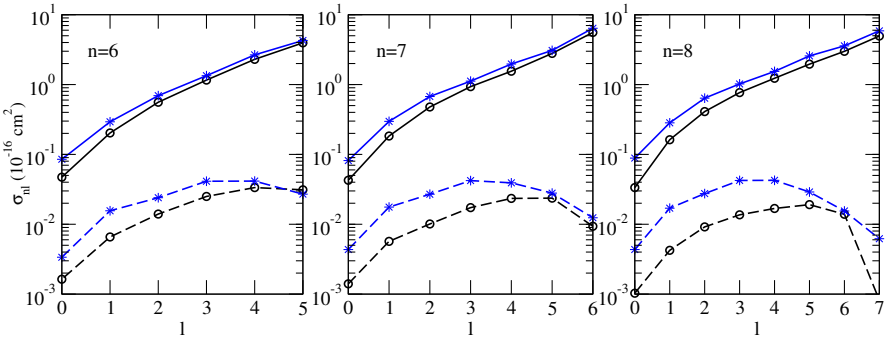

Figure 3.35: Partial nl-resolved electron capture cross sections as functions of the quantum number l, for the collisions C^{6+}+H($n = 2$): Full lines: $E =$ 25 keV/amu; dashed lines: $E = 100$ keV/amu. ($\circ - \circ$) hydrogenic-CTMC and ($* - *$) AOCC [93] results.

The decrease of population as l increases at 100 keV/amu can be explained by using the classical argument of Olson [35]: The charge exchange process takes place when the electron approaches the projectile nucleus in collisions with relatively large b, which is only possible for highly eccentric (low l) electron trajectories. This decrease is, however, not observed for the collisions with H($n = 2$) at $E = 25$ keV/amu, where transitions take place at large internuclear separations for trajectories with large l, as a consequence of the above-mentioned charge exchange mechanism at low E.

In conclusion, we have calculated total and partial cross sections for charge exchange and total ionization cross sections for C^{6+} and N^{7+} + H(n=2) collisions in the intermediate energy range $5 \leq E \leq 300$ keV/amu. Although

charge exchange cross sections for ion collisions with H(n=2) are required in the CXRS diagnostics, few works have considered collisions with excited hydrogen. Both considered initial distributions yield very similar results for collisions with H(n=2), as a consequence of the relatively good description of quantal electron distribution by the microcanonical distribution of the excited states.

Our total hydrogenic-CTMC charge exchange cross sections show general good agreement with recent AOCC results by Igenbergs *et al.* [93] for the four studied systems. The quality of the CTMC partial electron capture cross sections improves as n increases and it is the only method applicable to calculate them for high-lying n final states and to simultaneously evaluate ionization cross sections.

The ionization and charge exchange, total and n-,$nl-$resolved, obtained cross sections are tabulated in the Appendix B, for $5 \leq n \leq 12$.

Semiclassical calculations for Be^{4+} + H(1s)

Electron capture in the reaction Be^{4+} + H(1s)

Beryllium will be used as the armour material of the first wall of the ITER reactor [109] and the ITER-like wall (ILW), which is being tested in JET since 2011, is already composed of Be and W [110, 111]. Fully stripped beryllium ions may be found in the plasma core due to chemical and physical erosion of the first wall and, therefore, can be used in the CXRS technique explained in Chapter 1. Due to this fact and because it is a benchmark in atomic collisions, we study the collision

$$Be^{4+} + H(1s) \rightarrow Be^{3+}(nlm) + H^{+} \tag{3.26}$$

with the Grid Time Dependent Schrödinger Equation (GTDSE) introduced in section 2.4. We start this section showing the soft-core parameters which have been used in this collision for the different employed grids, which are defined by their different values of Δ_q, the separation between points. In the table (3.4) these soft-core parameters are shown for the different grids. They have been obtained with the Lanczos algorithm explained in (2.4.3.1).

Table 3.4: Soft-core parameters ϵ_{H}, ϵ_{Be} (eq. 2.100) employed for different grid densities.

Δ_q (a.u.)	ϵ_{H}	ϵ_{Be}
0.2 (G1)	3.65E-03	5.40E-03
0.137 (G2)	1.70E-03	2.22E-03
0.1 (G3)	8.00E-04	1.10E-03
0.05 (G4)	1.75E-04	2.29E-04
0.025 (G5)	9.64E-06	4.99E-05

One purpose of this work is to appraise the validity of the GTDSE method for different energy ranges; therefore, we have performed calculations from E = 1 keV/amu to E = 500 keV/amu.

1 keV/amu

The collision impact energy of 1 keV/amu is out of the range of interest in fusion plasma cross sections needs. Nevertheless, it has interest in order to

check the validity of the grid method at low energies, as it has been commented. The Impact Parameter Approximation would be the only conjecture that could turn not valid for this low energy impact, but it was checked by Errea *et al.* in [112] that, for 250 eV/amu, eikonal and full quantum mechanical results for Be^{4+} + H($1s$) collision showed differences on the order of 1% for the total and the $n = 3$ partial electron capture cross section, and of the order of 5% for the $n = 4$ partial cross section. Accordingly, since the eikonal approximation turns to be more accurate as E increases, we can expect uncertainties due to the eikonal approximation to be smaller than 1% at $E \gtrsim 1$ keV/amu for the dominant channels. As a reference to compare with, we use the molecular close-coupling calculations from [91] with a 88-term basis set.
It is known [91] that only the $Be^{3+}(n = 3, 4)$ levels are notably populated in reaction (3.26); the population to the $n = 2$ and $n = 5$ levels is about 100 times smaller. We find that results from grids G1 and G3 are indistinguishable, and therefore the calculation does not need to be improved by minimizing the separation between points. In figure (3.36) the $bP(b)$ for capture into $n = 3$, the most populated level, and $n = 4$ is shown, as well as the MOCC results from [91]. There is a difference in the partial cross sections of $\sim 5\%$ with respect to the MOCC calculations, due mainly to the difference in the maximum of the $bP(b)$, for the impact parameter of 6.7 a.u.. But, as it has been commented, an improvement of the grid density does not imply a change in the probability. However, the oscillation of the transition probability is reproduced and, therefore, the collision mechanism is the same in both the MOCC and GTDSE results. It has been checked that the eigenvalues of the molecular Hamiltonian obtained with the GTDSE method are quite close to those energies of the molecular orbitals. The gap in the pseudocrossing between the electronic energies of the orbitals $4f\sigma$ and $3d\sigma$ is 0.0985 a.u. (GTDSE) and 0.0984 a.u. (MOCC), particularly relevant since the transitions in this pseudocrossing provide the main mechanism in the electron capture process at low velocities.

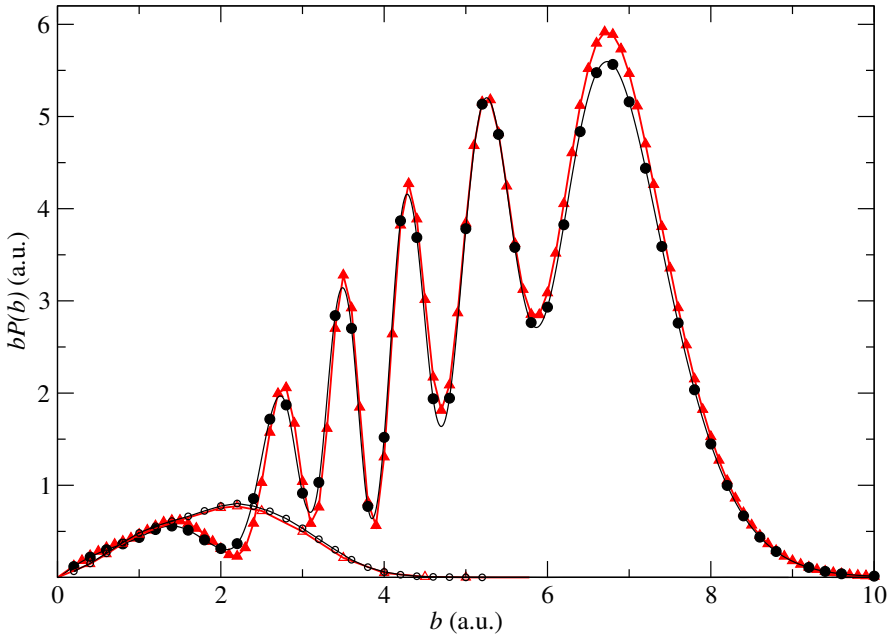

Figure 3.36: $bP(b)$ for electron capture in Be^{4+} + H($1s$) collisions at $E = 1$ keV/u. bP_3^{EC}: (●−●), GTDSE; (−▲-), 88-state MOCC. bP_4^{EC}: (−○−), GTDSE; (− △ −), 88-state MOCC

30 keV/amu

In figure (3.37) we show the state-selective cross sections up to $n = 8$ for 30 keV/amu. At this impact energy the ionization process starts to be relevant, and MOCC calculations without pseudostates will imply a population of the molecular channels, correlated to high-n capture levels [113], with the ionization flux. Therefore, in figure (3.37) we only compare the GTDSE cross sections to those of Igenbergs *et al.* [114, 115], AOCC calculations which include 42 pseudostates to describe the continuum, Slater-type orbitals (STOs) named united atom states. In general, we find an excellent agreement between GTDSE and AOCC calculations. The main exception is for $n = 8$, where the relative difference between the data of the two calculations is much greater than for lower n states. This is probably due to an overpopulation in the close-coupling results due to the ionization flux.

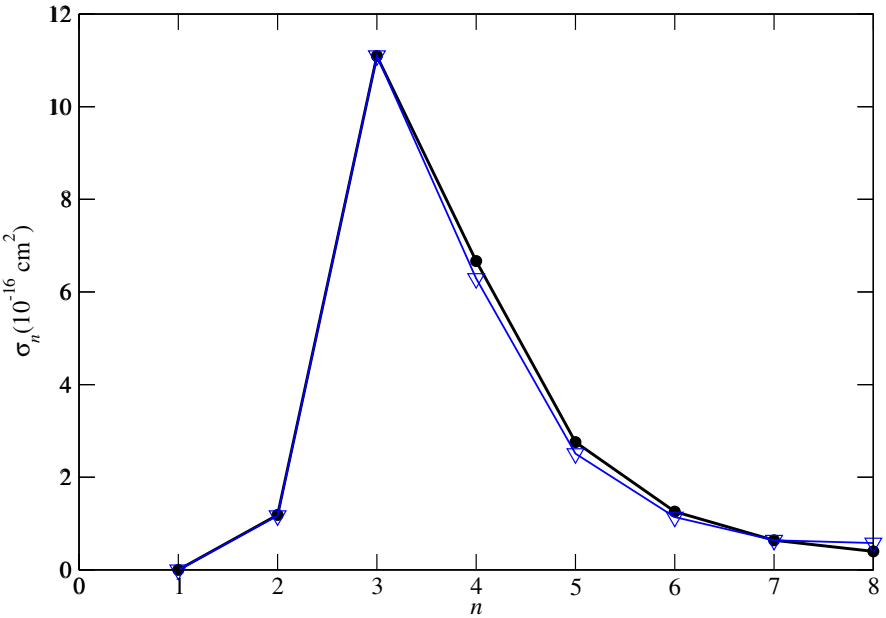

Figure 3.37: n-partial cross sections for EC in Be^{4+} + H($1s$) collisions at E = 30 keV/u. (•), GTDSE calculation(•), ▽, AOCC calculations from [114, 115]

100 keV/amu

In figure (3.38) we show the n-partial cross sections at E = 100 keV/amu. At this energy ionization is an important process and the highest n levels are overpopulated in the AOCC calculation due to the ionization and electron excitation fluxes. Therefore, we also show the CTMC results to compare with. As it has been commented in section 3.1, the population of the $n = 1, 2$ levels is not well described with the initial hydrogenic distribution. But for the fall of the cross sections as n increases the CTMC hydrogenic results are probably the most accurate at this energy range. Due to the importance of this impact energy for fusion (it is expected that the neutral beam injectors that will be used in ITER will work at 100 keV/amu) we have carried out calculations for different grid densities. These are G1, G2 and G3, and the convergence in the cross sections are shown in table (3.5). The calculations show convergence for the considered n levels but for the lowest state, where the value obtained with the grid G3 is close to that from the AOCC method [115] (1.0×10^{-19} cm^2), which could imply that a separation of 0.1 a.u. between points in the grid is

not small enough to describe the $Be^{3+}(1s)$ wavefunction. This problem will be treated with more detail for the next considered impact energy, 500 keV/amu. For $n \geq 3$ the GTDSE and the CTMC cross sections agree with differences smaller than 13%.

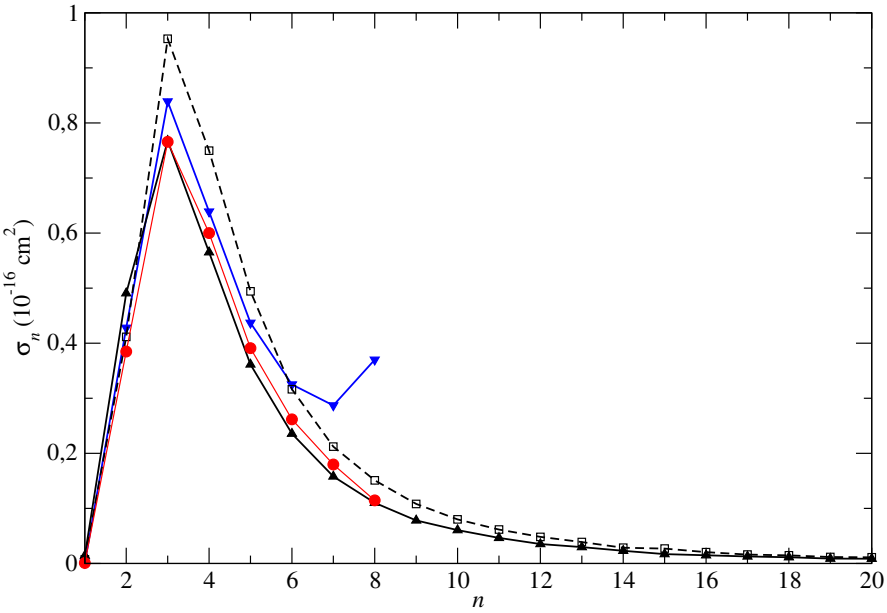

Figure 3.38: n-partial cross sections for EC in Be^{4+} + H($1s$) collisions at E=100 keV/u. (●) Present GTDSE with grid G2, (▲) Hydrogenic CTMC, (□) Microcanonical CTMC, (▼) AOCC calculations from [114, 115].

Table 3.5: n-partial cross sections for reactions (3.26) at $E = 100$ keV/amu obtained with the hydrogenic-CTMC and GTDSE with the grids G1, G2 and G3 (in 10^{-16} cm^2)

n	CTMC	GTDSE (G1)	GTDSE (G2)	GTDSE (G3)
1	0.014	3.6×10^{-4}	3.3×10^{-4}	9.1×10^{-4}
2	0.49	0.39	0.39	0.38
3	0.77	0.77	0.77	0.77
4	0.57	0.58	0.60	0.60
5	0.36	0.40	0.39	0.39
6	0.23	0.26	0.26	0.26
7	0.16	0.18	0.17	–
8	0.11	0.12	0.11	–

500 keV/amu

The collision energy of 500 keV/amu has been studied in order to check the validity of the GTDSE method at high energies. The n-partial capture cross sections are shown in figure (3.39), compared to results from AOCC [114] and the Eikonal Impulse Approximation (EIA) [82, 71], which are the reference to compare with at this collision energy. For $n \geq 4$, the AOCC results probably start to be overestimated due to the ionization flux. The partial cross sections of Minami *et al.* [56] are practically identical to our G3 results. The CTMC obtained with both the microcanonical and hydrogenic distributions are overestimated (see section 3.1) and are not shown.

Very dense grids are required in order to reproduce the fast oscillation of the plane wave associated to the electron translation motion and as well to reproduce accurately the wavefunctions associated to the lowest n levels in $Be^{3+}(nlm)$. At this energy we find a strong limitation due to the large memory needed to perform the calculation; the most dense grids, G4 and G5, were only used at this velocity in order to study the convergence of the lowest n capture levels. With a limitation of memory of 256 GB to store the wave function and the Hamiltonian matrix along the trajectory, the maximum extension of the grid G4 turns to be $-11 \leq x \leq 11$, $0 \leq y \leq 11$ and $-15 \leq z \leq 11$, which implies that states with $n > 3$ could not be included (see section 2.4). In the case of G5, the box is limited to $-5.5 \leq x \leq 5.5$, $0 \leq y \leq 5.5$, $-15 \leq z \leq 5.5$ and only capture to $n = 1$ can be included. We compare in table (3.6) the

cross sections of partial capture to $n = 1$ to the EIA value. We can make an estimation of the cross section for the value of Δ_q of 0 a.u. by doing a least squares fitting of our cross sections to a polynomial of degree 2 of Δ_q^{-1}. This estimation offers a cross section for the $n = 1$ of 9.3×10^{-20} cm^2, which would mean a relative error of 0.5% with respect to the EIA result.

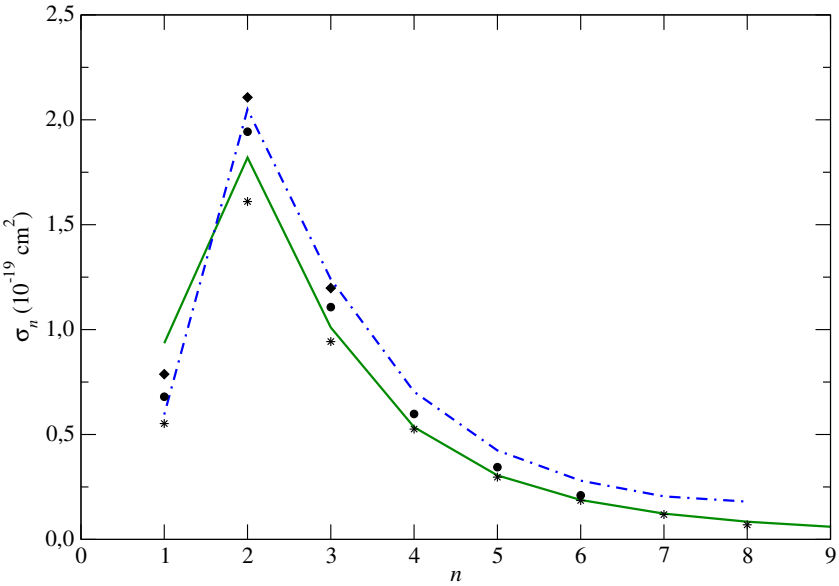

Figure 3.39: n-partial cross sections for EC in Be^{4+} + H($1s$) collisions at $E = 500$ keV/amu. (⧫), (•) and (*) present GTDSE cross sections obtained with grids G4, G3 and G1, respectively, (—) EIA calculations from [82, 71] and ($\cdot - \cdot$) AOCC results from [114, 115].

The main limitation of the GTDSE method is clearly shown at this impact energy, where capture to low n-levels is of great importance and a sufficiently dense grid implies a huge memory needed. As n increases the situation changes, not so dense grids are needed to simulate the wavefunctions of the Be^{3+} and the G1 results are in agreement with the EIA values.

Total cross sections

The total electron capture cross section is obtained in close-coupling and grid methods by adding the n-partial ones. Depending on the impact energy and the maximum value of n included in a calculation, the evaluation of the con-

Table 3.6: n-partial cross section for $n = 1$ in reaction (3.26) at $E = 500$ keV/amu, as function of the grid spacing Δ_q, compared with the result of te EIA method [82]

$\Delta_q(a_0)$	Cross section 10^{-20} cm^2
0.2 (G1)	5.52
0.137 (G2)	6.21
0.1 (G3)	6.80
0.05 (G4)	7.87
0.025 (G5)	8.63
EIA	9.35

tribution of channels not included can be determinant to obtain an accurate value of the total cross section. It was shown in section (3.1) that, for higher energies than 100 keV/amu (see figure 3.2) capture to $n > 10$ levels is not negligible. As in close-coupling methods the limitation is the basis set employed, in GTDSE this limitation comes from the size of the box used. The capture total cross section in the CTMC calculations comes from the fraction of electron trajectories bound to the projectile at the end of the collision, and we do not have therefore this limitation.

In figure (3.40) we show the total capture cross section for the Be^{4+} + H($1s$) collision, compared to data from the bibliography. The two AOCC results [90, 114] disagree for impact energies higher than 25 keV/amu, due to the limited number of channels ($n \leq 5$) included in the calculation of Toshima [90]. The calculation of Igenbergs *et al.* includes up to $n = 8$, and there is a compensation of the not included higher n levels with the overestimation of the included highest n values (see figure 3.38). Minami *et al.* [56] estimated the total cross section for $E \geq 50$ keV/u by adding the contributions from $n = 6 - 10$ obtained using the n^{-3} rule, leading to a total cross section slightly higher than that of Toshima (see the inset of figure 3.40). The total cross section from the GTDSE is estimated as the sum of the partial cross sections for $n = 1 - 8$ tabulated in table (3.5), which lies between those of Toshima ($n_{\max} = 5$) and Minami *et al.* The GTDSE calculation can be easily extrapolated to $n = 50$ joining with the CTMC-hydrogenic cross sections at $n = 8$, since they follow the n^{-3} rule. By doing this, the value of the total cross section, 3.11×10^{-16} cm^2 at $E = 100$ keV/amu, is almost identical to

the CTMC-hydrogenic cross section.

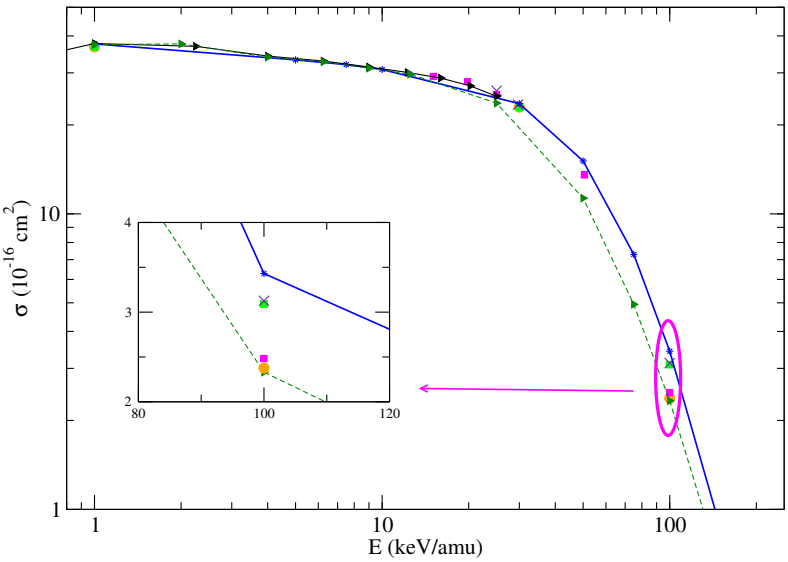

Figure 3.40: Total cross section for electron capture in Be^{4+} + H(1s) collisions, as function of the impact energy. (●) and (■) present GTDSE calculations without and with inclusion of states $n > 8$; (×) present CTMC-hydrogenic. Previous calculations: (■) GTDSE [56], (–∗–) AOCC [114]; (- - ▶ - -) AOCC [90]; (–▶–) MOCC [91]

The most important uncertainty from the CTMC result comes from the overestimation of the transitions to low-n levels. At 100 keV/amu, the overpopulation of the $n = 2$ level is estimated in about a 3% of the total cross section.

The GTDSE method has been proved to provide realiable cross section in a wide energy range which comes from the lowest to the highest impact energy considered in this thesis. It can be used to estimate the accuracy of the existing data of the bibliography. At $E = 1$ keV/amu, the cross sections from AOCC and MOCC disagree in less than 5%, and the differences with the GTDSE are on the order of 3-6%, which allows us to estimate the uncertainty of these data in about 5%. At $E = 30$ keV/amu, the partial cross sections for $2 \leq n \leq 8$, calculated using AOCC and and GTDSE differ in less than 10%. At $E = 100$ keV/amu, the GTDSE allows us to evaluate the accuracy of the CTMC results, being the differences between them smaller than 15% for $n > 2$

. We have also studied the convergence of the capture cross section at this energy, where important discrepancies remain. The total cross section obtained using the GTDSE method extrapolated with the CTMC-hydrogenic results for high n yields an uncertainty smaller than 3%. At $E = 500$ keV/amu, the convergence of GTDSE calculation increasing the density is very slow, and the numerical calculation of the cross sections requires vast computational resources.
In conclusion, the numerical solution of the time-dependent Schrödinger equation is an accurate manner to calculate electron capture cross sections in ion-atom collisions at intermediate energies, where these data are required in fusion plasmas.

Excitation in the reaction Be^{4+} + H(1s)

In the case of the excitation of H($1s$) to H(nlm) we find a different behaviour with respect to capture to the Be^{3+}. Since the extension of the radial functions of the nlm states in atomic hydrogen is much longer than that of the B^{3+}, proper results for low n levels can be found with the grid G1, but this implies the need of much bigger grids in order to include high n levels. We have run some calculations for this process in order to confirm this fact. The electron loss probability is also computed as

$$P_{\text{eloss}} = 1 - |\Psi|^2 \tag{3.27}$$

where Ψ is the wavefunction which remains in the box at the end of the calculation.
In figure (3.28) we show the GTDSE results, obtained with the grid G1, for the reaction

$$Be^{4+} + H(1s) \rightarrow Be^{4+} + H(nlm) \tag{3.28}$$

compared to monocentric calculations from Errea *et al.* [116], for $n = 2, 3$ and electron loss. It can be checked the good agreement for both n levels considered, which implies that a separation between points of 0.2 a.u. is sufficient to accurately represent the wavefunctions associated to the H($n = 2$) and H($n = 3$).

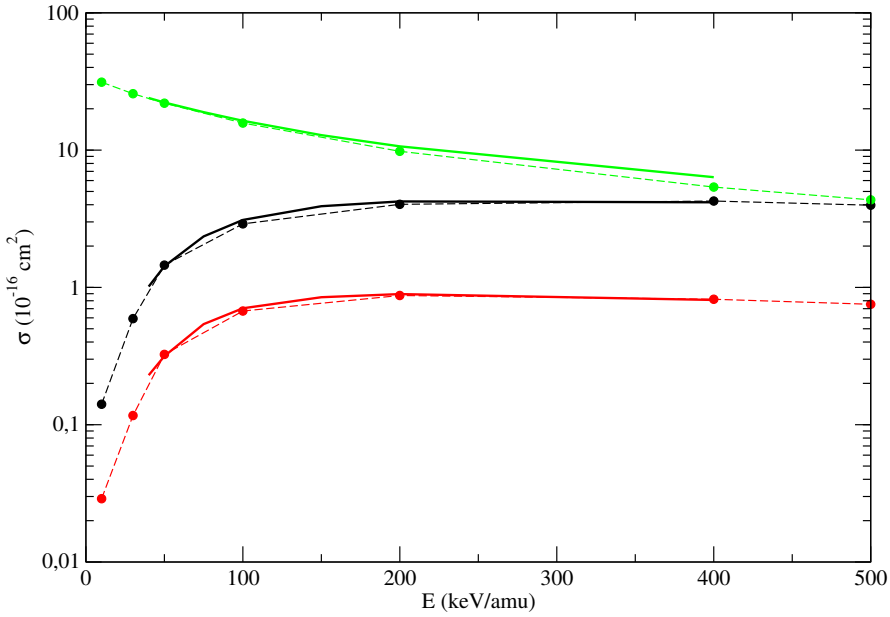

Figure 3.41: n-partial excitation cross section for reaction (3.28), for $n = 2$ (in black) and $n = 3$ (in red) and for electron loss (in green). GTDSE results ($\bullet - -\bullet$), monocentric calculation from Errea *et al.* (—) [116]

The electron loss is well represented until the excitation to n levels higher than $n = 3$ becomes important, which in fact can be observed for $E \geq 200$ keV/amu in figure (3.41), where the electron loss cross section starts to be overestimated. We conclude that the GTDSE method can accurately compute excitation cross sections in a wide collision energy with the same limitations found in the electron capture process, due to the huge computational cost.

Chapter 4

Results for two active electron collisions

Collisions involving many electrons are usually treated by considering one active electron and computing later probabilities for multiple processes with the probabilities obtained in the one-active electron collision, under the independent particle model (IPM). However, a full treatment taking into account more than one active electron has been a matter of interest in the latter times [117]. The first step is the treatment of two-active electrons, and the most simple collisions are H($1s$) + H($1s$) and H^+ + H^-($1s1s$). In the following we present the results for these two collisions under the classical switching approach presented in section 2.3. We focus specially in the formation of H^- in the first reaction, and in the neutralization process in the second one, since they both comprise a switch from the full four-body system to the two independent three-body systems. We have used 500 trajectories in the two initial distributions describing the two electrons, giving rise to a total statistics of 250000 trajectories (for each impact parameter).

H + H collision

We consider the collision bewteen two atomic hydrogens in their ground state. The possible processes for this collision are shown in equation (4.1).

$$\mathrm{H}(1s) + \mathrm{H}(1s) \rightarrow \begin{cases} \mathrm{H}(1s) + \mathrm{H}(1s) & \text{Elastic/Excitation} \\ \mathrm{H} + \mathrm{H}^+ + \mathrm{e} & \text{Target ionization} \\ \mathrm{H}^+ + \mathrm{H} + \mathrm{e} & \text{Projectile ionization} \\ \mathrm{H}^+ + \mathrm{H}^+ + 2\mathrm{e} & \text{Double ionization} \\ \mathrm{H}^+ + \mathrm{H}^- & \text{Target electron capture} \\ \mathrm{H}^- + \mathrm{H}^+ & \text{Projectile electron capture} \end{cases} \tag{4.1}$$

We are specially interested in the target and projectile electron capture, since in these final states the two active electrons are bound to the same nucleus. As it was explained in section 2.3, a system in which two electrons are classically bound to the same nucleus is not stable, since at some point during the time integration one (or both) of the electrons will be ejected due to the Coulomb interaction with the other electron. We find that, with a four-body treatment of the collision (4.1), pairs of electrons get attached to form an H^-. This electron capture process occurs in the surrounding of the target, in around 5 a.u. of distance with respect to it in the z-axis. In order to obtain converged probabilities, integration in time is done up to $2000/v$ a.u.. During this time most of the H^- systems formed are lost due to autoionization, leading to probability for H^- formation which converges to zero when all pairs of bound electrons are lost. In figure (2.6) we showed the behaviour of this probability as a function of the integration time, for an impact energy of 30 keV/amu and an impact parameter b of 1 a.u.. We proposed in section 2.3.2 to switch the four-body (4b) treatment to two independent three-body system (2×3b) when two electrons get bound to the same nucleus. In this three-body treatment, each of the electrons would be under the interaction of a model potential, instead of the sum of the Coulomb potentials from the nucleus and the other electron, which describes the interaction of an electron in the presence of a nucleus and a frozen electron. This potential is of the type

$$V_{3\mathrm{b}} = -\frac{(Z-N)}{r} - \frac{N}{r}(1+\alpha r)\exp(-2\alpha r) \tag{4.2}$$

where $Z = N = 1$ and $\alpha = 0.65$ (a.u.)$^{-1}$. This switch is done under the assumption that the four-body treatment describes well the capture process and therefore needs to be executed to obtain the fraction of trajectories leading to

H^-. After the formation, this treatment cannot describe anymore the stability on time of the formed ion. Therefore the switching maintains the conditions needed for capture, taking into account the interaction of all particles in the four-body treatment, as well as it can describe the dynamics of the two electrons once they belong to the same nucleus. Since the two indepedendent three-body systems formed after the switching are stable, due to the static screening description of the electron-electron repulsion, we can find converged probabilities for both the target and projectile electron capture from equation (4.1). We show in figure (4.1) the evolution of electron capture probability with both a full four-body treatment and with the switching approach, in H($1s$) + H($1s$) to form an H^- anion, for the impact energy of $E = 30$ keV and impact parameter $b = 1$ a.u.. It can be checked that the probability of H^- formation converges to a given value under the switching approach.

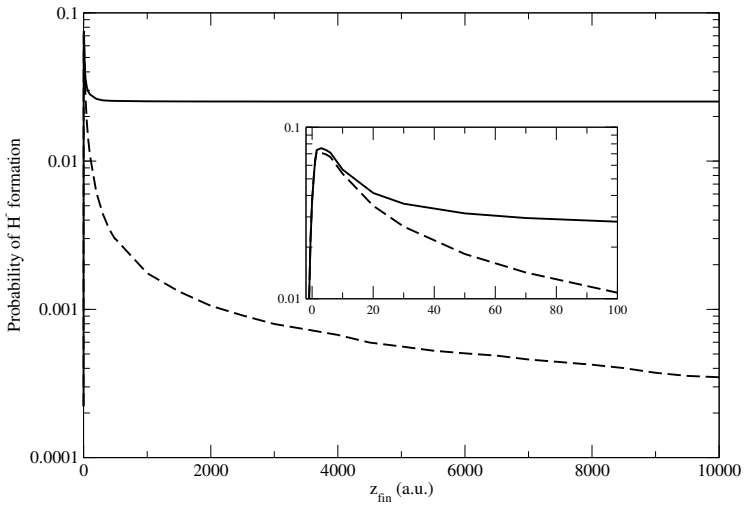

Figure 4.1: Evolution of electron capture transition probability as a function of $Z = vt$ in H($1s$) + H($1s$) collisions with $E = 30$ keV and $b = 1$ a.u. Results from switching (—) and 4b (- - -) CTMC calculations. In the inset, we zoom in on the $-5 \leq Z \leq 100$ a.u. interval.

In figure (4.2) we illustrate the switching, for these same impact energy and impact parameter, for a given pair of trajectories which form an H^- in the target, by showing the distances bewteen the electrons and projectile with respect to the target as a function of the time.

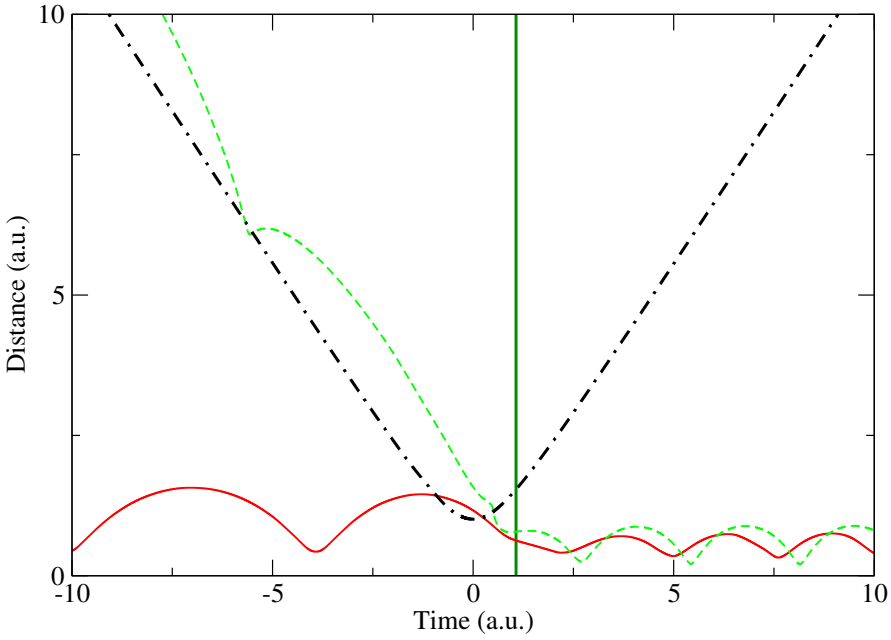

Figure 4.2: Illustration of the switching between 4b- and 2×3b CTMC calculations in H($1s$) + H($1s$) collisions. The figure shows the time evolution of electron distances, r_1 (full line) and r_2 (dashed line), to the target nucleus, and the distance from the projectile to the target nucleus (dashed-dotted line), for a trajectory initially defined by $E = 30$ keV and $b = 1$ a.u. that leads to H^- formation. The vertical line indicates the time when the switching takes place ($t \sim 1$ a.u.).

One can note the smooth behaviour of r_1 and r_2 around $t = 0$ a.u., where we switch from 4b- to 2×3b-CTMC propagations because of H^- formation.

H($1s$)+H($1s$) collisions have been experimentally investigated [52, 51, 118]. These experiments reported total cross sections for electron capture by the projectile

$$H + H \rightarrow H^- + H^+ \tag{4.3}$$

and for positive ion formation

$$H + H \rightarrow H^+ ... \tag{4.4}$$

This last process refers to the production of H^+ in the projectile, which is formed by the projectile simple ionization, double ionization and target electron capture from equation (4.1).

Negative projectile production

The electron capture by the projectile has been studied theoretically by means of semiclassical close-coupling [119], perturbative first Born [120] and four-body CTMC (4b-CTMC) [50, 47, 121] approaches. As it was remarked in section 2.3.1, the 4b-CTMC calculations of Becker and MacKellar [47] drastically underestimated the experimental cross section for reaction (4.3), while the 4b-CTMC calculations of Olson [50] overestimated it, due to a short integration time. A more recent 4b-CTMC calculation, by Dimitriou *et al.* [121], has yielded a clear underestimation of this cross section, as expected from artificial autoionization that follows the formation of the classical H^-, and it is in agreement with the findings of Becker and MacKellar.

We present in figure (4.3) the total cross section for negative projectile ion formation (reaction (4.3)), calculated with both the 4b- and switching-CTMC treatments, with a final time of integration of $2000/v$ a.u.. The differences with those cross sections calculated with a final integration time of $500/v$ a.u. are around 4%, and therefore the calculation can be considered as converged. We have also analyzed the convergence with statistics (we have used around 250000 trajectories per impact parameter) and we have found errors smaller than 3%, by estimating the standard deviation error of the probability as explained in [122]. These cross sections are compared to the experimental data from [52, 118], the above mentioned previous 4b-CTMC [50, 121] and semiclassical atomic close-coupling [119] calculations. Our 4b-CTMC cross section agree with that of Dimitriou *et al.* [121], as it could be expected since these authors also employed the standard 4b-CTMC method. Both calculations are found to strongly underestimate the experimental cross section because of the instability of the H^-. As it was also mentioned before, the 4b-CTMC results of Olson [50] lie high above the experimental data, probably due to an excessively short integration final time in his calculations. On the other hand, our switching-CTMC approach yields converging probabilities and the associated cross section shows nice agreement with the experiments from McClure and Hill *et al.* [52, 118]. The agreement with the close-coupling results of Wang *et al.* [121] is also remarkable.

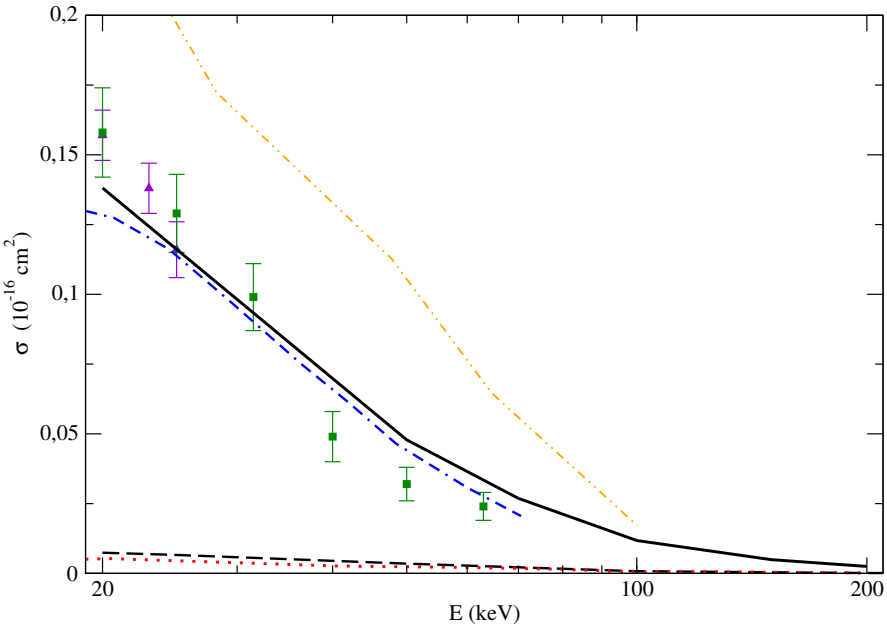

Figure 4.3: Total cross section for negative projectile ion formation (eq. (4.3)) as a function of the incident energy E in the lab frame. Present switching (—) and 4b (- - -) CTMC calculations. Previous 4b-CTMC results from Dimitriou *et al.* [121] (· · ·) and Olson [50] (- · - ·). Two-center two-electron close-coupling calculations from Wang *et al.* [119] (- - · - -). Measurements from Hill *et al.* [118] (▲) and McClure [52] (■).

Positive projectile production

The probability of this process is the sum of projectile ionization, double ionization an target electron capture:

$$\mathrm{H}(1s) + \mathrm{H}(1s) \rightarrow \mathrm{H}^+ + ... = \begin{cases} \mathrm{H}^+ + \mathrm{H} + \mathrm{e} & \text{Projectile ionization} \\ + & \\ \mathrm{H}^+ + \mathrm{H}^+ + 2\mathrm{e} & \text{Double ionization} \\ + & \\ \mathrm{H}^+ + \mathrm{H}^- & \text{Target electron capture} \end{cases} \tag{4.5}$$

We compare in figure (4.4) the present results for this process for both the 2x3b- and 4b-treatments with the available measurements from the biblio-

graphy.

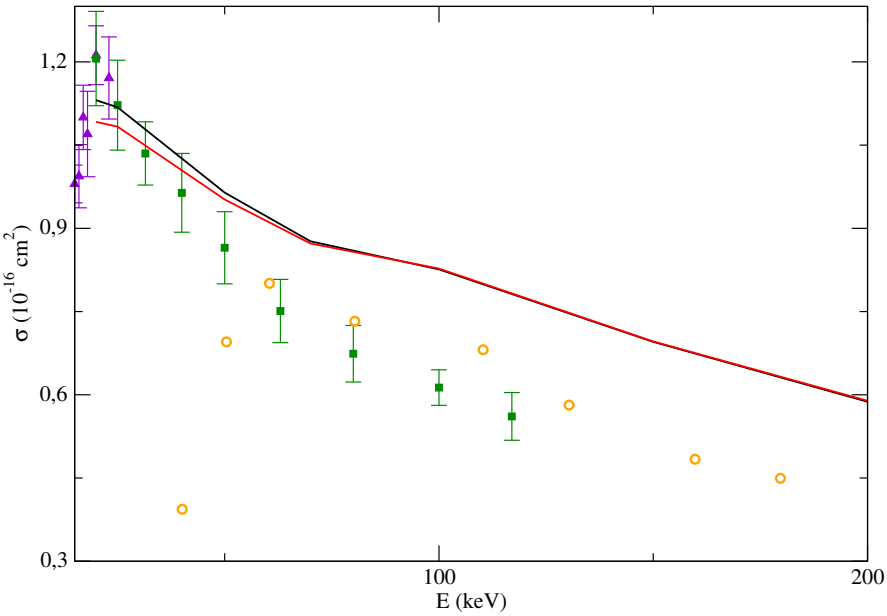

Figure 4.4: Total cross section for positive projectile ion formation (reaction (4.4)) as a function of the incident energy E. Present switching (—) and 4b (—) CTMC calculations. Measurements from Hill *et al.* [118] (▲), McClure [52] (■) and Wittkower *et al.* [51] (o).

One can observe that, in this case, there is almost no difference between the results of the two CTMC approaches except at the lowest energy regime considered, where cross sections obtained with the switching approach are slighty higher than those of the 4b-treatment. We find that both CTMC results are overestimated with respect to the experiments in almost all the energy range. The switching target and projectile ionization cross sections are smaller than those obtained with the four body treatment, since ejected trajectories in H^- due to autodetachment end in target or projectile ionization. This behaviour is only important at the lowest energies where the formation of H^- is not negligible. In figure (4.5) we show how important the contributions of each individual process from equation (4.5) are. For the switching approach (upper panel) and 4b-treatment (lower one), we show the positive projectile formation cross sections as well as its individual contributions from equation (4.5). One can note that slightly higher cross sections for the simple projectile

ionization are found with the 4b- approach at the lowest energies. However, due to the target electron capture importance at the lowest impact energies, which implies the formation of an H^-, the total positive projectile formation is finally higher with the switching approach at $E = 20$ keV. When target electron capture starts to be negligible in the contribution the 4b- and 2x3b- results are indistinguishable and, as commented, overestimated with respect to the experimental values. This overestimation is probably due to the double ionization process, since the best comparison between the CTMC results and experiments is found when its contribution is less important.

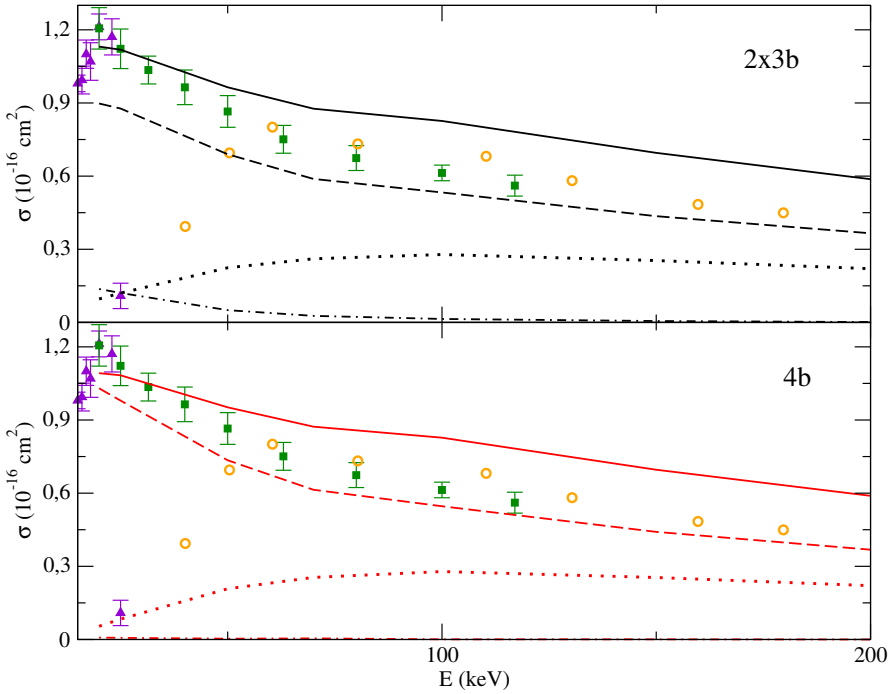

Figure 4.5: Total cross section for positive projectile ion formation (reaction (4.4))and its components from equation (4.5) as a function of the incident energy E. Present switching (in the uper panel, in black) and 4b (in the lower one, in red) CTMC calculations. Positive projectile formation (—), simple projectile ionization (− − −), double ionization (···) and target electron capture (− · −). Measurements from Hill *et al.* [118] (▲), McClure [52] (■) and Wittkower *et al.* [51] (o).

$H^+ + H^-$ collision

The collision

$$H^+ + H^-(1s, 1s) \tag{4.6}$$

is studied under the switching approach. Both the H($1s$) + H ($1s$) and the H^+ + $H^-(1s, 1s)$ are the most simple collisions which involve two electrons. In this case, the aim is to study the behaviour of the switching approach with an initial ion with two electron. It turns impossible to treat this collision with the 4-body treatment, since the initial condition would not be time-independent due to the auto-ionization that the initial target would suffer. In the switching approach, the initial anion is described with two microcanonical distributions with energy E = -0.027 a.u. and whose hamiltonian for each of them is

$$H = \frac{p^2}{2\mu} - \frac{1 + \alpha r}{r} \exp(-2\alpha r) \tag{4.7}$$

with $\alpha = -0.65$ (a.u.)$^{-1}$. As it was explained in (2.3.2) we find that the total atom energy, obtained including the complete hamiltonian with the Coulomb and interelectronic repulsion potentials (from eq. 2.92), has an expected value of -0.45 a.u., close to the experimental one, while the bound energy of each of the electrons remains constant. We can summarize the processes presented in (2.77) as follows:

$$H^+ + H^-(1s, 1s) \rightarrow \begin{cases} H^+ + H^- & \text{Elastic + excitation} \\ H + H & \text{Mutual neutralization} \\ H + H^+ + e & \text{Transfer ionization} \\ H^+ + H + e & \text{Detachment} \\ H^+ + H^+ + 2e & \text{Double ionization} \\ H^- + H^+ & \text{Charge exchange} \end{cases} \tag{4.8}$$

We are mainly interested in the mutual neutralization process, since it implies a switching between the two 3-body systems for each electron to the complete 4-body problem. In addition, it has been studied, as well as the detachment process, theoretically with molecular and atomic close coupling calculations and first Born approximation ([123, 119, 124, 125, 126, 127, 128, 129]) and experimentally ([130, 131, 132, 133]) through the years. Some experiments do not measure the final charge of the projectile and, therefore, the cross section for neutral target formation is defined as the sum of mutual neutralization and

detachment.

$$H^+ + H^-(1s, 1s) \rightarrow ... + H = \begin{cases} H + H & \text{Mutual neutralization} \\ & + \\ H^+ + H + e & \text{Detachment} \end{cases} \tag{4.9}$$

The usual description of H^- generally involves the concept of inner and outer electrons, even when in quantum mechanics both electrons are equivalent. In the CTMC switching approach, a two-electron ion is described in terms of independent systems for each electron. We gave some details on the H^- under the 2x3b assumption in section 2.3.2, and the mean value of energy for the total hamiltonian was obtained under no external perturbation. Now we can make a similar analysis for the case in which the projectile H^+ collides with it. We show in figure (4.6) the time evolution of the mean monoelectronic energies of the two electrons, computed by averaging $E_i^{(T)} = p_i^2/2 - 1/r_i$ over all independent trajectories. This is done for all the statistics and also only for trajectories leading to final total neutralization. The figure shows a zoom of the region where the projectile and target are closer and the different processes take place, for the impact energy of 30 keV and the impact parameter of 1 a.u.. We find values of mean energy for the two electrons close to -0.5 a.u., considering all the trajectories and also considering only those which give rise to neutralization. It is also shown the mean repulsion $< 1/r_{12} >$, which approaches +0.5 a.u. Moreover, if we focus only on the trajectories leading to neutralization (the lines in figure 4.6) we find that the mean monoelectronic energy of those electrons which are ejected and captured by the projectile is lower than that of those which remain with the proton. Therefore, the mean total energy of the H^- described with two microcanonical distributions with an initial ionization energies of -0.027 a.u., is quite close to the quantum value also under the interaction of a projectile.

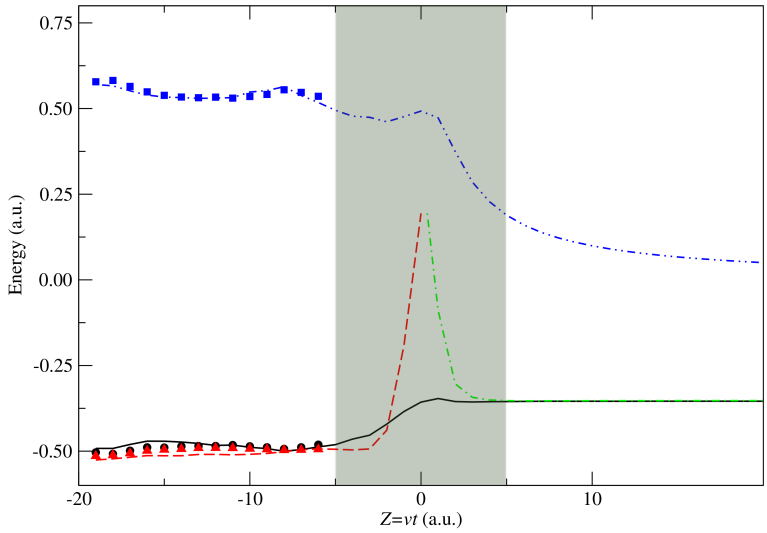

Figure 4.6: Illustration of the temporal evolution of mean monoelectronic energies $< E_1^{(\mathrm{T})} >$ (—, •), $< E_2^{(\mathrm{T})} >$ (- - -, ▲), $< E_2^{(\mathrm{P})} >$ (- · - ·) and mean interelectronic repulsion, $< 1/r_{12} >$, (- · · -, ■) for a nuclear trajectory with $E = 30$ keV and $b = 1$ a.u. in H^++H^- collisions. The lines refer to averages over the electron pairs (e_1,e_2) leading to direct neutralization, while the dots refer to averages over all $\mathcal{N}^2$ electron pairs. The shaded area indicates the region where the switching between 2×3b- and 4b- CTMC descriptions takes place.

Once we have shown the reasonable behaviour of the switch from the 2x3b to the 4b system, we analyze the neutralization process.

Mutual neutralization

Mutual neutralization is usually studied not considering all the possible final states for the final target hydrogen, but only the ground-state $1s$. Therefore we will name this procces as neutralization $nlm - 1s$

$$H^+ + H^-(1s^2) \rightarrow H(nlm) + H(1s) \tag{4.10}$$

We analyze first the total neutralization cross sections, which has been measured by Schön *et al.* in [130]. It has also been studied from a theoretical point of view by Shingal and Brandsden [123], who spectrally calculated it with a two-centre expansion and a basis of 23 states for each heavy particle. They performed calculations for both the total and $nlm - 1s$ neutralization processes. The comparison of the switching results for the total neutralizacion process with the experimental and theoretical values, from [130] and [123] respectively, is shown in figure (4.7).

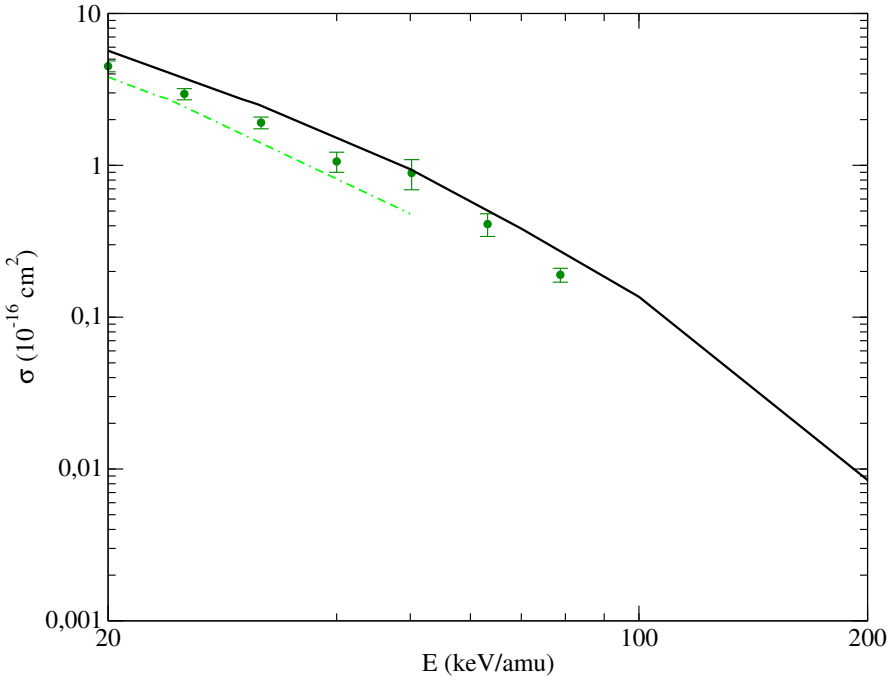

Figure 4.7: Total cross section for mutual neutralization $H^+ + H^-(1s^2) \rightarrow H(nlm) + H(n'l'm')$ as a function of the collision energy E. Present CTMC results are obtained under the switching (—) approach. Coupled-channel calculations from Shingal and Bransden [123] (- - · - -). Experimental results from Schön *et al.* [130] (•).

The $nlm - 1s$ neutralization is shown in figure (4.8).

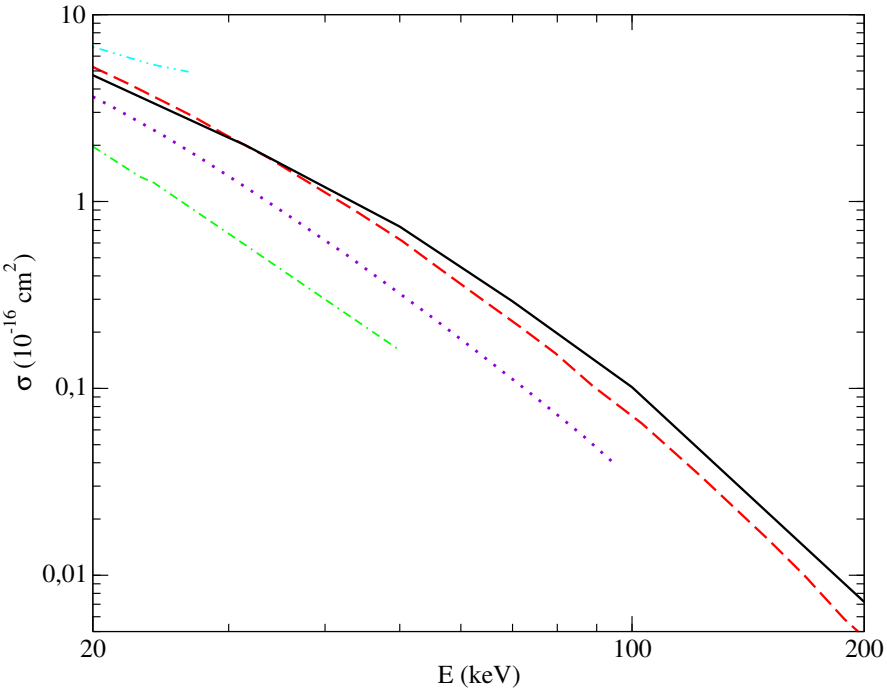

Figure 4.8: Partial $nlm - 1s$ neutralization cross section $H^+ + H^-(1s^2) \rightarrow H(nlm) + H(1s)$. Present CTMC results are obtained under the switching (—)approach. Coupled-channel calculations from Shingal and Bransden [123] (- - - -), Wang *et al.* [119] (- · · -), and Ling and Wang [124] (···). CB1-4B results from Mancev *et al.* [125] (- - - -).

One can note the good agreement with the experimental values for total neutralization in figure (4.7) and with the most recent calculations of Mancev *et al.* in the case of $nlm - 1s$ neutralization in figure (4.8). However, we find an slight overestimation for the highest impact energies. We relate this ovestimation with the studied behaviour of the classical capture results in the high energy range, made in section 3.1. In that section, we found that CTMC capture cross sections for the collision $C^{6+} + H(1s)$ started to be overestimated for collision enegies greater than $\simeq$ 250 keV/amu. Here, the behaviour is the same but with a shift in energy due to the charge of the projectile. This shift can be clearly observed in figure (4.12) and will be discussed later. Nevertheless, we find that the switching approach is able of describing the neutralization in the $H^+ + H^-(1s, 1s)$ collision, as well as the

initial H^- anion. It is important to remember that this system cannot be described in any case with a CTMC four body treatment, since the initial H^- would not be stable.

Detachment

In figure (4.9) the obtained cross section for the detachment process is compared to available theoretical [126, 128, 129] and experimental [132] data. With respect to these experimental values, which agree with the calculations of Belkić *et al.* [126], the switching CTMC results are clearly underestimated.

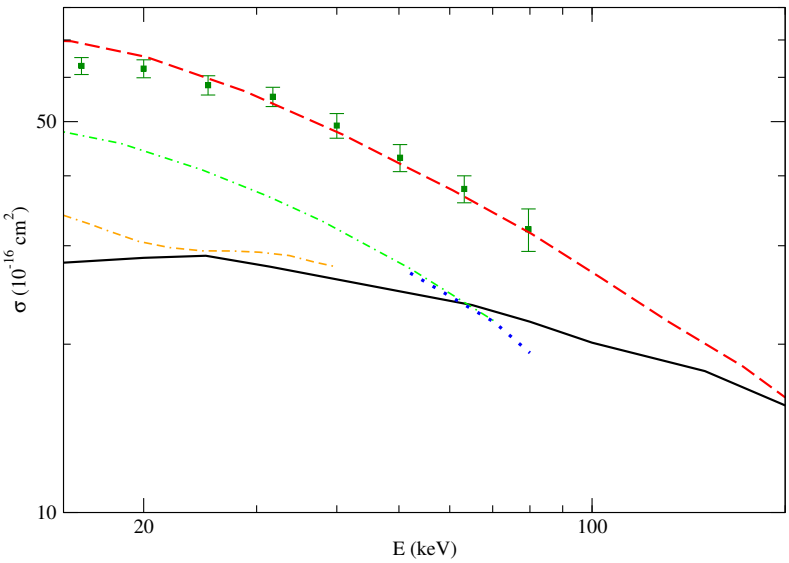

Figure 4.9: Detachment cross sections $H^+ + H^-(1s^2) \rightarrow H^+ + H(nlm)$. Present CTMC cross sections (—), FB from Belkić [126] (– – –), Close-coupled calculations from Ermolaev [128] with 36 states (· — ·) and 51 states (···), molecular expansion with translation factor from Errea *et al.* [129] (– – · – –). Measurements from Melchert *et al.* [132] (■).

The same behaviour is, therefore, found for the neutral target formation, since its main contribution is the detachment process (see equation 4.9). Results for neutral target formation are shown in figure (4.10).

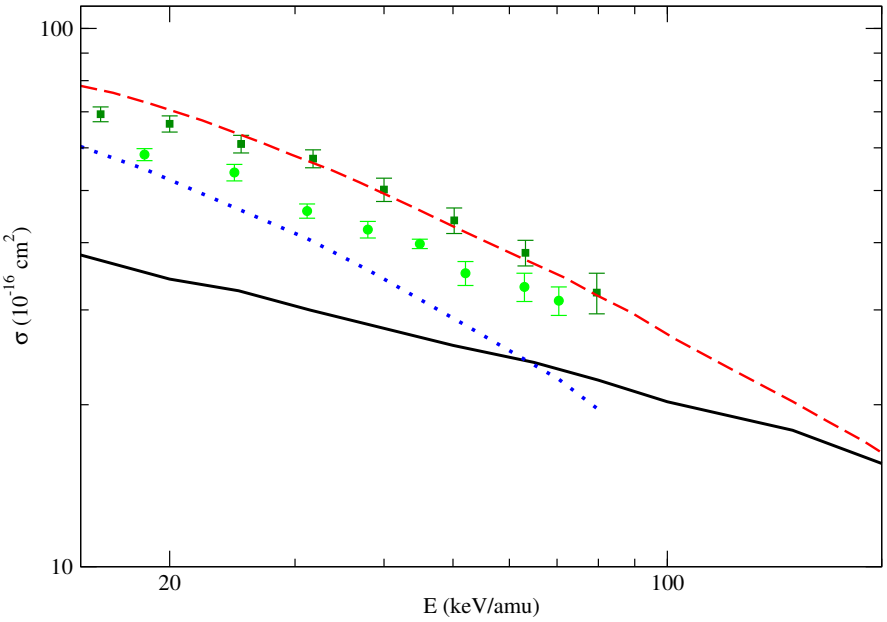

Figure 4.10: Neutral target formation cross sections $H^+ + H^-(1s^2) \rightarrow ... + H(n'l'm') + e$. Present CTMC cross sections (—), FB, sum from Belkić [126] and Mancev *et al.* [125] (– – –), Close-coupled calculations from Ermolaev [128] (· · ·). Measurements from Melchert *et al.* [132] (■) and Peart *et al.* [133](●).

We analyze this problem by looking at the initial distribution which has been used for the description of the H^-. In figure (4.11) the radial density obtained from the microcanonical distribution ($\rho^M(r)$) for the H^-, created with (4.7), $\alpha = -0.65$ (a.u.)$^{-1}$ and E = -0.027 a.u., is shown compared to the quantum-mechanical one ($\rho^Q(r)$). In the inset we show the same for the H, to display the differences between them.

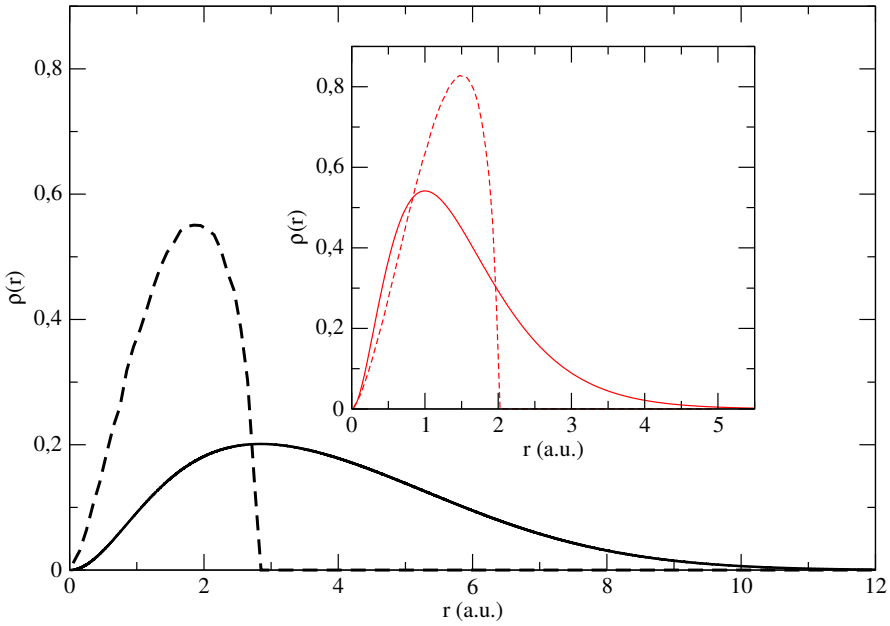

Figure 4.11: Radial density obtained with a microcanonical distribution (– – –), compared to its quantum-mechanical one (—), for H^- (black) and H (red, in the inset).

The presence of a cut-off in the radial density obtained from a microcanonical distribution is known, and can be solved with other kind of initial distribution, as it has been explained in section (2.2.2.3). Nevertheless, it is worth noting in figure (4.11) that, even when the initial distribution is not improved, the description of H^- ion with the microcanonical distribution is worse than that of H. It is worse in the sense that

1. If we denote with $r^{\mathrm{H}}_{\mathrm{max}} = 1.0$ a.u. to the value of r for which $\rho^Q_{\mathrm{H}}(r)$ is maximum (and equivalently $r^{\mathrm{H}^-}_{\mathrm{max}}$=2.85 a.u. for H^-), we find that $\rho^M_{\mathrm{H}}(r^{\mathrm{H}}_{\mathrm{max}}) = 0.63$, while in H^- we have $\rho^M_{\mathrm{H}^-}(r^{\mathrm{H}^-}_{\mathrm{max}}) = 0$, since $r^{\mathrm{H}^-}_{\mathrm{cut-off}} = r^{\mathrm{H}^-}_{\mathrm{max}}$.

2. The % of the quantum density which is not represented because $r > r_{\mathrm{cut-off}}$ is much bigger in the case of H^- than in the case of H. We find

$$\int_{\mathrm{cut-off}}^{\infty} \rho^Q_{\mathrm{H}}(r)\mathrm{d}r = 0.24 \qquad \int_{\mathrm{cut-off}}^{\infty} \rho^Q_{\mathrm{H}^-}(r)\mathrm{d}r = 0.65 \qquad (4.11)$$

Indeed, the results from figures (4.7) and (4.9) remind to their equivalents in the one-electron case. We compare the presented neutralization and detachment cross sections to the corresponding simple electron capture and ionization in the $C^{6+} + H(1s)$, calculated with a microcanonical and an hydrogenic initial distribution. This comparison is shown in figure (4.12). In the left panels we show the cross sections obtained with the switching approach for the detachment (upper panel) and neutralization (lower panel) processes. In the right, we have their equivalents ionization (upper) and electron capture (lower) results. We only show CTMC results obtained with an initial microcanonical distribution (full black lines) and an hydrogenic one (stripped red line), compared to available experiments for these reactions. For the C^{6+} + H collision we have that the fall of the electron capture cross section is well represented by both the initial distributions, while in the ionization case we have very different results. It is known that this last process is better described with an hydrogenic distribution than with a microcanonical one [24], due to the contribution of the electrons belonging to the tail of the radial density. This is the same behaviour that we find in the $H^+ + H^-$ reaction. The ionization (detachment) is not well represented since we are not taking into account in our distribution electrons with $r > r_{\mathrm{cut-off}}$, but we still have a good representation of the fall of the electron capture (neutralization) [24].

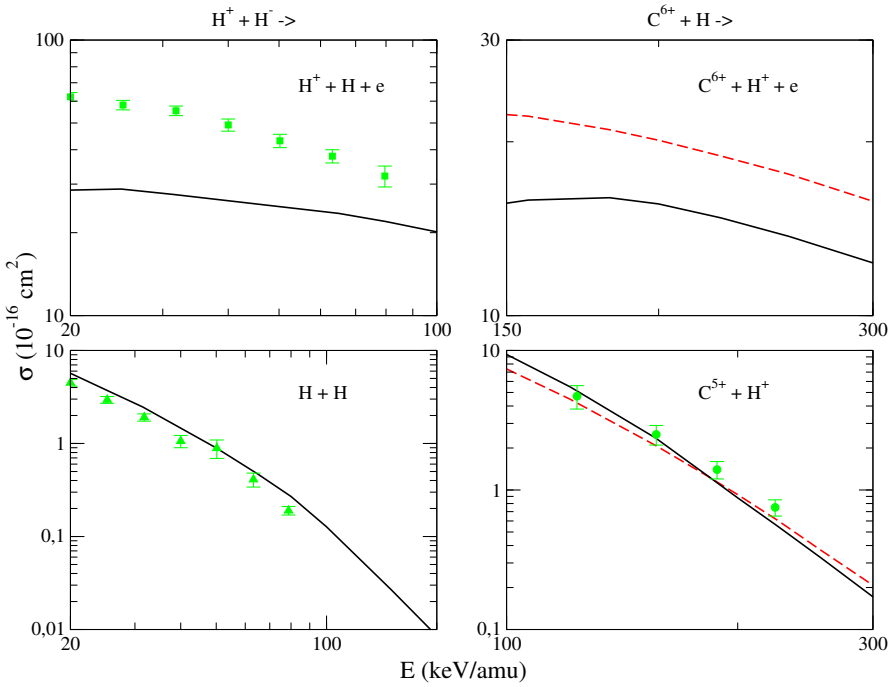

Figure 4.12: Left panels: $H^+ + H^-$ giving rise to detachment (upper) and neutralization (lower). Right panels $C^{6+} + H$ giving rise to ionization (upper) and electron capture (lower). Full black lines are for microcanonical CTMC results, stripped red lines for hydrogenic CTMC results. Experimental cross sections in green: (■) Melchert *et al.* detachment results from [132]; (▲) Schon *et al.* neutralization results from [130]; (●) Goffe *et al.* electron capture results from [69].

Therefore, the next step would be to construct an improved initial distribution for the H^- following the idea presented in section (2.2.2.3). We need a weighted combination of microcanonical distributions, with different values of energy E_j, which fulfill that the sum of the energies multiplied by their respective weights is as close as possible to the real ionization potentials (see equation 2.67). Since we are representing an H^- anion, and we need two initial distributions to represent both electrons, we have to implement two different weighted sums of microcanonical distributions. The mean energies of these distributions, $\overline{E}_1$ and $\overline{E}_2$, have to be as close as possible to the ionization

potential $U = -0.027$ a.u.

$$\begin{aligned} \overline{E}_1 &= \sum_j^n a_j E_j \simeq U = -0.027\text{a.u.} \\ \overline{E}_2 &= \sum_i^m b_i E_i \simeq U = -0.027\text{a.u.} \end{aligned} \tag{4.12}$$

An additional condition is introduced in order to have, for each couple of electrons in each run trajectory, the value of two times the ionization potential U. This implies that the number of microcanonical distributions used in each weighted sum must be the same and, also, that the energies and weights must be equal but opposed for each sum.

$$\begin{aligned} &n = m \\ &b_j = a_{j-n-1} \\ &E_i + E_j = 2 \cdot U \end{aligned} \tag{4.13}$$

We show three examples of weights and energies which suit these conditions in tables (4.1, 4.2 and 4.3). However, we find that even with the extreme ionization energies of table (4.1) the extension of the radial distribution does not almost change, as it can be checked in figure (4.13).

Weight	E_i(a.u.)	E_j(a.u.)
5.35%	-0.053	-0.01
10.71%	-0.047	-0.07
16%	-0.04	-0.014
35.71%	-0.027	-0.027
16%	-0.014	-0.04
10.71%	-0.07	-0.047
5.35%	-0.01	-0.053

Table 4.1: Proposed weighted sum 1

Weight	E_i(a.u.)	E_j(a.u.)
10%	-0.047	-0.07
20%	-0.04	-0.014
40%	-0.027	-0.027
20%	-0.014	-0.04
10%	-0.07	-0.047

Table 4.2: Proposed weighted sum 2

Weight	E_i(a.u.)	E_j(a.u.)
25%	-0.042	-0.012
50%	-0.027	-0.027
25%	-0.012	-0.042

Table 4.3: Proposed weighted sum 3

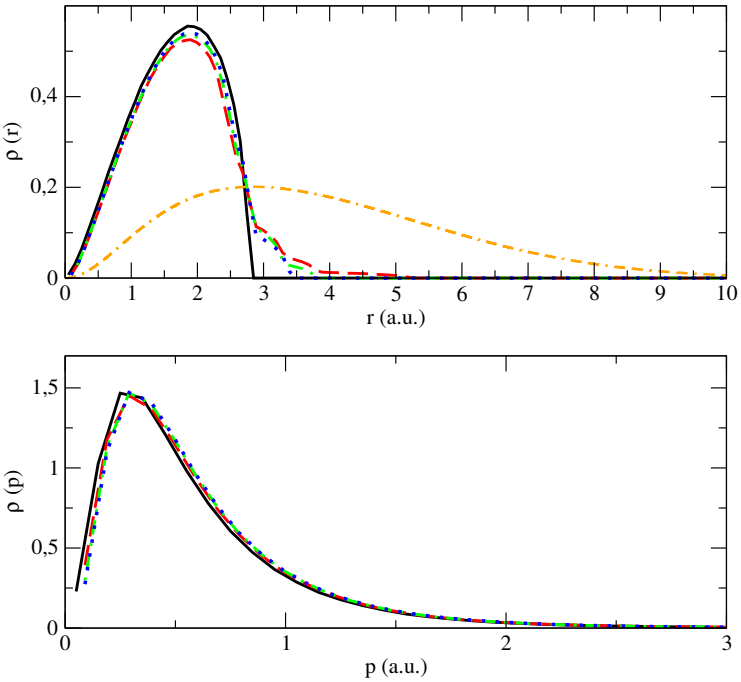

Figure 4.13: Radial (upper panel) and momentum (lower panel) distributions of the H^- with the microcanonical (—) and the proposed improved distributions: weighted sum 1(– – –), weighted sum 2(· – ·), weighted sum 3(· · ·). The quantum radial distribution is also shown (· – –·)

This means that the main advantadge of an improved hydrogenic-type distribution is not achieved for the H^-. Nevertheless, the behaviour of the obtained cross sections with the switching approach is understood in the frame of the CTMC method. We have shown that we can model an stable ion with two active electrons, with a correct value of mean energy, and which can interact with a projectile through the switching method providing reasonable values of capture and ionization cross sections. The main disadvantages, coming from the bad description of the radial distribution for the H^-, are not expected to be found with other two-electron system which is not an anion. By analizing the most two simple two-electron reactions, H($1s$) + H ($1s$) and H^+ + $H^-(1s, 2s)$, we have shown the usefulness of the switching approach. We extend this method to more complex systems in the next Chapter.

Chapter 5

Results for many electron systems

Multielectronic classical collisions with an Ar target

Collisions involving the argon atom have been extensively studied during the recent years, both theoretical [134, 15, 14, 16] and experimentally [19, 20]. This makes the argon atom a benchmark system to study multiple electronic processes. With respect to the chosen projectiles, we are specially interested in the Li^{2+} ion, due to recent measurements [20] and because we can deal with two active electrons, one in each collision center. As an introduction to test the most adequate IPM to be used, considering together or separately the $3s$ and $3p$ argon electrons, we study first the He^{2+} projectile. In addition, we have studied collisions with the C and C^+ projectiles in a joint experimental and theoretical work which treats cluster-Ar collisions with the Independent Atom Electron (IAE) model [31]. We give details on the calculations carried out for this joint work at the end of the chapter.

We study classically collisions with the Ar target

$$A^{q+} + \mathrm{Ar} \tag{5.1}$$

for different A^{q+} projectiles. In the considered energy range (50-500 keV/amu) we can assume that K and L shells in the argon keep frozen and therefore we deal with the M shell electrons. Therefore, we describe the Ar taking into account only electrons in the $3s$ and $3p$ states for the He^{2+} and Li^{2+} projectiles. To do so, we assume that the 6 electrons in the $3p$ are equivalent, as well as the 2 electrons in the $3s$. Multiple probabilities for multielectronic

processes, such as double capture, triple ionization, etc will be computed under the independent particle model (IPM, see section 2.5).

We are going to apply one-active CTMC model to simulate collisions of He^{2+} impinging on Ar, being the active electron of the Ar target a $3s$ or a $3p$:

$$\begin{array}{c} He^{2+} + Ar(3p) \\ He^{2+} + Ar(3s) \end{array} \tag{5.2}$$

We will apply two-active CTMC for the collision of Li^{2+} + Ar, being the second active electron the one in the Li^{2+}:

$$\begin{array}{c} Li^{2}(1s) + Ar(3p) \\ Li^{2}(1s) + Ar(3s) \end{array} \tag{5.3}$$

For these collisions, we will run calculations with the 4-body CTMC as well as with the switching approach (see section 2.3) in order to check the validity of the switching approach, known that the Li^{2+} + Ar is a much more complex system than the H + H, previously presented.

It must be noted that the $3p$ and $3s$ collisions are independent and different calculations must be done for each of them. The way of combining the final probabilities of these two indepedent collisions will be explained in the following. But before going on, we give some details on the description of the active electron $3p$ or $3s$ in the argon target.

Initial state of the active electron in the Ar^+ ion

In order to implement CTMC calculations with an argon target with an active electron, we need an initial distribution which describes the radial and momentum variables of the electron. In order to generate a microcanonical distribution with the Reinhold and Falcon [43] method explained in section 2.2.2.1, we need a model potential which describes the interaction of the active electron in the argon with the remaining frozen 17 electrons and nucleus, as well as the value of the ionization energy of the active electron. The model potential which has been used is a Muller potential from [135, 136]:

$$V = -\frac{Z-N}{r} - \frac{Ae^{-Br} + (N-A)e^{-Cr}}{r} \tag{5.4}$$

where $Z = 18$ is the nuclear charge of the Ar, $N = 17$ the number of frozen electrons, and the parameters $A = 5.4$, $B = 1$ and $C = 3.682$ are fitted values to reproduce the eigenenergies of an electron bound in different states (including the $3s$ and $3p$) [135]. This potential fulfills the conditions in the limits,

$\lim_{r\to 0} V = -18$ and $\lim_{r\to\infty} V = -1$. We use the experimental ionization energies for the $3p$ and $3s$ electrons in the neutral Ar, which are -0.58 and -1.06 a.u., respectively. The radial densities obtained with the microcanonical distribution, compared to the quantum ones, are shown in figure (5.1).

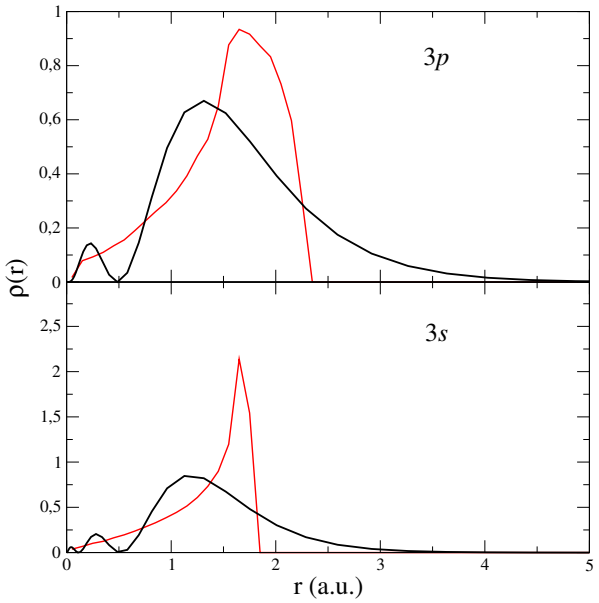

Figure 5.1: Radial distributions for the $3p$ (upper panel) and $3s$ (lower panel) using the potential from equation (5.4) and ionization energies of -0.58 and -1.06 a.u., respectively, with a microcanonical distribution (in red), compared to the quantum one (in black).

In general we find a reasonable representation of the $3s$ and $3p$ electronic clouds. The area not covered by the microcanonical distribution, from the cutoff, implies a 18% and a 24% of the quantum radial density, for $3p$ and $3s$, respectively. The area covered by the microcanonical distribution but which is over the quantum one due to the maximum of the microcanonical density, is a 25% and a 33% of the total. The maximum of the microcanonical radial density is shifted for the two states compared to the quantum ones, in about 0.5 a.u.. In all these facts the distribution for the $3p$ turns to be more accurate than the one of the $3s$, and we can expect, therefore, better results. However, the main contribution for any of the studied processes comes from the $3p$, not only because it has a less bound ionization energy, but also for the contribution

of 6 electrons instead of 2.

In the following, we analyze the results obtained for the different collisions involving an argon target, which are computed under the IPM approach for multiple processes.

He^{2+} + Ar

We study the collision of an He^{2+} ion impinging on Ar, implementing two different CTMC calculations for each initial state of the active argon electron, the $3s$ and $3p$ one:

$$\begin{array}{l} He^{2+} + Ar(3p) \rightarrow \\ He^{2+} + Ar(3s) \rightarrow \end{array} \begin{cases} He^{2+} + Ar & \text{elastic/excitation } P_e \\ He^{2+} + Ar^{+} + e & \text{ionization } P_i \\ He^{+} + Ar^{+} & \text{capture } P_c \end{cases} \tag{5.5}$$

resulting in two sets of probabilities (P_e, P_i, P_c) for each considered state.

Multielectronic procceses for the He^{2+} + Ar collision

We are interested on the computation of multiple processes, which may happen due to the presence of 6 and 2 equivalent electrons in the $3p$ and $3s$ subshells. Before explaining how we compute multielectronic probabilities under the Independent Particle Model (IPM), we have to select first which multiple process we want to simulate. In the bibliography we find measurements from Dubois and from Rudd *et al.* [137, 138] to compare with, labeled as $\sigma_{0,j-2,q}$ with $(0, j)$ the initial and final charges of the target and $(2, q)$ the initial and final charges of the projectile. This collision has been extensively studied during the years with different theoretical approaches [134, 15, 14]. Since we deal with this system as an introduction to the Li^{2+} projectile, and we are mainly interested in testing the application of the IPM considering together and separately the $3p$ and $3s$ argon electrons, we omit comparison with the theoretical data from the bibliography. The multiple processes which have been measured by Dubois [137] are:

$$He^{2+} + Ar \rightarrow He^{q+} + Ar^{j+} + (j - 2 + q)e^{-} \tag{5.6}$$

for j values from 1-2 to 5-6 and q values from 0 to 2. Rudd *et al.* [138] measured (as well as Dubois) the total single and double capture to helium cross sections, $\sigma_{2,1}$ and $\sigma_{2,0}$ respectively.

In section 2.5 we defined the inclusive and exclusive probabilities. We set that, if we want to simulate an experiment in which the final charges of both projectile and target are known, we have to use an exclusive probability. This is the case for all the $\sigma_{0,j-2,q}$ cross sections. We defined the exclusive probability as *Multielectronic probability for a given procces K derived from its monoelectronic equivalent k and from the monoelectronic probability for the electron resting in its initial ion.*. The monoelectronic probability for the electron resting in its initial ion is P_e. In contrast, we set that the inclusive

probability should be used to compare with experiments which did not distinguish the final charge of some of the ions, which are the cases for the $\sigma_{2,2}$, $\sigma_{2,1}$ and $\sigma_{2,0}$ cross sections. We defined the inclusive probability as *probability for a given multielectronic procces K derived from its monoelectronic equivalent k and from all the monoelectronic probabilities which do not give rise to k*. The monoelectronic probability which includes any other process than k is $1 - \mathrm{P}_k$.

We will start applying an exclusive IPM for the all the $\sigma_{0,j-2,q}$ cross sections and next, we will apply an inclusive IPM for the $\sigma_{2,1}$ and $\sigma_{2,0}$ cross sections. The monoelectronic probabilities will be those obtained from the calculation of equation (5.5).

In principle, the IPM (inclusive or exclusive) should be applied taking into account all the 8 equivalent electrons, 6 from $3p$ and 2 from $3s$. However, since the ionization potentials for the $3s$ and $3p$ electrons in the Ar are quite diffent (-1.06 and -0.58 a.u., respectively), we can expect that the inelastic processes from the two $3l$ levels are independent of each other, an assumption that has already been applied in the treatment of molecular collisions [139]. At this step, we present two different independent particle models, the above mentioned, for all the multielectronic processes K, which we name as $\mathrm{P}_K^{\mathrm{Comb}}$ and $\mathrm{P}_K^{\mathrm{Sum}}$ and we define as follows:

1. $\mathrm{P}_K^{\mathrm{Comb}}$: Combined IPM probability for a given multielectronic process K, obtained taking into account 8 electrons, 6 from $3p$ and 2 from $3s$.

2. $\mathrm{P}_K^{\mathrm{Sum}}$: Sum of separated IPM probability for a given multielectronic process K, obtained adding the independent IPM multielectronic probabilities from $3s$ and $3p$: $\mathrm{P}_K^{\mathrm{Sum}} = \mathrm{P}_K^{3s} + \mathrm{P}_K^{3P}$. It must be noted that P_K^{3s} and P_K^{3P} must fulfill

$$\begin{aligned} \mathrm{P}_K^{3s} &= \lim_{\mathrm{P_e}^{3p}\to 1} \mathrm{P}_K^{\mathrm{Comb}} \\ \mathrm{P}_K^{3p} &= \lim_{\mathrm{P_e}^{3s}\to 1} \mathrm{P}_K^{\mathrm{Comb}} \end{aligned} \tag{5.7}$$

Since in our CTMC calculations $1 = \mathrm{P_i} + \mathrm{P_c} + \mathrm{P_e}$, the limit of $\mathrm{P_e}^{3p}$ tending to 1 is equivalent to $\mathrm{P_c}^{3p}$ and $\mathrm{P_i}^{3p}$ tending to 0 (as well as for $3s$), being $\mathrm{P_i}$, $\mathrm{P_c}$ and $\mathrm{P_e}$ the monoelectronic probabilities from reaction (5.5).

In the following we apply the IPM, both the combined and the sum models, for all the processes measured by Dubois [137] and Rudd *et al.* [138]. We will show that the Sum model fits better with the experimental data.

$\sigma_{0,j-2,2}$ **- Multiple-ionization of Ar without capture by the** $\mathbf{He^{2+}}$

We study the reaction:

$$\mathrm{He}^{2+} + \mathrm{Ar} \rightarrow \mathrm{He}^{2+} + \mathrm{Ar}^{j+} + j\mathrm{e}^{-} \tag{5.8}$$

1. **Combined probabilities IPM:** $\sigma^{\mathrm{Comb}}_{0,j-2,2}$ The events which are happening are:

   (a) From 8 initial electrons, j are being ionized. From $3s$, k electrons may be ionized, being $k = 0, 1$ or 2 (if $j \geq 2$). $2-k$ electrons will remain in the argon target:

   $$\sum_{\substack{k=0 \\ j-k\geq 0 \\ j-k\leq 6}}^{2} \binom{2}{k} (\mathrm{P}^{3s}_{\mathrm{e}})^{2-k} (\mathrm{P}^{3s}_{\mathrm{i}})^{k}$$

   (b) The rest of ionized $j-k$ electrons come from the $3p$, with $j-k \leq 6$. $6-j+k$ electrons will remain in the argon target:

   $$\binom{6}{j-k} (\mathrm{P}^{3p}_{\mathrm{e}})^{6-j+k} (\mathrm{P}^{3p}_{\mathrm{i}})^{j-k}$$

   The multielectronic probabilities for $\mathrm{P}^{\mathrm{Comb}}_{0,j-2,2}$ are, therefore,

   $$\mathrm{P}^{\mathrm{Comb}}_{0,j-2,2} = \sum_{\substack{k=0 \\ j-k\geq 0 \\ j-k\leq 6}}^{2} \binom{2}{k} \binom{6}{j-k} (\mathrm{P}^{3s}_{\mathrm{e}})^{2-k} (\mathrm{P}^{3s}_{\mathrm{i}})^{k} (\mathrm{P}^{3p}_{\mathrm{e}})^{6-j+k} (\mathrm{P}^{3p}_{\mathrm{i}})^{j-k} \tag{5.9}$$

2. **Sum of separated probabilities IPM:** $\sigma^{\mathrm{Sum}}_{0,j-2,2} = \sigma^{3s}_{0,j-2,2} + \sigma^{3p}_{0,j-2,2}$ The events which are happening for each $3l$ state are:

$3p$	argon target:
(a) From 6 initial electrons, j are being ionized: $\binom{6}{j}(\mathrm{P}^{3p}_{\mathrm{i}})^{j}$	$(\mathrm{P}^{3p}_{\mathrm{e}})^{6-j}$
(b) $6-j$ electrons remain in the	$3s$
	(a) From 2 initial electrons, j are

being ionized:

$$\binom{2}{j}(\mathrm{P}_{\mathrm{i}}^{3s})^{j}$$

(b) $2-j$ electrons remain in the argon target:

$$(\mathrm{P}_{\mathrm{e}}^{3s})^{2-j}$$

The multielectronic probabilities for $\mathrm{P}_{0,j-2,2}$ are, for the $3p$ and $3s$ respectively,

$$\mathrm{P}_{0j-22}^{3p} = \binom{6}{j}(\mathrm{P}_{\mathrm{i}}^{3p})^{j}(\mathrm{P}_{\mathrm{e}}^{3p})^{6-j} \tag{5.10}$$

$$\mathrm{P}_{0j-22}^{3s} = \binom{2}{j}(\mathrm{P}_{\mathrm{i}}^{3s})^{j}(\mathrm{P}_{\mathrm{e}}^{3s})^{2-j} \tag{5.11}$$

Once we compute the $\sigma_{0,j-2,2}^{3s}$ and $\sigma_{0,j-2,2}^{3p}$ with these probabilities, we can add them:

$$\sigma_{0,j-2,2}^{\mathrm{Sum}} = \sigma_{0,j-2,2}^{3s} + \sigma_{0,j-2,2}^{3p} \tag{5.12}$$

This sum only has sense if $j \leq 2$, for $j > 2$ we use the $3p$ cross section obviously.

Now, we can compare our IPM cross sections with the measurements of Dubois for $\sigma_{0,j-2,2}$. In figures (5.2-5.5) we show our results for $j = 1-4$. As it has been commented, in the cases of $j = 3, 4$ the only contribution to the $\sigma_{0,j-2,2}^{\mathrm{Sum}}$ is the $\sigma_{0,j-2,2}^{3p}$. $\sigma_{0,j-2,2}^{\mathrm{Comb}}$ are shown in red and $\sigma_{0,1-2,2}^{\mathrm{Sum}}$ in black.

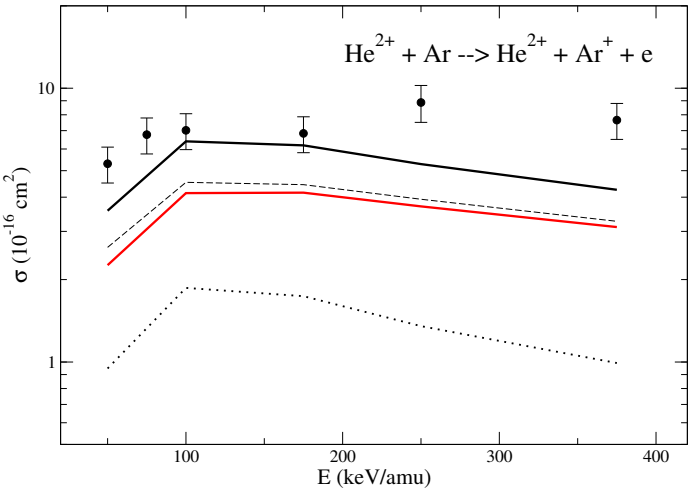

Figure 5.2: Cross sections for single target ionization. $\sigma^{\text{Comb}}_{0,1-2,2}$ (—), $\sigma^{3p}_{0,1-2,2}$ ($- - -$), $\sigma^{3s}_{0,1-2,2}$ ($\cdots$), $\sigma^{\text{Sum}}_{0,1-2,2}$ (—). Measurements from [137] (•).

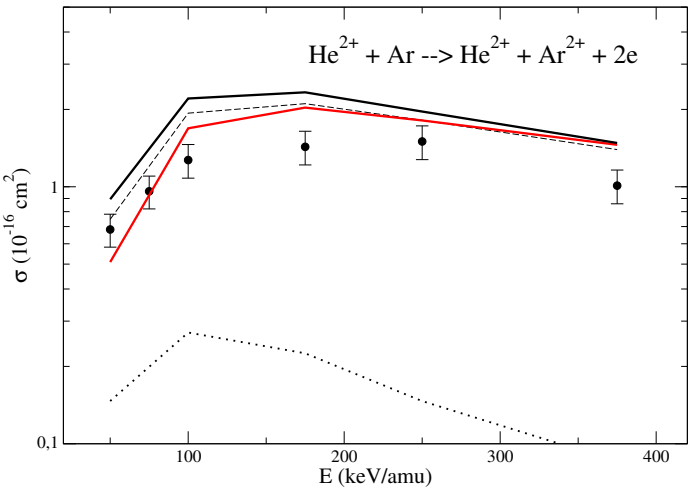

Figure 5.3: Cross sections for double target ionization. $\sigma^{\text{Comb}}_{0,2-2,2}$ (—), $\sigma^{3p}_{0,2-2,2}$ ($- - -$), $\sigma^{3s}_{0,2-2,2}$ ($\cdots$), $\sigma^{\text{Sum}}_{0,2-2,2}$ (—) Measurements from [137] (•).

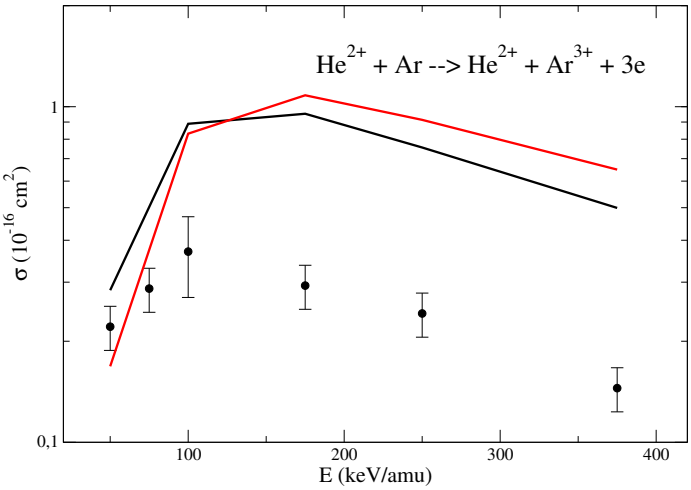

Figure 5.4: Cross sections for triple target ionization. $\sigma^{\mathrm{Comb}}_{0,3-2,2}$ (—), $\sigma^{3p}_{0,3-2,2} = \sigma^{\mathrm{Sum}}_{0,1-2,2}$ (—) Measurements from [137] (•).

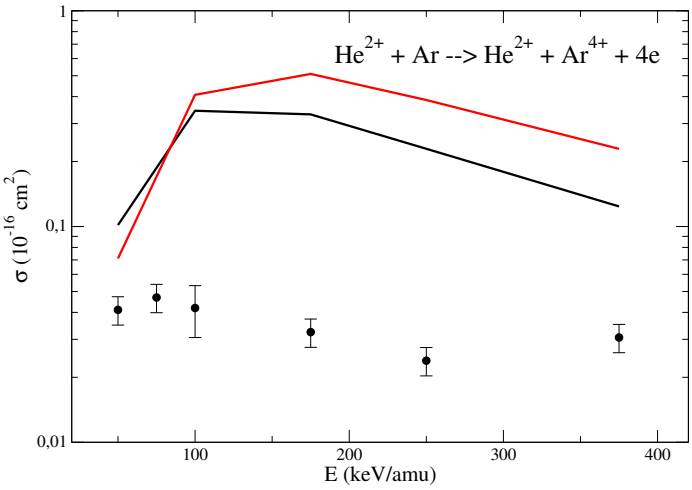

Figure 5.5: Cross sections for quadruple target ionization. $\sigma^{\mathrm{Comb}}_{0,4-2,2}$ (—), $\sigma^{3p}_{0,4-2,2} = \sigma^{\mathrm{Sum}}_{0,4-2,2}$ (—) Measurements from [137] (•).

In the case of single ionization, we find a good agreement with experiments only for the low impact energies considered. Measurements from [137] for

single ionization cross sections (figure 5.2) show a constant shape for $E \gtrsim 100$ keV/amu, while computed cross sections display a fall. Single ionization of argon should be well described by CTMC and IPM approaches, but we observe a dominant process at high energy that cannot be represented in our calculation. The cross sections computed as the sum of $\sigma^{3p}_{0,2-2,2}$ and $\sigma^{3s}_{0,2-2,2}$ show a better agreement with the experimental results. Double ionization (figure 5.3) is the best described process under the IPM and CTMC approaches, while cross sections for ionization of more than two electrons are highly overestimated with respect to the measurements of Dubois.

$\sigma_{0,j-2,1}$ - Multiple ionization of Ar accompanied by single-electron capture by the He^{2+} projectile

We study the reaction:

$$He^{2+} + Ar \rightarrow He^{+} + Ar^{j+} + (j-1)e^{-} \tag{5.13}$$

As in the preovious case, we show the two proposed IPM model to obatin multiple probabilities

1. **Combined probabilities IPM:** $\sigma^{\text{Comb}}_{0,j-2,1}$ The events which are happening are:

   (a) From 8 initial electrons, 1 is being captured. The captured electron may come from the $3s$ ($k=1$) or from the $3p$ ($k=0$).

   $$\sum_{k=0}^{1} \binom{2}{k} \binom{6}{1-k} (\mathrm{P}_{\mathrm{c}}^{3s})^{k} (\mathrm{P}_{\mathrm{c}}^{3p})^{1-k}$$

   .

   (b) From the remaining 7 electrons, $j-1$ are being ionized. From $3s$, k' electrons may be ionized from the remaining $2-k$ electrons. From the $3p$, $j-k'-1$ electrons will be ionized from the remaining $6-1+k$, if it is fulfilled $j-k'-k \leq 6$:

   $$\sum_{\substack{k'=0 \\ j-k'-1\geq 0 \\ j-k'-k\leq 6}}^{2-k} \binom{2-k}{k'} \binom{6-1+k}{j-k'-1} (\mathrm{P}_{\mathrm{i}}^{3s})^{k'} (\mathrm{P}_{\mathrm{i}}^{3p})^{j-k'-1}$$

   (c) $2-k-k'$ electrons will remain in the $3s$ level without being captured or ionized, as well as $6-j+k+k'$ electrons in the $3p$:

   $$(\mathrm{P}_{\mathrm{e}}^{3s})^{2-k-k'} (\mathrm{P}_{\mathrm{e}}^{3p})^{6-j+k+k'}$$

The multielectronic probabilities for $\mathrm{P}^{\mathrm{Comb}}_{0,j-2,1}$ are, therefore,

$$\mathrm{P}^{\mathrm{Comb}}_{0,j-2,1} = \sum_{k=0}^{1} \binom{2}{k} \binom{6}{1-k} (\mathrm{P}^{3s}_{\mathrm{c}})^k (\mathrm{P}^{3p}_{\mathrm{c}})^{1-k} \sum_{\substack{k'=0 \\ j-k'-1\geq 0 \\ j-k'-k\leq 6}}^{2-k} \binom{2-k}{k'} \binom{6-1+k}{j-k'-1} \cdot$$

$$(\mathrm{P}^{3s}_{\mathrm{i}})^{k'} (\mathrm{P}^{3p}_{\mathrm{i}})^{j-k'-1} (\mathrm{P}^{3s}_{\mathrm{e}})^{2-k-k'} (\mathrm{P}^{3p}_{\mathrm{e}})^{6-j+k+k'} \tag{5.14}$$

2. **Sum of separated probabilities IPM:** $\sigma^{\mathrm{Sum}}_{0,j-2,1} = \sigma^{3s}_{0,j-2,1} + \sigma^{3p}_{0,j-2,1}$
The events which are happening for each $3l$ state are:

$3p$

(a) From 6 initial electrons, one is being capture from the argon to the helium:

$$\binom{6}{1} \mathrm{P}^{3p}_{\mathrm{c}}$$

(b) From the remaining 5 electrons, $j-1$ are being ionized from the argon to the continuum:

$$\binom{5}{j-1} (\mathrm{P}^{3p}_{\mathrm{i}})^{j-1}$$

(c) $6-j$ electrons remain in the argon target:

$$(\mathrm{P}^{3p}_{\mathrm{e}})^{6-j}$$

$3s$

(a) From 2 initial electrons, one is being capture from the argon to the helium:

$$\binom{2}{1} \mathrm{P}^{3s}_{\mathrm{c}}$$

(b) The remaining electron rests in the argon if $j = 1$ or is ionized from the argon to the continuum if $j = 2$:

$$\binom{1}{j-1} (\mathrm{P}^{3s}_{\mathrm{e}})^{2-j} (\mathrm{P}^{3s}_{\mathrm{i}})^{j-1}$$

The multielectronic probabilities for $\mathrm{P}_{0,j-2,1}$ are, for the $3p$ and $3s$ respectively,

$$\mathrm{P}^{3p}_{0j-21} = \binom{6}{1} \mathrm{P}^{3p}_{\mathrm{c}} \binom{5}{j-1} (\mathrm{P}^{3p}_{\mathrm{i}})^{j-1} (\mathrm{P}^{3p}_{\mathrm{e}})^{6-j} \tag{5.15}$$

$$\mathrm{P}^{3s}_{0j-21} = \binom{2}{1} \mathrm{P}^{3s}_{\mathrm{c}} \binom{1}{j-1} (\mathrm{P}^{3s}_{\mathrm{i}})^{j-1} (\mathrm{P}^{3s}_{\mathrm{e}})^{2-j} \tag{5.16}$$

Once we compute these two contributions, we simply obtain the Sum cross section by adding $\sigma^{3s}_{0,j-2,1}$ and $\sigma^{3p}_{0,j-2,1}$:

$$\sigma^{\mathrm{Sum}}_{0,j-2,1} = \sigma^{3s}_{0,j-2,1} + \sigma^{3p}_{0,j-2,1} \tag{5.17}$$

This sum is valid only for $j \leq 2$, while for $j > 2$ no contribution from the $3s$ is found.

Now, we compare our multielectronic cross sections with the measurements from Dubois for $\sigma_{0,j-2,1}$. In figures (5.6-5.9) we show results for $j = 1 - 4$. As it has been remarked, for $j = 3, 4$ $\sigma^{3p}_{0,j-2,1}$ is the only contribution to the $\sigma^{\text{Sum}}_{0,j-2,1}$. $\sigma^{\text{Comb}}_{0,j-2,1}$ are shown in red and $\sigma^{\text{Sum}}_{0,1-2,1}$ in black.

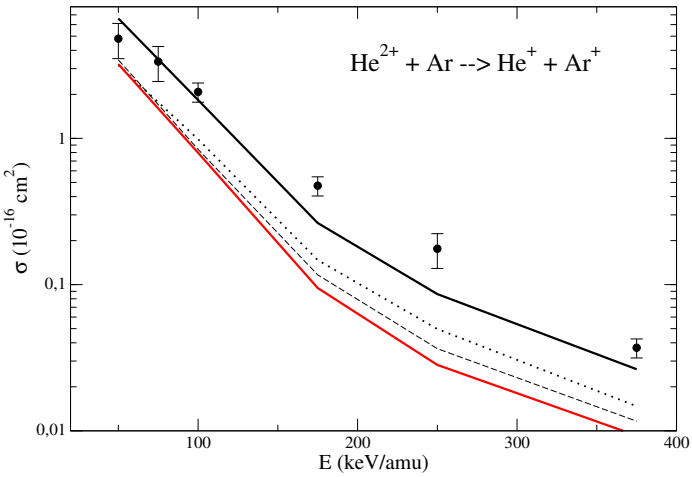

Figure 5.6: Cross sections for projectile electron capture. $\sigma^{\text{Comb}}_{0,1-2,1}$ (—), $\sigma^{3p}_{0,1-2,1}$ ($- - -$), $\sigma^{3s}_{0,1-2,1}$ ($\cdots$), $\sigma^{\text{Sum}}_{0,1-2,1}$ (—). Measurements from [137] (•).

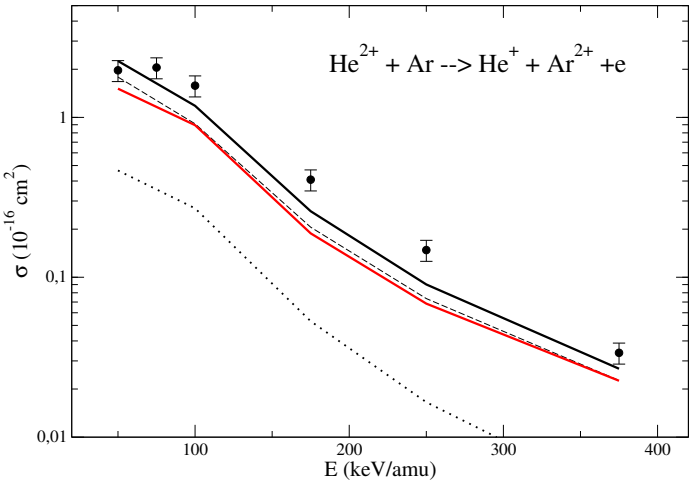

Figure 5.7: Cross sections for projectile electron capture and single target ionization. $\sigma^{\text{Comb}}_{0,2-2,1}$ (—), $\sigma^{3p}_{0,2-2,1}$ ($- - -$), $\sigma^{3s}_{0,2-2,1}$ ($\cdots$), $\sigma^{\text{Sum}}_{0,2-2,1}$ (—) Measurements from [137] (•).

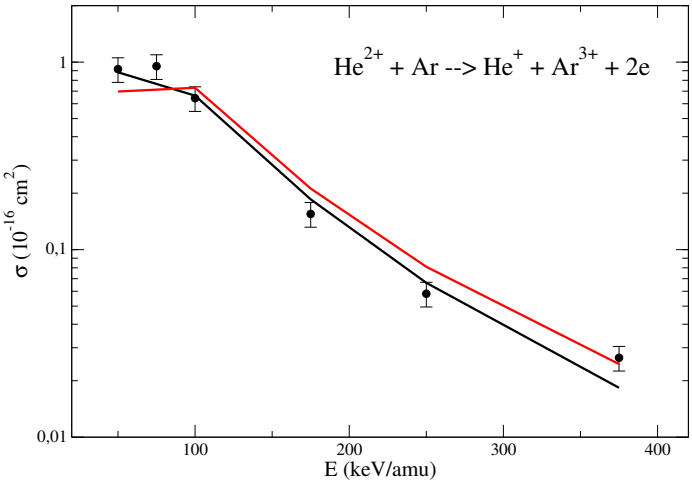

Figure 5.8: Cross sections for projectile electron capture and double target ionization. $\sigma^{\text{Comb}}_{0,3-2,1}$ (—), $\sigma^{3p}_{0,3-2,1} = \sigma^{\text{Sum}}_{0,1-2,1}$ (—) Measurements from [137] (•).

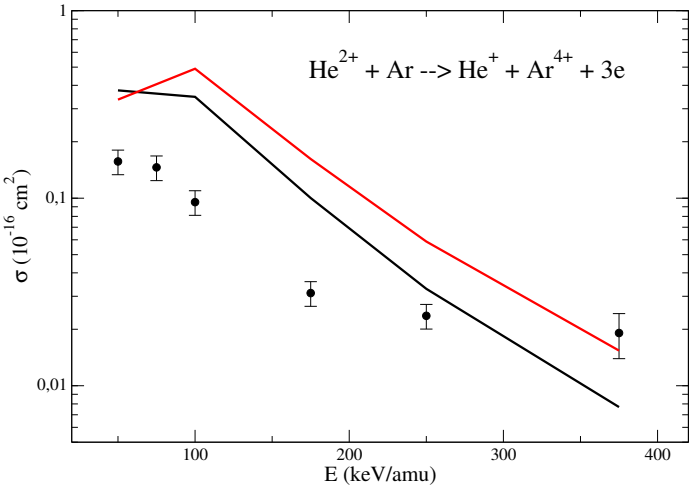

Figure 5.9: Cross sections for projectile electron capture and triple target ionization. $\sigma^{\text{Comb}}_{0,4-2,1}$ (—), $\sigma^{3p}_{0,4-2,1} = \sigma^{\text{Sum}}_{0,4-2,1}$ (—) Measurements from [137] (•).

We find a much better agreement with experiments for computed $\sigma_{0,j-2-1}$ than we found for $\sigma_{0,j-2-2}$. CTMC multiple cross sections show an excellent qualitatively behaviour for $j = 1, 2$ and 3, while $\sigma^{\text{Sum}}_{0,j-2,1}$ are quantitatively better than $\sigma^{\text{Comb}}_{0,j-2,1}$ when compared to experiments for all the considered j values. A high overestimation of computed cross sections starts to be significant for $j = 4$, while for pure multiple ionization this same effect started at $j = 3$, where the total number or ionized electrons is the same. Multiple ionization accompanied by electron capture is better described by the IPM than pure multiple ionization probably due to the contribution of (P^{3p}_i). Electron loss of two electrons in the target is better described if one is captured to the projectile and, therefore, the same effect happens for a higher number of electrons ejected.

$\sigma_{0,j-2,0}$ - Multiple ionization of Ar accompanied by double-electron capture by the He^{2+} projectile

We study the reaction:

$$He^{2+} + Ar \rightarrow He + Ar^{j+} + (j-2)e^{-} \tag{5.18}$$

It must be noted that there is not a $j = 1$ reaction of this type.

1. **Combined probabilities IPM:** $\sigma^{\text{Comb}}_{0,j-2,0}$ The events which are happening are:

   (a) From 8 initial electrons, $k = 2$ are being captured. The captured electron may come from the $3s$ ($k = 1, 2$) or from the $3p$ ($k = 0, 1$).

   $$\sum_{k=0}^{2} \binom{2}{k} \binom{6}{2-k} (\mathrm{P}_{\mathrm{c}}^{3s})^{k} (\mathrm{P}_{\mathrm{c}}^{3p})^{2-k}$$

   .

   (b) From the remaining 6 electrons, $j - 2$ are being ionized. From $3s$, k' electrons may be ionized from the remaining $2 - k$ electrons. From the $3p$, $j - k' - 2$ electrons will be ionized from the remaining $6 - 2 + k$, if it is fulfilled $j - k' - k \leq 6$:

   $$\sum_{\substack{k'=0 \\ j-k'-2\geq 0 \\ j-k'-k\leq 6}}^{2-k} \binom{2-k}{k'} \binom{6-2+k}{j-k'-2} (\mathrm{P}_{\mathrm{i}}^{3s})^{k'} (\mathrm{P}_{\mathrm{i}}^{3p})^{j-k'-2}$$

   (c) $2-k-k'$ electrons will remain in the $3s$ level without being captured or ionized, as well as $6 - j + k + k'$ electrons in the $3p$:

   $$(\mathrm{P}_{\mathrm{e}}^{3s})^{2-k-k'} (\mathrm{P}_{\mathrm{e}}^{3p})^{6-j+k+k'}$$

   The multielectronic probabilities for $\mathrm{P}^{\text{Comb}}_{0,j-2,0}$ are, therefore,

   $$\mathrm{P}^{\text{Comb}}_{0,j-2,0} = \sum_{k=0}^{2} \binom{2}{k} \binom{6}{2-k} (\mathrm{P}_{\mathrm{c}}^{3s})^{k} (\mathrm{P}_{\mathrm{c}}^{3p})^{2-k} \sum_{\substack{k'=0 \\ j-k'-2\geq 0 \\ j-k'-k\leq 6}}^{2-k} \binom{2-k}{k'} \binom{6-2+k}{j-k'-2} \cdot$$

   $$(\mathrm{P}_{\mathrm{i}}^{3s})^{k'} (\mathrm{P}_{\mathrm{i}}^{3p})^{j-k'-2} (\mathrm{P}_{\mathrm{e}}^{3s})^{2-k-k'} (\mathrm{P}_{\mathrm{e}}^{3p})^{6-j+k+k'} \tag{5.19}$$

2. **Sum of separated probabilities IPM:** $\sigma^{\text{Sum}}_{0,j-2,0} = \sigma^{3s}_{0,j-2,0} + \sigma^{3p}_{0,j-2,0}$

The events which are happening for each $3l$ state are:

$3p$

(a) From 6 initial electrons, two are being captured from the argon to the helium:

$$\binom{6}{2}(\mathrm{P}_{\mathrm{c}}^{3p})^2$$

(b) From the remaining 4 electrons, $j-2$ are being ionized from the argon to the continuum, while $6-j$ electrons remain in the argon target:

$$\binom{4}{j-2}(\mathrm{P}_{\mathrm{i}}^{3p})^{j-2}(\mathrm{P}_{\mathrm{e}}^{3p})^{6-j}$$

$3s$

(a) From 2 initial electrons, both are being capture from the argon to the helium. $(\mathrm{P}_{\mathrm{c}}^{3s})^2$. This is the unique possibility.

The multielectronic probabilities for $\mathrm{P}_{0,j-2,0}$ are, for the $3p$ and $3s$ respectively,

$$\mathrm{P}_{0j-20}^{3p} = \binom{6}{2}(\mathrm{P}_{\mathrm{c}}^{3p})^2\binom{4}{j-2}(\mathrm{P}_{\mathrm{i}}^{3p})^{j-2}(\mathrm{P}_{\mathrm{e}}^{3p})^{6-j} \tag{5.20}$$

$$\mathrm{P}_{02-20}^{3s} = \binom{2}{2}(\mathrm{P}_{\mathrm{c}}^{3s})^2 \tag{5.21}$$

Once we compute the $\sigma_{0,j-2,0}^{3s}$ and $\sigma_{0,j-2,0}^{3p}$ with these probabilities, we can add them:

$$\sigma_{0,j-2,0}^{\mathrm{Sum}} = \sigma_{0,j-2,0}^{3s} + \sigma_{0,j-2,0}^{3p} \tag{5.22}$$

The sum will be valid only for $j = 2$. For $j > 2$ we only use the $3p$ contribution.

In figures (5.10-5.12) we show our results for $j = 2-4$ compared to the measurements of Dubois. $\sigma_{0,j-2,0}^{\mathrm{Comb}}$ are shown in red and $\sigma_{0,1-2,0}^{\mathrm{Sum}}$ in black.

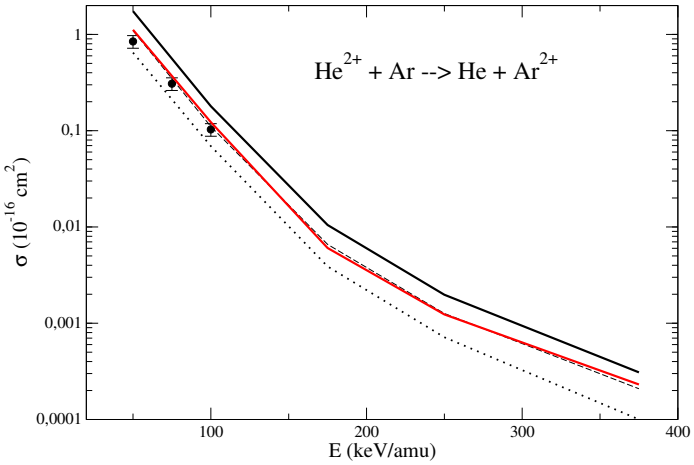

Figure 5.10: Cross sections for double projectile electron capture. $\sigma^{\text{Comb}}_{0,2-2,0}$ (—), $\sigma^{3p}_{0,2-2,0}$ ($- - -$), $\sigma^{3s}_{0,2-2,0}$ ($\cdots$), $\sigma^{\text{Sum}}_{0,2-2,0}$ (—) Measurements from [137] (•).

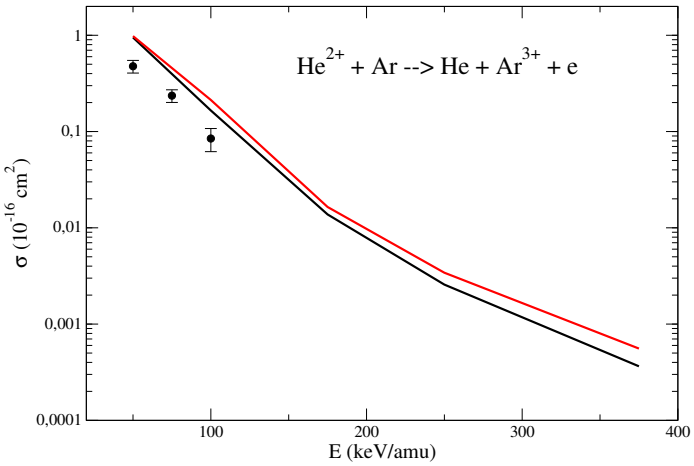

Figure 5.11: Cross sections for double projectile electron capture and single target ionization. $\sigma^{\text{Comb}}_{0,3-2,0}$ (—), $\sigma^{3p}_{0,3-2,0} = \sigma^{\text{Sum}}_{0,1-2,0}$ (—) Measurements from [137] (•).

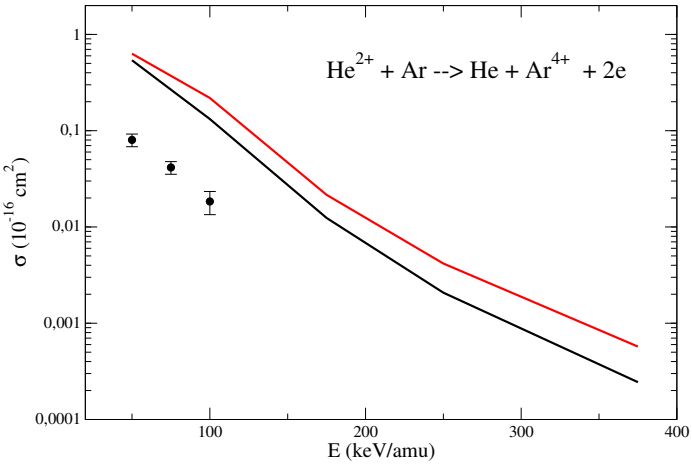

Figure 5.12: Cross sections for double projectile electron capture and double target ionization. $\sigma^{\mathrm{Comb}}_{0,4-2,0}$ (—), $\sigma^{3p}_{0,4-2,0} = \sigma^{\mathrm{Sum}}_{0,4-2,0}$ (—) Measurements from [137] (•).

In this case we only have a contribution of $\mathrm{P_i}$ in the $j = 3$ and $j = 4$ cases, where the overestimation of computed cross sections starts to be important, being the $(\mathrm{P_c})^2$ contribution also responsible.

$\sigma_{2,1}$ and $\sigma_{2,0}$ - Total single and double capture to helium cross sections

Once we have analyzed the individual $\sigma_{0,j-2,q}$, we focus in the total $\sigma_{2,q}$, comparing with the measurements from Rudd *et al.* and Dubois [138, 137]. The reactions are

$$\mathrm{He}^{2+} + \mathrm{Ar} \rightarrow \mathrm{He}^{+} + ... \tag{5.23}$$

$$\mathrm{He}^{2+} + \mathrm{Ar} \rightarrow \mathrm{He} + ... \tag{5.24}$$

To calculate the probabilities $\mathrm{P}_{2,1}$ and $\mathrm{P}_{2,0}$ for total single and double capture to helium, we need to apply the IPM using the inclusive probabilities, since we do not know the final charge of the target. We compute both the combined and the sum IPM of the independent $3p$ and $3s$ contributions.

1. **Total single capture to helium cross sections $\sigma_{2,1}$**

   (a) **Combined probabilities IPM: $\sigma^{\mathrm{Comb}}_{2,1}$**

$$\mathrm{P}_{2,1}^{\mathrm{Comb}} = \sum_{k=0}^{1} \binom{2}{k}\binom{6}{1-k} (\mathrm{P}_{\mathrm{c}}^{3s})^{k} (\mathrm{P}_{\mathrm{c}}^{3p})^{1-k} (1-\mathrm{P}_{\mathrm{c}}^{3s})^{2-k} (1-\mathrm{P}_{\mathrm{c}}^{3p})^{6-1+k} \quad (5.25)$$

(a) **Sum of $3s$ and $3p$ separated contributions IPM: $\sigma_{2,1}^{\mathrm{Sum}} = \sigma_{2,1}^{3s} + \sigma_{2,1}^{3p}$**

$$\mathrm{P}_{2,1}^{3p} = 6\mathrm{P}_{\mathrm{c}}^{3p}(1-\mathrm{P}_{\mathrm{c}}^{3p})^{5} \quad (5.26)$$

$$\mathrm{P}_{2,1}^{3s} = 2\mathrm{P}_{\mathrm{c}}^{3s}(1-\mathrm{P}_{\mathrm{c}}^{3s})^{2} \quad (5.27)$$

1. **Total double electron capture to helium cross sections $\sigma_{2,0}$**

(a) **Combined probabilities IPM: $\sigma_{2,0}^{\mathrm{Comb}}$**

$$\mathrm{P}_{2,0}^{\mathrm{Comb}} = \sum_{k=0}^{2} \binom{2}{k}\binom{6}{2-k} (\mathrm{P}_{\mathrm{c}}^{3s})^{k} (\mathrm{P}_{\mathrm{c}}^{3p})^{2-k} (1-\mathrm{P}_{\mathrm{c}}^{3s})^{2-k} (1-\mathrm{P}_{\mathrm{c}}^{3p})^{6-2+k} \quad (5.28)$$

(a) **Sum of separated probabilities IPM: $\sigma_{2,0}^{\mathrm{Sum}} = \sigma_{2,0}^{3s} + \sigma_{2,0}^{3p}$**

$$\mathrm{P}_{2,0}^{3p} = 15(\mathrm{P}_{\mathrm{c}}^{3p})^{2}(1-\mathrm{P}_{\mathrm{c}}^{3p})^{4} \quad (5.29)$$

$$\mathrm{P}_{2,0}^{3s} = (\mathrm{P}_{\mathrm{c}}^{3s})^{2} \quad (5.30)$$

It is worth noting that we could obtain the $\mathrm{P}_{2,q}$ probabilities also as the sum of all possible $\mathrm{P}_{0,j-2,q}$. For the combined probabilities, the sum must be done over up to $j = 8$. For the independent $3p$ and $3s$ probabilities, the additions of the $\mathrm{P}_{0,j-2,q}^{3l}$ must be done up to 6 and 2, respectively. For example, for the $\mathrm{P}_{2,1}^{3p}$:

$$\begin{aligned}
\mathrm{P}_{2,1}^{3p} &= \sum_{j=1}^{6} \mathrm{P}_{0,j-2,1}^{3p} = 6\mathrm{P}_{\mathrm{c}}^{3p}(\mathrm{P}_{\mathrm{e}}^{3p})^{5} + 6\cdot 5\mathrm{P}_{\mathrm{c}}^{3p}\mathrm{P}_{\mathrm{i}}^{3p}(\mathrm{P}_{\mathrm{e}}^{3p})^{4} + 6\cdot 10\mathrm{P}_{\mathrm{c}}^{3p}(\mathrm{P}_{\mathrm{i}}^{3p})^{2}(\mathrm{P}_{\mathrm{e}}^{3p})^{3} \\
&+ 6\cdot 10\mathrm{P}_{\mathrm{c}}^{3p}(\mathrm{P}_{\mathrm{i}}^{3p})^{3}(\mathrm{P}_{\mathrm{e}}^{3p})^{2} + 6\cdot 5\mathrm{P}_{\mathrm{c}}^{3p}(\mathrm{P}_{\mathrm{i}}^{3p})^{4}\mathrm{P}_{\mathrm{e}}^{3p} + 6\mathrm{P}_{\mathrm{c}}^{3p}(\mathrm{P}_{\mathrm{i}}^{3p})^{5} \\
&= 6\mathrm{P}_{\mathrm{c}}^{3p}[(\mathrm{P}_{\mathrm{e}}^{3p})^{5} + 5\mathrm{P}_{\mathrm{i}}^{3p}(\mathrm{P}_{\mathrm{e}}^{3p})^{4} + 10(\mathrm{P}_{\mathrm{i}}^{3p})^{2}(\mathrm{P}_{\mathrm{e}}^{3p})^{3} + 10(\mathrm{P}_{\mathrm{i}}^{3p})^{3}(\mathrm{P}_{\mathrm{e}}^{3p})^{2} \\
&+ 5(\mathrm{P}_{\mathrm{i}}^{3p})^{4}\mathrm{P}_{\mathrm{e}}^{3p} + (\mathrm{P}_{\mathrm{i}}^{3p})^{5}] = 6\mathrm{P}_{\mathrm{c}}^{3p}(\mathrm{P}_{\mathrm{i}}^{3p} + \mathrm{P}_{\mathrm{e}}^{3p})^{5} \\
&= 6\mathrm{P}_{\mathrm{c}}^{3p}(1-\mathrm{P}_{\mathrm{c}}^{3p})^{5}
\end{aligned} \quad (5.31)$$

The last step is obtained using the condition $1 = \mathrm{P_i} + \mathrm{P_c} + \mathrm{P_e}$. The sum of all exclusive probabilities gives rise to the inclusive one. In figure (5.13) we compare the total single and double capture cross sections with both the measurements from Rudd *et al.* and Dubois.

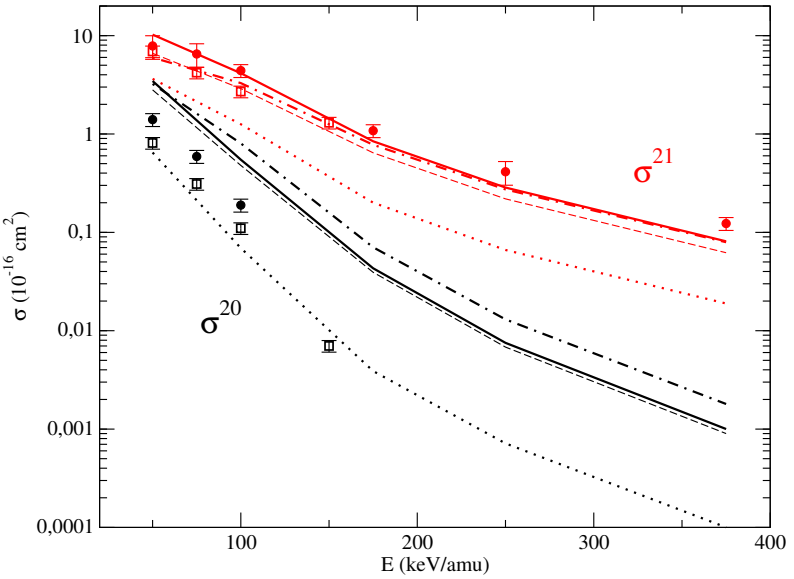

Figure 5.13: Total single $\sigma_{2,1}$ (in red) and double $\sigma_{2,0}$ (in black) capture to helium cross sections. σ^{Comb} results $(\cdot - \cdot)$, σ_{3p} results $(- - -)$, σ_{3s} results $(\cdots)$, $\sigma_{3p} + \sigma_{3s}$ results (—) Measurements from [137] (•), measurements from [138] (□)

In the case of $\sigma_{2,1}$ we find an excellent agreement with experiments, since individual $\sigma_{0,j-2,1}$ were already accurate for all the cases considered except for $j = 4$, whose contribution is negligible. However, in the case of $\sigma_{2,0}$ the computed individual $\sigma_{0,2-2,0}$, $\sigma_{0,3-2,0}$ and $\sigma_{0,4-2,0}$ have similar contributions, which is not the case of the experimental values, which show differences of an order of magnitude between $\sigma_{0,2-2,0}$ and $\sigma_{0,4-2,0}$. We find again a better behaviour by adding the individual $3s$ and $3p$ cross sections than combining probabilities from the two $3l$ calculations.

In conclusion, we find a correct description of single σ_{01}^{2q} and double σ_{02}^{2q} electron loss of the target, accompanied by none, single and double capture by the projectile. For electron loss in the target higher than 2, the probabilities computed under the IPM overestimate the measurements of Dubois *et al.* in a proportional degree with the number of lost electrons. We have checked that we can assume that $3s$ and $3p$ electrons do not interact to give multiple electron loss in this energy range, and that it is sufficient to treat them separately and finally add their individual cross sections.

Once we have studied the general behaviour of the multielectronic cross sections of the He^{2+} + Ar collision, obtained under the IPM with monoelectronic CTMC results, we continue with the Li^{2+} + Ar collision. We can expect similar results to those of the He^{2+} + Ar due to the same initial charge of the projectile. Now, we are interested in improving the description under the IPM approach by taking into account two electrons instead of one, one in the target and one in the projectile. This has been done including an active electron in the initial Li^{2+}, apart from the one in the argon, with a 4-body and a 2x3-body CTMC treatments.

Li^{2+} + Ar

In this section we study the collision Li^{2+} + Ar in the intermediate energy range $100 < E < 500$ keV/amu with CTMC considering one active electron in the target and another one in the projectile. Therefore, we can run calculations with both the 4-body and the switching approach. We consider, as in the previous He^{2+} + Ar study, both the $3s$ and $3p$ initial states, while the electron in the Li^{2+} is in a $1s$ state. We choose this collision for different reasons: recent measurements from Losqui *et al.* of different multiple processes [20], same projectile charge as in He^{2+} + Ar and the presence of an electron in the projectile, which allows us to test the switching approach combined with the IPM. For this collision we can find the following bielectronic processes:

$$\left.\begin{array}{l} Li^{2+}(1s) + Ar(3p) \rightarrow \\ Li^{2+}(1s) + Ar(3s) \rightarrow \end{array}\right\{ \begin{array}{ll} Li^{2+} + Ar & \text{Elastic/Excitation } P_e \\ Li^{2+} + Ar^+ + e & \text{Target ionization } P_{ti} \\ Li^{3+} + Ar + e & \text{Projectile ionization } P_{pi} \\ Li^{3+} + Ar^+ + 2e & \text{Double ionization } P_{di} \\ Li^{3+} + Ar^- & \text{Target electron capture } P_{tc} \\ Li^+ + Ar^+ & \text{Projectile electron capture } P_{pc} \end{array} \tag{5.32}$$

In reactions (5.32), we also show the labels associated to each bielectronic probability P_i.

The switching approach in the Li^{2+} + Ar collision

We consider two active electrons, one in the target and one in the projectile. We can study this collision with a 4-body CTMC approach, but we will not obtain converged probabilities for the formation of Li^+ and Ar^- (target or projectile electron capture) due to the classical autodetachment (see figure 4.1). We are mainly interested in obtaining a good representation of projectile electron capture, since it has been measured accompanied by multiple ionization of argon in [20]. When applying the Switching approach, if target or projectile electron capture occurs, we switch to two 3-body collisional systems. If this happens in the target, we need to include a model potential which describes the interaction of an electron with an argon, forming therefore an Ar^- anion. If capture occurs in the projectile, the model potential should simulate the interaction of the active electron with a Li^{2+} ion, forming a Li^+ ion. In the two 3-body systems, both electrons will be under the effect of these model potentials, which have been obtained using the Talman method and program

[53, 54] (see Appendix D). To form the Ar^-, the electron will feel the effect of a neutral argon, described by the following form:

$$V^{\mathrm{Ar}}(r) = -\frac{A\mathrm{e}^{-Br} + (18 - A)\mathrm{e}^{-Cr}}{r} \tag{5.33}$$

with $A = 9.54$, $B = 5.05$ and $C = 0.89$. In the case of the Li^+, the potential describing a Li^{2+} ion which has been used is:

$$V^{\mathrm{Li}^{2+}}(r) = -\frac{2}{r} - \frac{1}{r}\exp(-2\alpha r)(1 + \alpha r) \tag{5.34}$$

with α=2.5. It can be checked that the boundary conditions are fulfilled:

$$\begin{array}{ll} \lim\limits_{r\to\infty} V^{\mathrm{Ar}}(r) = 0 & \lim\limits_{r\to 0} V^{\mathrm{Ar}}(r) = -\frac{18}{r} \\ \lim\limits_{r\to\infty} V^{\mathrm{Li}^{2+}}(r) = -\frac{2}{r} & \lim\limits_{r\to 0} V^{\mathrm{Li}^{2+}}(r) = -\frac{3}{r} \end{array} \tag{5.35}$$

Multielectronic procceses for the Li^{2+} + Ar collision

The different processes which have been measured by in [20] are multiple ionization of the target with different final charges of the projectile. Therefore, our main interest is to properly describe argon ionization. The monoelectronic probabilities which give rise to a final Ar^+ target are P_{ti}, P_{di} and P_{pc} (see equation 5.32), but only the first one keeps the projectile in its initial charge. Therefore, we can define the *pure* (P) and *full* (F) ionization probabilities for the target ionization as follows:

$$\begin{aligned} \mathrm{P}^{\mathrm{P}}_{\mathrm{TI}} &= \mathrm{P}_{\mathrm{ti}} \\ \mathrm{P}^{\mathrm{F}}_{\mathrm{TI}} &= \mathrm{P}_{\mathrm{ti}} + \mathrm{P}_{\mathrm{di}} + \mathrm{P}_{\mathrm{pc}} \end{aligned} \tag{5.36}$$

In the following, we apply the IPM for the different processes measured in [20]. In the computation of the different multiple probabilities under the IPM, we will use both P^P_{TI} and P^F_{TI} as the monoelectronic probability for argon ionization to elucidate which one is better. We will discuss in the analysis which one should be used depending on the final charge state of the projectile.

The cross sections for the processes measured in [20] are labeled as $\sigma_{0,j-2,q}$ with $(0, j)$ the initial and final state of the target and $(2, q)$ the initial and final state of the projectile. The multiple processes which have been measured are:

$$\mathrm{Li}^{2+} + \mathrm{Ar} \to \mathrm{Li}^{\mathrm{q}+} + \mathrm{Ar}^{j+} + (j - 2 + q)\mathrm{e}^- \tag{5.37}$$

for j values from 1 to 5 and q values from 1 to 3.

We are taking into account both $3s$ and $3p$ electrons, as stated in equation (5.32). From the experience with the He^{2+} + Ar collision, we assume that electrons from the $3s$ and $3p$ do not interact between them. Therefore, for a given process the IPM can be applied separately to the monoelectronic probabilities from the $3s$ and $3p$ calculations, and finally obtain the cross section for that given process, like in equations (5.12,5.17,5.22) for He^{2+} + Ar collision, as

$$\sigma_{0,j-2,q} = \sigma^{3p}_{0,j-2,q} + \sigma^{3s}_{0,j-2,q} \tag{5.38}$$

In the following, we analyze the possible combination of monoelectronic probabilities from equations (5.32, 5.36) to compute multiple probabilities under the IPM for each procces measured in [20].

Multiple-ionization of Ar accompanied by single-electron capture by the Li^{2+} - $\sigma_{0,j-2,1}$

We study the reaction:

$$Li^{2+} + Ar \rightarrow Li^{+} + Ar^{j+} + (j-1)e^{-} \tag{5.39}$$

The events which are happening for each $3l$ state are:

$3p$

1. From 6 initial electrons, one is being captured from the argon to the lithium:

$$\binom{6}{1} P^{3p}_{pc}$$

2. From the remaining 5 electrons, $j-1$ are being ionized and $6-j$ electrons rest in the argon:

$$(P^{3p}_{e})^{6-j} (P^{3p}_{TI})^{j-1}$$

$3s$

1. From 2 initial electrons, one is being captured from the argon to the lithium:

$$\binom{2}{1} P^{3s}_{pc}$$

2. The remaining electron rests in the argon if $j = 1$ or is ionized if $j = 2$:

$$\binom{1}{j-1} (P^{3s}_{TI})^{j-1} (P^{3s}_{e})^{2-j}$$

We define therefore two different IPM probabilities, named as model 1 (m1) if we use the P^{P}_{TI}, pure ionization probability, and model 2 (m2) if we use P^{F}_{TI}, full ionization probability, for the processes from equation (5.39):

$$P^{3p,m1}_{0j-21} = \binom{6}{1} P^{3p}_{pc} \binom{5}{j-1} (P^{3pP}_{TI})^{j-1} (P^{3p}_{e})^{6-j} \tag{5.40}$$

$$\mathrm{P}_{0j-21}^{3p,\mathrm{m2}} = \binom{6}{1}\mathrm{P}_{\mathrm{pc}}^{3p}\binom{5}{j-1}(\mathrm{P}_{\mathrm{TI}}^{3p\mathrm{F}})^{j-1}(\mathrm{P}_{\mathrm{e}}^{3p})^{6-j} \tag{5.41}$$

$$\mathrm{P}_{0j-21}^{3s,\mathrm{m1}} = \binom{2}{1}\mathrm{P}_{\mathrm{pc}}^{3s}\binom{1}{j-1}(\mathrm{P}_{\mathrm{TI}}^{3s\mathrm{P}})^{j-1}(\mathrm{P}_{\mathrm{e}}^{3s})^{2-j} \tag{5.42}$$

$$\mathrm{P}_{0j-21}^{3s,\mathrm{m2}} = \binom{2}{1}\mathrm{P}_{\mathrm{pc}}^{3s}\binom{1}{j-1}(\mathrm{P}_{\mathrm{TI}}^{3s\mathrm{F}})^{j-1}(\mathrm{P}_{\mathrm{e}}^{3s})^{2-j} \tag{5.43}$$

Once we have computed the individual $3p$ and $3s$ cross sections using equations (5.40-5.43), we sum them to obtain the cross section for multiple target ionization accompanied by single electron capture to the projectile:

$$\sigma_{0j-21}^{\mathrm{m1}} = \sigma_{0j-21}^{3p,\mathrm{m1}} + \sigma_{0j-21}^{3s,\mathrm{m1}} \tag{5.44}$$

$$\sigma_{0j-21}^{\mathrm{m2}} = \sigma_{0j-21}^{3p,\mathrm{m2}} + \sigma_{0j-21}^{3s,\mathrm{m2}} \tag{5.45}$$

We can now compare the calculated cross sections with the measured data of [20]. We will show CTMC results obtained with the 4-body (broken lines in the figures) and switching approach (full lines). The model 1 IPM cross sections will be shown in black, and the ones obtained with the model 2 will be in red. It is worth noting that, for $j = 1$, model 1 and model 2 cross sections are equal $\sigma_{01-21}^{\mathrm{m1}} = \sigma_{01-21}^{\mathrm{m2}}$, since P_{TI}) has a power of $j - 1$.

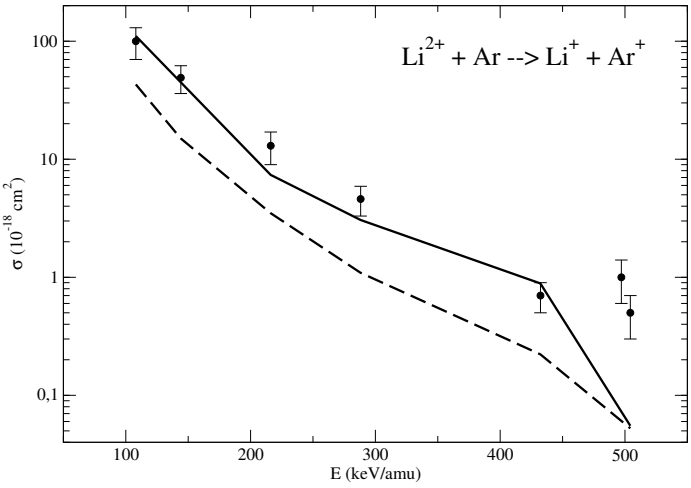

Figure 5.14: Cross sections for reaction (5.39) with $j = 1$. Present switching (full lines) and 4-body (broken lines) CTMC results, with model 1 IPM. Measurements from [20] (•).

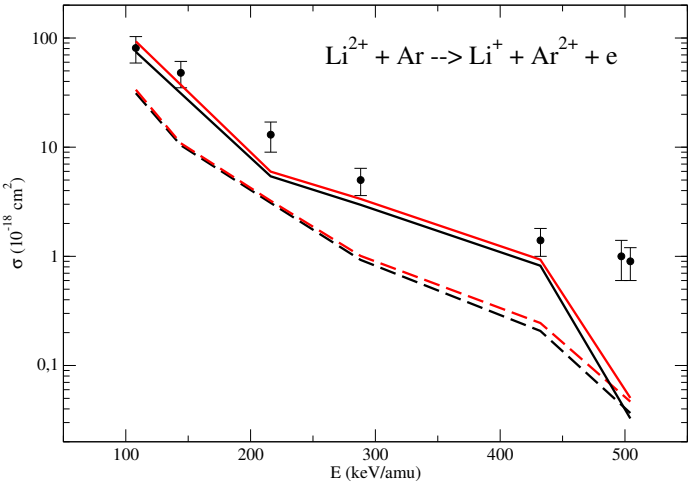

Figure 5.15: Cross sections for reaction (5.39) with $j = 2$. Present switching (full lines) and 4-body (broken lines) CTMC results, with model 1 (in black) and model 2 (in red) IPM. Measurements from [20] (•).

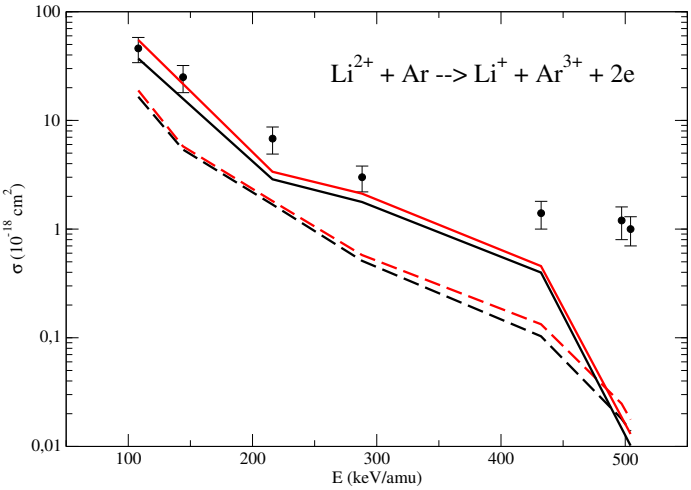

Figure 5.16: Cross sections for reaction (5.39) with $j = 3$. Present switching (full lines) and 4-body (broken lines) CTMC results, with model 1 (in black) and model 2 (in red) IPM. Measurements from [20] (•).

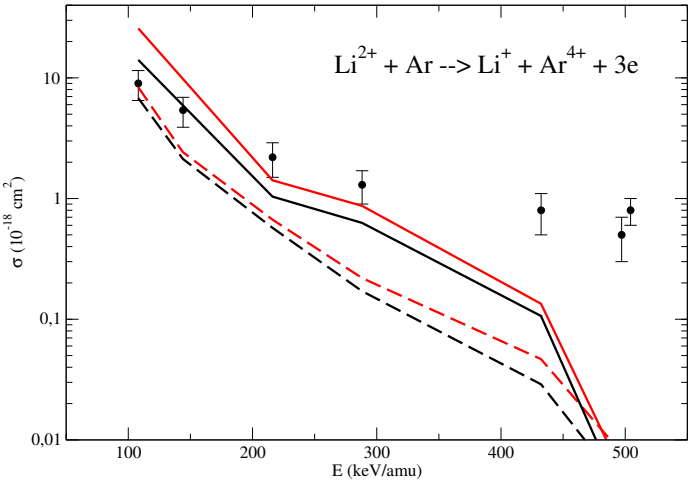

Figure 5.17: Cross sections for reaction (5.39) with $j = 4$. Present switching (full lines) and 4-body (broken lines) CTMC results, with model 1 (in black) and model 2 (in red) IPM. Measurements from [20] (•).

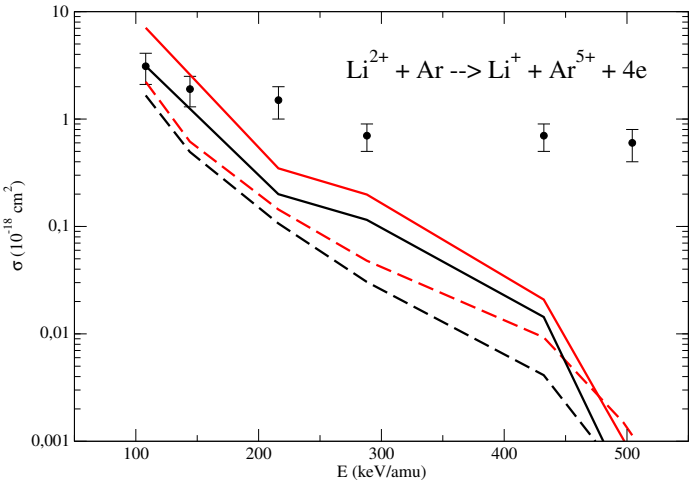

Figure 5.18: Cross sections for reaction (5.39) with $j = 5$. Present switching (full lines) and 4-body (broken lines) CTMC results, with model 1 (in black) and model 2 (in red) IPM. Measurements from [20] (•).

Except for the highest impact energies, around 500 keV/amu, we obtain in general a good agreement of the switching CTMC results compared to the measurements from [20] for $j = 1, 2$ and 3. CTMC calculations performed with the 4-body approach are unable to describe the Li^+ formation due to classical autoionization and, in fact, a converged probability of projectile and target electron capture would be zero if we had integrated the Hamilton equations a sufficient time (present calculations have been integrated up to $500/v$ a.u.). That would mean that all the $\sigma_{0,j-2,1}$ cross sections would have been null. As in the case of the H + H collision, 4-body cross sections are only calculated and compared to experiments to show their behaviour for a typical final integration time. Therefore, this discussion and conclusions will be made only for the switching results.

With respect to the two proposed models for computing multiple probabilities, we find in general a better description with model 2, which describes the ionization of Ar taking into account all the probabilities which give rise to Ar^+ ion in equation (5.32), because we have a change of charge of the projectile.

Multiple ionization of argon accompanied by projectile electron capture has already been studied for the He^{2+} impinging on argon, and we can take the advantage of comparing both collisions. For $j < 4$ we find, in general, good results for the two considered projectiles. The typical overestimation in the

computed probabilities with the IPM, for multiple electron loss, is found to be important for $j = 4$ in the case of the He^{2+} projectile, while this same happens for $j = 5$ in the case of Li^{2+}. This is reasonable, because in the treatment of Li^{2+} + Ar collision we have taken into account two active electrons instead of one, increasing accordingly the level of validity of the IPM for multiple electron loss.

Pure multiple-ionization of Ar - $\sigma_{0,j-2,2}$

In this section we study the reaction:

$$Li^{2+} + Ar \rightarrow Li^{2+} + Ar^{j+} + je^{-} \tag{5.46}$$

where only the target changes its charge. The events which may happen for each $3l$ state are:

$3p$

1. From 6 initial electrons, j are being ionized:

$$\binom{6}{j} P_{TI}^{3p})^j$$

2. $6 - j$ electrons rest in the argon:

$$(P_e^{3p})^{6-j}$$

$3s$

1. From 2 initial electrons, j are being ionized:

$$\binom{2}{j} P_{TI}^{3s})^j$$

2. $2 - j$ electrons rest in the argon:

$$(P_e^{3s})^{2-j}$$

We define, as in the previous case, two different IPM probabilities, (P_{0j-21}^{m1}) if we use the P_{TI}^{P}) and (P_{0j-21}^{m2}) if we use P_{TI}^{F}), for the process from equation (5.46):

$$P_{0j-22}^{3p,m1} = \binom{6}{j} (P_{TI}^{3pP})^j (P_e^{3p})^{6-j} \tag{5.47}$$

$$P_{0j-22}^{3p,m2} = \binom{6}{j} (P_{TI}^{3pF})^j (P_e^{3p})^{6-j} \tag{5.48}$$

$$P_{0j-22}^{3s,m1} = \binom{2}{j} (P_{TI}^{3sP})^j (P_e^{3s})^{2-j} \tag{5.49}$$

$$P_{0j-22}^{3s,m2} = \binom{2}{j} (P_{TI}^{3sF})^j (P_e^{3s})^{2-j} \tag{5.50}$$

Once computed the individual $3p$ and $3s$ cross sections with these probabilities, we sum them to obtain

$$\sigma^{\mathrm{m1}}_{0j-22} = \sigma^{3p,\mathrm{m1}}_{0j-22} + \sigma^{3s,\mathrm{m1}}_{0j-22} \tag{5.51}$$

$$\sigma^{\mathrm{m2}}_{0j-22} = \sigma^{3p,\mathrm{m2}}_{0j-22} + \sigma^{3s,\mathrm{m2}}_{0j-22} \tag{5.52}$$

We can now compare the obtained cross sections with the measurements of Losqui *et al.* [20].

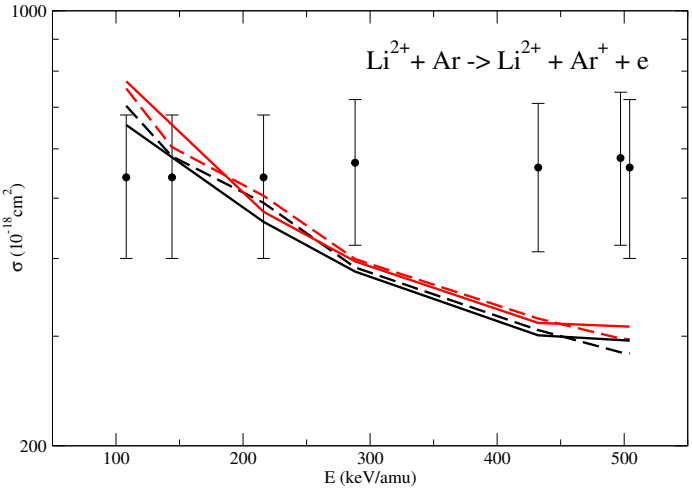

Figure 5.19: Cross sections for reaction (5.46) with $j = 1$. Present switching (full lines) and 4-body (broken lines) CTMC results, with model 1 (in black) and model 2 (in red) IPM. Measurements from [20] (•).

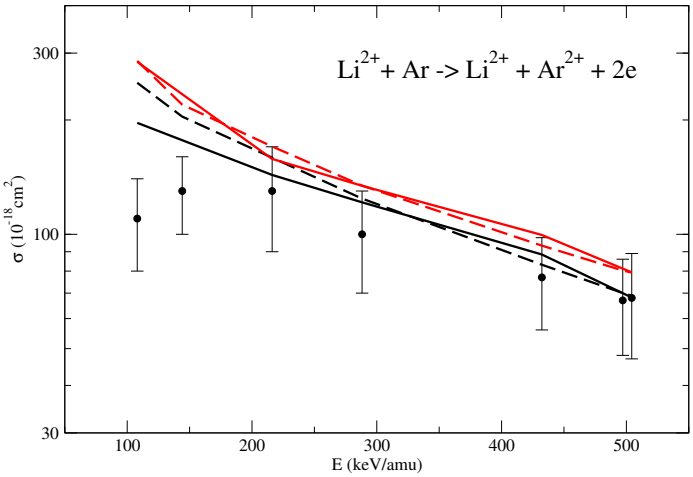

Figure 5.20: Cross sections for reaction (5.46) with $j = 2$. Present switching (full lines) and 4-body (broken lines) CTMC results, with model 1 (in black) and model 2 (in red) IPM. Measurements from [20] (•).

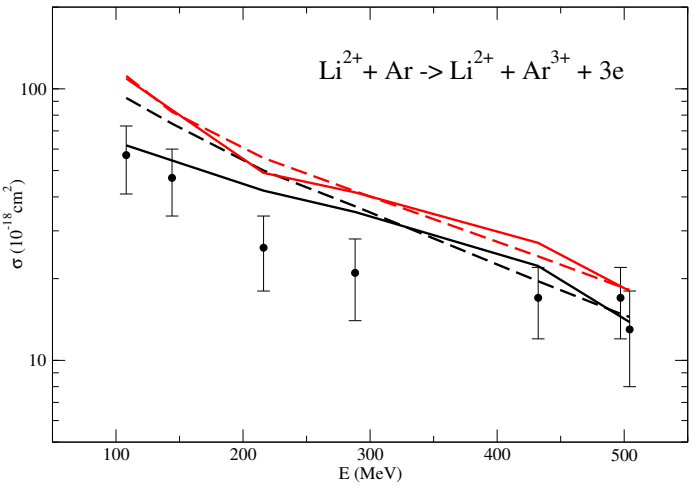

Figure 5.21: Cross sections for reaction (5.46) with $j = 3$. Present switching (full lines) and 4-body (broken lines) CTMC results, with model 1 (in black) and model 2 (in red) IPM. Measurements from [20] (•).

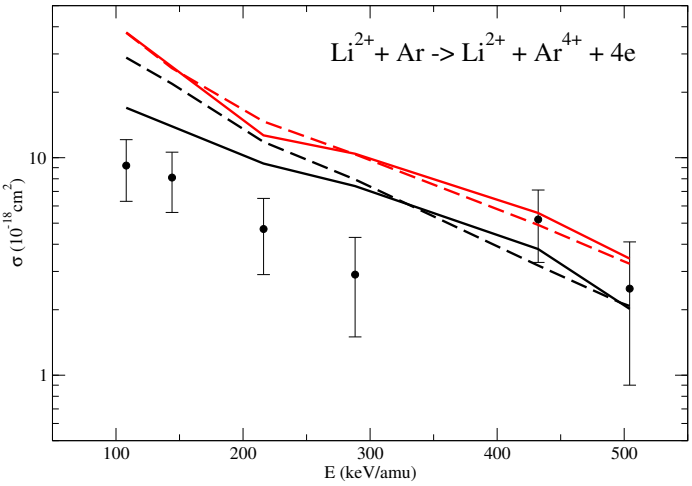

Figure 5.22: Cross sections for reaction (5.46) with $j = 4$. Present switching (full lines) and 4-body (broken lines) CTMC results, with model 1 (in black) and model 2 (in red) IPM. Measurements from [20] (•).

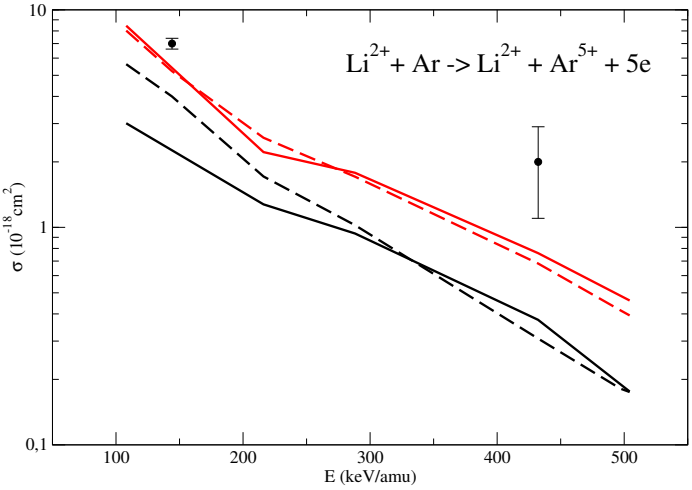

Figure 5.23: Cross sections for reaction (5.46) with $j = 5$. Present switching (full lines) and 4-body (broken lines) CTMC results, with model 1 (in black) and model 2 (in red) IPM. Measurements from [20] (•).

We can analyze these results, like we did for $\sigma_{0,j-21}$ cross sections, comparing the proposed IPM models, the switching and 4-body CTMC approaches, and the grade of validity of the IPM description for one and two active electrons, comparing to the equivalent process for He^{2+} + Ar. We start comparing with the He^{2+} projectile, since an special remark has to be done for the $j = 1$ case. The experimental single ionization of argon in collision with the Li^{2+} projectile shows the same behaviour as for the He^{2+} projectile, a flat shape in all the studied energy range. The CTMC calculations show a fall of the cross section with the increasing collision energy, being unable of describing the mechanism which is taking place in both collisions. For the rest of processes ($j > 1$), and compared to the He^{2+} projectile, we find again a *shifted* j value for which the cross sections start to be appreciably overestimated. While this loss of accuracy was manifest for $\sigma_{0,3-22}$ in the case of the He^{2+} + Ar collision, in the case of the Li^{2+} the overestimation of the IPM probabilities starts being important for $\sigma_{0,4-22}$.

With respect to the proposed IPM models, we find a much better description of multiple target ionization when using the *pure* target ionization probability P^{P}_{TI}, which implies that the projectile keeps its initial charge. This is a different behaviour than the one we found for $\sigma_{0,j-21}$ cross sections, where the P^{F}_{TI} probability offered better results. This makes sense if we look at the initial and final charge of the projectile. Multiple argon ionization is better described with the *pure* ionization probability if the projectile charge does not change.

Comparing the two performed CTMC calculations, we observe that again a better description is found with the switching approach than with the 4-body treatment at the lowest energies considered. At high energies (E $\gtrsim$ 300 keV/amu) capture to the target or projectile, to form an Ar^{-} or Li^{+}, is negligible and the switching and 4-body methods rise to similar cross sections. When autoionization from the Ar^{-} or Li^{+} happens, trajectories which would have belong to target and projectile capture are counted as ionization and, therefore, the σ^{m1}_{0j-22} is overestimated with the 4-body method at low energies.

Multiple-ionization of Ar accompanied by single-electron electron loss of the Li^{2+} - $\sigma_{0,j-2,3}$

We study the reaction:

$$Li^{2+} + Ar \rightarrow Li^{3+} + Ar^{j+} + (j+1)e^{-} \tag{5.53}$$

where the projectile captures one electron and there are $j+1$ emitted electrons. The events which are happening for each $3l$ state are:

$3p$

1. From 6 initial electrons in the argon one is being ionized, accompanied also by ionization in the projectile:
$$\binom{6}{1}\mathrm{P}_{\mathrm{di}}^{3p}$$
2. From the remaining 5 electrons, $j-1$ are being ionized:
$$\binom{5}{j-1}(\mathrm{P}_{\mathrm{TI}}^{3p})^{j-1}$$
3. $6-j$ electrons remain in the argon:
$$(\mathrm{P}_{\mathrm{e}}^{3p})^{6-j}$$

$3s$

1. From 2 initial electrons in the argon one is being ionized, accompanied also by ionization in the projectile:
$$\binom{2}{1}\mathrm{P}_{\mathrm{di}}^{3p}$$
2. The remaining electron rests in the argon if $j=1$ or is ionized if $j=2$:
$$\binom{1}{j-1}(\mathrm{P}_{\mathrm{TI}}^{3s})^{j-1}(\mathrm{P}_{\mathrm{e}}^{3s})^{2-j}$$

As in the previous studied reactions, we define model 1 and 2 probabilities using $\mathrm{P}_{\mathrm{TI}}^{\mathrm{P}}$ and $\mathrm{F}_{\mathrm{TI}}^{\mathrm{P}}$, respectively.

$$\mathrm{P}_{0j-23}^{3p,\mathrm{m1}} = \binom{6}{1}\mathrm{P}_{\mathrm{di}}^{3p}\binom{5}{j-1}(\mathrm{P}_{\mathrm{TI}}^{3p\mathrm{P}})^{j-1}(\mathrm{P}_{\mathrm{e}}^{3p})^{6-j} \tag{5.54}$$

$$\mathrm{P}_{0j-23}^{3p,\mathrm{m2}} = \binom{6}{1}\mathrm{P}_{\mathrm{di}}^{3p}\binom{5}{j-1}(\mathrm{P}_{\mathrm{TI}}^{3p\mathrm{F}})^{j-1}(\mathrm{P}_{\mathrm{e}}^{3p})^{6-j} \tag{5.55}$$

$$\mathrm{P}_{0j-23}^{3s,\mathrm{m1}} = \binom{2}{1}\mathrm{P}_{\mathrm{di}}^{3s}\binom{1}{j-1}(\mathrm{P}_{\mathrm{TI}}^{3s\mathrm{P}})^{j-1}(\mathrm{P}_{\mathrm{e}}^{3s})^{2-j} \tag{5.56}$$

$$\mathrm{P}_{0j-23}^{3s,\mathrm{m2}} = \binom{2}{1}\mathrm{P}_{\mathrm{di}}^{3s}\binom{1}{j-1}(\mathrm{P}_{\mathrm{TI}}^{3s\mathrm{F}})^{j-1}(\mathrm{P}_{\mathrm{e}}^{3s})^{2-j} \tag{5.57}$$

Once computed the individual $3p$ and $3s$ cross sections with these probabilities, we sum them to obtain

$$\sigma_{0j-23}^{\mathrm{m1}} = \sigma_{0j-23}^{3p,\mathrm{m1}} + \sigma_{0j-23}^{3s,\mathrm{m1}} \tag{5.58}$$

$$\sigma^{\mathrm{m2}}_{0j-23} = \sigma^{3p,\mathrm{m2}}_{0j-23} + \sigma^{3s,\mathrm{m2}}_{0j-23} \tag{5.59}$$

We can now compare the calculated cross sections with the measurements of Losqui *et al.* [20]. Similarly to the case of $\sigma_{0,j-2,1}$, for $j = 1$ model 1 and model 2 give rise to equal cross sections $\sigma^{\mathrm{m1}}_{01-23} = \sigma^{\mathrm{m2}}_{01-23}$.

$$\mathrm{Li}^{2+} + \mathrm{Ar} \rightarrow \mathrm{Li}^{3+} + \mathrm{Ar}^{j+} + (j+1)\mathrm{e}^- \tag{5.60}$$

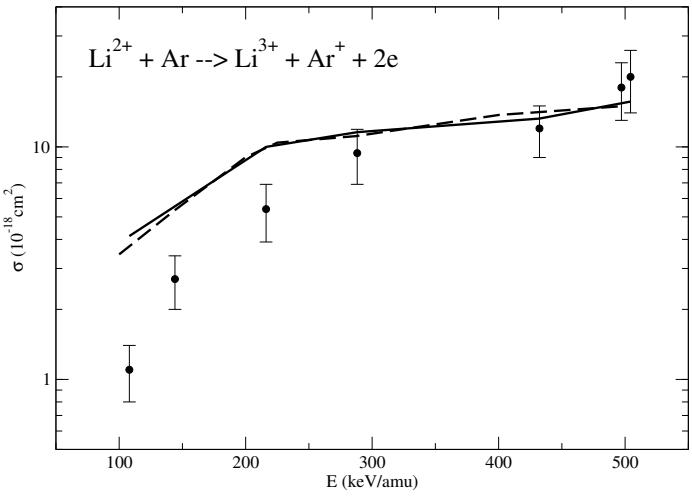

Figure 5.24: Cross sections for reaction (5.60) with $j = 1$. Present switching (full lines) and 4-body (broken lines)CTMC results, with model 1 IPM. Measurements from [20] (•).

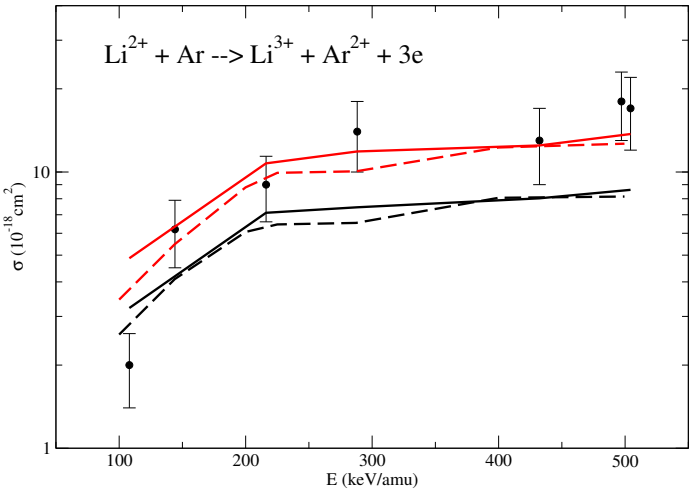

Figure 5.25: Cross sections for reaction (5.60) with $j = 2$. Present switching (full lines) and 4-body (broken lines) CTMC results, with model 1 (in black), model 2 (in red) IPM. Measurements from [20] (•).

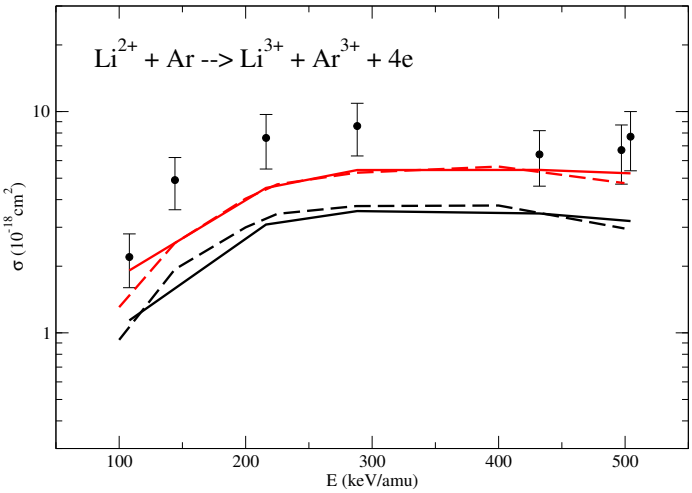

Figure 5.26: Cross sections for reaction (5.60) with $j = 3$. Present switching (full lines) and 4-body (broken lines) CTMC results, with model 1 (in black) and model 2 (in red) IPM. Measurements from [20] (•).

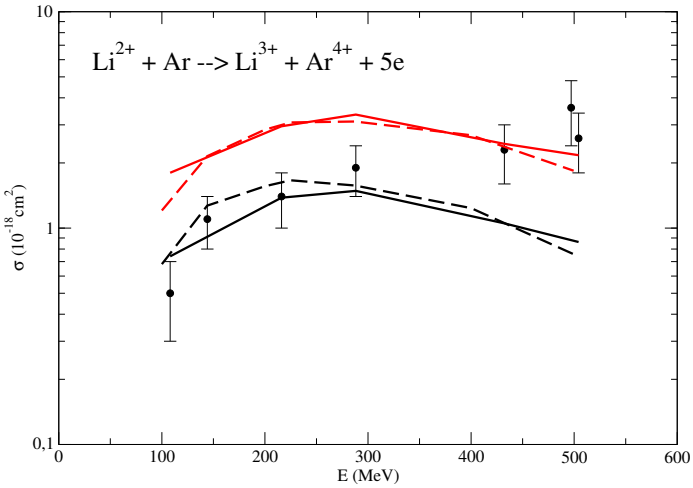

Figure 5.27: Cross sections for reaction (5.60) with $j = 4$. Present switching (full lines) and 4-body (broken lines) CTMC results, with model 1 (in black) and model 2 (in red) IPM. Measurements from [20] (•).

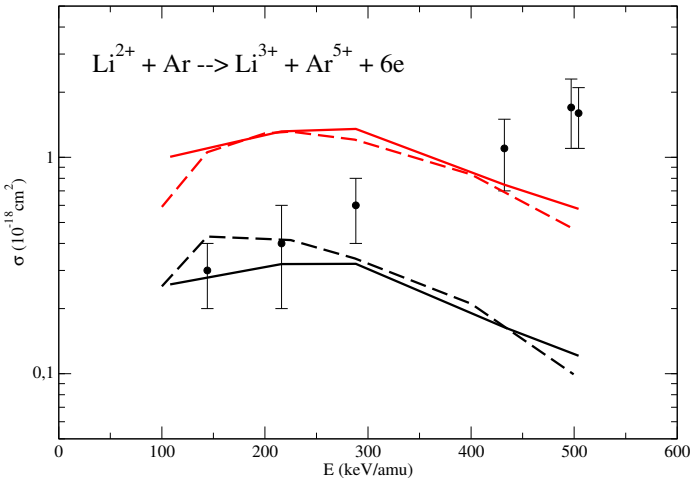

Figure 5.28: Cross sections for reaction (5.60) with $j = 5$. Present switching (full lines) and 4-body (broken lines) CTMC results, with model 1 (in black) and model 2 (in red) IPM. Measurements from [20] (•).

For this process, we could expect a better behaviour using the *full* target ionization probability, P_{TI}^{F}, to describe electron loss of argon, since the projectile charge changes. One conclusion of this study is that, when computing IPM probabilities with two active electron probabilities in a collision like Li^{2+} + Ar, *pure* target ionization probabilites has to be used if the final charge of the projectile does not change, and *full* target ionization probabilities if the final charge of the projectile changes respect to the initial one.

With respect to the 4-body and switching approach, results are very close for the two collisions since, as we had already seen with the H + H collision (see figure 4.5), double ionization probabilities are very similar with the two CTMC approaches. Besides, the contribution of target ionization, which is the one contaminated by projectile electron capture trajectories due to autoionization in the 4-body treatment, is smaller than in the previuos analyzed reaction (5.46).

In summary, we have studied the Ar target in collisions with He^{2+} and Li^{2+} projectiles, obtaining cross sections for different multiple processes which, in general, show a good comparison with the measurements of Dubois, Rudd *et al.* and Losqui *et al.* We have checked that, in the considered energy range, we can treat independently the different $3l$ electrons, due to the large difference of ionization $3s$ and $3p$ potential energies that they have. We have also checked that increasing the number of active electrons in the collision, from one to two, implies an improvement of the computed probabilities for multiple electron loss under the Independent Particle Model. It has also been shown that multiple target ionization is better described taking into account all processes which give rise to an Ar^{+} in equation (5.32) if the projectile change its initial charge, both by capture or electron loss. If the projectile keeps its initial electron, argon ionization must be described with a probability which counts for keeping the projectile in its initial charge. We have also checked that 4-body CTMC calculations can properly describe multiple ionization processes under a two-electron IPM, but if such a process includes target or projectile capture, the switching approach presents better results. We include in table (5.1) a summary of the two-electron IPM, for each studied process, which give rise to better classical results compared to the experimental data. The multielectronic probabilities are given in terms of the bielectronic probabilities from equation (5.32).

Table 5.1: Recommended two-electron IPM models

Process: $Li^{2+} + Ar \rightarrow$	IPM
$Li^{+} + Ar^{j+} + (j-1)e^{-}$	$P^{3p}_{0j-21} = \binom{6}{1} P^{3p}_{pc} \binom{5}{j-1} (P_{ti} + P_{di} + P_{pc})^{j-1} (P^{3p}_{e})^{6-j}$ $P^{3s}_{0j-21} = \binom{2}{1} P^{3s}_{pc} \binom{1}{j-1} (P_{ti} + P_{di} + P_{pc})^{j-1} (P^{3s}_{e})^{2-j}$
$Li^{2+} + Ar^{j+} + je^{-}$	$P^{3p}_{0j-22} = \binom{6}{j} (P_{ti})^{j} (P^{3p}_{e})^{6-j}$ $P^{3s}_{0j-22} = \binom{2}{j} (P_{ti})^{j} (P^{3s}_{e})^{2-j}$
$Li^{3+} + Ar^{j+} + (j+1)e^{-}$	$P^{3p}_{0j-23} = \binom{6}{1} P^{3p}_{di} \binom{5}{j-1} (P_{ti} + P_{di} + P_{pc})^{j-1} (P^{3p}_{e})^{6-j}$ $P^{3s}_{0j-23} = \binom{2}{1} P^{3s}_{di} \binom{1}{j-1} (P_{ti} + P_{di} + P_{pc})^{j-1} (P^{3s}_{e})^{2-j}$

Independent atom electron model: Approach to clusters collisions

Collisions between polyatomic systems, such as clusters or molecules, and atoms or ions have been studied for biological [10, 140] or astrophysical [141, 142] interest in the last years. In these works, it has been studied mainly the relaxation of the excited polyatomic system, while the collisional process has received relatively less attention.

Labaigt *et al.* [21] have recently measured single and double electron capture cross sections, as well as single and multiple projectile ionization cross sections, in $C^+_{n=1-5}$ + He, $C^+_{n=1,2,4}$ + Ar collisions at 125 keV/amu impact energy. These processes, for the Ar target, can be summarized in the following reactions:

$$\begin{aligned} C_n^+ + Ar &\rightarrow {C_n}^{(j+1)+} + ... \\ C_n^+ + Ar &\rightarrow C_n + ... \\ C_n^+ + Ar &\rightarrow {C_n}^- + ... \end{aligned} \tag{5.61}$$

Single electron capture cross sections in C + Ar collisions have also been measured.

$$C + Ar \rightarrow C^- + ... \tag{5.62}$$

As it was explained in section (2.5), the Independent Atom Electron (IAE) model make use of one-electron ion-atom and atom-atom probabilities to model the cluster-atom collision, where the cluster is assumed to be made of independent atoms in which electrons move independently. This approximation has sense at sufficiently high collision energies. In the case of the argon target, we have performed these ion-atom and atom-atom collisions with the CTMC method, considering both a C and C^+ projectiles. In the following section we show the details of these CTMC calculations for the argon target. More details on the experimental set-up, the IAE model and the results concerning the helium target can be found in [21], where the joint experimental and theoretical study of these carbon clusters - He and Ar collisions was presented.

C + Ar and C^+ + Ar collisions

We have studied collisions of C and C^+ impinging on Ar, with both a one-active and two-active electrons CTMC approach. In the case of the monoelectronic collisions, the active electron is placed in the Ar with an initial state $3p$. In the

case of two-active electrons calculations, we have considered the $3p$ electron in the argon as well as one $2l$ electron in the C^+, performing different calculations for both the $2s$ and $2p$ initial state of the carbon electron. We can summarize these collisions in the following:

$$\begin{array}{lll} \text{One} - \text{active electron} & C^+ + Ar(3p) & C + Ar(3p) \\ \text{Two} - \text{active electrons} & C^+(2p) + Ar(3p) & C^+(2s) + Ar(3p) \end{array} \tag{5.63}$$

Separated calculations have been carried out for all the systems of reactions (5.63) in order to provide mono and bielectronic probabilities to later compute cluster-atom cross sections, under the Independent Atom electron model (IAE) [31] outlined in section (2.5).

One-active electron calculations have been performed to obtain the probability of electron capture from the argon target to the projectile, for both the C and C^+:

$$\begin{array}{l} C^+ + Ar \rightarrow C + ... \\ C + Ar \rightarrow C^- + ... \end{array} \tag{5.64}$$

Two-active electron calculations have been carried out to obtain projectile ionization probability in C^+ + Ar collisions:

$$C^+ + Ar \rightarrow C^{2+} + ... \tag{5.65}$$

These two-active electron collisions have been performed with the 4-body CTMC approach. It must be noted that, due to the classical autoionization which will occur to C or Ar^- if one electron capture happens, there will be a contamination of the genuine single ionization process. But this contamination has been found to be small (1-3%) and, therefore, the 4-body CTMC approach is valid to model projectile ionization.

In order to run both one- and two-active calculations, we need model potentials to represent the interaction of an electron in the presence of an C^{2+}, C^+ and C. The form of the model potentials which have been used for these carbon systems is:

$$V = -\frac{Z-N}{r} - \frac{Ae^{-Br} + (N-A)e^{-Cr}}{r} \tag{5.66}$$

In table (5.2) the A, B and C values are shown, as well as the number of frozen electrons N, for each carbon [21].

Table 5.2: A, B, C and N values for model potentials from equation (5.66) for the interaction of an electron with a C, C^+ and C^{2+} to form a C^-, C and C^+, respectively.

	A	B	C	N
$C^- = \{C+e^-\}$	1.964	7.136	0.840	6
$C = \{C^+ + e^-\}$	1.904	0.808	2.518	5
$C^+ = \{C^{2+} + e^-\}$	2.044	1.256	3.202	4

In the case of one-active electron calculations, we use the model potentials of $\{C^+ + e^-\}$ and $\{C + e^-\}$ for the first and second reaction of equation (5.64). In the case of two-active electrons calculations, we use the model potential of $\{C^{2+} + e^-\}$ for the reaction (5.65). More details on how these model potentials have been obtained can be found in [21].

In all the calculations we have removed the final trajectories which corresponded to occupied inner shells of Ar, C^+ and C atoms. This has been done in a similar manner as the exclusion of forbidden trajectories explained in section (3.1.1). But, instead of removing trajectories depending on their final binding energy, here we apply the method developed by Rakovic *et al.* [40] to obtain the final nl level in which the electron is bound. If this nl level belongs to an occupied shell, the trajectory is removed and the final probabilities are renormalized as explained in section (3.1.1).

Applying the IPM, inclusive probabilities model, with the obtained mono and bielectronic probabilities, we can compare directly the results for $n = 1$ reactions from (5.61) and for reaction (5.62). These results are shown in table (5.3) compared to the measurements from Labaigt *et al.* .

Table 5.3: Comparison between measured and calculated cross sections (in cm^2) for ionization and charge exchange processes in C^+,C-Ar collisions at v=2.25.

Process	Experiments (rel. error)	CTMC+IPM
$C^+ \rightarrow C^{2+}$	2.9×10^{-16} (28%)	2.9×10^{-16}
$C^+ \rightarrow C$	1.4×10^{-17} (29%)	4.1×10^{-17}
$C^+ \rightarrow C^-$	3.1×10^{-20} (33%)	2.0×10^{-18}
$C \rightarrow C^-$	5.8×10^{-18} (33%)	1.1×10^{-17}

Perfect agreement is observed for single ionization of C^+, whose IPM cross section has been computed with the bielectronic calculations from equation (5.65). The electron capture cross sections, both single and double, have been obtained with the IPM applied to the monoelectronic probabilities of first reaction from equation (5.64). We find a worse comparison for the single capture process C^++Ar $\rightarrow$ C+Ar^+ and huge discrepancy between experiments and theory appears for the double electron transfer process C^++Ar $\rightarrow$ C^-+Ar^{2+}. In the case of C impact, monoelectronic probabilities are obtained from second reaction in equation (5.64) to compute the IPM cross section shown in table (5.3). The observed discrepancies for the capture processes may be due to a failure of inclusive IPM, which we can analyze with the experience obtained for similar monoelectronic systems along this thesis. On one hand, we found in section (3.1.1) that the capture process of a C^+ ion impinging on H($1s$), where the C^+ was described with a more simple model potential than the one considered in these calculations, could be described within an error less than 20% with respect to experimental values. Since the ionization energies of the $1s$ electron in H and $3p$ electron in Ar are quite similar (-0.5 and -0.58 a.u., respectively), the main difference here is the use of an IPM for the 6 equivalent electrons in the argon. On the other hand, we studied single and double capture for the He^{2+} + Ar($3p$) collision in section (5.1.2), obtaining, in general, a good agreement of the computed IPM cross sections with the experimental data from the bibliography. The main difference between the projectiles C^+ and He^{2+} is, apart from the charge, the use of a model or Coulomb potential to describe them. It is known [143, 144] that ionization of a given target by a dressed projectile is rather well described with a Coulomb potential with an effective charge ($-Z_{eff}/r$). In contrast, capture to a dressed projectile is properly simulated with a model potential describing the projectile, as it was shown for the C^+ on H($1s$) in section (3.1.1). Even when monoelectronic capture is well represented with a model potential describing the dressed ion, if ionization is not also properly described, inclusive IPM (1-P_c) will not describe accurately the multielectronic capture.

In the following we show the results, once the IAE model is applied, for the considered cluster-atom collisions in comparison with the measurements from Labaigt *et al.*

$C^+_{n=1,2,4}$ + Ar systems

In tables (5.4, 5.5, 5.6) the experimental measurements performed by Labaigt *et al.* for the C^+_n-Ar are shown. These results are for ionization, neutralization

and anion formation of the C_n^+, and are accompanied by their associated IAE computed cross sections.

Table 5.4: Experimental and calculated (IAE) projectile ionization cross sections (cm^2) in C_n^+-Ar at v=2.25 a.u..

Process	Exp. (Ar target)	IAE (Ar target)
$C^+ \rightarrow C^{2+}$	2.9×10^{-16} (28%)	2.9×10^{-16}
$C_2^+ \rightarrow C_2^{2+}$	2.9×10^{-16} (24%)	4.0×10^{-16}
$C_4^+ \rightarrow C_4^{2+}$	4.0×10^{-16} (28%)	5.3×10^{-16}
$C_4^+ \rightarrow C_4^{3+}$	2.2×10^{-16} (28%)	3.4×10^{-16}
$C_4^+ \rightarrow C_4^{4+}$	1.4×10^{-16} (35%)	2.5×10^{-16}
$C_4^+ \rightarrow C_4^{5+}$	6.8×10^{-17} (35%)	1.9×10^{-16}

Table 5.5: Experimental and calculated (IAE) neutralization cross sections (cm^2) in C_n^+-Ar collisions at v=2.25 a.u..

Process	Exp.(Ar)	Calc.(Ar)
$C^+ \rightarrow C$	$1.4\ 10^{-17}$ (30%)	$4.1\ 10^{-17}$
$C_2^+ \rightarrow C_2$	$2.2\ 10^{-17}$ (25%)	$3.0\ 10^{-17}$
$C_4^+ \rightarrow C_4$	$1.5\ 10^{-17}$ (27%)	$2.6\ 10^{-17}$

Table 5.6: Experimental and calculated (IAE) anionic production cross sections (cm^2) in C_n^+-Ar collisions at v=2.25 a.u..

Process	Exp.(Ar)	Calc.(Ar)
$C^+ \rightarrow C^-$	$3.1\ 10^{-20}$ (50%)	$2.0\ 10^{-18}$
$C_2^+ \rightarrow C_2^-$	$1.8\ 10^{-20}$ (36%)	$1.2\ 10^{-18}$
$C_4^+ \rightarrow C_4^-$	$2.7\ 10^{-21}$ (52%)	$8.1\ 10^{-19}$

The good agreement found between measurements and computed IAE cross sections for the projectile ionization, shown for different clusters in table (5.4), confirms the good behaviour obtained of the IAE modelization. The

discrepancies found for the neutralization and anionic production results is due to a fail of the IPM applied to the monoelectronic calculations for C + Ar and C^+ + Ar, as it has been commented in section (5.2.1).

Chapter 6

Conclusions

The first part of this thesis is focused on collisions of fusion reserach interest. In this respect, we pointed out in the Introduction the need of evaluating the uncertainties existing in cross sections for inelastic processes in collisions of bare ions with ground-state hydrogen. Most of collision theoretical methods have dealt whith these systems through the years; elaborating recommended sets of data for relevant fusion ions is currently the main task for collisions involving the ground state hydrogen target. Collisions involving excited states of the hydrogen target are, however, less studied, and for some relevant projectile ions (like the N^{7+}) charge-exchange data is not available at the ADAS database [8]. In this regard, we have studied different collisions involving the ground and first excited state hydrogen target. We have tested model potentials to describe one-electron collisions of dressed ions with hydrogen, specifically for carbon ions with charges from 1 to 5, since carbon ions are one of the main impurities in fusion tokamaks. We found a good description even when dealing with open shell projectiles in those systems for which capture is due to a one-electron mechanism. We have calculated total and partial cross sections for charge exchange and total ionization cross sections for C^{6+} and N^{7+} + H($n = 2$) collisions, since these ions are both expected impurities in ITER and cross sections for collisions with excited hydrogen are still scarce. We have employed the CTMC treatment and we have used both the microcanonical and the hydrogenic initial distributions to describe the initial H($n = 2$). Cross sections computed with the two initial distributions are very similar, in contrast to the case of H($1s$) [24], as a consequence of the good description of quantal electron distribution by the microcanonical distribution of the excited states. We provide in Appendix B tables with the obtained total, $n-$ and $nl-$resolved capture cross sections for the collision energy and

states relevant in fusion diagnostics.

We have also shown the results of a joint work with Gravielle *et al.* , where a scaling for n- and nl- resolved capture cross section for collisions of bare ions with ground state has been presented. This scaling law is valid for the intermediate charged bare ions of interest in fusion and for capture to the n levels which give rise to photoemission in de-excitation, which are in fact the ones which are needed in the CXRS diagnostic; it also provides l-resolved capture cross sections, for which data are quite scarce. We have provided a simple formula and tabulated data (which can be found in Appendix C) which can be used to obtain state-resolved electron capture cross sections in a wide energy range.

In the case of the beryllium ion, which will be used as the armour material of the first wall of the ITER reactor, we have checked the applicability of the Grid Time Dependent Schrödinger Equation (GTDSE) method in the Be^{4+} + H($1s$) collision, which is capable of describing electron capture from 1 to 500 keV/amu. For the expected neutral beam energy in ITER, 100 keV/amu, we have obtained converged probabilities for capture to $Be^{3+}(n)$ with $n = 2 - 8$ using different grid densities. We also find that the total capture cross section obtained taking into account n levels up to 50, which has been done extrapolating with the CTMC hydrogenic results, has a uncertainty smaller than 10^{-17} cm^2 (3%). We have provided converged values of $n-$resolved cross sections for those levels of interest in fusion research.

The second part of this thesis is focused on the classical treatment of many-electron systems. Collisions involving multi-electronic atoms or molecules are currently a relevant area of study, specially when involving biomolecules. The study of inelastic processes concerning the neutral argon target has been chosen as a first step to deal with more complex systems. Due to recent experimental and theoretical interest, it has become a benchmark system at present.

The first studied systems have been the two most simple two-active electrons collisions, H + H and $H^+ + H^-$. We have proposed a classical description of a two-electron atom or ion with two non-interacting 3-body systems, where each electron is under the interaction of a model potential which assumes frozen the other electrons. We have checked that the mean value of the energy of the total 4-body hamiltonian in this situation reproduces the total energy of the atom or ion. Due to the good description of a bielectronic system, which is stable in time, reproduces the ionization energies of the electrons and offers a good mean value of the total energy, we have tried to simulate collisions with two-active electrons with a new CTMC approach. For collisions where

the two electrons are initially in different centers, we start the collision in a 4-body scheme, switching to two 3-body systems if the two electrons get bound to the same nucleus, and switching back to a 4-body treatment is imposed if one of them dettachs. Under this approach, we have handled the main problem that multielectronic CTMC treatment presents, the time instability of a many-electron atom or ion due to classical autoionization, and capture to H^- in H + H has been properly described. We have also satisfactorily described neutralization in the H^+ + H^- collision under this approach.

For more complex systems, considering an argon target, we have performed one-electron collisions for a bare projectile, He^{2+}, to study how to compute multielectronic probabilities with the IPM for $3s$ and $3p$ electrons in the argon (considering the L and K shells frozen). We have checked that considering them as independent from each other is a good approximation and, therefore, we can simply add the cross sections obtained for each initial state to provide the total cross sections and compare to experimental results. We have also studied two-electron IPM models for multielectronic processes in the Li^{2+} + Ar collision. When compared to the one-electron IPM model for the He^{2+} + Ar collision, we find that the IPM starts to appreciably fail for triple ionization of the argon target without electron capture with the He^{2+} projectile. In the case of the Li^{2+} projectile it is fourth target ionization which starts to fail. Similar behaviour is found when dealing with multiple argon ionization accompanied by single electron capture to the projectile; overestimated results are found for cross sections leading to a final Ar^{4+} with the He^{2+} projectile, while this same process is still reasonably described for the Li^{2+} projectile. We find that IPM provides reasonable multielectronic probabilities that are better if two instead of one active electrons are taken in consideration in the calculation. This result does not depend on the CTMC approach employed, the 4-body or Switching; however, the formation of Li^+ can only be described with the last one. A similar conclusion is found in the study of the C, C^+ + Ar collisions, where multiple projectile ionization probabilities are more accurate than multiple projectile capture, since the first ones were obtained with a 4-body CTMC calculation and the last one under a 3-body treatment.

Future work should aim at the study of more complex multielectronic systems, such as molecules of biological interest, where further work is needed in the treatment of collisions of charged particles with biomolecules. The proposed classical description for a many electron system can be further explored for systems with more than one center, like the water molecule in collisions with bare or dressed projectiles.

Conclusiones

La primera parte de este trabajo ha estado enfocada en el estudio de colisiones de interés para fusión. En la Introducción señalábamos la importancia de las colisiones de iones desnudos con hidrógeno atómico, tanto en su estado fundamental como en el excitado. Con respecto al primero, existen múltiples trabajos que han investigado estos sistemas a lo largo de los años con diversos métodos teóricos. Sin embargo, resulta necesario establecer los errores asociados a cada conjunto de datos y poder generar bases con datos recomendados para cada ión y rango energético de inters. Por otro lado, encontramos un número mucho menor de trabajos que hayan estudiado los estados excitados del hidrógeno en colisión con iones desnudos, encontrando iones de especial interés (como el N^{7+}) para el cual no existen archivos en la base de datos de ADAS [8]. Con respecto a colisiones de interés para fusión, hemos estudiado diferentes sistemas que involucran el estado fundamental y primer excitado del hidrógeno. Hemos utilizado potenciales modelo para la descripción de la captura electrónica en colisiones de iones de carbono, con carga inicial de uno hasta cinco, con hidrógeno en el estado fundamental, puesto que los iones de carbono son impurezas comunes en los tokamaks. Hemos encontrado buenos resultados incluso tratando capas abiertas, siempre y cuando la captura en el sistema descrito fuese debida a un mecanismo monoelectrónico. También hemos tratado colisiones de C^{6+} y N^{7+} con hidrógeno en su primer estado excitado, $H(n = 2)$, calculando secciones totales de ionización y captura electrónica, además de captura parcial a niveles n y nl en los iones resultantes C^{5+} y N^{6+}, ya que son impurezas que existirán en ITER y a que los datos atómicos que consideran niveles excitados del hidrógeno son todavía escasos. Hemos utilizado el método CTMC con las distribuciones iniciales microcanónica e hidrogenoide en la descripción del $H(n = 2)$ inicial. Los resultados obtenidos con ambas distribuciones son muy similares, en contraste con lo que ocurre en el caso de la descripción del $H(1s)$ [24], consecuencia de la buena descripción de la distribución radial de la distribución

microcanónica, muy similar a la cuántica. En el Apéndice B tabulamos los resultados obtenidos para las secciones totales de ionización y captura, así como para las secciones parciales, para aquellos estados y energías relevantes en los diagnósticos de fusión. También hemos mostrado el trabajo conjunto realizado con Gravielle *et al.* , en el cual proponemos una ley de escala para obtener secciones parciales de captura n y nl para colisiones de iones desnudos con hidrógeno en estado fundamental. Esta ley de escala es válida para los iones de carga intermedia de interés para fusión, y para los niveles n que dan lugar a emisión en el espectro visible, además de permitir el cálculo de secciones parciales resueltas en l, más escasas en la literatura. Se ha propuesto la ley de escala con una sencilla fórmula y datos tabulados (que se encuentran en el Apéndice C), los cuales pueden ser utilizados de manera sencilla para obtener las secciones parciales de captura en un gran rango energético.

Hemos estudiado la aplicabilidad del método Grid Time Dependent Schrödinger Equation (GTDSE) para la colisión Be^{4+} + H($1s$), puesto que el berilio será usado como material de la primera pared en el reactor de fusión ITER, y hemos comprobado que este método es capaz de describir la captura electrónica en este sistema en un rango de energía de 1 a 500 keV/amu. Para la energía prevista del haz de partículas neutras en el ITER, 100 keV/amu, hemos obtenido probabilidades convergidas para la captura electrónica dando lugar a $Be^{3+}(n)$, para $n = 2 - 8$, usando distinta densidad de puntos en la grilla. Para el cálculo de la sección total de captura hemos extrapolado los resultados hasta $n = 50$ usando datos CTMC calculados con una distribución hidrogenoide, y hemos encontrado que la incertidumbre del dato es menor a 10^{-17} cm^2 (3%). Los niveles n parciales para los cuales hemos obtenido secciones convergidas incluyen aquellos de interés en fusión.

La segunda parte de esta tesis está centrada en el tratamiento clásico de sistemas de muchos electrones. Las colisiones de partículas cargadas y átomos o moléculas son actualmente un área de estudio importante, especialmente cuando involucran biomoléculas. El estudio de procesos inelásticos en colisiones con el átomo de argon neutro han sido elegidos como un primer paso al estudio de sistemas más complejos. Además, debido al reciente interés que ha adquirido este átomo tanto en el plano teórico como en el experimental, se ha convertido en un sistema de referencia en el estudio de colisiones multielectrónicas.

Los primeros sistemas estudiados han sido las colisiones con dos electrones activos más simples, H + H y H^+ + H^-. Hemos propuesto una descripción clásica de un átomo o ión bielectrónico basada en dos sistemas monoelectrónicos no interactuantes, compuesto cada uno de ellos en la inter-

acción del núcleo con el electrón a través de un potencial efectivo que modeliza al otro electrón como congelado. Hemos comprobado que esta descripción permite la estabilidad en el tiempo del átomo o ión bielectrónico, siendo el valor medio de la energía total (calculada con el hamiltoniano completo de tres cuerpos) muy próximo al valor real de energía del átomo completo. Puesto que este sistema tiene las energías exactas de ionización de los electrones y es estable en el tiempo, hemos tratado de simular colisiones con dos electrones activos con un nuevo enfoque clásico. Esta nueva aproximacin consiste en tratar la colisión en un sistema de cuatro cuerpos (incluyendo el proyectil) siempre y cuando los dos electrones no estén ligados al mismo núcleo. Si esto ocurriese, cambiamos a dos sistemas bielectrónicos regidos por un potencial modelo que considera congelado el otro electrón. De esta manera, para las colisiones en las que los electrones están inicialmente en dos centros empezamos con un tratamiento en el sistema a 4 cuerpos (H + H), mientras que si ambos electrones empiezan ligados al mismo núcleo el sistema inicial es de dos sistemas monoelectrónicos a 3 cuerpos ($H^+ + H^-$). De esta manera podemos precedir la captura electrónica que da lugar a la formación de H^- en la colisión H + H, evitando el problema conocido de autoionización que se da en los sistemas clásicos de dos electrones activos, y pudiendo obtener probabilidades convergidas en el tiempo para todos los procesos posibles. Esta nueva aproximacin la hemos aplicado a la colisión Li^{2+} + Ar, pudiendo reproducir la formación de Li^-. Con respecto a la colisión $H^+ + H^-$, hemos obtenido resultados de neutralización (formación de H) que se ajustan muy bien a las medidas experimentales.

En el estudio de sistemas más complejos hemos tratado colisiones con el átomo de argon. El primer proyectil estudiado ha sido el ión He^{2+} para cuyo tratamiento hemos considerado un electrón activo en el argon, realizando separadamente cálculos para los estados inicial $3s$ y $3p$ (asumiendo que los electrones más internos están congelados). Hemos aplicado el Modelo de Partículas Independientes (IPM) considerando tanto que los electrones $3s$ y $3p$ son equivalentes como considerándolos independientes por capas, obteniendo mejores resultados bajo la segunda aproximación en el rango de energas estudiado. Este resultado es coherente en cuanto a que los potenciales de ionización de ambos son muy distintos. Posteriormente hemos estudiado la colisión del ión vestido Li^{2+} con Ar, considerando un electrón activo en cada centro. Las probabilidades de procesos múltiples han sido obtenidas con el IPM, y hemos encontrado una descripción mejor con este modelo al considerar dos electrones activos en vez de uno. Mientras que en la colisión He^{2+} + Ar el modelo IPM empieza a fallar para procesos de ionización triple, cuando consideramos la

colisión Li^{2+} + Ar encontramos que este fallo aparece en la cuádruple. Este resultado es independiente de utilizar un cálculo estándar de 4 cuerpos o la aproximación de Switching, aunque sólo con el último podemos reproducir la formación del Li^{+}. Esto mismo ocurre cuando tratamos las colisiones de C y C^{+} con argon, donde obtenemos una buena comparación con el experimento para los resultados bielectrónicos.

El plan futuro pasa por estudiar sistemas multielectrónicos más complejos, como moléculas de interés biológico, puesto que las colisiones de partículas cargadas con biomoléculas es en la actualidad un área muy importante de estudio. El tratamiento multielectrónico clásico propuesto puede ser explorado para incluir sistemas con más de un centro, como la molécula de agua en colisiones con iones desnudos o vestidos.

Appendix A

Proof of the instability of the initial distribution of Cariatore *et al.* [Phys. Rev. A 91, 042709 (2015)]

In a recent publication [106] we find a CTMC work of charge exchange cross sections for fusion diagnostics, in which the initial distribution is composed of an ensemble of fictitious hydrogenic atoms with different nuclear charges (Z_k), with the correct ionization potential. This distribution is called hydrogenic-Z-distribution (HZD) and it is constructed by imposing the quantal momentum distribution $\rho^{\mathrm{Q}}(p; n, l)$. The radial HZD is a linear combination with coefficients α_k of distributions $\rho_k(r; Z_k, E_n)$, where the values of α_k are chosen by a least-squares fitting of the quantal radial distribution.
The idea of having a weighted sum of distributions is the same as in the Hardie and Olson one (presented in section 2.2.2.3), but instead of having different energy distrbutions with a fixed Z, we have different Z with fixed energy. The main difference is that the HZD is not formed of microcanonical distributions, which are functions of the hamiltonian and therefore fulfill the Liouville equation, but of other kind of distribution, which are not functions of the hamiltonian. In the case of H($2s$), the momentum distribution obtained from HZD is surprising, since it has a node at $p = 0.5$ a.u., and the radial density has a minimum near the node at $r = 2.0$ a.u. of the quantal distribution (labeled as $t = 0$ in figure A.1). We have repeated the procedure from [106] to obtain an initial distribution of N classical trajectories. This procedure

consists, as an example for the case of H($2s$), on the following steps

1. We start with the quantal momentum distribution

$$\rho^{\mathrm{Q}}(p) = \frac{1024p^2}{\pi}\frac{(1-4p^2)^2}{(1+4p^2)^6}, \tag{A.1}$$

2. Two random numbers are obtained, p_r and ρ_r (where the subindex $_r$ is for random). If $\rho_r \leq \rho^{\mathrm{Q}}(p_r)$, then the value of p_r is selected; if not, we repeat the call for random numbers until we have obtained the number N of total valid trajectories.

3. For each p_r we obtain its associated radial coordinate r by imposing the energy condition $p_r^2/(2\mu) - Z/r = -0.125$ a.u. The value of Z varies as it has been explained previously.

4. Once we have N couples of values for the radial coordinate and momentum, four more random values are obtained to complete the full phase space

$$\nu_r, \nu_p \in [-1, 1] \qquad \varphi_r, \varphi_p \in [0, 2\pi] \tag{A.2}$$

so that

$$\begin{aligned} x &= r\sqrt{1-\nu_r^2}\cos\varphi_r \qquad y = r\sqrt{1-\nu_r^2}\sin\varphi_r \qquad z = r\nu_r \\ p_x &= p_r\sqrt{1-\nu_p^2}\cos\varphi_p \qquad p_y = p_r\sqrt{1-\nu_p^2}\sin\varphi_p \qquad p_z = p_r\nu_p \end{aligned} \tag{A.3}$$

We perform the linear combination with the Z_k from [106] and their respective coefficients α_k. Once we have repeated all the steps to construct the HZD for H($2s$), we integrate the Hamilton equations in absence of the projectile to study the stability in time of this distribution. The time evolution of the radial and momentum densities are shown in Fig. A.1. It is clear from this illustration that the HZD is not stable, i.e. $\partial\rho/\partial t \neq 0$. Moreover, the node of $\rho(p; 2s)$, which is the most astonishing fact of the illustration of [106], quickly disappears. Similarly, it is also found that the HZD for H($2p$) is not uniform. In the following, we prove the time instability of this distribution mathematically.

We consider the particular case of the H($2s$). The extension to other excited states is straightforward. We obtain first its analytical form, $\rho_C(\boldsymbol{r}, \boldsymbol{p})$ and substitute it into the Liouville equation.We have to prove that $\frac{\partial\rho}{\partial t}$ is different to 0.

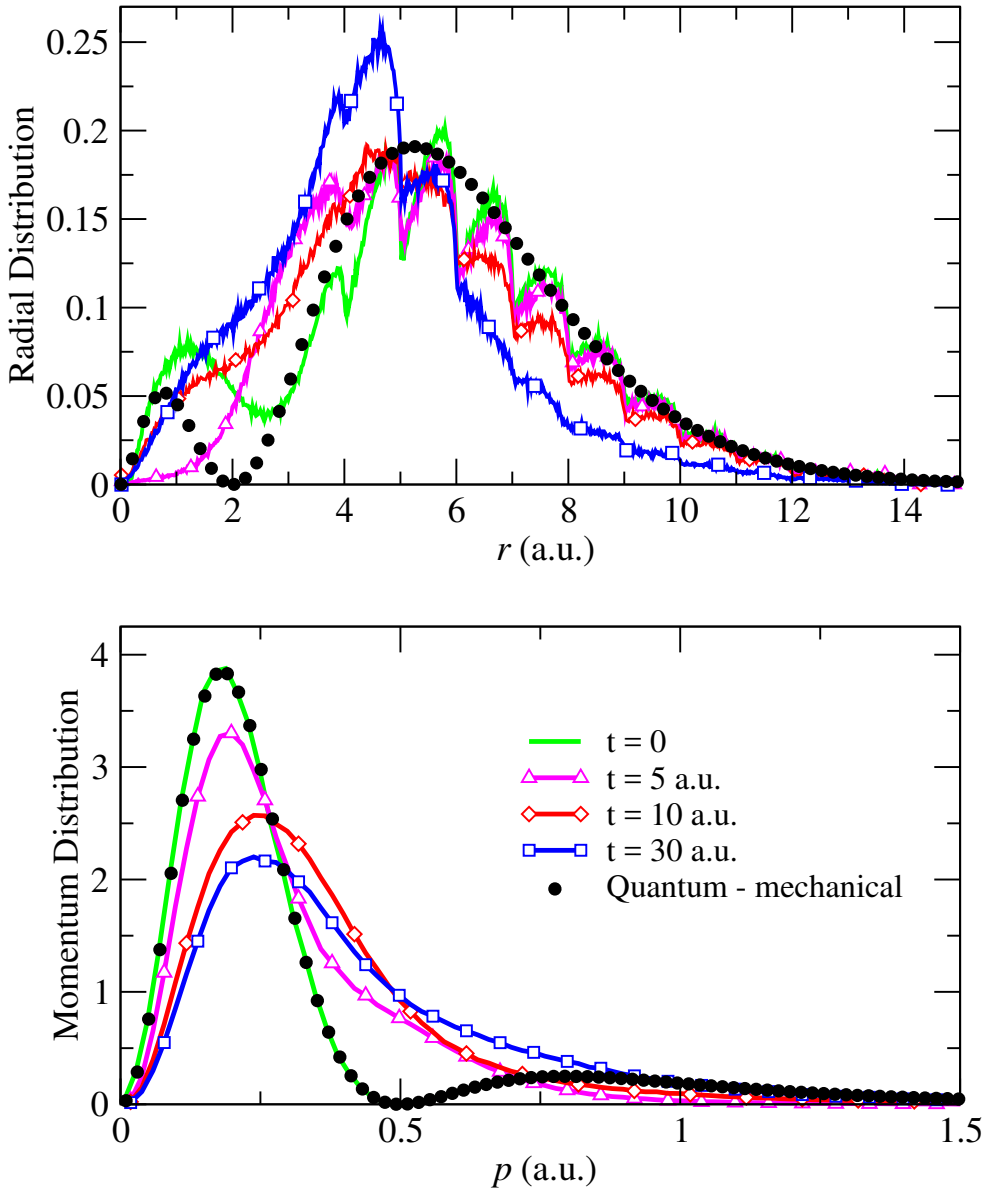

Figure A.1: Time evolution of radial (upper panel) and momentum (bottom panel) densities for the H($2s$) initial distribution from [106]. They are compared to the corresponding quantum-mechanical densities.

Analytical expression of the initial distribution of Cariatore *et al.*

We define $r_0(p)$ as the root of the equation $H[r_0(p), p] - E = 0$. Using the following relation

$$\delta(g(x)) = \sum_i \frac{\delta(x - x_i)}{|\frac{\partial g}{\partial x}|_{x_i}|}, \tag{A.4}$$

where x_i are the roots of $g(x)$, we can express $\delta(H - E)$ as a function of $\delta(r - r_0)$:

$$\delta(H - E) = \delta\left(\frac{p^2}{2} - \frac{Z}{r} - E\right) = \delta(g(r, p)) = \frac{\delta(r - r_0)}{\left|\frac{\partial g(r,p)}{\partial r}|_{r_0}\right|} = \frac{r_0^2}{Z}\delta(r - r_0) \tag{A.5}$$

We assume that the distribution ρ_C is of the form

$$\rho_C(r, p) = f(p)\delta(r - r_0) \tag{A.6}$$

We check the definition (A.6) by comparing the radial and momentum distributions obtained with

$$\rho_C(r) = 4\pi r^2 \int \rho_C \mathrm{d}\boldsymbol{p} \tag{A.7}$$

$$\rho_C(p) = 4\pi p^2 \int \rho_C \mathrm{d}\boldsymbol{r} \tag{A.8}$$

with the numerical ones of Cariatore *et al.* for the orbitals H($2s$) and H($1s$).

Distribution for H($2s$)

If we insert (A.6) in (A.8) and perform the integration, taking $E = -1/8$ a.u., we have

$$\begin{aligned} \rho_C(p) &= 16\pi^2 p^2 \int f(p)\delta(r - r_0) r^2 \mathrm{d}r = \\ &= 16\pi^2 p^2 f(p) \int r^2 \delta(r - r_0)\mathrm{d}r = 16\pi^2 p^2 f(p) Z^2 \left(\frac{8}{1 + 4p^2}\right)^2 \end{aligned} \tag{A.9}$$

where we have used the identity

$$\int \delta(x - x_0) f(x)\mathrm{d}x = f(x_0) \tag{A.10}$$

Since the initial momentum distribution from [106] is identical to the corresponding quantum mechanical one for H($2s$) given in (A.1), we find that $f(p)$ is

$$f(p) = \frac{1}{Z^2\pi^3}\frac{(1-4p^2)^2}{(1+4p^2)^4} \tag{A.11}$$

The associated radial distribution $\rho_C(r)$ can be obtained as

$$\rho_C(r) = \frac{16}{Z^2\pi}r^2\int\frac{(1-4p^2)^2}{(1+4p^2)^4}\delta(r-r_0)p^2\mathrm{d}p \tag{A.12}$$

using (A.4) we write $\delta(r-r_0)$ in the form

$$\delta(r-r_0) = \delta(p-p_0)\left|\left.\frac{\partial g(p)}{\partial p}\right|_{p_0}\right|^{-1}, \tag{A.13}$$

where $g(p) = r - \frac{8Z}{(1+4p^2)}$ and $p_0 = \sqrt{(\frac{2Z}{r} - \frac{1}{4})}$. This yields:

$$\rho_C(r) = \frac{1}{256\pi Z^5}r^4\sqrt{\left(\frac{2Z}{r}-\frac{1}{4}\right)}\left(2-\frac{8Z}{r}\right)^2 \tag{A.14}$$

Figures (A.2) and (A.3) show the numerical radial and momentum distributions, constructed as explained in [106] (see the beggining), for $Z = 1$, compared with expressions (A.14) and (A.1), respectively. These comparisons allow us to express the Cariatore's distribution as

$$\rho_C^{2s}(r,p) = \frac{1}{Z^2\pi^3}\frac{(1-4p^2)^2}{(1+4p^2)^4}\delta(r-r_0) \tag{A.15}$$

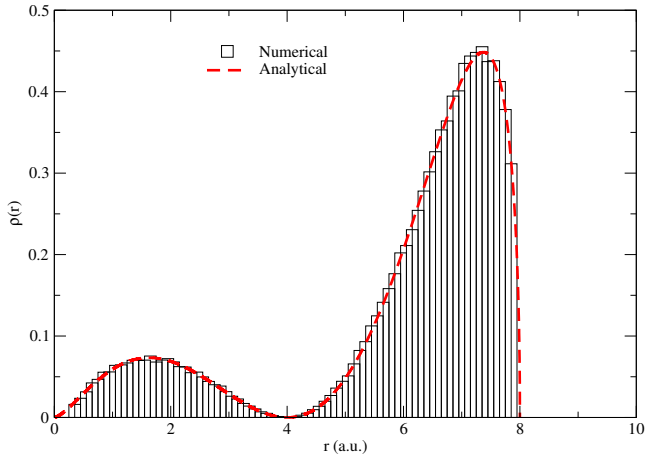

Figure A.2: Numerical and analytical $\rho_C(r)$ from [106] for H($2s$) and $Z = 1$

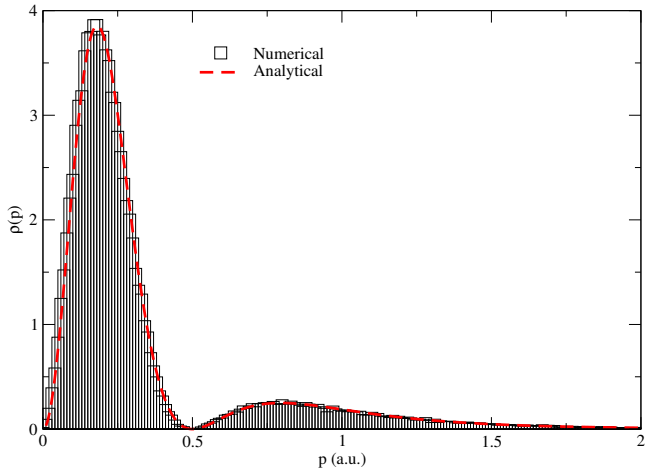

Figure A.3: Numerical and analytical $\rho_c(p)$ from [106] for H($2s$) and $Z = 1$

The radial density for H($2s$) from [106] is a linear combination of the form

$$\rho^{2s}(r) = \sum_k \alpha_k \rho_k^{2s}(r) \tag{A.16}$$

where $\rho_k^{2s}(r)$ are the radial distributions of equation (A.14) for different values

of the nuclear charge, Z_k. It can be reproduced by substituting the expression (A.14) into (A.16) with the weights α_k, as it can be checked in figure (A.4)

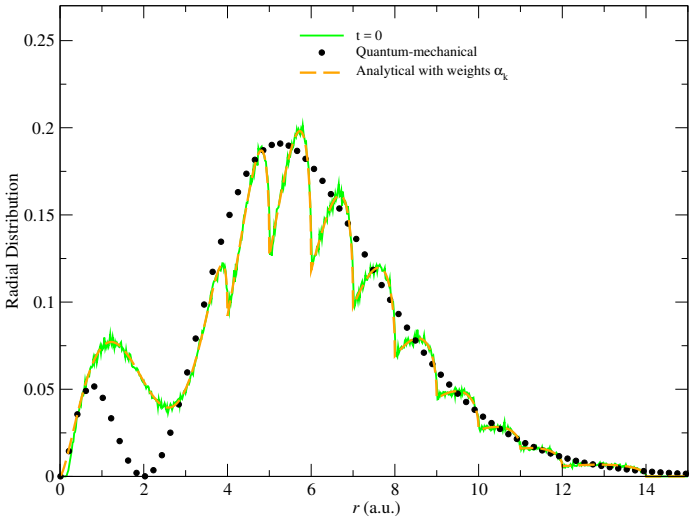

Figure A.4: Numerical and analytical $\rho_C(r)$, weighted with α_k for the different values of Z_k, from [106] for H($2s$), compared to its corresponding quantum-mechanical density.

Distribution for H(1s)

Following the same procedure for H(1s) we find:

$$\rho_C^{1s}(r,p) = \frac{1}{2Z^2\pi^3}\frac{1}{(1+p^2)^2}\delta(r-r_0) \tag{A.17}$$

Relation with the microcanonical distribution

Since the momentum density for H($1s$) with the microcanonical distribution turns to be equal to the quantum one (see figure 2.2), Cariatore's distribution from equation (A.17) is identical to the microcanonical one, which is expressed as

$$\rho_M(r,p) = \frac{(-2E)^{5/2}}{8\pi^3 Z^3}\delta(H-E) \tag{A.18}$$

Using (A.5) and (A.17) we have:

$$\begin{aligned}\rho_C^{1s}(r,p) &= \frac{1}{2\pi^3 Z^2}\frac{\delta(r-r_0)}{(1+p^2)^2} = \frac{1}{2\pi^3 Z^2}\frac{Z}{(1+p^2)^2}\frac{\delta(H-E)}{r_0^2} = \\ &= \frac{1}{2\pi^3 Z}\frac{\delta(H-E)}{(1+p^2)^2}\frac{(1+p^2)^2}{4Z^2} = \rho_M^{1s}(r,p)\end{aligned} \tag{A.19}$$

which is equal to (A.18) when $E = -0.5$ a.u. If we do the same with Cariatore's distribution for H($2s$) of equation (A.15), the relation with the microcanonical distribution takes the form:

$$\begin{aligned}\rho_C^{2s}(r,p) &= \frac{1}{\pi^3 Z^2}\frac{(1-4p^2)^2}{(1+4p^2)^4}\delta(r-r_0) = \frac{1}{\pi^3 Z}\frac{(1-4p^2)^2}{(1+4p^2)^4}\frac{\delta(H-E)}{r_0^2} = \\ &= \frac{1}{64\pi^3 Z^3}\frac{(1-4p^2)^2}{(1+4p^2)^2}\delta(H-E) = 4\frac{(1-4p^2)^2}{(1+4p^2)^2}\rho_M^{n=2}(r,p) = \\ &= F(p)\rho_M^{n=2}(r,p)\end{aligned} \tag{A.20}$$

We prove in the following that, due to the presence of this function $F(p)$, the Liouville equation is not satisfied.

Liouville equation

Substituing ρ_C^{2s} in the Liouville equation we have

$$\frac{\partial \rho_C^{2s}}{\partial t} = -\frac{\partial \rho_C^{2s}}{\partial \boldsymbol{r}}\frac{\partial H}{\partial \boldsymbol{p}} + \frac{\partial \rho_C^{2s}}{\partial \boldsymbol{p}}\frac{\partial H}{\partial \boldsymbol{r}} \tag{A.21}$$

Since the microcanonical distribution is a function of the Hamiltonian it fulfills

$$\frac{\partial \rho_M}{\partial \boldsymbol{r}} = \frac{\partial \rho_M}{\partial H}\frac{\partial H}{\partial \boldsymbol{r}}; \qquad \frac{\partial \rho_M}{\partial \boldsymbol{p}} = \frac{\partial \rho_M}{\partial H}\frac{\partial H}{\partial \boldsymbol{p}} \tag{A.22}$$

Therefore we get

$$\frac{\partial \rho_C^{2s}}{\partial t} = \rho_M^{n=2}\left[\frac{\partial F(p)}{\partial \boldsymbol{p}}\frac{\partial H}{\partial \boldsymbol{r}} - \frac{\partial F(p)}{\partial \boldsymbol{r}}\frac{\partial H}{\partial \boldsymbol{p}}\right] = \rho_M^{n=2}\frac{\mathrm{d}F}{\mathrm{d}p}\frac{\partial p}{\partial \boldsymbol{p}}\frac{\partial H}{\partial \boldsymbol{r}} \tag{A.23}$$

which can be expressed as

$$\frac{\partial \rho_C^{2s}}{\partial t} = \rho_M^{n=2}\frac{\mathrm{d}F}{\mathrm{d}p}\frac{\boldsymbol{r}\cdot\boldsymbol{p}}{rp}\frac{Z}{r^2} \neq 0 \tag{A.24}$$

The presence of the function $F(p)$ in equation (A.20) leads to a non-stationary distribution for the $2s$ orbital or any other excited orbital for which the microcanonical momentum distribution is not equal to the quantum-mechanical one.

This work has been published in [145].

Appendix B

Cross sections for the collisions C^{6+} + H($n = 2$) and N^{7+} + H($n = 2$)

Table B.1: C^{6+} + H(n=2) collisions. Ionization and charge exchange cross sections, in units of (10^{-16}) cm ^{2}

		Impact energies (keV amu^{-1})					
		10	25	50	100	200	300
CX		4.53E+02	1.34E+02	1.56E+01	9.57E-01	5.03E-02	8.17E-03
ION		37.77E+00	2.52E+02	2.62E+02	1.69E+02	9.38E+01	6.48E+01
n	l	State-selective capture cross sections in units of (10^{-16}) cm ^{2}					
5		6.40E+00	3.77E+00	8.96E-01	1.06E-01	7.32E-03	1.10E-03
5	0	2.46E-01	4.90E-02	1.07E-02	1.94E-03	1.54E-04	5.06E-05
5	1	7.60E-01	2.38E-01	4.78E-02	8.01E-03	1.01E-03	2.44E-04
5	2	1.22E+00	6.47E-01	1.15E-01	1.77E-02	1.78E-03	4.49E-04
5	3	1.82E+00	1.20E+00	2.43E-01	3.18E-02	2.72E-03	3.13E-04
5	4	2.34E+00	1.64E+00	4.79E-01	4.66E-02	1.65E-03	4.40E-05
6		3.12E+01	8.21E+00	1.28E+00	1.11E-01	5.97E-03	8.44E-04
6	0	2.37E-01	4.71E-02	1.06E-02	1.63E-03	1.23E-04	3.04E-05
6	1	1.19E+00	2.03E-01	4.44E-02	6.56E-03	4.71E-04	1.52E-04
6	2	3.03E+00	5.58E-01	1.03E-01	1.40E-02	1.65E-03	3.20E-04
6	3	5.84E+00	1.15E+00	1.97E-01	2.49E-02	1.62E-03	2.40E-04
6	4	9.78E+00	2.29E+00	3.33E-01	3.35E-02	1.81E-03	1.03E-04
6	5	1.12E+01	3.95E+00	6.00E-01	3.11E-02	2.99E-04	—
7		6.08E+01	1.15E+01	1.43E+00	9.09E-02	4.08E-03	3.71E-04
7	0	1.51E-01	4.26E-02	9.45E-03	1.40E-03	1.36E-04	3.04E-05
7	1	9.21E-01	1.83E-01	3.76E-02	5.68E-03	5.38E-04	2.31E-05
7	2	2.64E+00	4.77E-01	9.01E-02	1.01E-02	9.88E-04	1.39E-04

Table B.1: C^{6+} + H(n=2) collisions. Ionization and charge exchange cross sections, in units of (10^{-16}) cm ^{2} (Continued)

		Impact energies (keV amu^{-1})					
		10	25	50	100	200	300
n	l	State-selective capture cross sections in units of (10^{-16}) cm ^{2}					
7	3	5.82E+00	9.33E-01	1.57E-01	1.73E-02	1.08E-03	1.17E-04
7	4	1.11E+01	1.55E+00	2.63E-01	2.34E-02	8.56E-04	6.16E-05
7	5	1.70E+01	2.79E+00	3.77E-01	2.36E-02	3.96E-04	—
7	6	2.33E+01	5.57E+00	5.00E-01	9.35E-03	8.21E-05	—
8		6.67E+01	1.25E+01	1.41E+00	7.87E-02	2.93E-03	3.80E-04
8	0	1.12E-01	3.34E-02	8.40E-03	1.03E-03	4.32E-05	5.13E-06
8	1	6.61E-01	1.62E-01	3.24E-02	4.23E-03	2.37E-04	7.88E-05
8	2	1.83E+00	4.10E-01	7.13E-02	9.16E-03	6.28E-04	1.09E-04
8	3	3.92E+00	7.66E-01	1.28E-01	1.36E-02	8.01E-04	1.02E-04
8	4	7.10E+00	1.23E+00	2.01E-01	1.68E-02	8.56E-04	4.40E-05
8	5	1.07E+01	1.96E+00	2.96E-01	1.90E-02	3.72E-04	4.11E-05
8	6	1.62E+01	2.99E+00	3.68E-01	1.39E-02	—	—
8	7	2.62E+01	4.95E+00	2.98E-01	8.16E-04	—	—
9		5.94E+01	1.19E+01	1.26E+00	6.63E-02	2.58E-03	3.91E-04
9	0	8.70E-02	2.80E-02	6.66E-03	7.68E-04	7.59E-05	5.13E-06
9	1	5.10E-01	1.37E-01	2.62E-02	3.36E-03	1.90E-04	4.33E-05
9	2	1.31E+00	3.42E-01	5.77E-02	7.10E-03	6.00E-04	1.44E-04
9	3	2.72E+00	6.43E-01	1.05E-01	1.24E-02	8.98E-04	1.55E-04
9	4	4.58E+00	1.01E+00	1.60E-01	1.38E-02	4.96E-04	4.40E-05
9	5	6.40E+00	1.51E+00	2.23E-01	1.53E-02	3.25E-04	—
9	6	8.99E+00	2.19E+00	2.82E-01	1.12E-02	—	—
9	7	1.35E+01	2.86E+00	2.90E-01	2.09E-03	—	—
9	8	2.13E+01	3.24E+00	1.12E-01	—	—	—
10		4.77E+01	1.08E+01	1.10E+00	5.48E-02	1.87E-03	2.65E-04
10	0	6.31E-02	2.37E-02	5.04E-03	6.51E-04	2.53E-05	2.56E-06
10	1	3.80E-01	1.16E-01	2.07E-02	2.93E-03	8.36E-05	5.83E-05
10	2	9.50E-01	2.92E-01	4.63E-02	5.82E-03	5.10E-04	4.29E-05
10	3	1.93E+00	5.44E-01	8.46E-02	8.65E-03	4.54E-04	1.17E-04
10	4	3.13E+00	8.35E-01	1.34E-01	1.19E-02	4.96E-04	4.40E-05
10	5	4.23E+00	1.21E+00	1.77E-01	1.25E-02	2.84E-04	—
10	6	5.59E+00	1.70E+00	2.20E-01	9.94E-03	2.64E-05	—
10	7	7.63E+00	2.15E+00	2.43E-01	2.45E-03	—	—
10	8	1.03E+01	2.33E+00	1.62E-01	—	—	—
10	9	1.34E+01	1.68E+00	1.50E-02	—	—	—
11		3.64E+01	9.39E+00	9.73E-01	4.54E-02	1.64E-03	1.32E-04
11	0	5.27E-02	1.86E-02	4.53E-03	1.01E-03	5.06E-05	2.27E-05
11	1	2.86E-01	8.89E-02	1.66E-02	2.05E-03	1.23E-04	2.05E-05
11	2	7.12E-01	2.45E-01	3.90E-02	5.04E-03	2.78E-04	5.31E-05
11	3	1.40E+00	4.35E-01	7.25E-02	7.54E-03	4.31E-04	3.52E-05
11	4	2.17E+00	6.62E-01	1.11E-01	7.94E-03	6.80E-04	—
11	5	2.83E+00	9.63E-01	1.55E-01	9.30E-03	8.21E-05	—
11	6	3.59E+00	1.34E+00	1.71E-01	8.91E-03	—	—

Table B.1: C^{6+} + H(n=2) collisions. Ionization and charge exchange cross sections, in units of (10^{-16}) cm ^{2} (Continued)

		Impact energies (keV amu^{-1})					
		10	25	50	100	200	300
n	l	State-selective capture cross sections in units of (10^{-16}) cm ^{2}					
11	7	4.64E+00	1.68E+00	1.99E-01	3.66E-03	—	—
11	8	5.90E+00	1.82E+00	1.65E-01	—	—	—
11	9	7.23E+00	1.52E+00	3.73E-02	—	—	—
11	10	7.56E+00	6.03E-01	2.79E-04	—	—	—
12		2.77E+01	7.96E+00	8.18E-01	3.71E-02	9.66E-04	1.13E-04
12	0	4.25E-02	1.84E-02	3.93E-03	5.54E-04	7.70E-06	2.57E-06
12	1	2.17E-01	8.39E-02	1.39E-02	1.86E-03	1.94E-04	2.27E-05
12	2	5.05E-01	2.02E-01	3.21E-02	4.17E-03	1.73E-04	8.58E-05
12	3	9.76E-01	3.59E-01	5.98E-02	5.52E-03	3.07E-04	2.57E-06
12	4	1.46E+00	5.41E-01	8.78E-02	7.25E-03	1.99E-04	—
12	5	1.90E+00	7.64E-01	1.17E-01	6.61E-03	5.86E-05	—
12	6	2.44E+00	1.07E+00	1.44E-01	7.28E-03	2.64E-05	—
12	7	3.14E+00	1.33E+00	1.59E-01	3.77E-03	—	—
12	8	3.86E+00	1.41E+00	1.37E-01	1.26E-04	—	—
12	9	4.54E+00	1.25E+00	5.97E-02	—	—	—
12	10	5.12E+00	7.95E-01	1.10E-03	—	—	—
12	11	2.55E+00	1.34E-01	—	—	—	—

Table B.2: N^{7+} + H(n=2) collisions. Ionization and charge exchange cross sections, in units of (10^{-16}) cm ^{2}

		Impact energies (keV amu^{-1})					
		10	25	50	100	200	300
CX		5.52E+02	1.83E+02	2.26E+01	1.42E+00	7.54E-02	1.25E-02
ION		3.46E+01	2.90E+02	3.26E+02	2.20E+02	1.24E+02	8.65E+01
n	l	State-selective capture cross sections in units of (10^{-16}) cm ^{2}					
5		1.52E+00	1.89E+00	6.84E-01	1.20E-01	9.93E-03	1.95E-03
5	0	8.19E-02	4.72E-02	9.38E-03	1.91E-03	1.56E-04	3.81E-05
5	1	2.04E-01	1.95E-01	3.73E-02	7.40E-03	9.80E-04	2.31E-04
5	2	2.94E-01	3.94E-01	9.72E-02	1.60E-02	1.94E-03	5.83E-04
5	3	4.15E-01	5.70E-01	2.06E-01	3.16E-02	3.40E-03	8.62E-04
5	4	5.26E-01	6.84E-01	3.34E-01	6.30E-02	3.44E-03	2.34E-04
6		1.25E+01	5.69E+00	1.21E+00	1.35E-01	9.12E-03	1.08E-03
6	0	2.53E-01	3.95E-02	7.25E-03	1.51E-03	2.23E-04	1.02E-05
6	1	8.74E-01	1.80E-01	3.72E-02	5.60E-03	4.72E-04	1.42E-04
6	2	1.64E+00	5.09E-01	8.48E-02	1.35E-02	1.28E-03	2.79E-04
6	3	2.53E+00	1.05E+00	1.62E-01	2.58E-02	2.41E-03	4.96E-04
6	4	3.63E+00	1.72E+00	3.08E-01	3.69E-02	2.98E-03	1.55E-04
6	5	3.57E+00	2.19E+00	6.14E-01	5.15E-02	1.76E-03	—
7		4.27E+01	1.05E+01	1.62E+00	1.40E-01	7.27E-03	1.29E-03

Table B.2: N^{7+} + H(n=2) collisions. Ionization and charge exchange cross sections, in units of (10^{-16}) cm ^{2} (Continued)

		Impact energies (keV amu^{-1})					
		10	25	50	100	200	300
n	l	State-selective capture cross sections in units of (10^{-16}) cm ^{2}					
7	0	1.89E-01	4.22E-02	8.72E-03	1.17E-03	1.00E-04	2.57E-05
7	1	1.00E+00	1.73E-01	3.31E-02	4.84E-03	5.87E-04	2.15E-04
7	2	2.57E+00	4.38E-01	8.11E-02	1.19E-02	9.91E-04	3.10E-04
7	3	5.06E+00	8.80E-01	1.42E-01	2.03E-02	2.11E-03	3.85E-04
7	4	8.86E+00	1.55E+00	2.43E-01	2.99E-02	1.84E-03	2.32E-04
7	5	1.24E+01	2.78E+00	4.00E-01	3.84E-02	1.50E-03	1.23E-04
7	6	1.26E+01	4.61E+00	7.15E-01	3.35E-02	1.41E-04	—
8		6.98E+01	1.38E+01	1.79E+00	1.21E-01	5.50E-03	7.20E-04
8	0	1.22E-01	3.68E-02	7.87E-03	1.20E-03	1.06E-04	5.13E-06
8	1	7.72E-01	1.55E-01	2.84E-02	4.38E-03	4.31E-04	8.65E-05
8	2	2.15E+00	3.97E-01	7.21E-02	8.23E-03	8.03E-04	2.54E-04
8	3	4.47E+00	7.51E-01	1.27E-01	1.56E-02	1.33E-03	1.22E-04
8	4	8.30E+00	1.19E+00	1.94E-01	2.16E-02	1.48E-03	1.40E-04
8	5	1.28E+01	1.87E+00	3.06E-01	2.96E-02	1.16E-03	1.11E-04
8	6	1.76E+01	3.21E+00	4.48E-01	2.98E-02	1.87E-04	—
8	7	2.35E+01	6.20E+00	6.09E-01	1.05E-02	—	—
9		7.33E+01	1.49E+01	1.77E+00	1.08E-01	4.74E-03	5.66E-04
9	0	9.17E-02	3.02E-02	6.19E-03	9.31E-04	7.81E-05	2.53E-05
9	1	5.36E-01	1.42E-01	2.53E-02	3.42E-03	2.87E-04	6.31E-05
9	2	1.44E+00	3.60E-01	5.89E-02	7.51E-03	6.37E-04	1.11E-04
9	3	2.98E+00	6.45E-01	1.02E-01	1.38E-02	1.09E-03	1.53E-04
9	4	5.39E+00	1.01E+00	1.65E-01	1.92E-02	1.41E-03	9.09E-05
9	5	8.16E+00	1.48E+00	2.51E-01	2.29E-02	9.56E-04	1.23E-04
9	6	1.13E+01	2.20E+00	3.52E-01	2.41E-02	2.78E-04	—
9	7	1.70E+01	3.41E+00	4.35E-01	1.49E-02	—	—
9	8	2.64E+01	5.67E+00	3.81E-01	1.35E-03	—	—
10		6.70E+01	1.46E+01	1.68E+00	8.97E-02	3.55E-03	4.77E-04
10	0	7.31E-02	2.62E-02	4.80E-03	1.20E-03	3.55E-05	7.70E-06
10	1	4.22E-01	1.24E-01	2.03E-02	3.11E-03	3.18E-04	3.04E-05
10	2	1.09E+00	3.06E-01	4.64E-02	6.82E-03	3.91E-04	5.57E-05
10	3	2.19E+00	5.52E-01	8.45E-02	1.08E-02	8.54E-04	1.10E-04
10	4	3.73E+00	8.41E-01	1.35E-01	1.50E-02	9.64E-04	1.35E-04
10	5	5.21E+00	1.19E+00	2.08E-01	1.70E-02	5.92E-04	1.38E-04
10	6	6.94E+00	1.72E+00	2.72E-01	1.90E-02	3.31E-04	—
10	7	9.67E+00	2.49E+00	3.63E-01	1.34E-02	6.45E-05	—
10	8	1.43E+01	3.29E+00	3.81E-01	0.33E-03	—	—
10	9	2.34E+01	4.09E+00	1.73E-01	—	—	—
11		5.62E+01	1.35E+01	1.49E+00	7.18E-02	2.81E-03	4.10E-04
11	0	4.93E-02	2.28E-02	4.99E-03	6.14E-04	3.74E-05	2.57E-06
11	1	3.33E-01	9.82E-02	1.79E-02	1.98E-03	2.05E-04	7.70E-06
11	2	8.13E-01	2.54E-01	3.97E-02	4.60E-03	3.64E-04	2.20E-04
11	3	1.61E+00	4.62E-01	7.22E-02	8.55E-03	6.72E-04	1.15E-04

Table B.2: N^{7+} + H(n=2) collisions. Ionization and charge exchange cross sections, in units of (10^{-16}) cm ^{2} (Continued)

		Impact energies (keV amu^{-1})					
		10	25	50	100	200	300
n	l	State-selective capture cross sections in units of (10^{-16}) cm ^{2}					
11	4	2.69E+00	7.19E-01	1.11E-01	1.10E-02	6.73E-04	6.45E-05
11	5	3.62E+00	9.81E-01	1.62E-01	1.43E-02	6.13E-04	—
11	6	4.60E+00	1.39E+00	2.26E-01	1.39E-02	2.49E-04	—
11	7	6.01E+00	1.94E+00	2.84E-01	1.22E-02	—	—
11	8	8.24E+00	2.46E+00	2.99E-01	4.55E-03	—	—
11	9	1.18E+01	2.84E+00	2.44E-01	—	—	—
11	10	1.64E+01	2.40E+00	3.10E-02	—	—	—
12		4.39E+01	1.22E+01	1.32E+00	6.28E-02	2.17E-03	2.36E-04
12	0	3.97E-02	2.11E-02	3.48E-03	7.09E-04	6.05E-05	—
12	1	2.33E-01	8.38E-01	1.55E-02	1.94E-03	1.01E-04	4.80E-05
12	2	5.96E-01	2.20E-01	3.65E-02	4.43E-03	3.57E-04	7.08E-05
12	3	1.16E+00	4.02E-01	6.07E-02	6.67E-03	5.01E-04	8.76E-05
12	4	1.90E+00	5.91E-01	9.75E-02	9.65E-03	4.39E-04	2.93E-05
12	5	2.50E+00	8.25E-01	1.36E-01	1.19E-02	4.25E-04	—
12	6	3.13E+00	1.12E+00	1.81E-01	1.29E-02	2.28E-04	—
12	7	3.92E+00	1.53E+00	2.26E-01	9.33E-03	6.45E-05	—
12	8	5.07E+00	1.98E+00	2.55E-01	4.94E-03	—	—
12	9	6.61E+00	2.23E+00	2.29E-01	3.34E-04	—	—
12	10	8.49E+00	2.06E+00	8.47E-02	—	—	—
12	11	1.03E+01	1.10E+00	1.00E-03	—	—	—

Appendix C

U_{nl} values for the scaling law from section (3.1.2)

Table C.1: $100 \times U_{nl}$ values for $n = 4$

W_{P_z}	P_{40}	P_{41}	P_{42}	P_{43}
0.13	1	9	25	64
0.31	2	9	23	66
0.44	2	10	25	64
0.50	2	10	26	62
0.60	2	9	30	57
0.67	2	8	36	52
0.80	3	10	44	42
0.88	4	12	48	36
0.99	3	19	50	28
1.06	2	22	50	25
1.23	2	32	48	17
1.40	4	41	43	12
1.57	7	47	38	8
1.74	11	50	33	6
1.90	15	52	29	5
2.07	19	53	25	3
2.23	23	53	21	3
2.39	28	52	19	2
2.55	31	51	16	2
2.68	34	50	14	1

Table C.2: $100 \times U_{nl}$ values for $n = 5$

W_{P_z}	P_{50}	P_{51}	P_{52}	P_{53}	P_{54}
0.10	1	5	13	26	55
0.30	1	5	12	25	57
0.38	1	5	12	25	56
0.57	1	6	14	29	49
0.67	1	7	16	32	42
0.74	1	7	17	40	37
0.89	2	6	21	45	26
0.98	2	6	26	44	20
1.14	3	8	35	40	14
1.20	3	10	38	38	11
1.41	2	18	44	29	6
1.62	2	28	45	22	4
1.83	4	37	42	16	2
2.03	6	43	38	12	1
2.23	10	47	34	9	1
2.43	14	49	30	6	0
2.64	18	51	26	5	0
2.84	22	51	23	4	0
3.04	26	50	20	3	0
3.23	30	50	17	2	0

Table C.3: $100 \times U_{nl}$ values for $n = 6$

W_{P_z}	P_{60}	P_{61}	P_{62}	P_{63}	P_{64}	P_{65}
0.08	0	2	7	16	26	48
0.32	1	3	8	14	24	50
0.60	1	4	9	17	29	40
0.78	1	5	11	22	33	28
0.96	1	7	14	27	38	16
1.01	1	7	15	29	36	13
1.16	3	6	20	35	31	8
1.26	3	6	23	39	26	6
1.41	3	7	28	39	19	3
1.51	3	8	34	37	16	2
1.76	2	16	41	30	9	1
2.00	2	26	43	23	6	0
2.24	3	35	41	18	3	0
2.48	6	41	37	13	2	0
2.72	9	46	34	10	1	0
2.96	13	48	30	8	1	0
3.20	18	49	26	6	1	0
3.44	22	50	23	4	0	0
3.67	26	50	20	4	0	0
3.91	30	49	18	3	0	0

Table C.4: $100 \times U_{nl}$ values for $n = 7$

W_{P_z}	P_{70}	P_{71}	P_{72}	P_{73}	P_{74}	P_{75}	P_{76}
0.30	0	2	5	10	14	23	45
0.52	0	3	6	10	16	26	38
0.81	1	4	8	14	23	31	21
1.00	1	4	10	18	28	28	10
1.16	1	5	12	23	33	23	6
1.24	1	6	13	26	35	19	4
1.41	2	6	18	31	32	12	2
1.50	2	6	20	34	28	10	1
1.73	3	6	28	37	20	5	1
1.81	3	8	31	36	18	4	0
2.09	2	15	39	30	11	2	0
2.37	2	25	41	24	7	1	0
2.65	3	33	40	18	4	0	0
2.92	6	40	37	14	3	0	0
3.20	9	44	34	11	2	0	0
3.48	13	47	30	8	1	0	0
3.75	17	49	27	6	1	0	0
4.03	22	50	24	5	1	0	0
4.31	26	49	21	4	0	0	0
4.58	30	49	18	3	0	0	0

Table C.5: $100 \times U_{nl}$ values for $n = 8$

W_{P_z}	P_{80}	P_{81}	P_{82}	P_{83}	P_{84}	P_{85}	P_{86}	P_{87}
0.70	0	2	5	9	13	19	26	25
1.00	1	3	7	12	20	27	23	7
1.13	1	4	8	15	23	27	18	3
1.19	1	4	9	17	25	26	16	2
1.39	1	6	12	22	29	23	10	0
1.48	1	6	13	25	30	20	7	1
1.66	2	5	16	31	31	14	3	0
1.79	3	4	19	35	28	11	2	0
1.99	3	6	25	36	22	7	1	0
2.11	3	7	30	35	19	5	1	0
2.42	2	15	38	31	12	3	0	0
2.74	2	24	40	25	7	1	0	0
3.05	3	33	40	19	5	1	0	0
3.36	6	39	37	15	3	0	0	0
3.67	9	44	34	11	2	0	0	0
3.99	13	47	30	9	1	0	0	0
4.31	17	48	27	7	1	0	0	0
4.62	21	49	24	5	1	0	0	0
4.94	25	49	21	4	0	0	0	0
5.25	30	48	18	3	0	0	0	0

Table C.6: $100 \times U_{nl}$ values for $n = 9$

W_{P_z}	P_{90}	P_{91}	P_{92}	P_{93}	P_{94}	P_{95}	P_{96}	P_{97}	P_{98}
0.68	0	1	4	7	9	12	18	25	23
0.88	0	2	5	8	12	17	23	22	11
1.12	1	3	7	10	17	23	22	14	3
1.29	1	4	8	13	21	25	20	9	1
1.41	1	4	9	16	24	25	18	5	1
1.68	1	4	12	23	29	23	10	2	0
1.91	2	5	16	29	30	16	5	1	0
2.05	3	5	19	33	28	12	3	0	0
2.30	3	6	26	35	22	7	1	0	0
2.40	3	7	29	35	19	6	1	0	0
2.75	2	14	37	31	13	3	0	0	0
3.10	2	24	40	25	8	1	0	0	0
3.45	3	32	39	19	5	1	0	0	0
3.80	6	39	37	15	3	0	0	0	0
4.15	9	43	34	11	2	0	0	0	0
4.51	13	46	30	9	1	0	0	0	0
4.86	17	48	27	7	1	0	0	0	0
5.21	21	49	24	5	1	0	0	0	1
5.57	25	48	21	4	0	0	0	0	1

Appendix D

Model potentials

If we want to describe a dressed ion/atom, composed of an active electron and a frozen core with a nucleus and one or more electrons, the Coulomb potential is not a good approach. For an ion A^{q+}, with one active electron and core charge $q+1$, we need a potential $V(r)$ which fulfills

$$\begin{aligned} V(r) &\to -Z/r \qquad \text{if} \qquad r \to 0 \\ V(r) &\to -(q+1)/r \qquad \text{if} \qquad r \to \infty \end{aligned} \tag{D.1}$$

One simple form of $V(r)$ which fulfills these limits is [146, 147]

$$V = -\frac{(Z-N)}{r} - \frac{N}{r}(1+\alpha r)\exp(-2\alpha r) \tag{D.2}$$

A more complex form [135] is, for example

$$V = -\frac{Z-N}{r} - \frac{A\mathrm{e}^{-Br} + (N-A)\mathrm{e}^{-Cr}}{r} \tag{D.3}$$

In both expressions, N is the number of frozen electrons belonging to $A^{(q+1)+}$, Z the nuclear charge of the ion. The values α, A, B, and C are parameters which need to be fit to yield the ionization energies of the A^{q+} ion. In the case of equation (D.2) only the first ionization potential is considered; in the case of (D.3) the eigenenergies of different states can be considered. This is the method which has been applied to obtain the α parameters used in section 3.1.1, and to obtain A, B, and C for the Ar, C and C^+ in sections 5.2,5.1.

During this thesis we have also used the Talman's method and program [53, 54] in order to obtain the parameters α, A, B, and C, then employed in the description of the H^-, Li^+ and Ar^- ions. The Talman's program is an

iterative method to calculate the effective potential seen by the electrons in an atom or ion using the variational principle. The expectation value of the hamiltonian $\langle H \rangle$, for a Slater determinant formed from reduced radial wave functions $\phi_i(\boldsymbol{r})$, is minimized to obtain the effective potential $V(r)$.

$$\frac{\delta \langle H \rangle}{\delta V(r)} = 0 \tag{D.4}$$

For a given input formed of the number of shells, number of electrons with their quantum numbers nl, and the nuclear charge, the program provides in the output the form of the model potential. The parameters from equations (D.2, D.3) can be obtained with a nonlinear curve fitting of the output.

Model potentials for the Li, Be, B and C atoms

In section 2.3.2.1 we give the ground-state energies for the Li, Be, B and C atoms. In table (D.1) we give the parameters which have been used for the effective potential for each electron, with the form of equation (D.3). All these parameters have been obtained with the Talman's method, except for those of C($1s^2 2s^2 2p^2$), for which we have used the parameters from section 5.2.1.

Table D.1: Parameters Z, N, A, B and C from equation (D.3) used for each sub-shell in the Li, Be, B and C atoms.

	Z	N	A	B	C
Li($1s^2$)	3	1	8.83	1.51	1.35
Li($1s^2 2s$)	3	2	7.84	1.19	1.01
Be($1s^2$)	4	1	4.37	2.19	1.71
Be($1s^2 2s^2$)	4	3	0.13	0.14	1.86
B($1s^2$)	5	1	5.81	2.70	2.26
B($1s^2 2s^2$)	5	3	4.80	2.20	1.98
B($1s^2 2s^2 2p$)	5	4	3.41	2.16	0.24
C($1s^2$)	6	1	5.62	3.28	2.73
C($1s^2 2s^2$)	6	3	0	0	2.88
C($1s^2 2s^2 2p^2$)	6	5	1.90	0.81	2.52

Bibliography

[1] McDowell M R C and Coleman J P 1970 (Amsterdam, North Holland)

[2] Bransden B H and McDowell M H C 1992 *Charge Exchange and the Theory of Ion-Atom Collisions* (Oxford, Clarendon)

[3] Isler R C 1994 *Plasma Physics and Controlled Fusion* **36** 171 URL `http://stacks.iop.org/0741-3335/36/i=2/a=001`

[4] Skinner C H 2009 *Physica Scripta* **2009** 014022 URL `http://stacks.iop.org/1402-4896/2009/i=T134/a=014022`

[5] Delabie E, Brix M, Giroud C, Jaspers R J E, Marchuk O, O'Mullane M G, Ralchenko Y, Surrey E, von Hellermann M G, Zastrow K D and Contributors J E 2010 *Plasma Physics and Controlled Fusion* **52** 125008 URL `http://stacks.iop.org/0741-3335/52/i=12/a=125008`

[6] Mandl W, Wolf R C, von Hellermann M G and Summers H P 1993 *Plasma Physics and Controlled Fusion* **35** 1373 URL `http://stacks.iop.org/0741-3335/35/i=10/a=003`

[7] Summers H P 1994 **33** 275 – 319 ISSN 1049-250X URL `http://www.sciencedirect.com/science/article/pii/S1049250X08600397`

[8] `http://open.adas.ac.uk/`

[9] Fogle M, Wulf D, Morgan K, McCammon D, Seely D G, Draganić I N and Havener C C 2014 *Phys. Rev. A* **89**(4) 042705 URL `http://link.aps.org/doi/10.1103/PhysRevA.89.042705`

[10] de Vries J, Hoekstra R, Morgenstern R and Schlathölter T 2002 *Journal of Physics B: Atomic, Molecular and Optical Physics* **35** 4373 URL `http://stacks.iop.org/0953-4075/35/i=21/a=304`

[11] RR W 1946 *Radiology* **47** 48791

[12] Schardt D, Elsässer T and Schulz-Ertner D 2010 *Rev. Mod. Phys.* **82**(1) 383–425 URL http://link.aps.org/doi/10.1103/RevModPhys.82.383

[13] Boudaıffa B, Cloutier P, Hunting D, Huels M A and Sanche L 2000 *Science* **287** 1658–1660 ISSN 0036-8075 (*Preprint* http://science.sciencemag.org/content/287/5458/1658.full.pdf) URL http://science.sciencemag.org/content/287/5458/1658

[14] Montanari C C and Miraglia J E 2016 *Journal of Physics B: Atomic, Molecular and Optical Physics* **49** 175203 URL http://stacks.iop.org/0953-4075/49/i=17/a=175203

[15] Zhang C L, Hong X H, Wang F, Wu Y and Wang J G 2013 *Phys. Rev. A* **87**(3) 032711 URL http://link.aps.org/doi/10.1103/PhysRevA.87.032711

[16] Frémont F 2016 *Journal of Physics B: Atomic, Molecular and Optical Physics* **49** 065206 URL http://stacks.iop.org/0953-4075/49/i=6/a=065206

[17] Schenk G and Kirchner T 2015 *Phys. Rev. A* **91**(5) 052712 URL http://link.aps.org/doi/10.1103/PhysRevA.91.052712

[18] Ihani J S, Luna H, Wolff W and Montenegro E C 2013 *Journal of Physics B: Atomic, Molecular and Optical Physics* **46** 115208 URL http://stacks.iop.org/0953-4075/46/i=11/a=115208

[19] Wolff W, Luna H, Santos A C F, Montenegro E C and Sigaud G M 2009 *Phys. Rev. A* **80**(3) 032703 URL http://link.aps.org/doi/10.1103/PhysRevA.80.032703

[20] Losqui A L C, Zappa F, Sigaud G M, Wolff W, Sant'Anna M M, Santos A C F, Luna H and Melo W S 2014 *Journal of Physics B: Atomic, Molecular and Optical Physics* **47** 045202 URL http://stacks.iop.org/0953-4075/47/i=4/a=045202

[21] Labaigt G, Jorge A, Illescas C, Béroff K, Dubois A, Pons B and Chabot M 2015 *Journal of Physics B: Atomic, Molecular and Optical Physics* **48** 075201 URL http://stacks.iop.org/0953-4075/48/i=7/a=075201

[22] Abrines R and Percival I C 1966 *Proceedings of the Physical Society* **88** 861 URL http://stacks.iop.org/0370-1328/88/i=4/a=306

[23] Costley A, Sugie T, Vayakis G and Walker C 2005 *Fusion Engineering and Design* **74** 109 – 119 ISSN 0920-3796 proceedings of the 23rd Symposium of Fusion TechnologySOFT 23 URL http://www.sciencedirect.com/science/article/pii/S092037960500390X

[24] Illescas C and Riera A 1999 *Phys. Rev. A* **60**(6) 4546–4560 URL http://link.aps.org/doi/10.1103/PhysRevA.60.4546

[25] Errea L F, Guzmán F, Illescas C, Méndez L, Pons B, Riera A and Suárez J 2006 *Plasma Physics and Controlled Fusion* **48** 1585–1604

[26] Suarez J, Guzman F, Pons B and Errea L F 2013 *Journal of Physics B: Atomic, Molecular and Optical Physics* **46** 095701

[27] Guzmán F, Errea L F and Pons B 2009 *Phys. Rev. A* **80** 042708

[28] Kirschbaum C L and Wilets L 1980 *Phys. Rev. A* **21**(3) 834–841 URL http://link.aps.org/doi/10.1103/PhysRevA.21.834

[29] Zhou Y, Huang C, Liao Q and Lu P 2012 *Phys. Rev. Lett.* **109**(5) 053004 URL http://link.aps.org/doi/10.1103/PhysRevLett.109.053004

[30] Suarez J, Farantos S, Stamatiadis S and Lathouwers L 2009 *Computer Physics Communications* **180** 2025 – 2033

[31] Wohrer K, Chabot M, Rozet J P, Gardès D, Vernhet D, Jacquet D, Negra S D, Brunelle A, Nectoux M, Pautrat M, Beyec Y L, Attal P and Maynard G 1996 *Journal of Physics B: Atomic, Molecular and Optical Physics* **29** L755 URL http://stacks.iop.org/0953-4075/29/i=20/a=006

[32] Kirchner T, Lüdde H J, Horbatsch M and Dreizler R M 2000 *Phys. Rev. A* **61**(5) 052710 URL http://link.aps.org/doi/10.1103/PhysRevA.61.052710

[33] Belkić D 2009 *"Quantum Theory of High-Energy Ion-Atom Collisions"* (CRC Press)

[34] N Toshima T Ishihara A O and Watanabe T 1989 *Phys. Rev. A* **40** 2192

[35] Olson R 1981 *Phys. Rev. A* **24** 1726

[36] Errea L F, Illescas C, Méndez L, Pons B, Riera A and Suárez J 2004 *Phys. Rev. A* **70** 52713

[37] Hardie D J W and Olson R E 1983 *Journal of Physics B: Atomic and Molecular Physics* **16** 1983 URL http://stacks.iop.org/0022-3700/16/i=11/a=018

[38] D Eichenauer N G and Scheid W 1981 *J. Phys. B: At. Mol. Opt. Phys.* **14** 3929

[39] Cohen J S 1985 *J. Phys. B: At. Mol. Opt. Phys.* **18** 1759–1769

[40] Rakovic M J, Schultz D R, Stancil P C and Janev R K 2001 *Journal of Physics A: Mathematical and General* **34** 4753 URL http://stacks.iop.org/0305-4470/34/i=22/a=314

[41] Suárez J 2005 *Estudio comparativo clásico/cuántico de colisiones atómicas en plasmas de fusión termonuclear* Ph.D. thesis Université de Bordeaux-I / Universidad Autónoma de Madrid

[42] Illescas C 1998 *Tratamiento clásico de los procesos de ionización y captura en colisiones A^{q+} + H, H_2 a energías intermedias* Ph.D. thesis Universidad Autónoma de Madrid

[43] Reinhold C O and Falcón C A 1986 *Phys. Rev. A* **33** 3859

[44] Wigner E P 1932 *Phys. Rev.* **40** 749

[45] Becker R L and MacKellar A D 1984 *Journal of Physics B: Atomic and Molecular Physics* **17** 3923 URL http://stacks.iop.org/0022-3700/17/i=19/a=015

[46] Olson R E 1981 *Phys. Rev. A* **24**(4) 1726–1733 URL http://link.aps.org/doi/10.1103/PhysRevA.24.1726

[47] Becker R L and MacKellar A D 1979 *Journal of Physics B: Atomic and Molecular Physics* **12** L345 URL http://stacks.iop.org/0022-3700/12/i=12/a=004

[48] Cohen J S 1996 *Phys. Rev. A* **54**(1) 573–586 URL http://link.aps.org/doi/10.1103/PhysRevA.54.573

[49] Montemayor V J and Schiwietz G 1989 *Phys. Rev. A* **40**(11) 6223–6230 URL http://link.aps.org/doi/10.1103/PhysRevA.40.6223

[50] Olson R E 1979 *Journal of Physics B: Atomic and Molecular Physics* **12** L109 URL http://stacks.iop.org/0022-3700/12/i=3/a=008

[51] Wittkower A B, Levy G and Gilbody H B 1967 *Proceedings of the Physical Society* **91** 306 URL http://stacks.iop.org/0370-1328/91/i=2/a=307

[52] McClure G W 1968 *Phys. Rev.* **166**(1) 22–29 URL http://link.aps.org/doi/10.1103/PhysRev.166.22

[53] Talman J D and Shadwick W F 1976 *Phys. Rev. A* **14**(1) 36–40 URL http://link.aps.org/doi/10.1103/PhysRevA.14.36

[54] Talman J D 1989 *Computer Physics Communications* **54** 85 – 94 ISSN 0010-4655 URL http://www.sciencedirect.com/science/article/pii/0010465589900349

[55] http://cccbdb.nist.gov/energy2x.asp/

[56] Minami T, Pindzola M S, Lee T G and Schultz D R 2006 *Journal of Physics B: Atomic, Molecular and Optical Physics* **39** 2877

[57] Lanczos C 1950 *Journal of Research of the National Bureau of Standards* **45**

[58] Guantes R and Farantos S C 1999 *J. Chem. Phys.* **111** 10827–10835

[59] Fornberg B 1996 *A practical guide to pseudospectral methods* Cambridge monographs on applied and computational mathematics (Cambridge: Cambridge University Press) ISBN 0-521-49582-2 URL http://opac.inria.fr/record=b1098317

[60] Dundas D, McCann J F, Parker J S and Taylor K T 2000 *J. Phys. B: At. Mol. Opt. Phys.* **33** 3261

[61] Errea L, Illescas C, Méndez L, Rabadán I and Suárez J 2015 *Chemical Physics* **462** 17 – 22 ISSN 0301-0104

[62] Leforestier C, Bisseling R H, Cerjan C, Feit M D, Friesner R, Guldberg A, Hammerich A, Jolicard G, Karrlein W, Meyer H D, Lipkin N, Roncero O and Kosloff R 1991 *J. Comp. Phys.* **94** 59

[63] McGuire J H and Weaver L 1977 *Phys. Rev. A* **16** 41

[64] Ludde H J and Dreizler R M 1985 *Journal of Physics B: Atomic and Molecular Physics* **18** 107 URL http://stacks.iop.org/0022-3700/18/i=1/a=012

[65] Wohrer K and Watson R L 1993 *Phys. Rev. A* **48**(6) 4784–4786 URL http://link.aps.org/doi/10.1103/PhysRevA.48.4784

[66] Mezdari F, Wohrer-Béroff K, Chabot M, Martinet G, Negrâ S D, Désesquelles P, Hamrita H and LePadellec A 2005 *Phys. Rev. A* **72**(3) 032707 URL http://link.aps.org/doi/10.1103/PhysRevA.72.032707

[67] Jorge A, Errea L, Illescas C and Méndez L 2014 *The European Physical Journal D* **68** 227 ISSN 1434-6060

[68] Meyer F W, Howald A M, Havener C C and Phaneuf R A 1985 *Phys. Rev. A* **32**(6) 3310–3318 URL http://link.aps.org/doi/10.1103/PhysRevA.32.3310

[69] Goffe T V, Shah M B and Gilbody H B 1979 *Journal of Physics B: Atomic and Molecular Physics* **12** 3763 URL http://stacks.iop.org/0022-3700/12/i=22/a=021

[70] Igenbergs K 2011 *Calculation of Cross Sections Relevant for Diagnostics of Hot Fusion Plasmas* Ph.D. thesis University of Viena

[71] Jorge A, Illescas C, Miraglia J E and Gravielle M S 2015 *J. Phys. B: At. Mol. Opt. Phys.* **48** 235201

[72] Schultz D R, Reinhold C O and Olson R E 1992 *Phys. Rev. A* **46**(1) 666–669 URL http://link.aps.org/doi/10.1103/PhysRevA.46.666

[73] Reinhold C O and Falcón C A 1988 *Journal of Physics B: Atomic, Molecular and Optical Physics* **21** 2473 URL http://stacks.iop.org/0953-4075/21/i=13/a=014

[74] Suno H and Kato T 2006 *Atomic Data and Nuclear Data Tables* **92** 407 – 455

[75] Stancil P C, Gu J P, Havener C C, Krstic P S, Schultz D R, Kimura M, Zygelman B, Hirsch G, Buenker R J and Bannister M E 1998 *J. Phys. B: At. Mol. Opt. Phys.* **31** 3647

[76] Phaneuf R A, Meyer F W and McKnight R H 1978 *Phys. Rev. A* **17** 534–545

[77] Sant'Anna M M, Melo W S, Santos A C F, Shah M B, Sigaud G M and Montenegro E C 2000 *Journal of Physics B: Atomic, Molecular and Optical Physics* **33** 353 URL http://stacks.iop.org/0953-4075/33/i=3/a=305

[78] Ryufuku H and Watanabe T 1979 *Phys. Rev. A* **19** 1538

[79] Cornelius K R, Wojtkowski K and Olson R E 2000 *J. Phys. B: At. Mol. Phys.* **33** 2017

[80] Foster A 2008 *On the Behaviour and Radiating Properties of Heavy Elements in Fusion Plasmas.* Ph.D. thesis University of Strathclyde

[81] Janev R K 1983 *Physica Scripta* **1983** 208 URL http://stacks.iop.org/1402-4896/1983/i=T3/a=041

[82] Gravielle M S and Miraglia J E 1995 *Phys. Rev. A* **51** 2131

[83] Gravielle M S and Miraglia J E 1995 *Phys. Rev. A* **52**(1) 851–854 URL http://link.aps.org/doi/10.1103/PhysRevA.52.851

[84] Taulbjerg K 1983 *Electron Capture in Ion-Atom Collisions* (Boston, MA: Springer US) pp 349–388 ISBN 978-1-4613-3781-2 URL http://dx.doi.org/10.1007/978-1-4613-3781-2_10

[85] Miraglia J E 1982 *Journal of Physics B: Atomic and Molecular Physics* **15** 4205 URL http://stacks.iop.org/0022-3700/15/i=22/a=020

[86] Crothers D S F and Dubé L J 1992 *Advances in Atomic Molecular and Optical Physics* **30** 287–337

[87] Reinhold C O and Miraglia J E 1987 *Journal of Physics B: Atomic and Molecular Physics* **20** 1069 URL http://stacks.iop.org/0022-3700/20/i=5/a=023

[88] Gravielle M S and Miraglia J E 1988 *Phys. Rev. A* **38**(10) 5034–5037 URL http://link.aps.org/doi/10.1103/PhysRevA.38.5034

[89] Gravielle M S and Miraglia J E 1991 *Phys. Rev. A* **44**(11) 7299–7306 URL http://link.aps.org/doi/10.1103/PhysRevA.44.7299

[90] Toshima N 1994 *Phys. Rev. A* **50** 3940

[91] Harel C, Jouin H and Pons B 1998 *At. Data. Nucl. Data Tables* **68** 279

[92] Belkić D, Saini S and Taylor H S 1987 *Phys. Rev. A* **36** 1601–1617

[93] Igenbergs K, Schweinzer J, Veiter A, Perneczky L, Frühwirth E, Wallerberger M, Olson R E and Aumayr F 2012 *Journal of Physics B: Atomic, Molecular and Optical Physics* **45** 065203

[94] Meyer F W, Phaneuf R A, Kim H J, Hvelplund P and Stelson P H 1979 *Phys. Rev. A* **19**(2) 515–525 URL `http://link.aps.org/doi/10.1103/PhysRevA.19.515`

[95] Toshima N and Tawara H 1995 *Research Report NIFS-Data* **26**

[96] Schultz D R, Krstić P S and Reinhold C O 1996 *Physica Scripta* **1996** 69 URL `http://stacks.iop.org/1402-4896/1996/i=T62/a=012`

[97] Olson R E and Schultz D R 1989 *Physica Scripta* **1989** 71 URL `http://stacks.iop.org/1402-4896/1989/i=T28/a=013`

[98] Mandal C R, Datta S and Mukherjee S C 1983 *Phys. Rev. A* **28**(2) 1144–1146 URL `http://link.aps.org/doi/10.1103/PhysRevA.28.1144`

[99] Errea L F, Illescas C, Méndez L, Pons B, Riera A and Suárez J 2004 *Journal of Physics B: Atomic, Molecular and Optical Physics* **37** 4323 URL `http://stacks.iop.org/0953-4075/37/i=21/a=008`

[100] Saha G C, Datta S and Mukherjee S C 1987 *Phys. Rev. A* **36**(4) 1656–1662 URL `http://link.aps.org/doi/10.1103/PhysRevA.36.1656`

[101] Isler R C and Olson R E 1988 *Phys. Rev. A* **37** 3399

[102] Lisitsa V S, Bureyeva L A, Kukushkin A B, Kadomtsev M B, Krupin V A, Levashova M G, Medvedev A A, Mukhin E E, Shurygin V A, Tugarinov S N and Vukolov K Y 2012 *Journal of Physics: Conference Series* **397** 012015

[103] Hoekstra R, Anderson H, Bliek F W, von Hellerman M, Maggi C F, Olson R E and Summers H P 1998 *Plasma Phys. Control. Fusion* **40** 1541

[104] Summers H P, Anderson H, O'Mullane M G and von Hellermann M G 2001 *Physica Scripta* **2001** 80

[105] Kallenbach A, Dux R, Fuchs J C, Fischer R, Geiger B, Giannone L, Herrmann A, Lunt T, Mertens V, McDermott R, Neu R, Ptterich T, Rathgeber S, Rohde V, Schmid K, Schweinzer J, Treutterer W and Team A U 2010 *Plasma Physics and Controlled Fusion* **52** 055002

[106] Cariatore N D, Otranto S and Olson R E 2015 *Phys. Rev. A* **91** 042709

[107] Ryufuku H and Watanabe T 1979 *Phys. Rev. A* **20** 1828

[108] Ryufuku H, Sasaki K and Watanabe T 1980 *Phys. Rev. A* **21**(3) 745

[109] Pitts R, Carpentier S, Escourbiac F, Hirai T, Komarov V, Kukushkin A, Lisgo S, Loarte A, Merola M, Mitteau R, Raffray A, Shimada M and Stangeby P 2011 *Journal of Nuclear Materials* **415** S957 – S964

[110] Paméla J, Matthews G, Philipps V and Kamendje R 2007 *Journal of Nuclear Materials* **363-365** 1 – 11

[111] Neu R, Arnoux G, Beurskens M, Bobkov V, Brezinsek S, Bucalossi J, Calabro G, Challis C, Coenen J W, de la Luna E, de Vries P C, Dux R, Frassinetti L, Giroud C, Groth M, Hobirk J, Joffrin E, Lang P, Lehnen M, Lerche E, Loarer T, Lomas P, Maddison G, Maggi C, Matthews G, Marsen S, Mayoral M L, Meigs A, Mertens P, Nunes I, Philipps V, Pütterich T, Rimini F, Sertoli M, Sieglin B, Sips A C C, van Eester D, van Rooij G and Contributors J E 2013 *Physics of Plasmas* **20**

[112] Errea L F, Harel C, Jouin H, Méndez L, Pons B and Riera A 1998 *Journal of Physics B: Atomic, Molecular and Optical Physics* **31** 3527 URL `http://stacks.iop.org/0953-4075/31/i=16/a=007`

[113] Harel C, Jouin H, Pons B, Errea L F, Méndez L and Riera A 1997 *Phys. Rev. A* **55** 287

[114] Igenbergs K, Schweinzer J and Aumayr F 2009 *Journal of Physics B: Atomic, Molecular and Optical Physics* **42** 235206

[115] Igenbergs K 2011 *Calculation of Cross Sections Relevant for Diagnostics of Hot Fusion Plasmas* Ph.D. thesis Technischen Universität Wien

[116] Errea L F, Méndez L, Pons B, Riera A, Sevila I and Suárez J 2006 *Phys. Rev. A* **74** 012722

[117] Belkić D c v, Mančev I and Hanssen J 2008 *Rev. Mod. Phys.* **80**(1) 249–314 URL `http://link.aps.org/doi/10.1103/RevModPhys.80.249`

[118] Hill J, Geddes J and Gilbody H B 1979 *Journal of Physics B: Atomic and Molecular Physics* **12** 3341 URL http://stacks.iop.org/0022-3700/12/i=20/a=014

[119] Wang J, Hansen J P and Dubois A 2000 *Journal of Physics B: Atomic, Molecular and Optical Physics* **33** 241 URL http://stacks.iop.org/0953-4075/33/i=2/a=309

[120] cev I M 1995 *Physica Scripta* **51** 762 URL http://stacks.iop.org/1402-4896/51/i=6/a=010

[121] Dimitriou, K, Katsonis, K and Maynard, G 2000 *J. Phys. IV France* **10** Pr5–299–Pr5–302 URL http://dx.doi.org/10.1051/jp4:2000555

[122] Sattin F and Salasnich L 1998 *Physica Scripta* **58** 464 URL http://stacks.iop.org/1402-4896/58/i=5/a=007

[123] Shingal R and Bransden B H 1990 *Journal of Physics B: Atomic, Molecular and Optical Physics* **23** 1203 URL http://stacks.iop.org/0953-4075/23/i=7/a=016

[124] Ling L and Jian-Guo W 2007 *Chinese Physics Letters* **24** 3115 URL http://stacks.iop.org/0256-307X/24/i=11/a=027

[125] cev I M, Milojević N and Belkić D 2013 *EPL (Europhysics Letters)* **103** 23001 URL http://stacks.iop.org/0295-5075/103/i=2/a=23001

[126] Belkic D 1997 *Journal of Physics B: Atomic, Molecular and Optical Physics* **30** 1731 URL http://stacks.iop.org/0953-4075/30/i=7/a=011

[127] Belkić D 1997 *Nuclear Instruments and Methods in Physics Research Section B: Beam Interactions with Materials and Atoms* **124** 365 – 376 ISSN 0168-583X fast Ion-Atom Collisions URL http://www.sciencedirect.com/science/article/pii/S0168583X96010683

[128] Ermolaev A M 1988 *Journal of Physics B: Atomic, Molecular and Optical Physics* **21** 81 URL http://stacks.iop.org/0953-4075/21/i=1/a=007

[129] Errea L F, Harel C, Jimeno P, Jouin H, Méndez L and Riera A 1996 *Phys. Rev. A* **54**(1) 967–969 URL http://link.aps.org/doi/10.1103/PhysRevA.54.967

[130] Schon W, Krudener S, Melchert F, Rinn K, Wagner M and Salzborn E 1987 *Journal of Physics B: Atomic and Molecular Physics* **20** L759 URL http://stacks.iop.org/0022-3700/20/i=22/a=006

[131] Schön W, Krüdener S, Melchert F, Rinn K, Wagner M, Salzborn E, Karemera M, Szücs S, Terao M, Fussen D, Janev R, Urbain X and Brouillard F 1987 *Phys. Rev. Lett.* **59**(14) 1565–1568 URL http://link.aps.org/doi/10.1103/PhysRevLett.59.1565

[132] Melchert F, Krüdener S, Huber K and Salzborn E 1999 *Journal of Physics B: Atomic, Molecular and Optical Physics* **32** L139 URL http://stacks.iop.org/0953-4075/32/i=6/a=003

[133] Peart B, Grey R and Dolder K T 1976 *Journal of Physics B: Atomic and Molecular Physics* **9** 3047 URL http://stacks.iop.org/0022-3700/9/i=17/a=020

[134] Kirchner T, Horbatsch M and Lüdde H J 2002 *Phys. Rev. A* **66**(5) 052719 URL http://link.aps.org/doi/10.1103/PhysRevA.66.052719

[135] Muller H G 1999 *Phys. Rev. A* **60**(2) 1341–1350 URL http://link.aps.org/doi/10.1103/PhysRevA.60.1341

[136] Higuet J, Ruf H, Thiré N, Cireasa R, Constant E, Cormier E, Descamps D, Mével E, Petit S, Pons B, Mairesse Y and Fabre B 2011 *Phys. Rev. A* **83**(5) 053401 URL http://link.aps.org/doi/10.1103/PhysRevA.83.053401

[137] DuBois R D 1987 *Phys. Rev. A* **36**(6) 2585–2593 URL http://link.aps.org/doi/10.1103/PhysRevA.36.2585

[138] Rudd M E, Goffe T V and Itoh A 1985 *Phys. Rev. A* **32**(4) 2128–2133 URL http://link.aps.org/doi/10.1103/PhysRevA.32.2128

[139] Illescas C, Errea L F, Méndez L, Pons B, Rabadán I and Riera A 2011 *Phys. Rev. A* **83** 052704

[140] Hvelplund P, Liu B, Nielsen S B and Tomita S 2003 *International Journal of Mass Spectrometry* **225** 83 – 87 ISSN 1387-3806 URL http://www.sciencedirect.com/science/article/pii/S1387380602010394

[141] Postma J, Bari S, Hoekstra R, Tielens A G G M and Schlathölter T 2010 *The Astrophysical Journal* **708** 435 URL http://stacks.iop.org/0004-637X/708/i=1/a=435

[142] Holm A I S, Zettergren H, Johansson H A B, Seitz F, Rosén S, Schmidt H T, Ławicki A, Rangama J, Rousseau P, Capron M, Maisonny R, Adoui L, Méry A, Manil B, Huber B A and Cederquist H 2010 *Phys. Rev. Lett.* **105**(21) 213401 URL http://link.aps.org/doi/10.1103/PhysRevLett.105.213401

[143] McGrath C, McSherry D M, Shah M B, O'Rourke S F C, Crothers D S F, Montgomery G, Gilbody H B, Illescas C and Riera A 2000 *Journal of Physics B: Atomic, Molecular and Optical Physics* **33** 3693 URL http://stacks.iop.org/0953-4075/33/i=18/a=317

[144] Shah M B, McGrath C, Illescas C, Pons B, Riera A, Luna H, Crothers D S F, O'Rourke S F C and Gilbody H B 2003 *Phys. Rev. A* **67**(1) 010704 URL http://link.aps.org/doi/10.1103/PhysRevA.67.010704

[145] Jorge A, Errea L F, Illescas C and Méndez L 2016 *Phys. Rev. A* **93**(6) 066701 URL http://link.aps.org/doi/10.1103/PhysRevA.93.066701

[146] Meng L, Reinhold C O and Olson R E 1989 *Phys. Rev. A* **40** 3637

[147] Meng L, Reinhold C O and Olson R E 1990 *Phys. Rev. A* **42** 5286

List of publications

Refereed publications in journals

- Alba Jorge, L. F. Errea, Clara Illescas, and L. Méndez. Calculation of ionization and total and partial charge exchange cross sections for collisions of C^{6+} and N^{7+} with H. *The European Physical Journal D*, 68(8):227, 2014. http://dx.doi.org/10.1140/epjd/e2014-50109-4

- A Jorge, Clara Illescas, J E Miraglia, and M S Gravielle. Scaling for state-selective charge exchange due to collisions of multicharged ions with hydrogen. *Journal of Physics B: Atomic, Molecular and Optical Physics*, 48(23):235201, 2015. http://stacks.iop.org/0953-4075/48/i=23/a=235201

- G Labaigt, A Jorge, C Illescas, K Béroff, A Dubois, B Pons, and M Chabot. Electron capture and ionization processes in high-velocity C_n^+, C-Ar and C_n^+, C-He collisions. *Journal of Physics B: Atomic, Molecular and Optical Physics*, 48(7):075201, 2015. http://stacks.iop.org/0953-4075/48/i=7/a=075201

- A. Jorge, L. F. Errea, Clara Illescas, and L. Méndez. Comment on "classical description of $H(1s)$ and $H^*(n = 2)$ for cross-section calculations relevant to charge-exchange diagnostics". *Phys. Rev. A*, 93:066701, Jun 2016. http://link.aps.org/doi/10.1103/PhysRevA.93.066701

- A. Jorge, Clara Illescas, L. Méndez, and B. Pons. Switching classical trajectory monte carlo method to describe two-active-electron collisions. *Phys. Rev. A*, 94:022710, Aug 2016. http://link.aps.org/doi/10.1103/PhysRevA.94.022710

- A. Jorge, J. Suárez, Clara Illescas, L. F. Errea, and L. Méndez. Application of a grid numerical method to calculate state-selective cross sections for electron capture in $Be^{4+} + H(1s)$ collisions. *Phys. Rev. A*, 94:032707, Sep 2016. http://link.aps.org/doi/10.1103/PhysRevA.94.032707

Refereed publications in proceedings

- Alba Jorge, L F Errea, Clara Illescas, L Méndez, and J Suárez. Total and partial charge exchange and ionization cross sections for C^{6+} and N^{7+} colliding with $H(n = 1, 2)$. *Physica Scripta*, 2013(T156):014032, 2013. http://stacks.iop.org/1402-4896/2013/i=T156/a=014032,

- L F Errea, Clara Illescas, Alba Jorge, L Méndez, I Rabadán, and J Suárez. Calculation of total cross sections for electron capture in collisions of carbon ions with H(D,T)(1s). *Journal of Physics: Conference Series*, 576(1):012002, 2015. `http://stacks.iop.org/1742-6596/576/i=1/a=012002`

Posters and talks presented at conferences.

- 16^{th}International Conference Physics of Highly Charged Ions (HCI). Poster contribution. Heidelberg, Germany, 2012
- V Jornadas de Jóvenes Investigadores en Física Atómica y Molecular. Oral contribution. Madrid, Espaa, 2013
- XII Iberian Meeting on Atomic and Molecular Physics (IBER2013). Poster contribution. Sevilla, Espaa, 2013
- 17^{th} International Conference Physics of Highly Charged Ions (HCI). Poster contribution. San Carlos de Bariloche, Argentina, 2014
- VII Jornadas de Jóvenes Investigadores en Física Atómica y Molecular. Oral contribution. Jaén, Espaa, 2015
- 24^th International Symposium on Ion Atom Collisions (ISIAC). Poster contribution. Barcelona, Spain, 2015.
- XXIX International Conference on Photonic, Electronic and Atomic Collisions (ICPEAC). Poster contribution. Toledo, Espaa, 2015

List of Figures

Acronyms

- ADAS: Atomic Data and Analysis Structure
- AOCC: Atomic Orbital Close-Coupling
- CDW: Continuum Distorted Wave
- CTMC: Classical Trajectory Monte Carlo
- CXRS: Charge Exchange Recombination Spectroscopy
- EIA: Eikonal Impulse Approximation
- FBA: First Born Approximation
- GTDSE: Grid Time Dependent Schórodinger Equation
- IAE: Independent Atom Electron
- IPA: Impact Parameter Approximation
- IPM: Independent Particle Model
- MOCC: Molecular Orbital Close-Coupling